Application of Small Angle X-ray Scattering for the Characterization and Quality Control of Lipid mRNA Delivery Systems

Dissertation

zur Erlangung des Grades

„Doktor der Naturwissenschaft“

im Promotionsfach Pharmazie

am Fachbereich Chemie, Pharmazie, Geographie und Geowissenschaften

der Johannes Gutenberg-Universität Mainz

vorgelegt von

Christoph Wilhelmy

geboren in Mayen

Mainz, 2025

Dekanin: Univ.-Prof. Dr. Eva Rentschler
Erster Berichterstatter:
Zweiter Berichterstatter:

Tag der mündlichen Prüfung: 18.12.2025

Declaration of Authorship

I hereby declare that I wrote this doctoral thesis entitled “Application of Small Angle X-ray Scattering for the Characterization and Quality Control of Lipid mRNA Delivery Systems” without any external assistance and used only sources acknowledged in this work. The work was carried out entirely while in candidature for the research degree at the Johannes Gutenberg-University Mainz. All textual passages that are appropriated verbatim or paraphrased from published and unpublished texts are duly indicated and listed in accordance with bibliographical rules.

Mainz, 15.09.2025

_____

Christoph Wilhelmy

Usage of artificial intelligence (AI) tools

AI-Tool	Utilization	When
Microsoft Word integrated spelling & grammar examination **Grammarly**	Language support for American English	Throughout the entire thesis
DeepL Translate	Translation of single words and expressions into American English	Throughout the entire thesis
Elicit **Google scholar**	Literature research, finding relevant publications for distinct questions	Throughout the introduction

Danksagung

Zusammenfassung

mRNA basierte Arzneimittel repräsentieren eine neue Generation therapeutischer Ansätze mit vielseitigem Anwendungsgebiet. Die COVID-19 Pandemie im Jahr 2020 zeigte, dass ein großer Vorteil dieser Plattform ihre flexible Anpassungsfähigkeit an verschiedene Krankheiten ist. Neben der mRNA, die als Wirkstoff für die gewünschten Proteine codiert, stellt das Trägersystem einen wichtigen Bestandteil der Formulierung dar. Lipidbasierte Trägersysteme, wie zum Beispiel Lipid Nanopartikel, haben sich dabei als Goldstandard etabliert. Anders als bei klassischen Arzneiformen, bei denen Wirk- und Hilfsstoffe klar unterschieden werden können, fällt diese Differenzierung bei mRNA-basierten Arzneimitteln schwerer, da deren komplexe Formulierung nicht nur die Nukleinsäuren schützt und zur Zelle befördert, sondern auch die Wirksamkeit beeinflusst. Ein tiefgehendes Verständnis der strukturellen Organisation der Systeme ist daher sowohl für die Formulierungsentwicklung als auch für die Qualitätsbewertung von zentraler Bedeutung.

In den vergangenen Jahren wurde erheblicher Aufwand in die Entwicklung neuer Lipide und Herstellungsmethoden investiert, um eine Produktion verbesserter Lipidvehikel in skalierbaren Prozessen zu ermöglichen. Da bislang nur wenige rationale Ansätze zur Formulierungsentwicklung existieren, gestaltet sich das Screening neuer Lipide hinsichtlich ihrer Aktivität als zeit- und ressourcenintensiv. Dabei besteht die Gefahr, dass vielversprechende Kandidaten in frühen Entwicklungsphasen ausgeschlossen werden. Struktur-Wirkungs-Beziehungen sowie die Identifikation struktureller Merkmale mit prognostischer Aussagekraft zur Wirksamkeit können hier einen entscheidenden Beitrag zur Effizienzsteigerung beitragen. Mit der Zulassung der ersten mRNA-basierten Arzneimittel rücken auch regulatorische Anforderungen an Qualität, Wirksamkeit und Unbedenklichkeit zunehmend in den Fokus. Erste Leitlinien von Zulassungsbehörden definieren mittlerweile zentrale Qualitätsmerkmale und schaffen damit den Rahmen für die Bewertung entsprechender Formulierungen.

In dieser Arbeit wurde vor allem die Kleinwinkelröntgenstreuung- ergänzt durch weitere analytische Methoden- genutzt, um lipidbasierte mRNA-Trägersysteme im Detail zu charakterisieren und deren strukturelle Eigenschaften mit der Potenz in *in vitro* und *in vivo* Modellen zu korrelieren. Strukturaufklärung durch Kleinwinkelröntgenstreuung liefert dabei wertvolle Einblicke in die innere Struktur und allgemeine Morphologie der Nanopartikel. Dies ermöglicht die Detektion qualitätsrelevanter Merkmale sowie wirksamkeitsvoraussagender Struktureinheiten. Zusammengefasst ermöglichen die Ergebnisse dieser Arbeit, ein tieferes Verständnis von Struktur-Wirkungs-Beziehungen bei lipidbasierten mRNA-Trägersystemen, die in

Zukunft sowohl für die Entwicklung verbesserter Plattformen als auch für die Bewertung der Qualität dieser Systeme herangezogen werden können.

Abstract

mRNA-based drugs represent a novel class of therapeutics applicable in various treatments. As the COVID-19 pandemic in 2020 demonstrated, this platform enables the rapid development of drugs against emerging infectious diseases due to its flexible adaptability. Besides the mRNA, which encodes the desired proteins, the carrier system that delivers the mRNA to target cells is a crucial component of the formulation. Lipid-based carrier systems, such as lipid nanoparticles (LNPs), have established themselves as the gold standard for delivery. Unlike traditional drug formulations, where active pharmaceutical ingredients and excipients can be clearly distinguished, this differentiation is more challenging for mRNA-based drugs. The complex lipid composition not only protects and delivers the nucleic acids to cells but also influences efficacy. A deep understanding of the intermolecular interactions within these systems and their structural organization is therefore of great interest not only for formulation development but also for addressing quality issues.

In recent years, significant efforts have been made to develop new carrier systems, including novel lipids and manufacturing methods, to enable the production of improved lipid vehicles through scalable processes. Since only a few paradigms for rational lipid synthesis and formulation development exist, screening new lipids for their activity using *in vitro* and *in vivo* models remains a time-consuming process. Additionally, there is a risk that highly potent candidates may be excluded from further development at early stages. Here, structure-activity relationships and the identification of structural fingerprints that can predict high efficacy can help conserve resources and facilitate more efficient formulation development.

With the approval of the first mRNA-based drugs, the quality and safety requirements for these drugs must also be addressed. During the rapid approval process of the pandemic, not all quality standards were established; however, in the years that followed, initial guidelines from regulatory authorities emerged, defining the key quality attributes and setting the framework for the quality control of such formulations.

In this work, small angle X-ray scattering (SAXS) was used in conjunction with other characterization methods to elucidate the properties of lipid-based mRNA carrier systems and correlate their structural properties with potency in *in vitro* and *in vivo* models. Structural elucidation through SAXS can provide valuable information about the internal structure of nanoparticles and their overall morphology. This enables the detection of quality-relevant features and structural units that are indicative of high potency. In summary, the results of this work provide a deeper understanding of structure-activity relationships in lipid-based mRNA carrier systems, which can be used for both the development of improved platforms and the quality assessment of these systems in the future.

General Remarks

This work is divided into seven chapters. In Chapter 1, the theoretical background is examined, followed by general introductions to the two subprojects in Chapter 2, which discuss the motivation for the respective research work. The two subprojects are presented and discussed in Chapters 3 and 4. Each project is represented by accepted publications, which are accompanied by a brief summary that highlights the scientific objectives and key findings of the project, as well as the authors' contributions. The published text and supporting information of the respective publications are attached with permission from the journals. In Chapter 5, the results of the work are discussed, and an outlook for future research is presented. Chapter 6 provides the Lists of Figures, Tables, and Abbreviations, whereas in Chapter 7, the references for the general texts can be found.

All Figures were prepared originally using QTIPlot 5.12.8 and Adobe Illustrator 2025 if not mentioned otherwise.

List of Content

Declaration of Authorship III

Usage of artificial intelligence (AI) tools V

Danksagung VII

Zusammenfassung IX

Abstract XI

General Remarks XIII

List of Content XV

1 Theoretical Background 1

1.1 Messenger RNA Therapy and Challenges 1

1.2 Evolution of lipid formulations for drug delivery 5
1.2.1 Development of the first liposomal drug products 5
1.2.2 Development of lipid-based drug products for nucleic acid delivery 7

1.3 Manufacturing of lipoplexes and lipid nanoparticles 13
1.3.1 Production methods for lipoplex formulation 13
1.3.2 Manufacturing of lipid nanoparticles 15

1.4 State-of-the-art composition of RNA LNPs 17
1.4.1 Ionizable lipids 18
1.4.2 Phospholipids 20
1.4.3 Cholesterol 21
1.4.4 PEGylated lipids 22

1.5 Characterization and quality control of lipid delivery systems for RNA 24
1.5.1 General remarks about the quality of the mRNA drug product 26
1.5.2 Size-related quality attributes of mRNA LNPs and their determination 28

1.6 Structural analysis using small angle X-ray scattering 33

2 Subprojects and scientific aims 37

2.1 Subproject 1: Coupling of Asymmetrical-Flow Field-Flow Fractionation (AF4) and Small Angle X-ray Scattering (SAXS) for Enhanced Characterization of Lipid mRNA Delivery Systems 37
2.1.1 Publications obtained in this project 38

2.2 Subproject 2: In-Depth Characterization and Structure-Function-Correlation of mRNA Lipid Nanoparticles using Small Angle X-ray Scattering (SAXS) 39
2.2.1 Publications obtained in this subproject 40

3 Subproject 1: Coupling of Asymmetrical-Flow Field-Flow Fractionation (AF4) and Small Angle X-ray Scattering (SAXS) for Enhanced Characterization of Lipid mRNA Delivery Systems 41

3.1 Quantitative Size-Resolved Characterization of mRNA Nanoparticles by In-Line Coupling of Asymmetrical-Flow Field-Flow Fractionation with Small Angle X-ray Scattering 41
3.1.1 Summary and Contributions 41
3.1.2 Publication 44
3.1.3 Supporting Information 57

4 Subproject 2: In-Depth Characterization and Structure-Function-Correlation of mRNA Lipid Nanoparticles using Small Angle X-ray Scattering (SAXS) 65

4.1 Polysarcosine-Functionalized mRNA Lipid Nanoparticles Tailored for Immunotherapy 65
4.1.1 Summary and Contributions 65
4.1.2 Publication 68
4.1.3 Supporting Information 85

4.2 On the Influence of Fabrication Methods and Materials for mRNA-LNP Production: From Size and Morphology to Internal Structure and mRNA Delivery Performance In Vitro and In Vivo 89
4.2.1 Summary and Contributions 89
4.2.2 Publication 92
4.2.3 Supporting Information 106
4.3 Direct structural investigation of pH responsiveness in mRNA LNPs: refining paradigms 113
4.3.1 Summary and Contributions 113
4.3.2 Publication 116
4.3.3 Supporting Information 127
5 Discussion and Outlook 139
6 Appendix 149
6.1 List of Figures 149
6.2 List of Tables 152
6.3 List of Abbreviations 153
7 References 158
Curriculum Vitae 175

1

Theoretical Background

1.1 Messenger RNA Therapy and Challenges

Messenger RNA (mRNA) is an intermediate carrier for genetic information from gene to protein, being produced by transcription of DNA in the nucleus of the cell and subsequently transferred to the cytosol for translation into proteins at the ribosomes [1]. With the outbreak of the COVID-19 pandemic and the subsequent authorization of the first drug products, mRNA-based therapeutics have demonstrated their potential as a versatile platform for treating and preventing various diseases, including infectious diseases and oncology, among others. The short timeframes from target identification to phase 1 studies, the convincing safety profile of mRNA vaccines after being applied throughout the world, and the flexibility for adoption to every target protein underscore the potential that mRNA drug products may have in the future [2,3]. Using mRNA as an active pharmaceutical ingredient (API) was first investigated about thirty years ago, when mRNA was directly injected intramuscular, where it mediated protein expression at the site of injection [4,5]. Due to its low stability, other nucleic acid platforms, such as plasmid DNA, appeared to be more promising. Nevertheless, research in the field of mRNA therapeutics has paved the way from basic research to clinical trials and ultimately to application in approved drug products [6]. One advantage of RNA products over DNA-based therapeutic platforms is that they do not need to enter the nucleus of the cell to be functional, but only need to reach the cytosol of the targeted cell. Additionally, mRNA must not be integrated into the genome of the cell to possess functionality and therefore does not pose the risk of mutagenesis, and is only transiently active and completely degraded *in vivo* [5,7].

mRNA for therapeutic application is engineered to structurally resemble naturally occurring mRNA in the cell and is produced by *in vitro* transcription from a DNA template. Therefore, like natural mRNA, it is single-stranded, with a 5’ cap and a 3’ poly(A) tail, an open reading frame that encodes the desired protein, and untranslated regions at both the 5’ and 3’ termini. While extensive research has been invested in enhancing the translation and stability of mRNA, by nucleoside modifications or modifications of the poly(A) tail or the 5’ cap [8–11], the mRNA needs to be delivered to the desired cell using nanoparticulate vehicles to exhibit therapeutic efficiency.

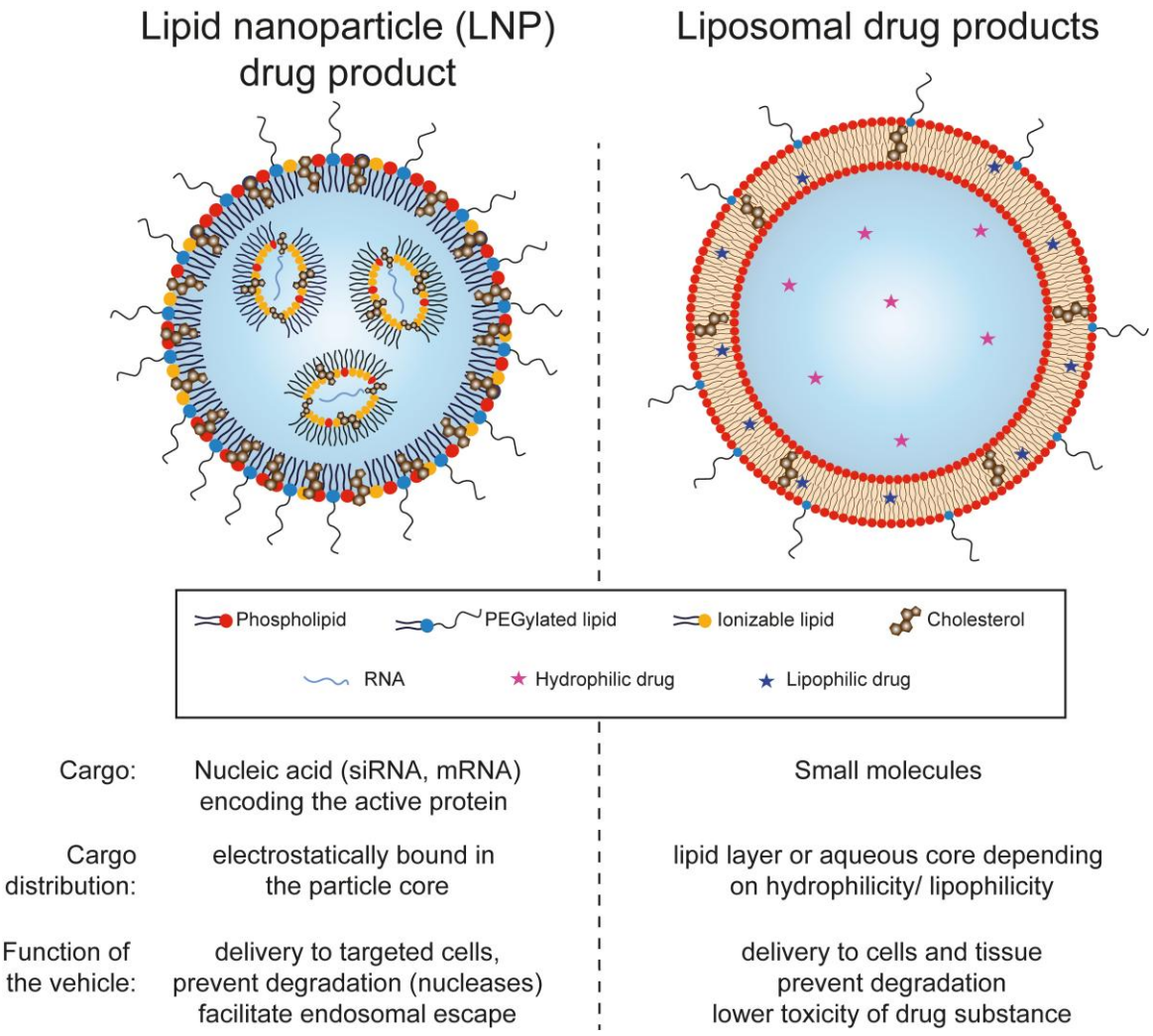

Figure 1.1-1: Comparison between structure and function of LNP vehicles tailored for nucleic acid delivery and classic liposomal drug carriers used in many approved drug products.

To date, lipidic delivery platforms are the gold standard, with lipid nanoparticles (LNPs) being the most clinically advanced nucleic acid delivery system already used within the authorized drug products. They differ from classic liposomal drug products in their composition, the cargo's binding, and the lipid vehicle's function (Figure 1.1-1). While liposomal drugs mostly stabilize the drug substance against degradation and lower the toxicity of the drug substance after application, LNPs actively facilitate cell uptake (e.g., endosomal uptake) by electrostatic interaction with endosomal membranes. Nevertheless, there remains space for further improvement, and many implications of LNPs remain unclear to the community.

One example of questions that occurred during the rapid development of the two mRNA-based COVID-19 vaccines was the stability and storage conditions of the drug products. One limitation of using these vaccines was the requirement for frozen storage, which complicated distribution throughout the world, especially in third-world countries with tropical climate conditions. The long-term storage integrity of the two vaccines, Comirnaty® and SpikeVax®, was only achieved at

subzero temperatures; however, upon thawing, the shelf life was significantly decreased [12]. Stability investigations revealed several reasons for the limited stability of the mRNA drug products, which also led to rapid formulation modifications to ease the storage of the vaccines. For example, it has been proposed that the ionizable amino lipids used in LNP formulations are a potential source of reactive electrophilic impurities, which are generated through the N-oxidation of the tertiary amine and subsequent hydrolysis. The resulting reactive aldehydes can form covalent adducts with the mRNA, leading to the inactivation of the nucleic acid cargo [12,13]. While the BioNTech/Pfizer vaccine Comirnaty® was initially formulated in a phosphate buffer (PBS buffer containing KCl/NaCl), the formulation was later modified to a second-generation formulation containing a Tris buffer, resulting in a prolonged storage time in the refrigerator in a non-frozen state [14]. Besides the avoided disadvantage of phosphate buffers during freezing because of its potential pH shifts, the Tris buffer also acts as a scavenger with aldehyde impurities, thereby reducing mRNA-lipid adduct formation [12,15]. Additionally, research was conducted on redesigning the ionizable lipid component to make it more susceptible to the described thermal instability. Here, piperidine-based lipids exhibited extended long-term stability at a non-frozen liquid state [16]. Another factor that determines stability is the shaking stress applied to it during, for example, distribution throughout the world. Here, vials with lower fill volumes resulting in higher headspace volumes are more sensitive to shear stress, which is a problem since the mRNA vaccine formulation is distributed in vials with relatively high headspace volumes [17]. Prefilled syringes would be beneficial in this regard, but they lack performance during freezing due to volume expansion. Nevertheless, Moderna recently marketed mRESVIA®, an mRNA LNP-based vaccine against respiratory tract disease caused by RSV, packed in prefilled syringes that require long-term storage in frozen conditions [18]. This highlights how research can lead to modifications in the formulation and packaging of approved drug products, and how this emerging delivery platform is still in its infancy, with considerable room for further improvement.

Other open questions include the delivery of LNPs to tissues beyond the liver [19,20]. The first nucleic acid-based drug product, Onpattro®, a small interfering RNA (siRNA) carrying LNP for the treatment of polyneuropathies in patients with hereditary transthyretin-mediated amyloidosis, was marketed in 2018 [21]. Its potency in inhibiting the synthesis of the transthyretin protein within hepatocytes was found to be mediated by a passive targeting of LNPs towards liver tissue due to adsorption of apolipoprotein B (apoE) onto the LNP. ApoE is an endogenous targeting ligand for the low-density lipoprotein receptor expressed on hepatocytes and therefore enables the successful delivery of the siRNA LNPs to the tissue of interest [22,23]. While this ability was crucial for the potency of Onpattro®, it hinders the delivery of nucleic acid LNPs towards other tissues, which need to be addressed to treat other diseases. To date, much research has been done on active and passive targeting strategies to overcome liver accumulation of LNPs. Active targeting strategies

focus on the modification of nanoparticle surfaces with biological or chemical moieties that allow selective binding to receptors of the targeted cell types. These moieties include antibodies, antibody fragments, peptides, or sugars, among others [20,24]. While active targeting is a straightforward approach to deliver nucleic acids to the desired tissues, it comes along with difficulties and costs of large batch production and *in vivo* stability. Passive targeting utilizes the variation of lipid composition to modify the physicochemical properties, such as size and surface composition, and subsequently the *in vivo* behavior of the formulation, such as the formation of a defined protein corona. For example, the addition of a permanently positively or negatively charged lipid to the standard LNP formulation mediated higher affinity to non-liver tissues like the spleen or the lung [25,26] and allowed for T-cell transfection within the spleen in the case of anionic lipids [27]. For passive targeting, it is crucial to gather as much information as possible about the physicochemical properties of the formulation to understand the advantages and disadvantages of certain formulations and to further develop novel drug product candidates on a rational basis.

Other frequently discussed challenges within the LNP research community cover the limited endosomal escape success [28], the formation of lipidic substructures (so-called blebs) and other particle inhomogeneities [29,30] as well as whether and to what extent there are empty LNPs, which do not carry mRNA [30]. Empty LNPs are frequently discussed within the research community because of potentially beneficial properties on the overall potency of the drug product. For example they are hypothesized to have a preference for phagocytic cells which would keep them occupied and improve non-phagocytic mRNA delivery. Controversially, the coexistence of empty and loaded LNPs rises questions of dose homogeneity and safety of the drug product[30]. Therefore gaining information about the extent and the morphology of unloaded LNPs could provide guidance on their actual effects on the formulations[31]. Along with these scientific questions, the ambition towards international standardization of analytical methods to characterize the novel drug products is rising. The need for analytical protocols to investigate chemical composition, drug loading, as well as particle size, size distribution profiles, and stability of the drug substance and drug product, led to many efforts towards novel methods and regulatory frameworks [32].

This highlights that, although first drug products have entered the market worldwide, many questions remain unanswered, and research in formulation development and quality determination is still in an evolving stage. In this work, the development and quality determination of LNP delivery systems are described from the perspective of structural analysis, aiming to elucidate further structure-function relationships that can inform future tailored formulation development.

1.2 Evolution of lipid formulations for drug delivery

1.2.1 Development of the first liposomal drug products

While the term LNPs came into use in the 1990s, when the era of nanotechnology began, the earliest lipidic nanosized particles were described in the 1960s, where the formation of closed lipid bilayer vesicles, which form spontaneously in water, was first reported [33]. While liposomes were initially primarily used as a model to study cellular membranes, this observation led to the development of colloidal drug delivery systems, an entirely new field of research in pharmaceutical technology. Following the first attempts at enzyme encapsulation for treatment of storage diseases [34,35], the delivery of small molecules with low water solubility became the focus of interest in the following years [36]. Within these molecules, cytotoxic drugs soon became popular cargos for cancer chemotherapy [37]. Longer circulation times and targeted delivery to malignant tissues were expected to enhance potency while reducing toxicity. Despite promising *in vitro* and *in vivo* results, early liposomal formulations lacked the necessary tissue selectivity and were predominantly taken up by the liver and spleen [38]. Besides the first attempts of active targeting strategies, using targeting ligands like antibodies and peptides on the liposome surface [39], improvement in circulation time and behavior was utilized to exploit tumor-related pathophysiological differences to normal tissue to enhance passive targeting (for example through the enhanced permeability and retention (EPR) effect) [40]. Especially the utilization of PEGylation, which was first described to alter the immunological properties of bovine serum albumin [41], triggered the development of long-circulating "stealth" liposomes [42,43]. These efforts led to the approval of the first liposomal drug product, Doxil®, by the United States Food and Drug Administration (FDA) in 1995 [44–46], providing higher potency and lower toxicological effects (e.g., cardiotoxicity, as the main dose-limiting factor) than unencapsulated doxorubicin [47]. Subsequently, more liposome-based drug products were approved in the late 1990s and 2000s, with applications in chemotherapy (e.g., DaunoXome®, DepoCyt®), antifungal therapy (e.g., Abelcet®, Ambisome®), and analgesic therapies (e.g., DepoDur®, Exparel®) among others [48,49]. To conclude the concepts for formulation development of most parenteral liposomal drug products, the lipidic vehicles should be smaller than 100 nm in diameter, composed of lipids that promote long circulation half-lives (PEGylated lipids for stealth properties, 1,2-distearoyl-sn-glycero-3-phosphocholin (DSPC) as phospholipid for rigid liposomes) and manufactured by procedures enabling encapsulation efficacy of approximately 100% [6]. To date, several drug products utilizing liposomal delivery systems have been authorized by the FDA or the European Medicines Agency (EMA) (Table 1.2-1), with applications primarily focused on cancer chemotherapy but also including infectious diseases and other conditions.

Table 1.2-1: Selection of parenteral liposomal drug products being approved by the FDA or EMA with their respective details and indications. List adopted from [50,51]

Drug product	API	Company	Year	Indication
Doxil®/Caelyx®	Doxorubicin	Baxter	1995 (FDA)/ 1996 (EMA)	Ovarian cancer, Kaposi´s sarcoma, multiple myeloma, metastatic breast cancer (only EMA)
AmBisome®	Amphotericin B	Astellas Pharma	1997 (FDA)	Fungal infections, visceral leishmaniasis, cryptococcal meningitis
Myocet®	Doxorubicin	CHEPLAPHARM Arzneimittel GmbH	2000 (EMA)	Metastatic breast cancer
Visudyne®	Verteporfin	Bausch + Lomb (FDA), CHEPLAPHARM Arzneimittel (EMA)	2000 (FDA, EMA)	Macular degeneration, degenerative myopia, ocular histoplasmosis
Mepact®	Mifamurtide	Takeda	2009 (EMA)	Osteosarcoma
Exparel®	Bupivacaine	Pacira	2011 (FDA), 2020 (EMA)	Post-operative pain
Onivyde®	Irinotecan	Ipsen Biopharmaceuticals (FDA), Les Laboratories Servier (EMA)	2015 (FDA), 2016 (EMA)	Pancreatic adenocarcinoma
Vyxeos®	Daunorubicin, Cytarabine	Celator Pharmaceuticals (FDA), Jazz Pharmaceuticals (EMA)	2017 (FDA), 2018 (EMA)	Acute myeloid leukemia

1.2.2 **Development of lipid-based drug products for nucleic acid delivery**

After the discovery of the DNA double helix structure in 1958 [52] and the beginning of modern biotechnologies in the 1970s, which enabled the synthesis of mRNA [53], the concept of gene therapy is rooted in basic science [6]. While the above-mentioned drug products were designed to deliver small molecules, advances in understanding the cellular pathogenesis of tumors and other diseases have triggered research into the delivery of nucleic acids as APIs. Encapsulation in potent delivery vehicles is crucial for the therapeutic performance of nucleic acids, since (i) passive cellular uptake of nucleic acids is hindered by the negative charge and (ii) high hydrophilicity, and in-circulation stability is impeded by serum protein association, phagocytic uptake, and rapid degradation by nucleases [54]. Within the lipidic delivery systems, the use of neutral liposomes was described for the encapsulation of RNA in 1978 [55]. Despite the entrapped RNA being protected from ribonuclease degradation and proving to be active after liposome disruption, no sufficient drug loading levels were obtainable [55]. Subsequently, cationic lipids were developed to form stable complexes with anionic nucleic acids [56,57]. While the encapsulation of nucleotides benefits from the positive charge excess, *in vitro* and *in vivo* toxicity has been observed, leading to inflammation, embolism, and organ-specific toxicity depending on the route of administration [58]. Additionally, the positive charge facilitated complement activation, nonspecific interactions with blood and immune system components, and plasma clearance [59,60]. Initial attempts to address these issues resulted in formulations with very low amounts of cationic lipid, showing longer circulation times and lower toxicity levels, but lacked a scalable manufacturing process [61]. The development of ionizable cationic lipids, bearing a tertiary amine group instead of a quaternary ammonium salt, exposed lower toxicity levels, while maintaining the beneficial positive charge excess for mRNA binding at acidic pH [57,62]. The amine group pK_a of these lipid excipients should be chosen so that within physiological conditions ($pH>pK_a$) the overall charge is near neutral, while in acidic conditions ($pH<pK_a$) the lipids are positively charged. This enables high circulation stability at neutral pH, while providing strong complexation and thus high incorporation of nucleic acids in acidic manufacturing buffers. Early studies demonstrated that by mixing liposomes, comprising the ionizable lipid DODAP and phospholipids, with nucleic acid in acidic buffer, high encapsulation of nucleic acid cargo alongside long circulation half-lives following i.v. administration was achieved [63]. This ultimately led to the development of modern lipid nanoparticle formulations for RNA delivery, which peaked with the approval of the first mRNA drug products in 2020 [64].

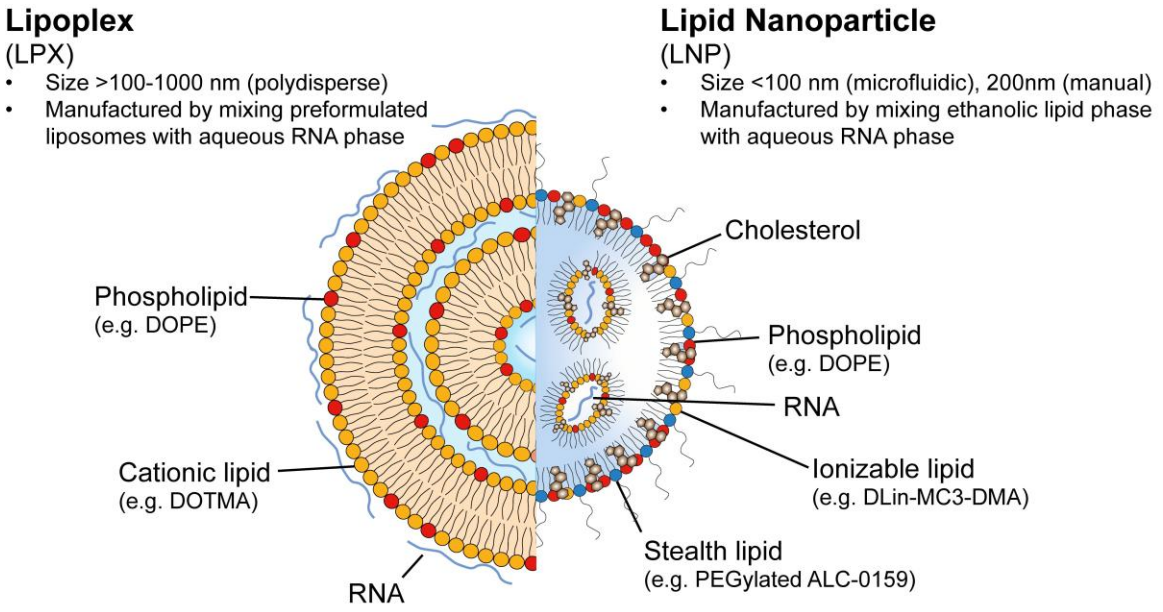

Figure 1.2-1: Schematic overview of the two main lipid delivery systems for mRNA: lipoplexes (LPX) and lipid nanoparticles (LNPs). The main differences are lipid composition, manufacturing process, and subsequently size and internal organization. Further implications are discussed in the following chapters

In this work, two types of lipid delivery systems were investigated (Figure 1.2-1): lipoplexes (LPX) and lipid nanoparticles (LNPs).

Lipoplexes were first described as the complex of cationic lipids with nucleic acids in the 1990s [65]. For the manufacturing of these systems, liposomes consisting of cationic lipids (e.g., DOTMA) and helper phospholipids (e.g., DOPC) were formed through dispersion in aqueous media and subsequent sonication to clarity [56]. After mixing these lipid vesicles with nucleic acids (as first described with plasmid DNA), lipoplexes are formed, carrying the cargo electrostatically bound either externally on their surface or internally enclosed by lipid bilayers. To produce liposomes, various approaches can be employed, including thin-film hydration processes and rapid ethanol injection in aqueous media (see Chapter 1.3.1). Despite the above-mentioned disadvantages regarding toxicity, cationic lipoplexes are one of the most studied lipid nano-vectors for RNA delivery, with *in vivo* studies on various routes of administration [66] (see Table 1.2-2). Not surprisingly, the composition of the lipid delivery system has a major influence on the therapeutic performance of the lipoplex formulations. For example, it has been demonstrated that adjusting the charge ratio of the formulation by varying the lipid-to-RNA ratio (N/P ratio) leads to targeting of different tissues or cell types [67]. There, negatively charged mRNA lipoplexes (formulated with an excess of mRNA) predominantly targeted the spleen, whereas those composed of an excess of cationic lipid triggered protein expression, especially in the lung, independently of the used lipids. Additionally, as shown for small-molecule-carrying liposomes, introduction of a PEG moiety led

to longer circulation times and subsequently to a higher probability of targeting solid tumors [68]. Despite considerable efforts in research, no lipoplex-based formulations have been approved for therapeutic use in humans to date. Nevertheless, lipoplex-based approaches are currently being investigated in clinical studies. One example, based on the delivery of mRNA encoding four different tumor antigens used for advanced malignant melanoma, is FixVac-BNT111 by BioNTech, currently in a Phase II trial in combination with cemiplimab [69]. Besides other ongoing clinical trials using the same lipid formulation platform (FixVac), which delivers mRNA encoding fixed tumor antigens, individualized immunotherapies are also being investigated using lipoplexes for delivery of mRNA encoding for patient-specific neoantigens. One example here is BNT122, which is investigated in a Phase II trial, for example, in patients with pancreatic ductal adenocarcinoma, colorectal cancer, and advanced melanoma [66].

Table 1.2-2: Selection of mRNA lipoplex based candidates currently being investigated in clinical trials adopted from [66]

Drug name	Developer/ Sponsor	Indication	Lipid platform	Stage	Trail number (NCT-number)
BNT111/ mRNA	BioNTech SE	Melanoma	LPX	II	NCT04526899
BNT113/ mRNA	BioNTech SE	Head and neck cancer	LPX	II	NCT04534205
BNT116/ mRNA	BioNTech SE	Non-small cell lung cancer	LPX	II	NCT04526899
Autogene cevumeran/ mRNA (patientspecific)	BioNTech SE	Colorectal Cancer	LPX	II	NCT04486378
Autogene cevumeran/ mRNA (patientspecific)	Genentech Inc.	Advanced melanoma/ Pancreatic ductal adenocarcinoma	LPX	II	NCT03815058/ NCT05968326

The other lipid delivery systems investigated in this dissertation are LNPs, which are nowadays the gold standard platform for RNA delivery, with four FDA- or EMA-approved drug products for RNA delivery. In the early 2000s, the first nucleotide delivery systems, carrying ionizable lipids such as DODAP or DLinDMA, were developed and subsequently launched LNPs as a platform for nucleic acid encapsulation and administration [63,70]. While the liposomes used for lipoplex formation are usually assembled from a cationic lipid and a helper phospholipid (e.g. DOTMA and DOPE), LNPs usually comprise four lipid components in varying ratios, where different lipids can be used in the respective lipid "group". The ionizable lipids are the key component of the formulation, since they complex the incorporated nucleic acids. Cholesterol and phospholipids, on the one hand, determine the structure and stability of the formulation, while also influencing the efficacy of RNA delivery. As a fourth lipid component, PEG-functionalized lipids are incorporated to provide colloidal stability against aggregation during storage and after administration [66,71]. The role of the respective lipids in state-of-the-art formulations is explained in detail in Chapter 1.4. Even though each lipid component is crucial for overall performance, the evolution of LNPs as nucleic acid delivery systems strongly correlates with the development of novel ionizable lipids (Figure 1.2-2). Starting with DODAP, the first advancements toward improved stability were achieved by substituting ester bonds with ether bonds, leading to DODMA [72]. To enhance the probability of fusion of the lipid carrier with endosomal membranes during cellular uptake, new lipids with improved fusogenicity were designed. Knowledge that a higher degree of saturation within the hydrophobic lipid domain leads to a higher tendency to form hexagonal liquid crystalline lipid phases and therefore higher fusogenicity, triggered the introduction of more double bonds within the hydrocarbon chains of the lipids (e.g., DLinDMA with two double bonds in each hydrocarbon chain) [70].

Besides modulations of the lipid tail domain, further research was started on the role of the ionizable headgroup and linker group of the lipids. Systematic investigation on the influence of changes in the three lipid domains on siRNA delivery showed a superior potency of Dlin-KC2-DMA, bearing a dimethylamine headgroup, a cyclic ketal linker region, and a double unsaturated dilinoleyl lipid tail [73]. Another systematic variation study of the headgroup and linker region revealed that the pK_a of the ionizable lipid correlates with biological activity for gene silencing therapy using siRNA, which remains one of the main paradigms for rational lipid synthesis for nucleic acid delivery [74].

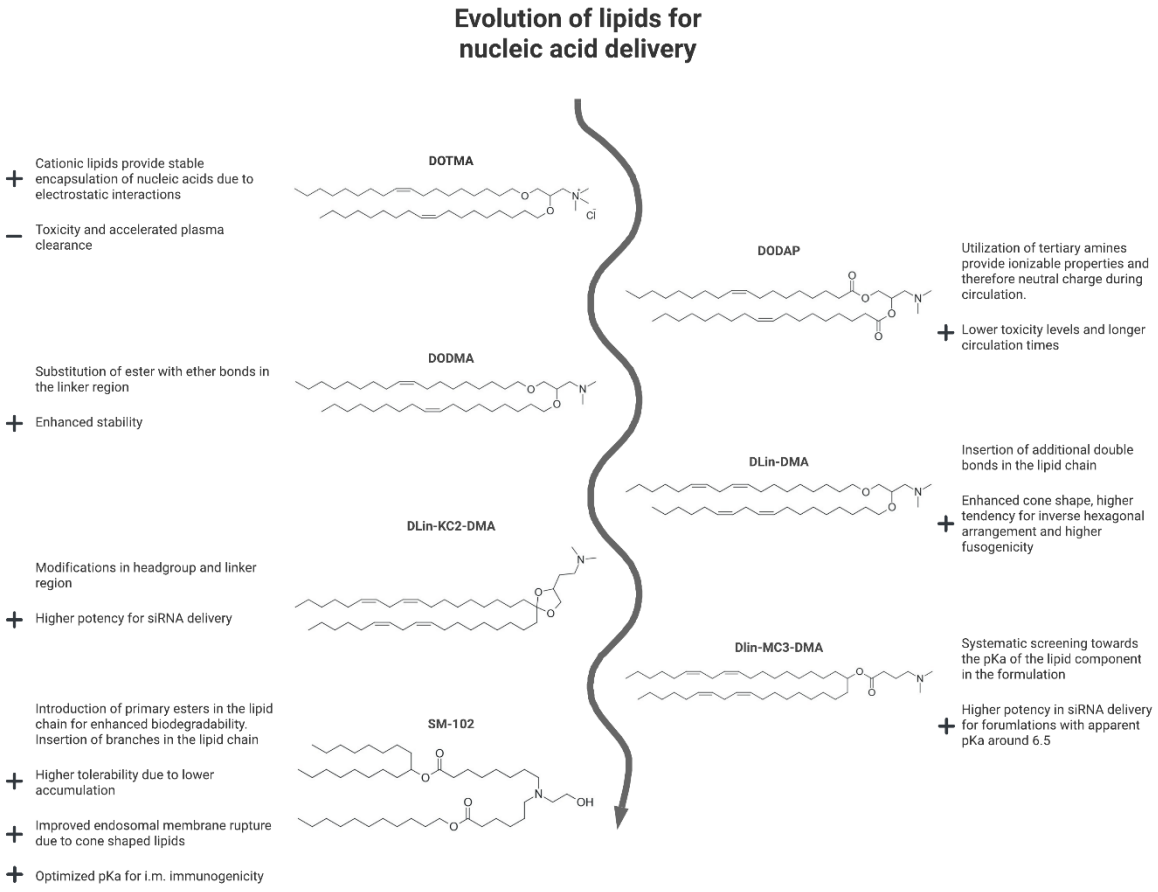

Figure 1.2-2: Evolution of ionizable lipids from permanently cationic transfection agents towards the ionizable lipids used in COVID-19 vaccines.

The optimal pK_a was observed to be between 6.2 and 6.5 for hepatic gene silencing after i.v. administration and revealed DLin-MC3-DMA as a lead molecule, which was later tested in clinical studies and eventually used in the first FDA- and EMA-approved RNA drug product, Onpattro®, in 2018 for the treatment of transthyretin-induced amyloidosis [21]. For exchanging siRNA to mRNA, LNPs with the same composition were tested in different administration routes [75]. While different expression kinetics were observed for different administrations, for most injection sites, protein expression in the liver was visible. Subsequent attempts were made to optimize the ionizable lipids and, thus, the LNP formulations for use as vaccines after intramuscular injection. The primary rationale was to increase the tolerability of the formulations without compromising their immunogenicity. To minimize adverse effects after administration, which may be related to the accumulation of lipid components due to low biodegradability, lipids with rapid clearance were designed. One concept for enhancing biodegradability is the introduction of primary esters in the alkyl chain of the lipid, allowing degradation by esterases *in vivo* [76]. Additionally, the insertion of branches in the alkyl chain leads to more cone-shaped lipid structures, which improves membrane disruption ability when paired with anionic phospholipids of endosomal membranes during

uptake [77]. Furthermore, it was stated that a pK_a value between 6.6 and 6.9 is optimal for i.m. immunogenicity, whereas lipids with these properties exhibited only poor performance after i.v. administration [78]. While formulation development in these times headed towards infectious diseases as influenza, Zika virus, HIV, or malaria, the SARS-CoV-2 outbreak in 2019/2020 triggered a rapid adoption of these delivery systems for the use in mRNA-based vaccines. The lead component (Lipid H or SM-102) of the study on optimizing i.m. delivery was eventually used in the Moderna vaccine Spikevax®, while ALC-0315 was used as an ionizable lipid in the Pfizer/BioNTech vaccine Comirnaty® [79]. Approval of the first mRNA-based vaccines introduced the delivery platform to a broad audience through vaccination campaigns worldwide, and massive efforts were invested in research afterwards. Several clinical trials for the next authorization are currently underway for various diseases (Table 1.2-3). Future prospects for improvements in the delivery system encompass the development of LNPs targeting extrahepatic tissues after i.v. administration as T-cells or hematopoietic stem cells in bone marrow [6,80,81]. Here, challenges arise because different cell types exhibit variations in endosomal acidification, thereby demanding different properties on the ionizable lipid, which need to be elucidated using orthogonal (complementary and independent) methods [78,82].

Table 1.2-3: Selection of mRNA LNP based drug products and investigational medicinal products currently investigated in clinical trials. Adopted from [6,66]

Drug name	Developer/ Sponsor	Indication	Stage	Trail number (NCT-number)
Comirnaty (tozinameran)/ mRNA	BioNTech SE, Pfizer	SARS-CoV-2	Approved	-
Spikevax (elasomeran)/ mRNA	Moderna	SARS-CoV-2	Approved	-
Onpattro (patisiran)/ siRNA	Alnylam, Inex/Tekmira	Transthyretin amyloidosis	Approved	-
mRESVIA/ mRNA	Moderna	Respiratory tract disease caused by RSV	Approved	-
V940/ mRNA	Merck Sharp & Dohme	Melanoma	III	NCT05933577
V940/mRNA	Merck Sharp & Dohme	Non-small Cell Lung Cancer	III	NCT06077760
V940/mRNA	Merck Sharp & Dohme	Cutaneous Squamous Cell Carcinoma	II/III	NCT06295809
mRNA-1647	ModernaTX	Cytomegalovirus	III	NCT05085366
mRNA-1010	ModernaTX	Influenza	III	NCT06602024
modRNA vaccine	Pfizer	Influenza	III	NCT05540522

1.3 Manufacturing of lipoplexes and lipid nanoparticles

General concepts for producing nanoparticles are typically categorized into two approaches: bottom-up and top-down. While bottom-up approaches use nucleation and growth out of dissolved materials for nanoparticle synthesis, top-down approaches use milling or other comminution techniques to break bulk materials into nanosized fragments [83]. For mRNA-carrying lipoplexes and LNPs, bottom-up approaches are typically used, with potential final downstream size adjustment, for example, through extrusion. In this work, two types of lipid delivery systems for mRNA were investigated, namely lipoplexes and lipid nanoparticles. These systems differ in their manufacturing methods: i) lipoplexes are formed through the mixing of mRNA with pre-formulated liposomes, whereas ii) LNPs are spontaneously formed after mixing mRNA in an acidic buffer with lipids dissolved in a water-miscible solvent, such as ethanol. Although these approaches are the gold standard for producing the respective formulations, various production steps and methods can be used for manufacturing both lipoplexes and LNPs, which will be discussed in the following sections.

1.3.1 Production methods for lipoplex formulation

The first step in producing lipoplexes involves the formulation of liposomes in an upstream process. The two most commonly used methods for liposome manufacturing are (i) thin-film hydration and (ii) the solvent injection method (Figure 1.3-1), whose details will be further explained in the following section.

In thin-film hydration processes, a preformed dry lipid film is rehydrated for several hours, resulting in a heterogeneous dispersion of liposomes in terms of size and lamellarity [84,85]. The film is prepared by dissolving lipids in chloroform or another easily evaporable solvent, and subsequently, the solvent is removed using a rotary evaporator (Figure 1.3-1A). This results in the formation of a thin film of dried lipids on the inner surface of the flask. When dry films are hydrated, the lamellae swell and grow into thin lipid tubules, which must be broken by mechanical agitation to form liposomes. Hereby, the level and type of agitation highly influence the resulting liposomes (size, lamellarity) [86]. Because of the high heterogeneity, downstream homogenization steps are necessary. Usual size uniformity can be applied by extrusion or sonication. In sonication, ultrasonic waves break down into larger vesicles; however, the possible degradation of encapsulated drugs and lipids limits the use of this method. Extrusion involves the repeated filtration of liposomes through pores of a defined diameter, resulting in monodisperse unilamellar vesicles. The mean size of the vesicles obtained decreases with the number of extrusion cycles and is dependent on the pore size of the filter [85]. Extrusion processes are easily applicable and relatively gentle for sensitive samples, but they lack the ability to scale up for production in large batches or continuous manufacturing approaches.

A more scalable approach for liposome synthesis is the solvent injection or ethanol injection method, also used in the manufacturing of LNPs (Figure 1.3-1B). A solution of lipids in a water-miscible solvent (e.g., ethanol) is injected into an aqueous medium, leading to the rapid dilution of ethanol and, consequently, the precipitation of lipids and the spontaneous formation of liposomes. While this can be applied in a lab-scale approach through injection using needles into a stirring aqueous solution, automation by microfluidic mixing channels can also be used. To remove the remaining solvent, purification steps such as dialysis should be applied. Typical maximal concentrations of residual solvents derived from the monographs USP <467> and Ph. Eur 5.4. are 0.5 % (w/w) for ethanol as the mainly used solvent.

Lipoplexes are eventually formed by mixing the preformulated liposomes with mRNA in an aqueous buffer. The approaches for this can range from simple pipetting steps to automated mixing systems.

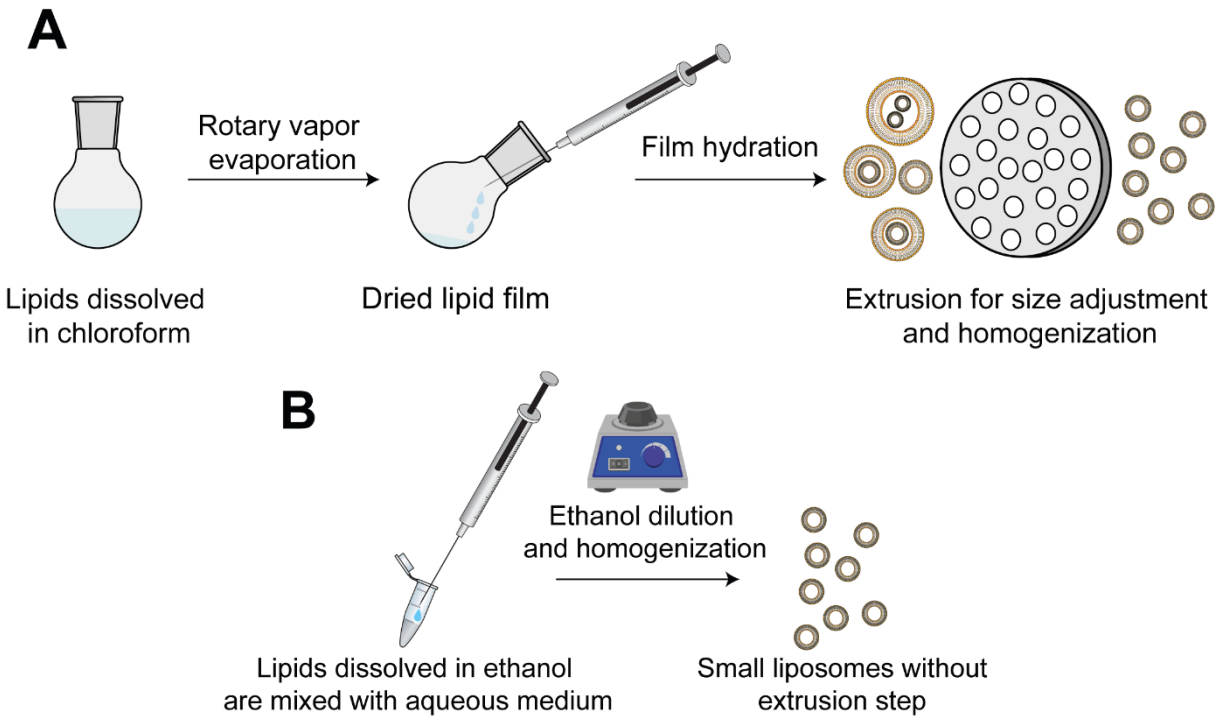

Figure 1.3-1: Manufacturing approaches for liposomes using thin-film hydration (A) or solvent injection (B) procedures. A. During the thin film hydration approach lipids get dissolved in an organic solvent that is subsequently evaporated. The remaining dried thin lipid film is then rehydrated with an aqueous phase, which leads to formation of polydisperse lipid vesicles. These must be homogenized (e.g., using an extruder) to receive relatively monodisperse liposomes. B. During solvent injection procedures, lipids get dissolved in a water miscible solvent (e.g., ethanol) and the aqueous phase is added by, for example, syringe-based injection. Ethanol dilution and homogenization can be supported through vortexing. The remaining liposomes are relatively small and monodisperse without downstream processing.

1.3.2 **Manufacturing of lipid nanoparticles**

While lipoplexes are formed in two steps, the manufacturing of lipid nanoparticles typically follows a one-step bottom-up approach, with downstream purification. The accepted gold standard is an ethanol-injection approach, utilizing a microfluidic setup for the rapid mixing of components. While this is also applicable for large batch sizes and continuous manufacturing through the parallelization of different mixers or high flow-through times, most microfluidic approaches encounter difficulties with very low batch sizes. Hence, for lab scale, some methods based on pipetting can also be used. Since the mixing properties highly affect the size and structure of the resulting particles, working with non-standardized pipetting methods leads to larger particles with higher polydispersity [87].

One method employed in this work is a simple, one-step lab-based approach, in which the aqueous dispersion of mRNA is pipetted into the ethanolic lipid mixture, followed by direct vortexing for homogenization and particle size adjustment. Due to the use of very low amounts of ethanol and a biocompatible buffer system consisting of glycylglycine, allowing for application without buffer exchange, no further processing steps are necessary. While with this approach, LNPs exhibit larger particle sizes compared to microfluidic-produced LNPs, they have proven to show similar internal organization and comparable transfection potency *in vitro* and *in vivo* [88,89].

The commonly used manufacturing approaches these days include microfluidic channels for the mixing of ethanolic and aqueous phases. In addition to the use of commercial microfluidizers, such as the NanoAssemblr®, various mixing channels with different geometries are also available, connected to syringe pumps or HPLC pumps. Microfluidic production techniques enable precise and reproducible control of particle size due to defined reaction times, continuous flow, and controlled diffusion distances within the channel. This provides high standardization and good scale-up ability. As explained above, the lipid nanoparticles are formed when the ethanolic phase with dissolved lipids is diluted by the aqueous phase. While slow dilution, due to low flow rates, results in larger particles, fast dilution with high flow rates yields smaller LNPs. Besides the flow properties, the different geometries of mixing channels influence the resulting variation in size and morphologies (Figure 1.3-2).

Independent of the type of micromixer, the geometry of the mixing channel (height and width dimension, obstacles), the total flow rate, and the flow rate ratio between the ethanolic and aqueous phase are the main determining factors for the outcome of nanoparticle formation and encapsulation of the cargo. The simplest form of mixing channel is a Y- or T-shaped mixer (Figure 1.3-2A), which directs the two phases to the mixing liquid-liquid interface, where ethanol dilution occurs. T-junction mixers require high flow rates, which cannot be scaled down to low amounts (<100 µl), thereby impeding their use in small lab scales [90]. Slow dilution and an ethanol-concentration gradient lead to relatively higher particle sizes and high polydispersity [87]. To improve this, a third inlet for these channels was added, leading to so-called sheath-flow or hydrodynamic focusing

devices [91], where a central stream of solvated lipids is surrounded by two streams carrying the aqueous buffer (Figure 1.3-2B). This increases the interface between ethanol and the aqueous buffer, which reduces the diffusion length scales and the time scale available for the growth of intermediate lipid fragments and yields smaller particles with a narrower size distribution [92]. Another attempt to overcome the slow mixing speeds in T- and Y-junction micromixers is the addition of obstacles inside the mixing channel to manipulate the streamlines of liquids by chaotic advection. These chaotic micromixers allow particle formation with high size control at low flow rates, by stretching and folding of merging fluid domains, which promotes rapid diffusion between the liquid phases [92]. The geometry of the mixing channels can include periodic turns, grooves, or branched flow paths to disrupt the laminar flow paths, which results in mixing through diffusion and advection.

One of the most commonly used chaotic mixer geometries is the staggered herringbone mixer (Figure 1.3-2C), which consists of periodic, asymmetrically angled protrusions in the base of the mixing channel. This induces passive mixing through chaotic advection, thereby creating short diffusion lengths between the streams and allowing for the controlled production of nanoparticles according to the flow rates. In comparison to mixers based on hydrodynamic flow, due to the lower flow rates, lower amounts of input solutions are also necessary, which is crucial when expensive cargos, such as nucleotides, need to be encapsulated [90]. One disadvantage is the limited production capacity, resulting from the restricted flow rates, as optimal mixing conditions can only be achieved at specific flow rates.

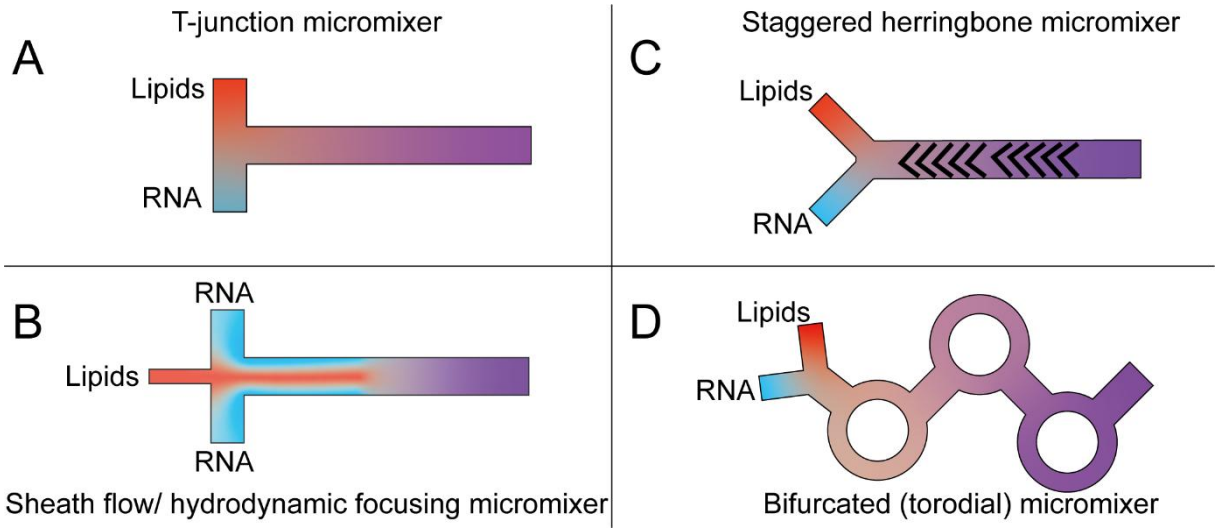

Figure 1.3-2: Microfluidic LNP production technologies based on different micromixer geometries. A. T-junction micromixer. B. Sheath flow or hydrodynamic focusing micromixer. C. Staggered herringbone micromixer. D. Bifurcated or toroidal micromixer.

The increasing interest in nanoparticulate drug products and the utilization of microfluidizers for their manufacturing have led to the development of commercial platforms that ensure the reproducible formation of distinct nanoparticles, thereby facilitating the development of drug products also for small companies such as start-ups. One of these platforms was developed by Precision NanoSystems® (now: Cytiva®), entitled NanoAssemblr™. The mixing channels consist of a series of toroidal or bifurcated mixers (Figure 1.3-2D), which induce chaotic advection through split channels. Because of the branched channels, the fluid travels along different paths within the channel and is then merged again. This induces rapid mixing in a single-layer device through large centrifugal forces, known as the Dean vortex. Compared to staggered herringbone mixers, higher flow rates are required for optimal mixing conditions, therefore resulting in higher possible production rates, while maintaining the high encapsulation efficacy, high reproducibility, and low nanoparticle size with narrow distribution [87,90].

Microfluidic technologies offer the opportunity for the fabrication of large batches of nanoparticulate drug products. This requires a scale-up in batch sizes, without changes to the physicochemical properties as size and morphology. Essentially, two approaches exist for scaling microfluidic processes: (i) using a single mixer with high flow-through times and higher flow rates, or (ii) utilizing multiple mixers in parallel and merging them into a single batch. The parallelization enables the scale-up of the process without altering the physics of nanoparticle self-assembly within the channel. Nevertheless, maintaining uniform performance across the parallel mixers is challenging, considering the need for quality control and the confinement of batches when one mixer does not perform as expected. As explained previously, flow rates significantly influence the physicochemical properties of drug products, so that increasing the flow rate will most likely also alter the size and size distribution of the nanoparticles. Therefore, scaling up devices with a single mixer is a challenging operation that requires extensive knowledge about the mixing properties within the channel and how they change during scale-up [92].

1.4 State-of-the-art composition of RNA LNPs

Alongside the manufacturing procedure, the second property that defines LNPs as well as their therapeutic potency is the lipid composition. All currently FDA- and EMA-approved LNP drug products are characterized by four lipid components: (i) an ionizable cationic lipid, (ii) a phospholipid, also referred to as helper lipid, (iii) cholesterol and (iv) a polyethylene glycol grafted lipid serving as a stealth lipid (Figure 1.4-1). Additionally, all authorized drug products are based on similar molar ratios of the respective lipid components [93]. This highlights the similarity of the LNP systems, despite their application through different routes (i.m. vs. i.v.) and diseases, and raises the question of where differences occur and how the different lipid components influence the therapeutic potency of the RNA nanomedicine. To reach optimal delivery performance, the lipid

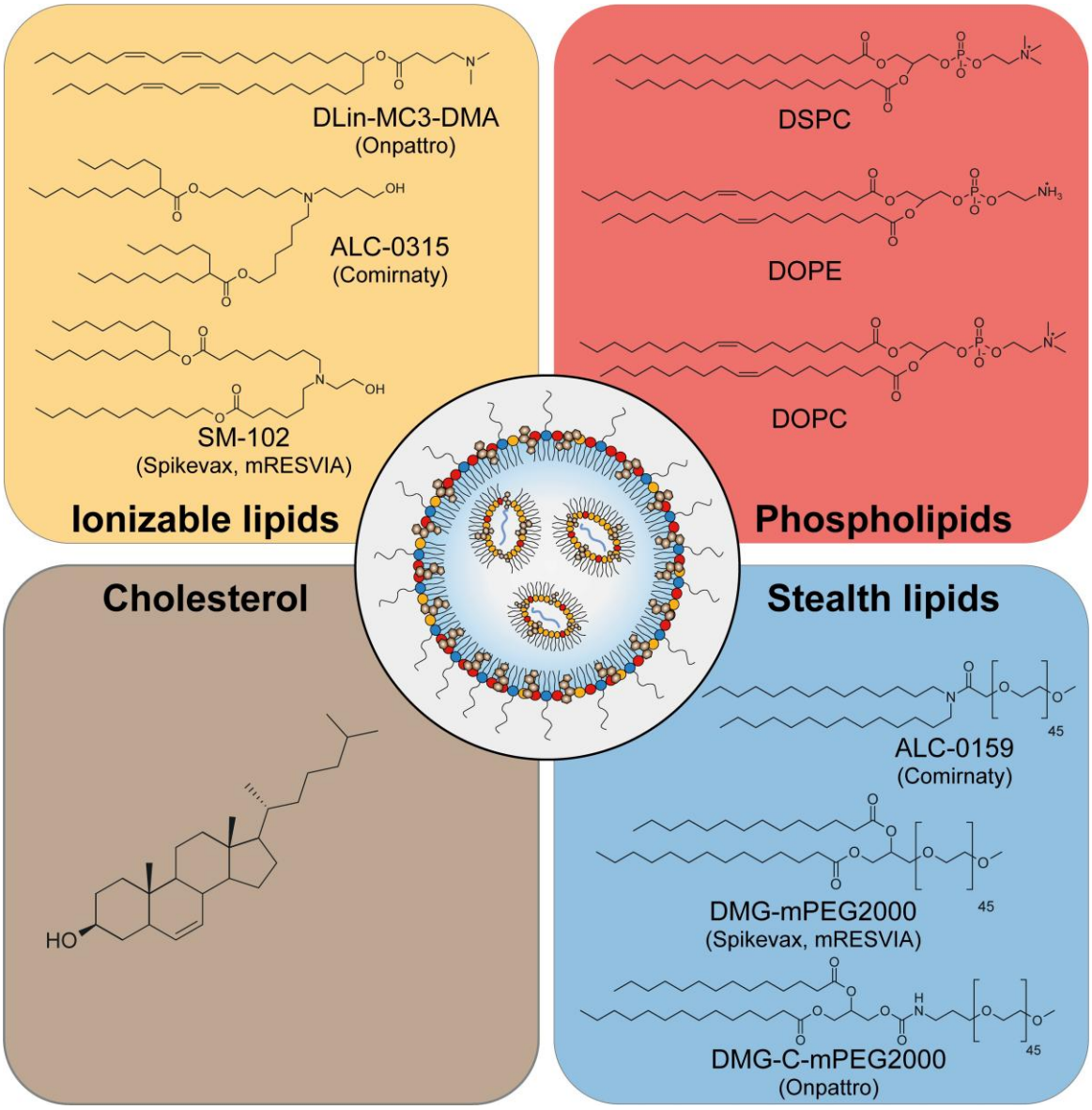

Figure 1.4-1. State of the art composition of mRNA carrying LNPs divided into the four essential lipid components: ionizable lipid (yellow), phospholipids (red), cholesterol (brown), and stealth effect mediating lipopolymers (blue). Together, these lipid components interact to form RNA-carrying LNPs, as illustrated in the center of the figure. For the ionizable and stealth lipids the usage in the respective approved drug products is stated in brackets.

vehicle must protect the mRNA from degradation and transfer the nucleotides to the targeted cells (e.g., antigen-presenting cells for mRNA vaccines). Successful delivery further includes the uptake of the cargo into the cytosol via the endosomal uptake pathway and the eventual release of the RNA from the vehicle. All lipidic components play crucial roles in the success of this procedure [54,94,95].

1.4.1 Ionizable lipids

The cationic ionizable lipids typically consist of a tertiary amine, which can be protonated, becoming positively charged under acidic conditions, while remaining uncharged at neutral pH. The pK_a of the ionizable lipid describes the pH-responsive behavior of the lipid. Carrasco *et al.* showed that the theoretical pK_as of some published and commonly used lipids are in the range

of 8 - 10, whereas the apparent pK_a of the LNP formulation manufactured with the same lipids results in pK_a values 2-3 pH units lower [96]. This highlights the need for accurate determination methods for the pK_a of LNP formulations. For determining pK_a values, a fluorescence-based assay utilizing 2-(*p*-toluidino)-6-naphthalene sulfonic acid (TNS) as a fluorescence dye is most commonly employed. TNS shows almost no fluorescence in aqueous solution, while fluorescence intensities rise upon binding to positively charged membranes. Therefore, the assay primarily reflects the surface charge properties, albeit to a lesser extent, the situation of lipids being complexed with RNA inside the LNP. Furthermore, the TNS assay is highly sensitive to experimental settings (such as the buffer media or sample concentration). Techniques using ^{1}H-NMR [96] can reveal more accurate values for the situation within the particle. Other approaches to estimating the apparent pK_a of an LNP formulation include computational techniques, which allow for estimation based on lipid structures [97] or molecular dynamics simulations [98]. These deliver promising insights but require further verification through experimental data to be widely applicable. Structural approaches using small angle X-ray scattering can detect pH-responsive structural motifs, and their behavior upon variation in pH can be utilized to determine structural pK_a values [99]. By analyzing, for example, the structural changes of the mRNA/lipid stacks, rather than just interfacial accessible lipid charges, the structural pK_a reflects the actual pH responsiveness of the active complex and is independently measurable. This information is also relevant from the perspective of potency and stability.

The ionizable properties of the lipid excipients enable complexation of the mRNA during manufacturing in acidic conditions, while providing net neutral LNPs after application at physiological blood pH 7.4 (e.g., during circulation in the bloodstream). In addition to the benefits during manufacturing, the pH-responsive behavior of the lipid component determines the *in vivo* behavior of LNPs. On one hand, the surface charge of the particle, determined by the pH-responsive behavior of the ionizable lipid, influences the binding of a protein corona to the particle surface. As shown for hepatocytes, the association of distinct proteins, such as apoE, with the LNPs surface can facilitate the uptake of the particles in liver tissue [22,100]. Additionally, the ionizable lipids enable improved endosomal uptake, the general expected uptake mechanism for LNPs (Figure 1.4-2). During endosomal maturation, the pH value decreases below the pK_a of the LNP formulation, thus yielding a high level of protonation of the ionizable cationic lipids. Due to electrostatic interactions of the positively charged LNP lipids with the anionic endosomal membrane, the endosome tends to disrupt and release the LNPs to the cytosol. In particular, oppositely charged lipids can facilitate a transformation from bilayer structures to a hexagonal lipidic structure, which destabilizes the endosomal membrane and leads to disruption [54,101]. Eventually, the ionizable lipids also must release the RNA to ensure that the translational mechanism can occur.

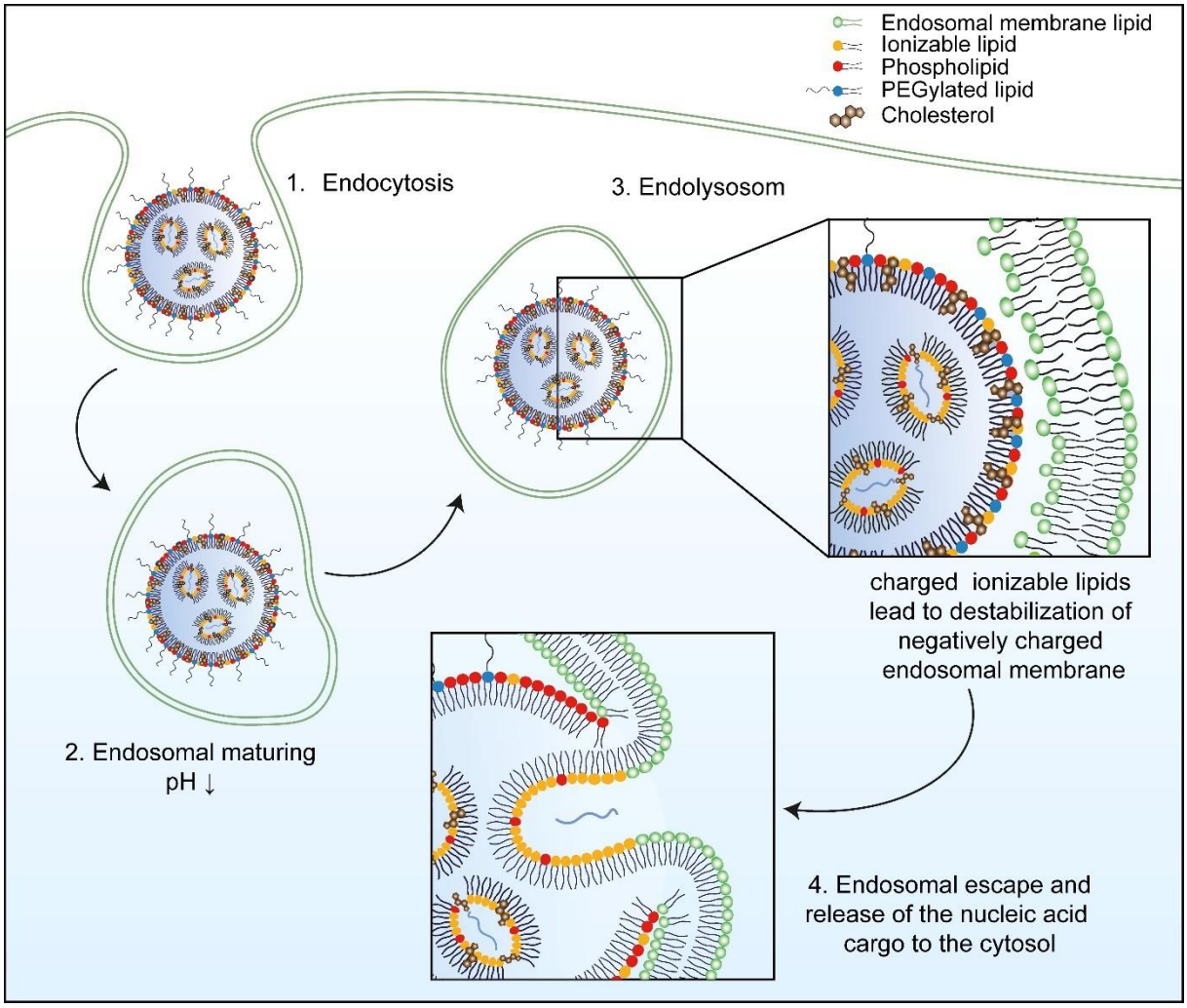

Figure 1.4-2. Endosomal escape mechanisms for mRNA LNPs. Following endocytosis, stepwise acidification during endosomal maturation leads to the protonation of ionizable lipids and subsequent interaction with negatively charged lipids within the endosomal membrane, resulting in the destabilization of the endosomal membrane. This facilitates the release of the nucleic acid cargo into the cytosol. Adopted from [102].

1.4.2 Phospholipids

In addition to the ionizable lipid, which is crucial for RNA complexation and transfection efficacy, helper lipids such as phospholipids, cholesterol, and PEGylated lipids are incorporated into the LNP formulation to enhance particle stability, improve blood compatibility, and facilitate delivery efficacy. The phospholipid used in the four approved LNP drug products is DSPC, a phosphocholine with saturated hydrocarbon chains. The use of DSPC for the novel RNA products is probably due to its established application in liposomal drug products (for example, as the main component in HSPC used in Doxyl®). Saturated phospholipids exhibit high melting temperatures and favor the formation of lipid bilayers due to their cylindrical geometry, which together drives the stabilizing function of the lipid and delivers optimal *in vivo* serum stability [71].

One drawback of DSPC as a saturated phospholipid is the lack of facilitating effects on endosomal release mechanisms. Comparatively, lipid mRNA delivery systems manufactured with DOPE showed higher expression levels than those formulated with DSPC [103]. DOPE carries two bulky unsaturated hydrocarbon chains and a relatively small headgroup, which gives it a cone-like shape (see Figure 1.4-1). This geometry tends to build non-bilayer hexagonal lipid liquid crystalline phases, which are known to facilitate membrane fusion [54,71,104]. While their fusogenicity enables a more successful endosomal escape, DOPE-based LNPs exhibit relatively low colloidal stability due to bilayer fusion during storage and subsequent size increase. Additionally, interactions with serum proteins during blood circulation are increased, which may hinder delivery to the targeted cells [71]. Like DOPE, DOPC shows lower melting temperatures, giving membranes a fluid state at physiological temperatures and making the LNP susceptible to serum protein opsonization [105]. The inclusion of cholesterol can stabilize this kind of lipid membrane. Nevertheless, due to the branched hydrophobic chains, it can facilitate endosomal escape by mediating membrane disruption. DOPC-based LNPs show higher stability than DOPE-based LNPs, but lower stability than analogues manufactured with DSPC, which could present a compromise between stability and efficacy [71].

1.4.3 **Cholesterol**

Cholesterol is commonly used in liposomes and LNPs to enhance colloidal stability and resistance to serum proteins. When combined with phospholipids that possess low melting temperatures, cholesterol decreases membrane fluidity by uncoiling their acyl chains and therefore increasing the bilayer thickness. Controversially, for phospholipids with higher melting temperatures, cholesterol increases the membrane fluidity and decreases membrane thickness[54]. In sum, cholesterol brings the lipid membranes towards a state of liquid-ordered phase [106]. By increasing the rigidity of membranes, it can reduce drug leakage, which is not a big problem in nucleic acid delivery, but can be beneficial when small-molecule drugs are incorporated. Furthermore, it has been demonstrated for liposomal drug products that cholesterol can reduce the amount of surface-bound proteins during circulation, thereby extending the circulation times [54]. Due to its stabilizing function, the approved RNA drug products contain approximately 40 mol% cholesterol, which is necessary for the stable encapsulation of siRNA [107]. While cholesterol, a well-known excipient, is used in all authorized mRNA drug products, investigations have been conducted on replacing this LNP component. By using cholesterol analogues, such as C-24 alkyl phytosterols, it was possible to enhance gene transfection efficiency by modulating the shape and intracellular trafficking of the nanoparticles. The cholesterol analogues contribute to higher cellular uptake and retention, facilitating a steady release from endosomes and enhancing intracellular diffusivity [108,109]. Additionally, the use of cholesterol analogues can influence cell-type-specific effectiveness. For example, LNPs comprising 7α-hydroxycholesterol led to increased delivery to primary human T-cells compared to cholesterol-based LNPs [110]. Utilization of bile acids as substitutes led to reduced liver delivery and improved

delivery to other cell types, like T-cells and B-cells [111]. By adding ionizable headgroups to the cholesterol, endosomal escape was enhanced, and mRNA delivery was significantly improved in mice [112]. These results highlight the critical role of cholesterol in optimizing the potency of mRNA LNPs.

1.4.4 PEGylated lipids

While PEGylated lipids exhibit the lipid compound within LNPs with the lowest molar percentage (1-2%), they play a crucial role in the LNP´s physicochemical properties as well as their potency. PEGylated lipids can differ in their lipid tail as well as in the structure and length of the PEG chain. While in all authorized RNA drug products (see Table 1.2-3), the molecular weight of the PEG chain is 2000 Da, which was also used in liposomal drug products, the lipid anchor is different within the four formulations (see Figure 1.4-1). PEGylation is a widely used approach for increasing *in vivo* circulation time, as it decreases nanoparticle clearance via the reticuloendothelial system, as first demonstrated in Doxyl® liposomes. While extended circulation times are desirable for the anticancer drug doxorubicin, as they lead to accumulation of the drug at the tumor site and reduce cardiotoxicity compared to free doxorubicin, the high circulation stability hinders cellular uptake and endosomal escape, thereby reducing the potency of RNA nanomedicines. To overcome this PEG dilemma, for liver targeting PEG-lipids can be applied, which tend to desorb from LNPs upon i.v. administration so that adsorption of lipoproteins, such as apoE, can exploit the liver uptake. The length of the PEG-lipid hydrocarbon chains can determine the ability to desorb from LNP surfaces since the hydrophobic acyl/alkyl chain is incorporated into the LNP outer membrane. PEGylated lipids with shorter chains are more likely to desorb from the LNP because they are prone to association with lipoproteins, extracellular lipidic vesicles, or proteins, such as albumin, with multiple hydrophobic pockets in the blood plasma during circulation [54,113]. Alternatively, reversible PEGylation of the LNPs can be achieved by using cleavable linked PEG chains, which are sensitive to degradation during circulation [71]. Further to the stabilizing function of PEGylated lipids during circulation, they also mediate stability during particle formation and determine the particle size after manufacturing of LNPs. While particles manufactured without any PEGylated lipid are aggregating, polydisperse, and exceeding 200 nm in particle size, increasing the molar ratios of PEGylated lipids causes a decrease in particle size independent of the other lipid composition [103,114,115]. Since the PEG-lipid resides on the outer surface of the LNP, an increase in its molar ratio leads to an increase in the surface area/volume ratio and consequently to a reduction in particle size [115].

Although PEGylated nanoparticles are thought not to exhibit antibody or complement protein binding due to their stealthy properties, it is well known that unanticipated immune reactions occur against PEG-conjugated nanomedicines after administration, ranging from local inflammation to accelerated clearance and severe hypersensitivities [116,117]. The immunogenicity and adverse effects

of PEGylated systems, along with general concerns about their application, led the FDA to call for the screening of anti-PEG-antibody responses during preclinical trials of new drug products containing PEGylated composites [118]. Due to its widespread use in numerous cosmetics, households, and over-the-counter (OTC) drug products as an excipient, the prevalence of anti-PEG antibodies in the population is very high, even when determined before the global use of PEGylated vaccines against SARS-CoV-2 [119]. One example of these reactions is the accelerated blood clearance (ABC) phenomenon, leading to rapid clearance of PEGylated nanomedicines due to the production of IgM and IgG antibodies after primary contact with PEGylated products, which is detectable after secondary applications. Subsequent activation of the complement system and facilitated particle phagocytosis can decrease circulation halftimes of PEGylated therapeutics [116]. Another adverse immune reaction is the complement activation-related pseudoallergy (CARPA). In contrast to the ABC phenomenon, it takes place directly after the primary administration of a PEGylated drug product, while the symptoms diminish in subsequent applications [116]. CARPAs are non-IgE-mediated hypersensitivity reactions that can also be observed after application of non-PEGylated drug products and range from mild allergic symptoms to fatal anaphylaxis. This reaction was first reported in the treatment using Doxyl® as a PEGylated liposome, where it could be mitigated by slow infusion rates and pre-treatment with corticosteroids [54]. Notably, the presence of anti-PEG IgM and IgG antibodies per se is not predictive of the prevalence of antibody-mediated toxicity [117]. Nevertheless, since the number of anti-PEG-antibody positive people will be immensely raised due to the COVID-vaccines, implies future hypersensitivity problems and arises the question of alternative stealth effect mediating LNP excipients. Alternative stealth polymers such as polyoxazolines or polyglycerols have been tested among others. While polyoxazolines demonstrated good biocompatibility and favorable biodegradability, high costs and impurities during synthesis result in problems for application in drug products[120]. Polyglycerols did not initiate the ABC phenomenon but exhibited skin sensitization and allergic contact dermatitis [116,117]. Despite several hopeful substitutes were found, none of them has by now led to a drug product excipient with stealth properties. One promising approach is the PEG substitution with polysarcosine (pSar), a polypeptoid derived from the endogenous amino acid sarcosine. While comparable stealth-like properties are observable for pSar [121,122], it also avoided production of polymer-related antibodies, which allowed repeated administration of pSar-grafted liposomes, without a note towards the ABC phenomenon [123,124]. The alternative usage as a stealth property providing excipient in RNA LNPs was also proven, where the molar ratio of the pSar-lipid also influenced particle sizes and biodistribution [125].

1.5 Characterization and quality control of lipid delivery systems for RNA

Despite the emergency use authorization of the two mRNA-based vaccines Comirnaty® and Spikevax® against SARS-CoV-2 by the FDA and EMA in 2020 [64] and of course also the other RNA-vaccines being authorized by, for example, the National Medical Product Administration of China (NMPA), the regulatory framework for mRNA nanomedicines is still evolving. While guidelines for liposomal drug products have already been published by the FDA [126], no such document was available for RNA vaccines. To cover these gaps, regulatory agencies are working on guidelines for the development and quality control of such vaccines, with several drafts currently under discussion among experts. In December 2020, the WHO published a draft for a guideline, which resulted in the technical document "Evaluation of the quality, safety and efficacy of messenger RNA vaccines for the prevention of infectious diseases: regulatory considerations", published in October 2021 [127]. In these WHO guidelines, information and regulatory considerations regarding key aspects of (i) manufacturing and quality control, (ii) nonclinical, and (iii) clinical evaluation of preventive mRNA-based vaccines for human use are provided. In 2022, USP published a first draft of the "Analytical Procedures for mRNA Vaccine Quality – Draft Guidelines", which was in the third draft from 2024 also extended to RNA therapies that are not vaccines [128]. Within these guidelines, various procedures for controlling identity, content, integrity, purity, potency, and safety of both the drug substance and the drug product are introduced. Additionally, the Ph. Eur. is currently working on three new general texts to be included in their pharmacopeia, which are scheduled for publication in 2025. In the general texts "mRNA vaccines for human use (5.36)", "mRNA substances for the production and control of mRNA vaccines for human use (5.39)" and "DNA template for the preparation of mRNA substances (5.40)" definitions, guidance for process development and testing of final product and mRNA substance are provided [129]. Besides this, other national regulatory authorities, such as the NMPA, published respective guidelines for industry [130].

All previously published and discussed guidelines cover, on the one hand, the production and characterization of RNA as an active ingredient, as well as the manufacturing and quality control of RNA-LNP as the final drug product. While analytical procedures for the drug substance are further discussed elsewhere [131], but include the attributes presented in Table 1.5-1.

Table 1.5-1 Characterization and Release Testing Criteria for mRNA Drug Substance and their respective analytical procedures proposed by Ph. Eur. (Edition 11.5) and USP (Edition 2025, Issue 3).

Quality	Attribute	Possible analytical methods
Identity	mRNA sequence	Sequencing (Sanger/ high-throughput sequencing), PCR
	RNA size	Electrophoresis (capillary gel electrophoresis)
Content	RNA concentration	Quantitative PCR, UV Spectroscopy
Integrity	mRNA intactness	Capillary gel electrophoresis, agarose gel electrophoresis
	5'capping efficacy	Ion-pair RP-HPLC, LC-MS
	3' poly(A) tail length	Ion-pair RP-HPLC, LC-MS
Purity	**Product-related impurities:**	
	dsRNA	Immunochemical methods (Ph. Eur. 2.7.1)
	Fragmented RNA	RP-HPLC
	Process-related impurities:	
	Residual DNA template	Quantitative PCR
	Free nucleotides	LC-MS
	Residual RNA polymerase content	ELISA, total protein test (Ph. Eur. 2.5.33)
Potency	Expression of target protein	Cell-based assay with detection by immunochemical assay Ph. Eur. 2.7.1 or flow cytometry 2.7.24
Safety	Bacterial endotoxins	USP <85>, Ph. Eur. 2.6.14/ 2.6.32
	Sterility/ Bioburden	USP <61> ,<62>, <1115>; Ph. Eur. 2.6.1
Other	Appearance	USP <790>
	Residual solvents	USP <467>
	pH	USP <791>, Ph. Eur. 2.2.3

1.5.1 General remarks about the quality of the mRNA drug product

The following section focuses on the characterization of the drug products (e.g., mRNA-LNPs). An overview of the most important critical quality attributes and their possible detection method required for batch release is described in Table 1.5-2. Nevertheless, further CQAs for monitoring throughout the manufacturing process need to be identified, and respective analytical methods must be developed. Hence, there remains space for further improvement, as many orthogonal methods must still be applied to generate quantitative datasets to date. The development of novel analytical methods, therefore, remains an unmet need for many CQAs of LNPs.

The identity and content are not only limited to the nucleic acid active ingredient, but also the lipids used for the delivery vehicle need to be investigated. The content and identity of lipids can be confirmed by chromatographic assays, such as those utilizing charged aerosol detectors (CAD), whereas for the sequence identity of RNA, sequencing or PCR investigations are required. The determination of mRNA content is usually described as either measurements of the total amount of RNA in the formulation or of the encapsulated amount of mRNA. Furthermore, the amount of mRNA per particle can be described, although it is often based on several estimated assumptions. For the quantification of RNA, usually UV spectroscopy measurements at an absorbance wavelength of 260 nm are used [132]. For determining the absolute RNA content encapsulated in the formulation, a pretreatment with a disrupting agent is usually required. For example, the Ph. Eur. describes an extraction of mRNA by precipitation with 2-propanol using a centrifugation step. Other methods include the detection of RNA using fluorescent dyes, such as the Quant-it ™ RiboGreen reagent®, after disruption of LNPs with surfactants, such as TritonX®100 [133]. The amount of accessible RNA can be measured using an untreated LNP sample, which further enables the calculation of the relative percentage of accessible RNA compared to the values from the disrupted sample, often referred to as the encapsulation efficiency. Here, it is noteworthy that this fluorescent-based assay is unable to differentiate between free RNA and RNA bound to the LNPs that is still accessible to the dye. This renders the term 'encapsulation efficiency' technically incorrect; the detection of accessible RNA would be a more accurate measure. To ensure if the RNA is freely distributed in the bulk phase, or bound to LNPs but still accessible, for example, agarose gel electrophoresis of untreated samples can be utilized [131].

Table 1.5-2 Characterization and Release Testing Criteria for mRNA Drug Product and their respective analytical procedures proposed by Ph. Eur. (Edition 11.5) and USP (Edition 2025, Issue 3). Alternative methods for quality determination were added according to [131]

Quality	Attribute	Possible analytical methods
Identity	RNA identification	Sequencing (Sanger/ high-throughput sequencing), PCR
	Lipid identity	RP-HPLC-CAD
Content	RNA concentration	UV Spectroscopy
	RNA encapsulation efficacy	Fluorescence-based assay, UV spectroscopy
	Lipid content	RP-HPLC-CAD
Integrity	RNA integrity	Capillary Gel electrophoresis
	LNP size and polydispersity	Dynamic light scattering (Ph. Eur. 2.9.50)
Purity	Aggregate quantification	SEC-HPLC, AF4-MALS-(SAXS)
	Fragment RNA	Ion pair RP-HPLC
Potency	Expression of target protein	Cell-based assay with detection by immunochemical assay (Ph. Eur. 2.7.1) or flow cytometry (Ph. Eur. 2.7.24)
Safety	Bacterial Endotoxin	USP <85>, Ph. Eur. 2.6.14/ 2.6.32
	Sterility	USP <71>, Ph. Eur. 2.6.1
Other	Appearance	USP <790>, Ph. Eur. 2.2.1/ 2.2.2/ 2.2.20
	Osmolality	USP <785>, Ph. Eur. 2.2.35
	Subvisible particles	USP <787>, Ph. Eur. 2.9.19
	Extractable volume	USP <1>, Ph. Eur. 2.9.17
	pH	USP <791>, Ph. Eur. 2.2.3
	Container closure integrity	USP <1207>

Other batch release attributes, such as sterility, osmolality, pH, and testing for bacterial endotoxins, can be executed according to the respective pharmacopeia monograph (see Table 1.5-2). For the determination of subvisible and visible particles, the particles in colloidal drug products pose some difficulties for execution. To face that, the USP differentiates between three types of particulate contaminations (<USP1790>), namely intrinsic, extrinsic, and inherent particles. Extrinsic particles are defined as particle contaminations derived from external sources (e.g., personnel, non-process related materials), while internal parameters derive from ingredients or processes connected to the process (cleaning processes, lubricants, primary packaging materials). Inherent particles, on the other hand, are present or expected within the formulation or drug product. These dosage-form-related particles must be characterized as accurately as possible in the development phase. For the optical control of drug products, it is necessary to consider that the inherent particles can lead to turbidity; therefore, extensive training and comparison with test sets are required. For subvisible particles, the detection of inherent particles with the method must also be demonstrated and considered for quality control measures. Here, also, automated detection by machine learning approaches for image analysis is gaining importance [134].

1.5.2 Size-related quality attributes of mRNA LNPs and their determination

One main concern regarding the integrity of the drug product is the size, polydispersity, and colloidal stability of the mRNA-LNPs. The integrity of the RNA containing particles is, on one hand, important for protecting the degradation of RNA molecules, but, in addition to this, variations in particle morphology and size can affect changes in *in vivo* potency. Particle size influences the biodistribution and cellular uptake, thereby affecting the transfection efficacy and immunogenicity of the formulations [135,136]. Furthermore, size can also influence the encapsulated amount of mRNA per particle and the downstream characterizations, such as the detection of subvisible particle contamination. Therefore, both USP and Ph. Eur. define size as one of the primary CQAs for LNPs. Both guidelines recommend Dynamic Light Scattering (DLS), also known as Photon Correlation Spectroscopy (PCS), for determining size and polydispersity, as indicated by the polydispersity index (PDI), without specifying a size or PDI limit. DLS is the most commonly used lab-based approach for determining the size distribution of nanoparticles in the range of up to 1000 nm. It detects the intensity fluctuations of scattered light as a function of time, caused by particles undergoing Brownian motion (Figure 1.5-1). The scattered light can be detected either in a 90° or 173° (non-invasive back scattering, NIBS) angle relative to the incident beam, where the latter brings benefit for concentrated samples, by avoiding long light diffusion paths through the sample, which could lead to multiple scattering. Since the size and, therefore, diffusional behavior influence how rapidly the intensity fluctuates, DLS allows for determining particle size [137]. After detection of the scattered light photons, a mathematical process, the correlation, is used, where the similarity of

two signals separated by a time delay is measured, which results in the autocorrelation function. This function decays to a mean value of the rapidity of the signal fluctuations and therefore to the diffusion coefficient D [138]. According to the Stokes-Einstein relation (eq.1), the hydrodynamic diameter (D_h) can be calculated using the universal Boltzmann constant (k_B), the temperature (T), the viscosity of the dispersing medium (η), and the translational diffusion coefficient (D), which can be determined from the intensity fluctuations. τ

$$D_h = \frac{k_B T}{3\pi\eta D} \qquad (1)$$

The polydispersity index (PDI) is a dimensionless parameter that corresponds to the square of the normalized standard deviation of the underlying size distribution, and a perfectly uniform sample would result in a PDI close to 0 [139]. Nevertheless, exact determination of the particle size underlies several assumptions, which limit the accuracy of DLS. These assumptions include: (i) particles are considered to be spherical, (ii) samples should not absorb or fluoresce the light in the used wavelength, (iii) particle-particle interactions should be prevented by dilution, (iv) variable sample parameters as viscosity, temperature, refractive index need to be known or determined, (v) large particles may mask smaller particles in an intensity-derived size determination [140]. Due to its limitations with polydisperse samples, DLS is only recommended for use as a quality control measure for samples with low polydispersity.

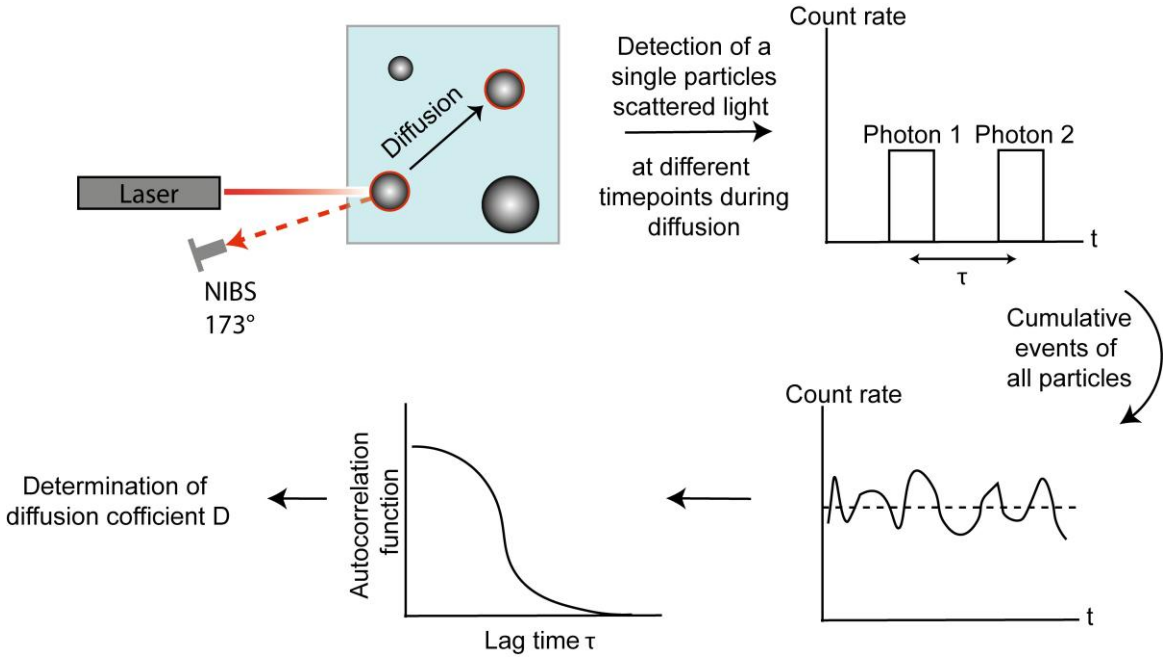

Figure 1.5-1: Schematic overview of size determination using Dynamic Light Scattering (DLS). The incoming monochromatic laser beam is scattered by particles and detected, e.g., at an 173° angle in non-invasive back scattering (NIBS) methods. Particles in Brownian motion can be detected at different positions and time points, so the lag time τ of correlating signals from the same particles can be detected. Cumulative events of the whole entity of particles result in a detected count rate of photons. Correlation analysis of the detector signals yields the autocorrelation function, from which the diffusion coefficient can be determined to calculate the hydrodynamic diameter.

In the early stages of product development, it is highly recommended to use complementary sizing measures, that rely on different physical principles (orthogonal methods). In comparison to DLS, multi-angle light scattering (MALS) utilizes static light scattering at various detector angles to determine particle size [141]. Here, no time-dependent fluctuations in the scattered light intensity, but the absolute intensity of scattered light as a function of the angle is measured. Since this scattering intensity depends on particle size, molecular weight, and particle concentration, MALS enables the determination of these parameters using established formalisms [142]. Here, in contrast to DLS, not the hydrodynamic diameter but the radius of gyration is detected, which is the root mean square distance of the detected matter of an object from its center of mass. MALS measurements typically require the use of an upstream size fractionation technique to produce reliable data [143].

Besides light scattering techniques, microscopic investigations (e.g., transmission electron microscopy (TEM) or scanning electron microscopy (SEM)) are a common tool to determine size distribution profiles of nanoparticulate formulations. One benefit here is that additional information about particle morphology and shape can be obtained. While this technique is useful in early stages of formulation delivery, it has several limitations for daily quality control, including the need for skilled operators, high maintenance costs, and analysis times. Furthermore, the sample preparation, i.e., freezing (for cryo-EM), drying, or staining, can possibly modulate the particle shape and size. Since microscopic analysis requires the investigation of representative images, it can also bear the risk of not detecting aggregates, especially when they rarely occur [140].

While the above-mentioned sizing techniques are so-called “batch-mode” methods where the sample is investigated without any fractionation or sample preparation, methods coupled to upstream size-dispersive separations can also be considered. This is beneficial, since most pharmaceutically used nanoparticles display a certain degree of polydispersity which impedes the interpretive strength of the analytical results. Common approaches for sample fractionation include field-flow fractionation (FFF) or size-exclusion chromatography (SEC), which can be coupled to DLS or multi-angle light scattering (MALS) detectors for size determination, among other possible detectors, such as UV for RNA quantification. While FFF separates analytes based on their size without a stationary phase, SEC utilizes densely packed separation columns with matrices featuring respective pore sizes, allowing samples of specific sizes to permeate into the pores and thereby leading to higher retention times. This leads to faster elution of larger particles, since lower interaction with the porous matrix is possible. Controversially, at FFF, smaller particles show lower retention times in the separation channel. There, the sample is injected into the fractionation channel, where it is diluted in the chosen buffer. This buffer passes the separation channel in a parabolic flow. The applied forces for sample separation may be a second liquid flow (e.g., cross-flow (asymmetrical flow FFF (AF4)), magnetic (magnetic FFF), or electrical field (electrical FFF), among others) [144,145]. The respective separation forces accumulate the analytes at a porous membrane on one side of the separation channel, from where the particles can diffuse back to the

parabolic main flow. Since smaller particles show higher diffusion coefficients and faster motion into the middle of the parabolic flow, they migrate faster through the channel than larger particles. This allows a gentle separation of the analytes with a lower risk of shear-force-related sample degradation or alteration. An additional combination of SAXS can generate particle size distribution profiles, further allowing the determination of particle number per size fraction and the quantification of mRNA encapsulated per particle [146,147].

Further possible methods include nanoparticle tracking analysis (NTA) and analytical ultracentrifugation (AUC). AUC separates the samples using high centrifugal forces according to their mass, which is determined by size and density [148]. The widely used NTA can reveal information on particle size distribution by correlating Brownian motion rates, detected with microscopic imaging, with nanoparticle size. This avoids the sample fixation step, which is necessary in electron microscopy, while providing the mean, mode, and span of the particle population. Drawbacks include the need for an appropriate sample dilution to obtain accurate size distribution profiles, which can influence the properties of nanoparticles in dispersion.

Besides particle size and particle size distribution, another size-related parameter needed for batch characterization is particle concentration. Some of the above-mentioned size determination methods can also deliver particle concentrations. NTA provides information about particle concentration by analyzing the number of particles detected in an image analysis of a given sample volume. MALS techniques, with optional coupling to SEC or FFF methods, also enable the determination of particle concentration by measuring photon count rates, along with material and optical properties, to calculate particle concentration distributions. There, the accurate determination of particle size distributions, as well as knowledge about particle shape and physicochemical properties of the sample medium, is crucial [149]. As explained earlier, all methods are subject to inherent biases due to sample dilution or preparation. To overcome the limitations of single methods, the use of orthogonal size determination approaches can help minimize method-specific biases and interferences by employing a second well-characterized procedure that applies a different measurement principle [150].

Another size-related parameter, which is of crucial importance in product development, is the structure of the nanoparticulate drug product. Besides the size of the LNPs, morphology and internal structure also influence stability, circulation time, endosomal uptake mechanism, and the release of the nucleic acid cargo. Methods for its determination include scattering and transmission electron microscopy, where SEM allows determination of surface morphologies up to a certain resolution, while TEM also reveals information about the internal structure within the nanoparticulate samples. Utilizing this, the effects of lipid composition on structural organization and detection of lipidic substructures, such as blebs or membrane defects, are possible [131]. Nevertheless, aside from the aforementioned sample preparation and experimental difficulties, the limited resolution and contrast of internal features hinder in-depth analysis of the organization.

Another advanced method for structural investigations is NMR spectroscopy, e.g., ^{31}P NMR in combination with the use of chemical shift reagents. It is well established that multilamellar large vesicles (MLV) composed of phospholipids lead to broad ^{31}P-NMR spectra, whereas small unilamellar vesicles (SUV) are characterized by narrow line spectra [151], due to disturbed molecular motions within multiple lipid layer systems. Signals derived from phospholipids present in surface layers of the particles can be influenced by shifting agents such as Mn^{2+}, which are assumed not to penetrate through the lipidic bilayers into the particle [140]. This technique further allows statements about the mobility of RNA, which is influenced by the degree of encapsulation and the level of complexation by cationic lipids [152].

Small angle scattering measurements, including small angle X-ray and neutron scattering (SAXS/SANS), allow investigation of the samples in solution without further sample treatment. These methods measure the intensities of the scattered beam upon interaction of the beam with the sample. Further insights into these powerful techniques are explained in Chapter 1.6. Since the scattering of the beam happens upon collision with electrons (SAXS) or nuclei (SANS), every material included in the sample is detectable and influences the overall scattering intensity. This enables quantification of nanoparticle composites as well as the RNA cargo. Additionally, repeating structural features, such as the mRNA/lipid stacks in LNPs, lead to a positive interference of scattering intensity, which allows for the determination of distinct length scales within the particle. These include the length of the mRNA/lipid stacks and their long-range order within the formulation (Figure 1.5-2). This enables the determination of the influence of lipid composition, lipid-to-RNA ratio, and manufacturing approaches on the lamellar spacing and, consequently, the packing density of mRNA inside LNPs.

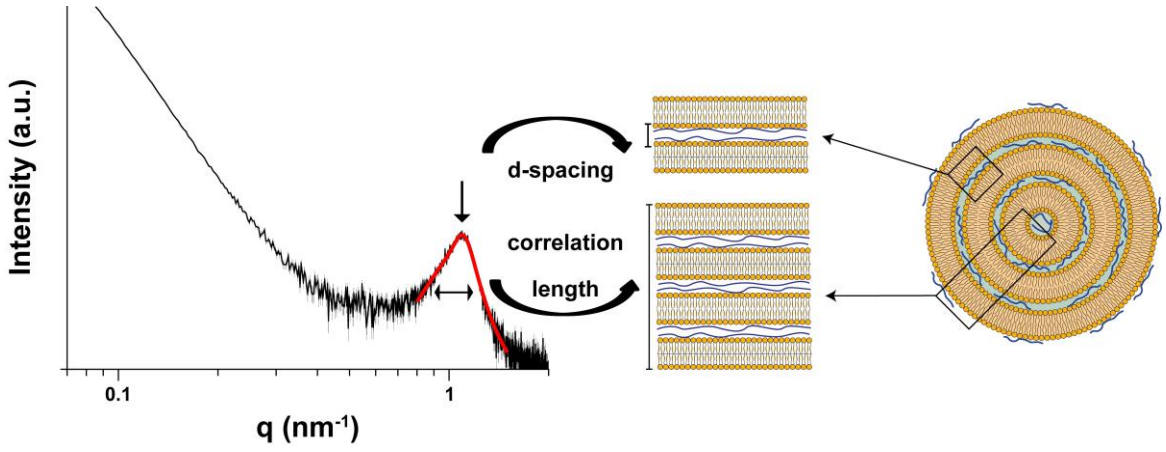

Figure 1.5-2: Structural features detectable by Lorentzian fitting of the SAXS-derived peak. Repeating structural motifs, as the mRNA/lipid stacks within lipoplexes (as displayed in the right) lead to peaks in the SAXS patterns of these systems (right). Lorentzian fitting (as indicated by the red line in the scattering pattern) of the observed peaks allows detection of peak position and width, which can be converted to length and long-range order of the repeating units, respectively (center).

Besides these determinations of distances in the Angstrom scale, information about particle sizes up to the micrometer scale, as well as information about shape and surface morphology, can be obtained. Selective deuteration of lipid or RNA components in SANS further enables determining the distribution of these components within the formulation. By doing so, it was revealed that helper lipids, such as DSPC, are mainly located at the surface layers of LNPs, whereas the ionizable lipids are located in the core of the particle [153,154]. Also, various drawbacks limit the application in daily quality control. Due to the low electron contrast of the LNP samples, high beam intensities are required, which are only attainable at synchrotron sources for SAXS and neutron sources for SANS. This limits the accessibility of the method. Furthermore, batch measurement of samples with an intrinsic degree of polydispersity results in overlapping signals from different structures, complicating the analysis. Here, coupling size-dispersive methods enables structural investigations in different size fractions of a single sample [146].
Further particle-related properties as zeta potential, surface hydrophobicity, and membrane polarity, also need to be characterized in drug product development, but are treated in detail elsewhere [131].

1.6 Structural analysis using small angle X-ray scattering

As explained above, SAXS is a powerful tool for exploring structural parameters that can be of interest not only in early development stages but also for determining the quality of nanoparticulate drug products. Despite SAXS being more of a platform for basic research and not yet fully implemented in industrial drug product control, considerably more information can be derived, which can be directly applied in daily quality measures.

In SAXS measurements, a collimated, monochromatic X-ray beam is scattered by the sample, with the scattered light intensity being captured on a radial 2D detector Figure 1.6-1. Since in SAXS experiments, the incident beam is scattered by electrons in the sample, the sample must have a different electron density than the surrounding matrix material (e.g., the solvent or the buffer used). Upon interaction of X-rays with material, one fraction will pass through the sample, one fraction will be absorbed (e.g., converted into any form of energy), and a last fraction will be scattered to other directions. To obtain SAXS data of sufficient quality, the absorption must be kept as small as possible, which can be adjusted by varying the sample thickness (e.g. by using flow through capillaries) and contrast to the solvent.

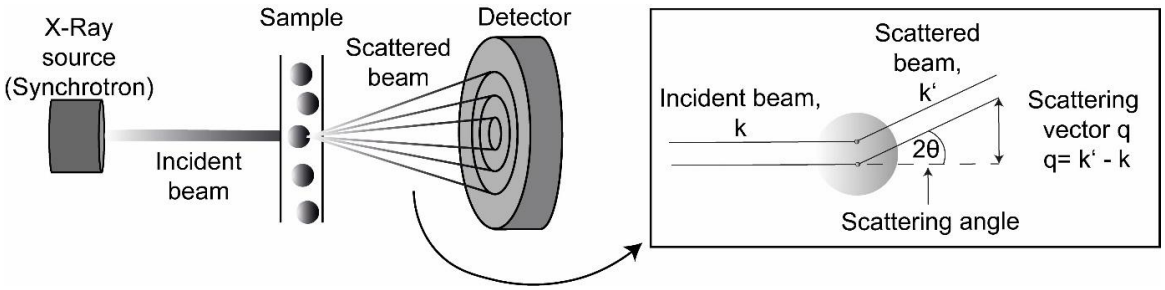

Figure 1.6-1: Schematic illustration of a SAXS experiment (left) and the scattering behavior at single X-Ray scattering events (right).

X-ray scattering involves elastic and inelastic processes [155]. When objects are exposed to monochromatic waves having a wavevector with the modulus k, atoms can absorb and re-emit spherical waves. In inelastic scattering, some photon energy is transferred to electrons, changing the wavelength and preventing interference, which means no derivable structural information. Elastic scattering occurs when photons interact without energy transfer, causing electrons to oscillate and emit light at the same wavelength (with the modulus k'), with interference patterns depending on the position and orientation of the scattering electron. This leads to varying intensities on the detector and therefore allows structural investigations. The angle between the vector of the incoming beam and the scattered light is defined as the scattering angle 2Θ, where the wave vectors of both are of the magnitude of $2\pi/\lambda$ (with the wavelength of the beam being λ, see Figure 1.6-1). The scattering vector q, which is used to describe the scattering patterns as a function of the detected intensity and has the dimension of inverse length units (e.g., nm^{-1} or $Å^{-1}$), describes the difference between the wave vectors of the incoming and scattered beams and is given in equation 2 [155],

$$q = \frac{4\pi}{\lambda} \sin\Theta \qquad (2)$$

Repeating structural features lead to constructive interference, resulting in a higher detected intensity for distinct scattering vectors. This can be, for example, used to investigate the structure of the lipid/mRNA stacks inside lipoplexes and LNPs. By analyzing the scattering patterns, it is possible to detect distances and structural organizations within the nanoparticle and the radius of gyration of the overall particle. Overall particle characteristics can also be described by the form factor of the particle, since all electrons in one particle contribute to the resulting interference pattern. This pattern oscillates in a manner characteristic of the shape and form of the particle.

To model these structures from small-angle X-ray scattering (SAXS) data, the Debye formula provides a foundational approach[156]. It relates the scattering intensity to the sum over all pairwise distances between scattering centers (e.g., electrons) within the particle, as in equation 3

$$I(q) = \sum_{i=1}^{N}\sum_{j=1}^{N} f_i f_j \frac{\sin(qr_{ij})}{qr_{ij}} \qquad (3)$$

where I(q) is the scattering intensity as a function of q, f_i and f_j are the respective scattering factors of two particles i and j, and r_{ij} is the distance between the two particles (see Figure 1.6-2). Each pair of scatterers contributes to the total scattering intensity depending on their distance and the scattering angle. To get an insight into real-space dimensions, the so-called pair-distance distribution function p(r) becomes a central concept [155]. This function describes the probability of finding a pair of points separated by a distance r within the particle and displays essentially a histogram of all particle-to-particle distances (r_{ij}) weighted by their scattering factors f. By applying an indirect Fourier transform (IFT) to the experimental scattering data, the p(r) function can be derived, offering real-space insights into the particle's internal structure and maximum dimension (Figure 1.6-2) [157]. From the shape of the p(r) function, the shape (spherical, core-shell, cylindrical) of the sample can be derived. Additional parameters, like the maximum dimension $D_{max,}$ can be obtained. By doing so, one can gain first impressions of the particle´s size and shape, and combined with the utilization of the Debye formula, SAXS curves can be simulated from candidate models and refined to match the experimental data. This process is the basis for ab initio modeling approaches, which are often used in protein biology to elucidate the structure of proteins and to investigate potential new targets and design novel APIs by molecular modeling techniques [158,159].

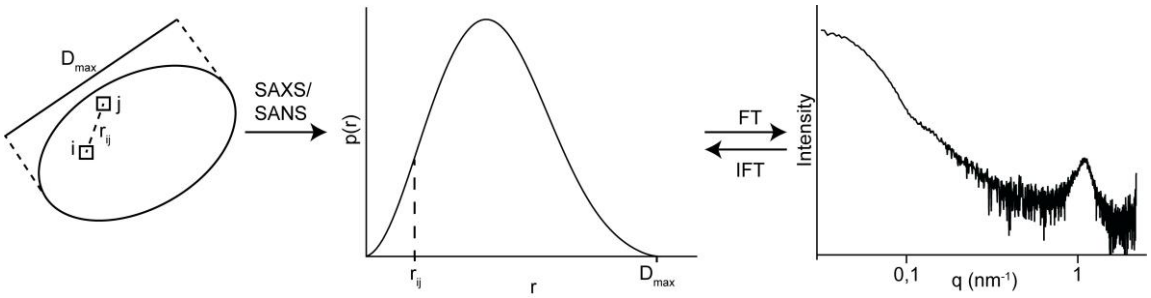

Figure 1.6-2: Relationship between particle structure (left, including internal distances (rij) between internal particles i and j), the pair distance distribution function (p(r) function, middle), and the scattering intensity measured by SAXS (right). The p(r) function can be derived from scattering patterns by indirect Fourier transformations (IFT) and vice versa by Fourier transformations (FT).

For the exact determination of overall particle features, the particle needs to be as monodisperse as possible and adequately diluted. Therefore, size-dispersive fractionation approaches are crucial for detecting properties as accurately as possible [160,161]. Additionally, the contrast to the solvent of the sample needs to be as high as possible to reach structural information in a high resolution. Since by SAXS analysis only point-to-point distances and their relative appearances inside the particles can be derived, especially for complex systems like mRNA-LNPs, complementary methods like cryo-EM or freeze-fracture EM measurements have to be performed to prove structural assumptions.

Further descriptions regarding the application of SAXS as a tool in quality determination and formulation development, as well as the underlying formalisms, can be found in the respective experimental sections of this work.

2

Subprojects and scientific aims

The results presented in this doctoral thesis can be divided into two subprojects. On the one hand, an analytical platform utilizing AF4 and SAXS was implemented to determine size distributions and quantify size-dependent critical quality attributes. Secondly, SAXS batch measurements were employed to investigate the impact of lipid composition, manufacturing approaches, and environmental conditions on the structural properties of lipid nanoparticles carrying mRNA, and to elucidate further structure-function relationships through various *in vitro* and *in vivo* experiments. Both subprojects were conducted in the framework of the CRC1066 (subproject B12) and the BMBF grant number 05K22UM3.

2.1 Subproject 1: Coupling of Asymmetrical-Flow Field-Flow Fractionation (AF4) and Small Angle X-ray Scattering (SAXS) for Enhanced Characterization of Lipid mRNA Delivery Systems

As mentioned in Chapter 1.5, the emerging delivery platforms for nucleic acids used therapeutically come with substantial analytical requirements to obtain in-depth characterization during development and to ensure quality through adequate quality control measures during clinical trials and in post-marketing stages. Here, size and size-related parameters, such as particle size distribution, morphology, content of the drug substance, and colloidal stability, need to be investigated in detail, because they can serve as batch release criteria and have a crucial influence on *in vivo* behavior and therapeutic potency. SAXS is a powerful tool for investigating the overall particle characteristics, including particle size, shape, and surface properties. It also allows for the investigation of internal structural features, including, for example, the mRNA-lipid stacks, whose morphology is assumed to influence the therapeutic performance and stability of the formulation. Additionally, because the SAXS signal is linearly correlated to the concentration of the analyte, it is a suitable method for absolute quantification of the sample. Nevertheless, discrete investigation of these parameters is only possible if the sample is as monodisperse as possible, which raises issues when investigating lipid mRNA delivery systems, which are always characterized by a certain

degree of intrinsic polydispersity. Therefore, size-dispersive fractionation upstream of the SAXS measurement is a necessary task to obtain results of the highest quality.

Within this project, an in-line coupling of two analytical methods was designed and, for the first time, implemented to assess the quality of nanoparticles, specifically those carrying mRNA. Particularly, the size-dispersive separation technique AF4 was used to separate particle fractions according to their size before in-line investigation of structural features using SAXS. This setup enables structural investigation of nanoparticles from nm to µm scale and overcomes the problem of SAXS during measurements of non-monodisperse samples. AF4, as an elution-based fractionation technique that does not utilize a stationary phase, enables the separation of shear-force-sensitive samples with a large size and polydispersity range, thereby providing a useful alternative to the widely established SEC-SAXS combination for lipidic nanoparticles. Due to the numerous available downstream detection methods, the AF4-SAXS combination enables the detection of several overall and internal structural features, as well as RNA quantification using UV spectroscopy and orthogonal size determination using MALS and DLS.

This project paved the way for applying the combination of AF4 and SAXS at the synchrotron facility Petra III at DESY Hamburg (Germany) and enabled the first-time acquisition of a quantitative dataset of size-related CQAs for mRNA-carrying nanoparticles, which our group continues to explore and develop for other pharmaceutical nanoparticles.

2.1.1 Publications obtained in this project

(1) Melissa A. Graewert[‡,] *, Christoph Wilhelmy[‡], Tijana Bacic[‡], Jens Schuhmacher, Clement Blanchet, Florian Meier, Roland Drexel, Roland Welz, Bastian Kolb, Kim Bartels, Thomas Nawroth, Thorsten Klein, Dmitri Svergun, Peter Langguth and Heinrich Haas*. Quantitative size-resolved characterization of mRNA nanoparticles by in-line coupling of asymmetrical-flow field-flow fractionation with small angle X-ray scattering. *Sci Rep* **13**, 15764 (2023). doi:10.1038/s41598-023-42274-z

2.2 Subproject 2: In-Depth Characterization and Structure-Function-Correlation of mRNA Lipid Nanoparticles using Small Angle X-ray Scattering (SAXS)

Not only since the authorization of the first mRNA based drug products during the COVID-19 pandemic, massive research capacities are used to design novel mRNA delivery systems which address issues and future challenges as (i) delivery to tissues and cells beyond the liver, (ii) endosomal escape and (iii) formation of morphological inhomogeneities (for example blebs and empty LNPs) among other questions (as discussed in Chapter 1.1). The basic concept of LNP delivery systems is very similar in FDA- and EMA-approved drug products; however, due to its complex lipidic composition, it offers several degrees of freedom to fine-tune the physicochemical properties and, consequently, the *in vivo* behavior of mRNA LNPs. This led to the development of hundreds of novel lipid components, primarily focusing on the ionizable cationic lipid, but also involving the substitution of other lipid components within the formulation. While this offers a large library of excipients that can be used for formulation development, the potency and toxicity testing of such novel lipids and formulations requires significant *in vitro* and *in vivo* capacities. While these experiments are indeed necessary and lay the groundwork for novel drug products, they are very time-consuming, costly, and even pose the risk of under- and overestimating the potency of lipids during early development stages. Having in mind that only a few general paradigms for rational synthesis of ionizable lipids exist, including adjustment of the lipid and formulation pK_a and the ability of the lipid to undergo lamellar to hexagonal phase transition, the necessity of additional tools to estimate the potency of delivery systems arose.

Within this project, we implemented SAXS as a tool to investigate structural features of mRNA LNPs and proposed distinct quality attributes, including the repeating unit of the mRNA-lipid stacks, the long-range order of the repeating unit, and the surface mass fractal dimension. Furthermore, we investigated the influence of manufacturing approaches, formulation composition, and environmental conditions (e.g., environmental pH) on the above-mentioned parameters to draw conclusions about critical process parameters, which significantly influence the SAXS-derived properties. By employing a combination of various characterization methods, including dynamic light scattering, ζ-potential measurements, and cryo-EM, among others, we were able to obtain an in-depth characterization of the LNP samples. By correlating these results with different *in vitro* (including different cell models) and *in vivo* (zebrafish embryo model) experiments, it was possible to elucidate novel structure-potency relationships. Particularly, we detected distinct structural features that are present in formulations with high transfection efficacy, which can be used as a quality target profile parameter in early formulation development stages. Additionally, these structural fingerprints can be used in quality determination testing.

Overall, the investigations within this project paved the way for a standardized approach to using SAXS as a characterization tool in the development and quality control of mRNA-carrying nanoparticles, by proposing distinct methods to elucidate the structural behavior of the overall particle and the internal organization within LNPs.

2.2.1 Publications obtained in this subproject

(1) Christoph Wilhelmy‡, Isabell Sofia Keil‡, Lukas Uebbing, Martin A. Schroer, Daniel Franke, Thomas Nawroth, Matthias Barz, Ugur Sahin, Heinrich Haas, Mustafa Diken* and Peter Langguth*. Polysarcosine-Functionalized mRNA Lipid Nanoparticles Tailored for Immunotherapy. *Pharmaceutics* **2023**, *15*, 2068. doi:10.3390/pharmaceutics15082068

(2) Dongdong Bi‡, Christoph Wilhelmy‡, Dennis Unthan, Isabell Sofia Keil, Bonan Zhao, Bastian Kolb, Roman I. Koning, Melissa A. Graewert, Bert Wouters, Raphaël Zwier, Jeroen Bussmann, Thomas Hankemeier, Mustafa Diken, Heinrich Haas, Peter Langguth*, Matthias Barz* and Heyang Zhang*. On the Influence of Fabrication Methods and Materials for mRNA-LNP Production: From Size and Morphology to Internal Structure and mRNA Delivery Performance In Vitro and In Vivo. *Adv. Healthcare Mater.* 2024, 13, 2401252. doi: 10.1002/adhm.202401252

(3) Christoph Wilhelmy‡, Lukas Uebbing, Bastian Kolb, Melissa A. Graewert, Thomas Nawroth, Heinrich Haas*, Peter Langguth*. Direct structural investigation of pH responsiveness in mRNA lipid nanoparticles: Refining paradigms. *Journal of Controlled Release* **2025**, 113848, doi:10.1016/j.jconrel.2025.113848.

3

Subproject 1: Coupling of Asymmetrical-Flow Field-Flow Fractionation (AF4) and Small Angle X-ray Scattering (SAXS) for Enhanced Characterization of Lipid mRNA Delivery Systems

3.1 Quantitative Size-Resolved Characterization of mRNA Nanoparticles by In-Line Coupling of Asymmetrical-Flow Field-Flow Fractionation with Small Angle X-ray Scattering

3.1.1 Summary and Contributions

Within this work, we designed and implemented a combinatory analytical method to investigate pharmaceutically used nanoparticles in terms of size and size-related properties. For this, we linked a size-dispersive fractionation technique (AF4) to in-solution small angle X-ray scattering (SAXS) at the synchrotron DESY, located in Hamburg, to enable structural investigations of separated size fractions of nanoparticles. The work presents a novel approach for the quantitative, size-resolved characterization of mRNA nanoparticles, addressing the challenges in determining size-related critical quality attributes, such as drug loading, free drug content, and internal structure, within pharmaceutical products.

First, the setup was successfully tested with the model protein BSA, which is commonly used for calibration of the SAXS setup and can be separated into its oligomers (monomer, dimer, and potentially aggregates). As a proof-of-concept system for pharmaceutical nanoparticles we subsequently chose mRNA lipoplexes, as a systems which is currently undergoing clinical trials for several applications (see Chapter 0) and display nanoparticles with a relatively high degree of intrinsic polydispersity in coexistence with a fraction of free, unbound mRNA, making it a

challenging sample for the novel setup. Traces of the downstream detectors connected to the AF4 exhibited a good separation of free mRNA in mixture with loaded LPX particles, with the UV signal allowing quantification of separated unbound mRNA. Furthermore, the overlay of the AF4 detectors with the measured scattering intensity by SAXS revealed a successful connection between the two analytical methods, with all signals being in good accordance with each other. The SAXS patterns of LPXs within a separated SAXS fraction further confirmed a successful separation, since no indication of larger moieties was visible and the SAXS pattern was significantly different from that of an unseparated batch measurement of the same sample. In addition, comparisons of fractionated and unfractionated mRNA revealed no differences, confirming that the separation process did not have an influence on drug substance stability.

By analyzing the SAXS patterns of the respective size fractions, we observed that distinct parameters like the position of the characteristic Bragg peak remained similar, while others like peak width and peak area changed as a function of particle size. This suggests that the type of ordered material within the nanoparticles was consistent, and only the amount of this material per particle varied with increasing particle size. Furthermore, the area of the Bragg peak could be taken to quantify the concentration of mRNA.

In combination, the different detection possibilities of the AF4-SAXS enabled the determination of distinct particle sizes, the quantification of total material within the respective particle size fractions, and the internal organization of the particles. By combining this information with generally accepted formalisms, it was possible to determine the particle size distributions of LPX and to obtain subsequent quantitative profiles of drug loading parameters, including the number of LPX particles, RNA copy number, and RNA copy number per particle.

This proof-of-concept experiment should pave the way for the application of this setup to all kinds of pharmaceutically used nanoparticulate drug products. To date, our group has further refined this setup with applications to other mRNA-based particles, such as LNPs, as well as liposomal products carrying small molecules as APIs.

This work was published in the following article:

Graewert, M.A.‡, Wilhelmy, C.‡, Bacic, T.‡ *et al.* Quantitative size-resolved characterization of mRNA nanoparticles by in-line coupling of asymmetrical-flow field-flow fractionation with small angle X-ray scattering. *Sci Rep* 13, 15764 (2023). https://doi.org/10.1038/s41598-023-42274-z

‡ These authors contributed equally to this work.

Own contribution:

Authorship:	First author
Investigations:	Execution of experiments at the beamline
Data analysis:	Gathering and organization of raw data, Structural analysis of SAXS data for lipoplex samples
Writing:	Writing of original draft, review and editing

Contribution of all authors:

Conceptualization: M.G., P.L., and H.H

Methodology: M.G., T.B., J.S., F.M., R.D., R.W., P.L., and H.H

Investigation: M.G., C.W., T.B., F.M., R.D., R.W., B.K., and K.B.

Project administration, supervision: M.G., T.K., D.S., P.L., and H.H

Data analysis: M.G., C.W., T.B., J.S., C.B., F.M., R.D., R.W., T.N., D.S., and H.H.

Writing—original draft: M.G., C.W., T.B., J.S., F.M., R.D., R.W., P.L., and H.H

Writing – review & editing: all.

www.nature.com/scientificreports

scientific reports

Check for updates

OPEN

Quantitative size-resolved characterization of mRNA nanoparticles by in-line coupling of asymmetrical-flow field-flow fractionation with small angle X-ray scattering

Melissa A. Graewert[1,6]✉, Christoph Wilhelmy[2,6], Tijana Bacic[3,6], Jens Schumacher[3], Clement Blanchet[1], Florian Meier[4], Roland Drexel[4], Roland Welz[4], Bastian Kolb[2], Kim Bartels[2], Thomas Nawroth[2], Thorsten Klein[4], Dmitri Svergun[1,5], Peter Langguth[2] & Heinrich Haas[2,3]✉

We present a generically applicable approach to determine an extensive set of size-dependent critical quality attributes inside nanoparticulate pharmaceutical products. By coupling asymmetrical-flow field-flow fractionation (AF4) measurements directly in-line with solution small angle X-ray scattering (SAXS), vital information such as (i) quantitative, absolute size distribution profiles, (ii) drug loading, (iii) size-dependent internal structures, and (iv) quantitative information on free drug is obtained. Here the validity of the method was demonstrated by characterizing complex mRNA-based lipid nanoparticle products. The approach is particularly applicable to particles in the size range of 100 nm and below, which is highly relevant for pharmaceutical products—both biologics and nanoparticles. The method can be applied as well in other fields, including structural biology and environmental sciences.

The success of messenger RNA (mRNA) nanoparticles for vaccination against Covid-19 has highlighted the potential of RNA nanomedicines as well as of nano-scaled pharmaceutical products in general[1–5]. In mRNA vaccines, so-called lipid nanoparticles (LNPs), which are characterized by a specific lipid composition and manufacturing process, are used for mRNA delivery. There is a wealth of different other nano-scaled pharmaceuticals which have reached various stages of clinical and preclinical development. The particles may be based on organic (e.g., lipids, polymers, polypeptides, proteins) as well as on inorganic materials (e.g., metals, metal oxides, silica)[6,7].

The majority of these products are intended for parenteral application with particle sizes typically below 200 nm (the limit for sterile filtration): LNPs measure 100 nm or less, and certain particle formats (e.g., for targeting tumors or crossing the blood–brain barrier) are in the range of tens of nanometers. With dimensions of a few or few tens of Angstroms, other types of drug formats such as biologics (therapeutic proteins, antibodies) or soluble polymers may be included for this category of nano-sized drugs. The characteristics of all these systems are dominated by their colloidal nature, where particle size and size-related attributes are of fundamental importance for quality, biological efficacy, and safety.

Determination of size-related parameters, such as internal structure and especially drug loading, poses particular challenges regarding quality control[8]. Obtaining information on size distribution profiles and size-dependent parameters is crucial for the identification of critical quality attributes (CQA) and critical process

[1]European Molecular Biology Laboratory, Hamburg Unit, Hamburg, Germany. [2]Department of Biopharmaceutics and Pharmaceutical Technology, Johannes Gutenberg-University, Mainz, Germany. [3]BioNTech SE, Mainz, Germany. [4]Postnova Analytics GmbH, Landsberg am Lech, Germany. [5]BIOSAXS GmbH, Hamburg, Germany. [6]These authors contributed equally: Melissa A. Graewert, Christoph Wilhelmy and Tijana Bacic. ✉email: melissa.graewert@embl-hamburg.de; haashein@uni-mainz.de

parameters (CPP)[9]. Size-related properties are especially important in the development of generic versions of originator products, as equivalence in physicochemical and biological characteristics needs to be demonstrated. In the case of protein-based therapeutics, controlling aggregation and potential denaturation is crucial, while for nanoparticle products size, particle size distribution, and the above-mentioned size-dependent attributes are significant.

Dynamic light scattering (DLS) is a widely accepted technique for regular size measurements in the control of pharmaceutical nanoparticle products. This high throughput method is easily applicable, robust, sensitive to delicate changes of size characteristics, and fulfills many requirements for regular application in quality control laboratories. By using standard algorithms such as the Koppel algorithm[10], DLS can provide numerical values that represent a length dimension (sphere-equivalent hydrodynamic diameter), interpreted as an average size, as well as a dimensionless value, the polydispersity index, which is used to indicate physical polydispersity. However, these values hold physical meaning primarily for relatively monodisperse samples. In fact, most nanoparticulate pharmaceutical systems, including liposomes, and lipid- or polymer-based nanoparticles, are characterized by a certain degree of intrinsic polydispersity. Quantitative information on the physical size distribution profiles and size-dependent parameters (e.g. loading, release, structure) are of superior importance for the development and quality control of such products[8,9]. There are algorithms that allow to calculate physical profiles from DLS data, but these are highly model-dependent and are usually not suitable for regular use[11]. Other methods that provide at least semi-quantitative insight into size distributions comprise nanoparticle tracking analysis, analytical ultracentrifugation as well as chromatography-based methods such as size exclusion chromatography (SEC) and asymmetrical-flow field-flow fractionation (AF4) in combination with multiple downstream detection systems. However, the individual methods have all certain specific drawbacks and can provide only semi-quantitative profiles, which depend in a complex manner on parameters such as size-dependent scattering intensities, refractive index gradients, densities, molecular conformation, swelling characteristics, and others[11].

To our best knowledge, so far, no method for in situ determination of absolute size distribution profiles for colloidal particulates in the size range of 100 nm and below is available. Here, we present a novel approach to obtain such data, providing, direct, quantitative size distribution profiles and further quality-indicating parameters by combining AF4 with small angle X-ray scattering (SAXS) measurements.

AF4 is an elution-based fractionation technique, allowing the separation of particulates according to hydrodynamic size in the range of approximately 1–1000 nm. Multiple detectors, including, for example, refractive index, UV absorption, circular dichroism, fluorescence, DLS, and multi angle light scattering (MALS) can be connected in-line to the AF4 separation set-up. For investigation of pharmaceutical nanoparticles, including liposomes and other colloidal systems, and protein-based drug products, it is a frequently applied tool in development[12–17].

Solution SAXS is a method that provides direct structural information in a size range from hundreds of nanometers down to the sub-Ångstrom scale, depending on instrumental settings. The SAXS signal is directly correlated to the analyte concentration (through the electron density gradient) in a linear manner, therefore it is suitable for absolute concentration measurements[18]. The obtained structural data are model-independent, as directly correlated to the squared autocorrelation function of the electron density distribution, from which real space structure can be revealed by different approaches using standard software packages from the respective research facilities[19].

SAXS may be considered as one of the 'gold standard' methods for the characterization of colloids, nanoparticles, proteins, and polymers in solution, as well as for various biomembrane systems. It is as well established for the characterization of different types of nano-scaled pharmaceutical products[20–24]. Due to the relatively low contrasts (e.g., the electron density gradients between particulates and bulk phase) of soft matter systems, for measurements with laboratory X-ray sources a certain analyte concentration is required. Therefore, for diluted systems with low contrast, measurements are often performed at synchrotrons.

One prerequisite for unambiguous quantitative SAXS data analysis is, that only one type of particulate is present, in an as far as possible monodisperse form. Therefore, for protein samples, for instance, careful sample preparation is important to avoid aggregates which scattering signal would contribute to the scattering curves[25]. A solution routinely adopted to overcome this limitation is to combine SAXS with with a method to separate the analyte as a function of size.

The combination of size-dispersive methods with SAXS has been successfully utilized in the field of structural biology, particularly by directly connecting SEC to the measuring cell, commonly referred to as SEC-SAXS. Here, the benefits of 'polishing the sample on-the-fly' was first demonstrated in 2004 at the biological SAXS beamline BioCAT in Chicago (APS, USA)[26] and have manifested themselves in such a way, that currently over 13 dedicated scattering beamlines (X-ray and neutrons) have implemented this separation technique at their beamlines and are in high demand by the whole global user community[20,21,27].

However, the use of SEC is not applicable to all systems. Its limitations include for example undesired shear forces through interactions with the stationary phase and restricted resolution in regards to more broadly dispersed samples[28]. In contrast to that, AF4 allows the variation of several instrumental parameters which facilitates the development of tailored methods for a given type of sample or product. AF4 allows separation over a bigger size range and polydispersity level, also for shear-force sensitive samples.

So far, to our knowledge, only one approach for combining AF4 directly with SAXS has been reported, in which polyelectrolytes in aqueous solutions were analysed[29]. The hesitancy for the direct hyphenation of AF4 and SAXS may be attributed to the fact that AF4 as a separation technique is still not as established in routine purification and analytical processes as chromatographic approaches are. In general, its potential is often underestimated[28].

Here, for the first time, we describe an approach of directly coupling AF4 to SAXS (AF4-SAXS) to thoroughly characterize nanoparticulate pharmaceutical products. A fully equipped AF4 instrumentation, comprising UV absorption and MALS detectors for analyzing the nanoparticles, was set up directly at the BioSAXS beamline,

allowing to obtain the full information from classical, multi-detector AF4 with subsequent in-line SAXS measurements from the same particles (Fig. 1).

We selected bovine serum albumin (BSA) as a model protein to represent the conditions for analyzing protein products for pharmaceutical applications (biologics), where we regarded the separation capacity from oligomers and aggregates, and compared the quality of the data from the monomer with results from the cuvette and SEC-separated measurements.

As a test system for the investigation of nanoparticulate samples by AF4-SAXS, we have chosen lipoplex (LPX) formulations. These LPXs can be tailored to display very high targeting selectivity to specific organs (spleen, lung), depending on the manufacturing protocol (e.g. mixing ratio between mRNA and cationic liposomes)[30–32]. Here we have selected LPXs with high targeting selectivity to lymphatic organs, such as spleen[30,32], which are assembled with an excess of mRNA. Such LPXs are currently undergoing late-stage clinical trials for cancer immunotherapy[30,31,33]. With their complex composition, consisting of a fraction of free mRNA in coexistence with polydisperse LPX nanoparticles, they are an ideal test system for evaluation of the method.

By applying sophisticated data analysis, we were able to accurately quantify the respective fractions in the formulations, to determine the absolute size distribution profiles of the LPX nanoparticles formulations, and to derive important size-related parameters such as the size-dependent structure and composition of the particles including the quantification of mRNA molecule per LPX. The method can be applied to all the above-mentioned nano-scaled pharmaceuticals as well as samples from life sciences or environmental sciences. In the context of pharmaceutical products, such novel, quantitative insight is of great relevance, for example, for formulation development, identification of critical product parameters, evaluation of manufacturing processes, evaluation of comparability, and product quality control in general.

Results

Application for proteins and biologics: BSA as a model protein

Control of aggregation state is of outstanding importance for quality control of biologics. Understanding protein misfolding as well as oligomerization processes are essential for optimal process design and formulation development[34,35]. Elucidation of oligomerization processes and the formation of aggregates has additionally become a hot topic ever since their role in the manifestation of various neurodegenerative diseases has become evident[36]. Furthermore, the preparation of monodisperse samples is essential in order to generate indicative data in life sciences and structural biology[25].

We demonstrated the overall functionality of the setup for analyzing biologics by testing the separation of the model protein BSA. BSA is an excellent model for studying the aggregation mechanisms of globular proteins[37] with its known formation of oligomeric states (monomeric, dimer, and higher oligomers including aggregates) under various experimental conditions.

BSA was successfully fractionated with AF4, and the elution profiles collected with all detectors (UV_{280}, MALS, SAXS) were in good agreement (Fig. 2A). Note, in comparison to UV and $LS_{90°}$ data, the SAXS elution profile shows slight band broadening due to a lower separation resolution because of the larger width of the SAXS flow cell. Nevertheless, the comparison to the data collected without fractionation (Fig. 2B; grey curve) clearly shows that larger species were removed from the sample through the separation process: The decrease in scattering at low q along with the decrease in radius of gyration, R_g (from 3.4 ± 0.1 nm to 2.9 ± 0.1 nm), maximum distance, D_{max} (from 13 + 0.4 nm to 9.1 + 0.2 nm), and the molecular weight (MW) estimate (based on the volume of correlation from 82 + 8 kDa to 69 + 7 kDa) are all in line with the scattering of monomeric BSA as opposed to the mixture containing roughly 10–20% dimeric and larger oligomeric fractions (supplementary Table 1). The constant MW distributions across the main elution peak as well as the second peak further confirm the successful separation into monodisperse fractions (Fig. 2A).

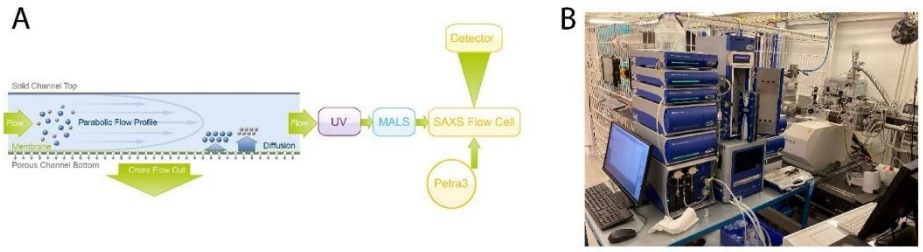

Figure 1. Overview of multi-detector AF4 setup. (**A**) Schematic overview of the set-up and the organization of different modules. After injection, the particles within the sample are fractionated by size in the AF4 channel. UV–Vis and multi-angle light scattering (MALS) detectors are placed before the flow-through SAXS capillary at P12 (PETRAIII) for characterization. (**B**) AF4- SAXS instrumentation as placed in the experimental hutch at the P12 beamline. AF4 setup with fractionation channel (left) connected to the P12 SAXS flow cell in-line (right). Sample separation and data collection are initiated remotely from the control hutch.

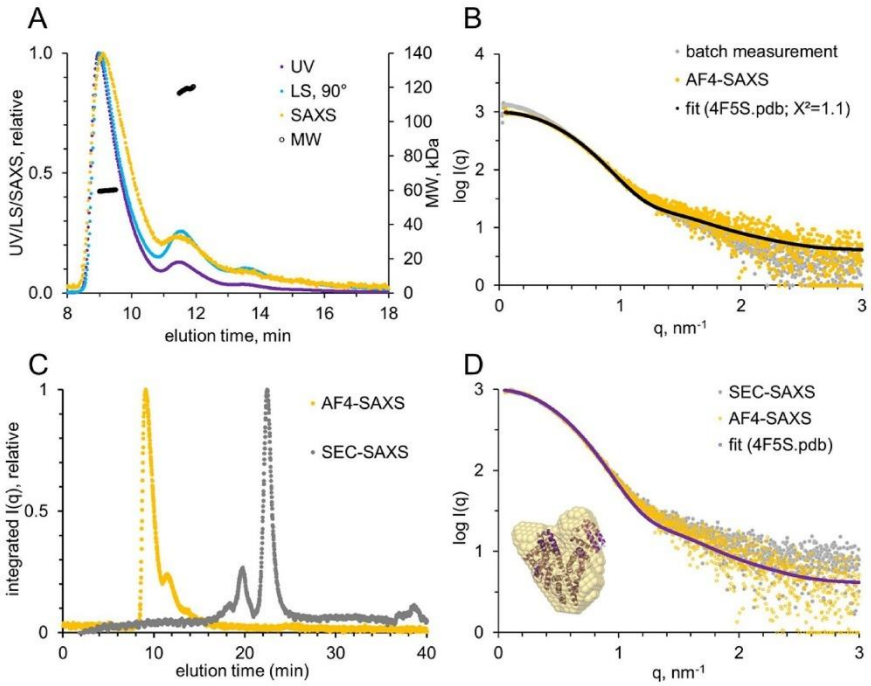

Figure 2. Set-up and system validation with the model protein BSA. SAXS data were collected from either AF4-coupled SAXS or SEC-coupled SAXS after injection of 40 µL BSA in PBS at 5 mg/mL. (**A**) Multi-detector overlay. MW distribution across the peaks suggests successful separation into monodisperse size fractions (monomers, dimers and even higher oligomeric states). (**B**) Comparison of scattering profiles from static measurement (batch, grey) and AF4-SAXS (orange). The fit of the theoretical scattering of the crystal structure is indicated (black). (**C**) Comparison of elution profiles from AF4-SAXS (orange) and SEC-SAXS (grey). Note, with SEC first the larger species elute, in AF4 the opposite is observed. (**D**) The derived SAXS curves from SEC-SAXS (grey) and AF4-SAXS (orange) are in good agreement with each other and can be fitted with the theoretical scattering data of monomeric BSA (purple, 4F5S.pdb, with $\chi^2 = 1.1$ for the AF4-derived scattering profile). The inlay shows the generated ab initio model as orange spheres overlaid with the cartoon representation of the crystal structure.

The obtained SAXS data frames corresponding to monomeric BSA displayed a good fit to the theoretical scattering curve derived from the atomistic crystal structure ($\chi^2 = 1.1$; 4F5S.pdb, Fig. 2D). In addition, the ab initio model derived from the purified scattering curve overlays well with the crystal structure.

Comparing AF4-SAXS and SEC-SAXS scattergrams (Fig. 2C) the opposite separation characteristic becomes obvious: While with AF4 smaller particles elute first, the contrary is the case for SEC. Both methods are able to separate the monomer from the oligomers properly. Data collection time, sample consumption and data quality are comparable for AF4-SAXS and standardised SEC-SAXS data mode which is commonly used to study volume mixtures of biological macromolecules at dedicated SAXS beamlines at synchrotron radiation (SR) facilities (Fig. 2C)[21]. The elution of the smaller component before the larger particles including aggregates that are often prone to radiation damage and subsequent capillary fouling, highlights the single benefit of AF4 in this case of protein oligomer separation.

Complex nanoparticulate pharmaceutical products: mRNA LPX formulations

As a test system for the investigation of nanoparticulate samples by AF4-SAXS, we have chosen LPX formulations, obtained by self-assembly between cationic liposomes and mRNA (Fig. 3A). For the present measurements, we specifically selected LPX systems which were formed with an excess of mRNA, resulting in negatively charged, polydisperse, LPX nanoparticles in coexistence with a fraction of free, unbound mRNA[30–32]. cryo-TEM measurements have demonstrated lamellar internal organization inside the LPXs[30]. This test system comprising polydisperse nanoparticles as well as negatively charged, free mRNA, is ideal to challenge and evaluate the AF4-SAXS approach while delivering information on the colloidal nature of such formulations, which is essential for assessing biological activity and quality. Note, that due to the opposite charge of the pure DOTMA:DOPE

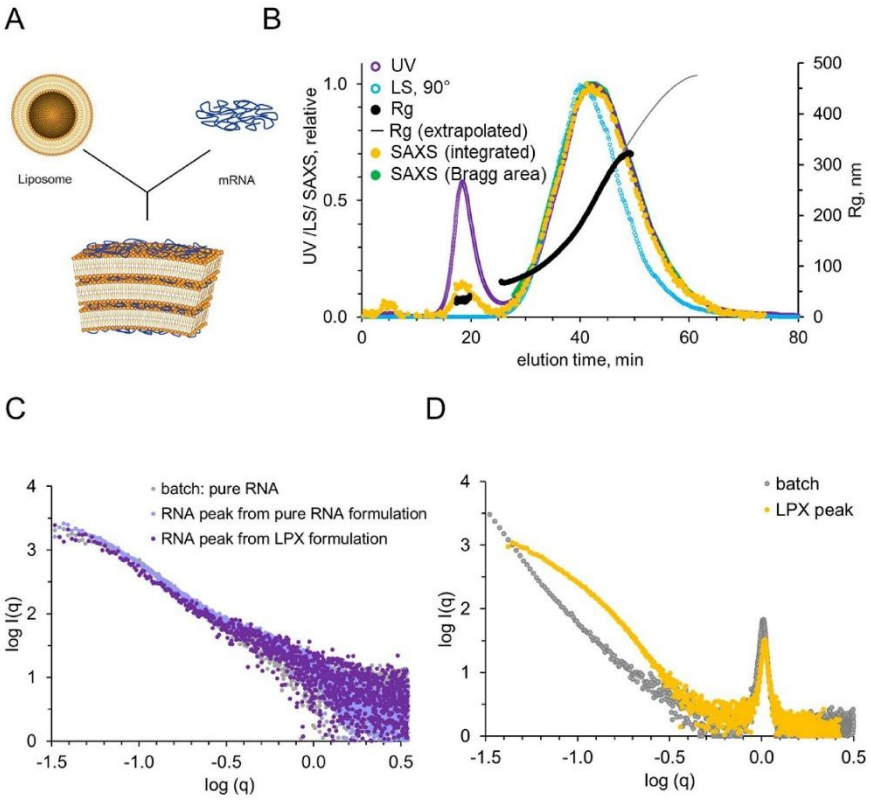

Figure 3. AF4 coupled SAXS analysis of LPX fractionated sample. (**A**) Self-assembly of mRNA LPXs by mixing of anionic mRNA (blue) with premanufactured cationic liposomes. (**B**) AF4-SAXS analysis of LPX formulation versus elution time with an overlay of fractograms derived from UV, LS, and SAXS including derived R_g values. The first peak, around 18 min, results from free mRNA, and the second peak, around 40 min, is from the mRNA lipoplex nanoparticles. (**C**) SAXS patterns derived from pure mRNA (grey) in a batch measurement compared with measurements of RNA after fractionation with AF4 (purple). (**D**) Comparison of a batch LPX sample with a purified LPX sample after fractionation. Note the much lower slope of the fractionated sample towards $q=0$, indicative for successful separation of other particulates.

vesicles, conducting a direct comparison of liposome size fractions without mRNA under identical experimental AF4 conditions was not feasible in this session.

The LPXs were injected, and the size-separated fractions were measured in-line by the subsequent detection systems. AF4 allowed for the effective separation and quantification of the two distinct fractions within the LPX formulations, as clearly demonstrated by the multiple elution traces obtained from the respective detectors (Fig. 3B). UV absorption measured at 260 nm, commonly used for mRNA quantification, revealed an initial peak, attributed to the presence of free mRNA, and a second, larger, peak corresponding to the LPX nanoparticles (Fig. 3B, purple trace). For the LPX peak it has to be kept in mind, that, further to UV absorbance, size-dependent scattering of the particles contributed to the signal. The X-ray scattering intensity (yellow trace), which is a measure of the absolute amount of material (Supplement Fig. 1), resulted in peaks for mRNA and LPXs at the same elution times as the UV peaks, however, the mRNA peak was relatively lower than in UV, in accordance with the above conjecture, that the UV signal of the LPXs was indeed influenced by scattering in addition to UV absorption (note, that the signals were scaled to 1 for the LPX peak). Light scattering at 90° (light blue trace) revealed also a pronounced peak for the LPXs, while the signal for the free mRNA was even lower relative to the LPX peak (as expected from the size dependence of scattering intensity).

Although the LS signal was weak, the radius of gyration (R_g) and the molecular weight of the mRNA could be calculated (Fig. 3B). A relatively constant R_g of about 25 nm, in accordance with a macromolecule with a discrete molecular weight (black horizontal line under the mRNA peak, Fig. 3B), was obtained. MALS allowed us to experimentally determine MW (~ 475 ± 50 kDa) which is well in accordance with the theoretical value

of ~ 400 kDa. This proves that the first peak resulted in fact from pure mRNA, without further molecular moieties (as, for example, lipid material) bound to it.

For the second peak, resulting from the LPXs, a clear separation of the particle size as a function of elution time from about 80 nm to about 470 nm (R_g) was determined (black line under the LPX peaks). This indicates the validity of the AF4 method for analysis of the LPX nanoparticles in the present samples (see also for complementary DLS measurements in Supplement Fig. 2).

SAXS offered direct structural insight into the respective fractions (Fig. 3C + D). Curves for the mRNA were indicative of unstructured random coil conformation (Supplement Fig. 3): the pair distance distribution function, p(r), displayed a skewed, extended shape, and in the Kratky plot a plateau towards large q, without intermediate maximum was obtained. With this structural organization, the mRNA differs substantially from the BSA which is characterized by a more globular packing. This highlights the strength of solution SAXS in offering structural information and its capability to assess compact, extended as well as flexible systems. The MW estimations from the SAXS curves were in accordance with the mRNA monomer found by MALS (440–450 kDa).

The LPX scattering curves were dominated by a Bragg peak (1 nm^{-1}), indicative of a lamellar organization of mRNA inserted into repeating lipid bilayers inside the nanoparticles[38]. The intensity at the q range below the peak displayed monotonous decay, where the slope of − 3.63 was in accordance with the presence of compact particles with smooth surface (Porod analysis, see Methods Part for details).

Notably, the fractionated LPX curves, as opposed to the bulk measurement, did not exhibit an increase in intensity towards q = 0, in agreement with the successful fractionation to rather monodisperse size fractions and removal of mRNA and any larger moiety. With that successful separation of the polydisperse LPXs into monodisperse and uniform moieties, further, quantitative data analysis was enabled.

Quantitative size distribution and size-dependent parameters

One aim of the present study was to obtain quantitative, absolute size distribution profiles for the particulates. This was made possible by in-line coupling of SAXS to classical multi-detector AF4, and a joint analysis of the data from the different detectors. For quantification of the free mRNA, UV absorption at 260 nm as used as well for cuvette measurements could be applied. The mRNA absorption dominates the UV signal of the material under the LPX peak, but for quantitative analysis as well scattering from the particulates has to be taken into account, which depends on particle properties such as size, shape and refractive index gradient. With such correction the concentration of RNA as a function of elution time is given, and with the knowledge of the lipid-to-mRNA ratio in combination with the size information from MALS, the absolute mass fraction of the particles at that size can be calculated.

X-ray scattering depends only on the electron density (gradient) and is therefore advantageous for the determination of absolute concentrations. In the standard approach for the determination of molecular weight from SAXS, the scattering intensity is extrapolated to zero scattering angle (I(0)), and with known concentration and electron density gradient, MW is given. Here we have used the particle size at a given elution time obtained from the MALS measurements and combined it with the SAXS scattering intensity to obtain the concentration.

With the applied settings for the experiments here, absolute determination of I(0) was hampered due to the missing data at very low q (Supplement Fig. 4). However, as the total concentration of the particulates is known (see Methods section) one can as well use the relative signal (e.g., from lowest measured q) and normalize over the known total concentration of LPX matter. This is also justified by the observation, that the fundamental characteristics of the particles did not change over the peak, and therefore the fundamental shape of the scattering curves should not substantially change.

As a second piece of information from the SAXS curves, one can analyze the evolution of the Bragg peak, which is measured for the LPX particles. Qualitative inspection of Bragg peaks from different LPX elution fractions (Fig. 4A) indicates, that only the area of the consecutive peaks changed over the elution time, while the peak position and shape were relatively similar. Therefore, the LPX nanoparticles consisted of the same type of ordered material with a characteristic d-spacing of about 6.0 nm independent of their size (which ranged from 80 to 470 nm), with the same lipid-to-mRNA stoichiometry for all particles (internal data, to be published).

We used Lorentz functions to quantitatively determine peak position, peak width, and peak area to calculate d-spacing, correlation length, and the total amount of ordered material (formalism in Methods section; Fig. 4B, Supplement Table 2). While the d-spacing (green), in fact, was basically similar over the elution time of the whole LPX peak, the correlation length (blue) increased slightly, in accordance with increasing size of the LPX stacks inside the larger particles. The peak area, indicative for the amount of ordered material, showed a similar peak shape over time as the UV and total SAXS signal (Fig. 4B, black trace). Apparently, all lipoplexes were characterized by the same type of internal order, with a continuous increase of organization with particle size. No fundamental change of structural characteristics at a certain size occurred, as also obvious from the plot of the peak area divided by peak with (Supplementary Fig. 5)[39].

Supplement Figure 4 shows the correlation of Bragg peak area, I(q), and UV signals as a function of elution time. One can see that the trace for detected forward scattering behaves like the UV absorption (and scattering), indicating that at the current setting the 'large particles' become 'invisible' in the Guinier analysis, and confirming the above conjecture of constant stoichiometry for all particles. We consider the ordered material as the one which is biologically active, therefore, we used the Bragg peak area for quantitative analysis of relative mass fractions. We obtain the amount and copy number of active (lipoplexed) mRNA in the particles, and, with the constant lipid stoichiometry, the total amount (mass) of the lipoplexed material at any given size fraction.

Valuable information can be drawn from this analysis: product characteristics such as LPX concentration in µg/mL, number of particles (Fig. 4C, red columns, green dots), mRNA copy number, and the mRNA copy number per particle (Fig. 4D, green columns, red dots) are obtained as a function of the particle size (formalism

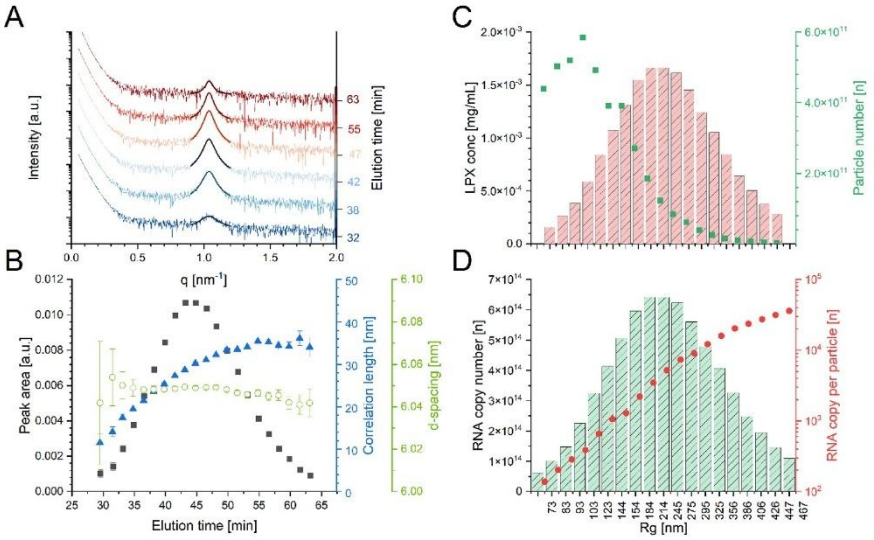

Figure 4. Detailed analysis of the fractionated samples. Adding AF4 separation directly before the SAXS data collection allows the correlation of SAXS derived information as a function of size (elution time). (**A**) SAXS patterns derived from different size fractions with respective Lorentzian fits (shifted on y-axis by increasing elution time). (**B**) Derived parameters from peak analysis of the individual scattering curves (d-spacing in green; correlation length in blue, peak area in black). (**C**) Absolute material concentration (LPX conc. in mg/mL) derived from SAXS signal for LPX peak (red bars) and the calculated absolute number of particles as a function of radius of gyration (R_g) derived from MALS (green dots). (**D**) The total number of mRNA copies calculated from SAXS traces in certain fractions of different particle sizes (R_g from MALS) (green bars) and calculated mRNA copies per particle of size segment (red dots).

see Methods section). The largest amount of LPX material (in µg/mL) is present in the form of particles of about 200 to 250 nm, while the highest number of particles is at the size fraction of about 100 nm (see methods and materials for calculations). However, not only the number of mRNA copies per particle, but also the total number of copies is much lower at the 100 nm than for the 200 nm fraction (Fig. 4D).

Furthermore, several other parameters which are relevant for the quality of particulate products (in the size range of the wavelength of light and above using counting methods), such as median and mean values (D10/D50/D90) with respect to mass concentration, particle concentration, and other parameters, can be readily derived.

Discussion

Quantitative determination of size-dependent parameters for nano-scaled colloidal systems is still an unmet need in many fields, including pharmaceutical research and development, as well as life and environmental sciences. This is, in particular, the case for small particles (smaller than the wavelength of light, when the particles are too small to be determined by counting methods such as laser light obscuration). Although some methods to generate size distribution profiles are available, they generally provide only qualitative information, while it is still difficult to obtain absolute data.

Here we addressed this challenge by in-line coupling of classical multi-detector AF4 with synchrotron SAXS measurements, methods which usually are only applied separately from each other. SAXS signals per se provide information on absolute concentrations. With the advantage of the high flux synchrotron beam allowing focusing on the small flow-through capillary, measuring low concentrations of solutes, and adjusting q from the USAXS range to WAXS, information on particle size, shape, packing (conformation) and internal order and crystallinity is obtained. Such information can be generated at synchrotron sources regularly within short exposure times and for a variety of different sample types.

For analysis of SAXS data, it is important to provide samples as much as possible in a single state (size, shape conformation), which is realized by the AF4 separation in the best possible manner. By in-line coupling of AF4 with simultaneous detection applications of standard methods (UV, MALS, and DLS) and SAXS comprehensive data on the fractionated samples are quantitatively obtained.

The high adaption of the use of SEC-SAXS by the structural biology community[20,21] clearly demonstrates the advantage of SAXS analysis with in-line separation techniques. With using AF4 for size separation, we can eliminate certain drawbacks of SEC. Pressure issues and unfavorable shear forces often cause the biggest problems while the samples pass through the column matrix (stationary phase). In contrast, in the AF4 separation

technique, a liquid-filled channel is used and thus these effects are not observed. Especially for weak-binding complexes these shear forces may affect the complexation state and, thus, cannot be used to get information on the native conformation. Other drawbacks of SEC include limitations in the choice of buffer and additives for a successful SEC separation. AF4 allows adjustment of buffer and flow parameters in a wider range, and therefore, tailored protocols for different types of particulates can be developed.

This makes AF4-SAXS particularly interesting for the investigation of complex systems, allowing to reveal quantitative profiles of broadly disperse systems, and to determine different fractions of nanoparticulates concerning degree of loading, structure, or functionalization. The capability of AF4 to separate molecular drugs or small proteins from nanocarriers, and nanocarriers from particles of micrometric size, is a major advantage for investigation of drug-loaded nanoparticles[28]. Also, different protein moieties with similar properties can be separated and analysed, with applications to pharmaceutically relevant proteins, as well as to basic structural biology research.

By optimizing the SAXS capillary in conjunction with the AF4 system, the scope of application can be also extended to low concentration samples. Thus, our upcoming experiments will entail dedicated beamtime sessions to fine-tune capillary lengths and diameters (all while maintaining the necessary backpressure for consistent AF4 fractionation). Furthermore, implementing the co-flow system could present an elegant prospect for mitigating the undesired dilution[40].

Here we have demonstrated the capabilities of AF4-SAXS for analyzing pharmaceutical formulations comprising lipoplex nanoparticles in coexistence with free mRNA. With our set-up of in-line coupling multi-detector AF4 SAXS measurements, we quantified and characterized the two fractions and obtained in-depth information on LPX particle characteristics such as drug-load and structure as a function of size.

While other approaches investigate this with confocal spectrometry methods by using labeled mRNA, lipids, and fluorescent dyes[41], our setup allows us to investigate formulations as they are used in clinical studies without further modifications. Additionally, it applies to other nanoparticulate formulations with different payloads as mRNA.

This allows us to apply the method for investigation of nanoparticles from various scientific fields, which either encounter issues regarding sample monodispersity and homogeneity or, by their nature, are broadly polydisperse and consist of different moieties. In pharmaceutical sciences, the method provides an invaluable contribution to characterizing the various types of colloidal nano-scaled products including liposomes, lipid nanoparticles, polymer nanoparticles as well as inorganic systems like SiO_2 or metal particles. As well, information on large molecules such as DNA, RNA therapeutic proteins (biologics), or dissolved polymers can be obtained. As shown in the present measurements for samples comprising a disordered biopolymer together with polydisperse nanoparticles, information on complex systems, can be obtained. The fractions in samples comprising different nanoparticle or colloidal moieties, or having different structures, shapes or molecular organization, can be quantitatively assessed. Further to pharmaceutical products, samples from life sciences, other industrial nanoparticles, and bio-eco particulate systems can be measured. For example, the separation of particles from environmental studies through AF4 coupled to other techniques such as Raman spectroscopy has allowed comprehensive studies of nanoplastics[42]. Obviously, here too, the additional information gained by X-ray scattering can deliver accurate information for example on the size, shape, and surface of environmentally relevant nanoparticles.

Conclusion

In summary, we have introduced a novel and versatile approach for obtaining quantitative, size-dependent information on nano-pharmaceuticals and colloids. As demonstrated with a model protein and complex mRNA lipoplex formulations, the method enabled the successful separation of the respective fractions comprised inside the products and, thus, allowed for their unequivocal quantification and characterization. The data are highly relevant in pharmaceutical development from a quality and safety perspective. The method has the potential to become a basic tool for the characterization of all these systems.

Methods

LPX formulation

LPX were formed by mixing cationic liposomes containing (R)-N,N,N-trimethyl-2-3-dioleyloxy-1-propanaminium chloride (DOTMA) and 1,2-dioleoyl-sn-glycero-3-phosphoethanolamine (DOPE) (both Merck KGaA, Darmstadt, Germany) lipids with the negatively charged messenger RNA (mRNA), using the semi-automated microfluidic path process, internal protocols based on previously described batch protocols[31,32]. Briefly, for incubation with the mRNA, a pumping system was used to mix equal volumes of two aqueous phases, comprising mRNA and liposomes. The mRNA was synthesized at BioNTech using internal protocols. The liposomes consisted of DOTMA and DOPE in a molar ratio of 2:1. Concentrations were adjusted to achieve a molar (charge) ratio between the positively charged DOTMA molecules in the liposomes and the negatively charged nucleotides of the mRNA of 0.65 to 1.

AF4 separation

Ultrapure water (UPW) was obtained from a Milli-Q system (Integral 5 system, Merck KGaA, Darmstadt, Germany). A carrier liquid of 10 mM HEPES (C. Roth GmbH Co. KG, Karlsruhe, Germany), 5 mM sodium chloride (Avantor Performance Materials Poland S.A.) and 0.1 mM tetra sodium salt of ethylenediaminetetraacetic acid (EDTA) (Merck KGaA, Darmstadt, Germany) was prepared and the pH was adjusted to 7.4 using 2 M NaOH (Chemsolute, Th. Geyer GmbH Co. KG, Karlsruhe, Germany). For system qualification and proof-of-concept study, a PBS buffer solution with 10 mM phosphate salts (potassium dihydrogen phosphate and sodium hydrogen phosphate salts, both obtained from Th. Geyer GmbH Co. KG, Karlsruhe, Germany), 137 mM sodium chloride,

2.7 mM potassium chloride (C. Roth GmbH Co. KG, Karlsruhe, Germany) at a pH of 7.4 was produced. Afterwards, all carrier liquids were filtered with a vacuum filtration unit through a 0.1 µm pore membrane (Durapore, Merck Millipore Ltd., Tullagreen, Ireland).

For the normalization of the MALS detector angles a polystyrene nanoparticle (PS-NP) size standard with a nominal diameter of 62 nm ± 4 nm at a concentration of 1% (w/w) (Nanosphere™ Size Standard 3060A, Thermo Fisher Scientific, Waltham, MA, USA) was fractionated. A carrier liquid of 0.2% (v/v) NovaChem (Postnova Analytics (PN), Landsberg am Lech, Germany) was used for the fractionation of PS-NP.

No sample preparation or dilution was performed prior to fractionation. The samples were fractionated by an AF4 system (PN AF2000 MT). Additionally, the system included an autosampler (PN 5300) and slot outlet function (PN 1650). A semi-preparative frit-inlet AF4 (FI-AF4) channel (shoulder width 50 mm, tip width 5 mm, tip-to-tip length 277 mm) was equipped with a polyethersulfone PES membrane with 10 kDa molecular weight cut-off and a Mylar spacer of 350 µm height. Preliminary offline tests using this channel suggesed that this configuration can accommodate the injection of up to 150 µg of mRNA. The temperature of the autosampler was set to a constant temperature of 4 °C. The system was hyphenated to a UV detector (PN 3211) and a MALS detector (PN 3621, 21 angles). The UV absorbance wavelength was set to 260 nm. The MALS detector angles were normalized with respect to 90° using a fractionated 62 nm PS-NP size standard. The MALS was directly connected to the SAXS flow capillary using a minimal tubing length with an ID of 250 µm. MALS data of LPX samples were evaluated by applying a 1st order Berry model fit to at least 9 active angles[15]. The number of forward scattering angles was limited due to the strong scattering contribution of the larger LPX particles. As a result, the derived R_g distribution ranged up to around 320 nm with a squared correlation coefficient R^2 of the fit higher than 0.99.

The injected volume varied from 250 µL up to 1000 µL. The fractionation method consisted of an exponential cross flow decay covering the sample size range in one single fractionation run. The slot outlet function with a flow rate of 0.2 mL min^{-1} was applied to concentrate the sample constituents after fractionation. Moreover, a sufficient rinse step of 12 min was implemented to minimize carryover and potential memory effects.

To test the suitability of the semi-preparative FI-AF4 channel all samples were also characterized on a standard FI-AF4 channel with the same tip-to-tip length, but smaller width of 20 mm. Here, all samples were analyzed in triplicate injecting only 40 µL to avoid potential overloading effects. The extrapolation of the R_g distribution (Fig. 1C) was carried out based on the last-mentioned measurements using a polynomial fit with excellent agreement. Here the aforementioned Berry 1st order model fit was applied to the scattering intensities derived from at least 11 active scattering angles. Instrument control and data evaluation were performed by the NovaFFF AF2000 software (PN, Version 2.2.0.1) and Excel (Microsoft Corporation, Office 2013). To comprehensively characterize the samples the MALS detector was connected to a Zetasizer Nano S (MALVERN Panalytical Instruments Ltd., Malvern, UK) in flow mode to derive hydrodynamic sizes from DLS.

SAXS data collection

AF4-SAXS data was collected at the P12 bioSAXS beamline of the European Molecular Biology Laboratory (EMBL) at the PETRA III synchrotron, DESY Hamburg (Germany)[43], using an incident beam size of 200 × 110 µm² (full width at half maximum). The eluent of the employed fractionation technique was passed through a 1 mm quartz capillary held under vacuum.

The SAXS data were recorded on a Pilatus 6 M area detector (Dectris) at a sample-to-detector distance of 3 m and the wavelength $\lambda = 0.155$ nm (X-ray energy 8 keV). Series of individual 1 s exposure X-ray data frames were measured from the continuously flowing column eluate across one column volume. The 2D SAXS intensities were reduced to $I(q)$ versus q using the integrated analysis pipeline SASFLOW. The q-axis was calibrated with silver behenate, and the resulting profiles were normalized for exposure time and sample transmission. This results in one-dimensional scattering intensity curves I(q) presented as functions of momentum transfer

$$q = \frac{4\pi \cdot \sin(\theta)}{\lambda} \tag{1}$$

where 2θ is the scattering angle and λ is the X-ray wavelength.

Additional data was collected with an automated sampler changer and in SEC-SAXS mode. Data collection details are summarized in Extended Data Table 1.

The 1D scattering curves were further analysed with Chromixs–allowing us to define the frames of interest as well as frames for buffer subtraction.

DATTOOLS were used to average data and facilitate downstream processing as well as increase the overall signal-to-noise ratio.

SAXS analysis

Data transformation and analysis were performed using QtiPlot 1.0.1 (IONDEV, Romania) and the ATSAS package (EMBL Hamburg, Germany)[19]. The LPX SAXS curves were characterized by a single Bragg peak, indicative of the repeat order inside the particles. The Lorentzian fit functionality in QtiPlot 1.0.1 was utilized for peak fitting of the Bragg peaks in the SAXS curves

$$I(q) = I_0 + \frac{2A}{\pi} \cdot \frac{w}{4 \cdot (q - q_c)^2 + w^2} \tag{2}$$

with $I(q)$ being the scattering intensity, I_0 the baseline intensity at q = 0, extrapolated from the peak position, A the peak area, w the peak width (FWHM), and q_c the peak position. From the peak position q_c the corresponding repeat distance of the scattering moiety d was calculated using the Bragg equation[44]

$$d = \frac{2\pi}{q_c} \tag{3}$$

From the peak width, w, the correlation length, ξ inside the ordered stacks was calculated. Assuming liquid crystalline organization, ξ can be defined as the distance, at which the positional correlation decays to the value 1/e and is given as[45]:

$$\xi = \frac{2}{w} \tag{4}$$

The area of the peaks, A, was taken as a measure for the total amount of material present in the respective state of the organization.

Additional information can be revealed by analyzing the intensity decay using the power law as shown in the following equation:

$$I(q) = I_0 \cdot q^{-x} \tag{5}$$

The so-called Porod exponent *x*, is a measure for the fractal dimension of the particle surface. For an ideal flat interface, the Porod exponent is 4 (Porod law) while with increasing roughness (more specifically increasing fractal dimension) the Porod exponent decreases[46,47].

For the processed BSA scattering profiles further analysis was performed including ab initio reconstruction (DAMMIF[48]) and model fitting (CRYSOL[49]). Basic structural parameters and MW estimates were determined with the tools implemented in PRIMUS.

The BSA data were deposited in the Small Angle Scattering Biological Data Bank (SASBDB). The accession codes are listed in Extended Data Table 1.

Formalisms for the quantitative determination of size-dependent parameters

. Size-dependent mass fractions of LPX nanoparticles

For the calculation of the absolute mass of LPX as a function of size, we used the following premises:

- *Total concentration of mRNA* in the lipoplex formulations (in our measurements 0.15 mg/mL)
- *Mixing ratio (charge ratio) between liposomes and RNA for lipoplex* formation (here: DOTMA/RNA = 0.65, using 330 Da as the average mass of the negatively charged nucleotide and assuming one positive charge per DOTMA molecule)
- *Liposome composition* (here DOTMA/DOPE in a molar ratio of 2 to 1, with the MW of DOTMA-cation of 635 Da and of (zwitterionic) DOPE of 740 Da. The total lipid MW per charge was therefore 1005 Da (635 + 740/2)
- *Composition of lipoplex nanoparticles* (here we use a one-to-one stoichiometry between DOTMA and RNA nucleotide, as previously determined by independent measurements, to calculate the composition of the lipoplexes[50])

Therefore, in the LPXs, each mRNA nucleotide of 330 Da was bound to lipids with 1005 Da, nucleotide and lipids having then a total $MW_{nucleotide+lipids}$ of 1335 Da.

The total LPX concentration, $c_{LPXtotal}$ in mg/mL, was calculated using the following general equation:

$$c_{LPXtotal} = \left(c_{RNAtotal} - c_{RNAfree}\right) \cdot \frac{MW_{nucleotide+lipids}}{MW_{nucleotide}} \tag{6}$$

where $c_{LPXtotal}$ is the total concentration of LPXs (mRNA + lipid), $c_{RNAtotal}$ the total mRNA concentration in the formulation, $c_{RNAfree}$ the free mRNA concentration, $MW_{nucleotide+lipids}$ the molecular weight of the lipids and nucleotide complexes, $MW_{nucleotide}$ the molecular weight of nucleotide for LPXs.

The experimentally determined value for the free mRNA concentration was 0.045 mg/mL, corresponding to about 30% of the total amount, which is in very good accordance with the expectation (35%). For $c_{LPXtotal}$, one obtains:

$$c_{LPXtotal} = (0.15 - 0.045) \cdot \frac{1335}{330} = 0.425\left[\frac{\text{mg}}{\text{mL}}\right] \tag{7}$$

From the experimental data, the peak area of the LPX peak from AF4 measurements was integrated (more specifically, the Bragg peak area from Lorentz fitting was integrated). This value was normalized with respect to the calculated total LPX content, $c_{LPXtotal}$, given above, and the normalization factor was used to calculate the differential absolute LPX concentration, c_{LPXdif}, as a function of size.

Size-dependent particle number and composition

Particle numbers as a function of size were calculated from the above obtained absolute mass fractions by using simplified models for particle shape. As LPX particles are known to be globular and compact entities, they were approximated as solid spheres with the volume:

$$V = \frac{4}{3}\pi R^3 \tag{8}$$

The experimentally determined radius of gyration, R_g, correlated therefore with the radius, R, of the solid sphere to

$$R = \sqrt{\frac{5}{3}} R_g \tag{9}$$

With the further approximation of the density, ρ_{LPX}, of the material which forms the LPX nanoparticles (1.11 g/mL, using $\rho_{RNA} \approx 1.68$ g/mL and $\rho_{lipid} \approx 1.0$ g/mL), the mass per particle, m_p is given as:

$$m_p = \mathrm{V} \cdot \rho \tag{10}$$

The number concentration of particles within a given size fraction, n_{LPXdif}, is given from the differential LPX concentration c_{LPXdif}:

$$n_{LPXdif} = \frac{c_{LPXdif}}{\mathrm{m}_p} \tag{11}$$

The number of mRNA copies, $n_{mRNA/particle}$, in a single particle is given by the particle mass, m_p, the molar mass of the lipid-complexed nucleotide, $MW_{nucleotide+lipid}$, the number of nucleotides of the mRNA, $n_{nucelotide}$, and Avogadro's number, N_A:

$$\mathrm{n}_{mRNA/particle} = \frac{m_p \cdot N_A}{MW_{nucleotide+lipid} \cdot n_{nucleotide}} \tag{12}$$

The total number concentration of mRNA copies in particles at a certain size fraction is given by the concentration fraction, c_{LPXdif}, the molar mass of the lipid-complexed nucleotide, $MW_{nucleotide+lipid}$, the number of nucleotides per RNA copy, $n_{nucelotide}$, and Avogadro's number, N_A:

$$n_{RNA/dif} = \frac{c_{LPXdif} \cdot N_A}{MW_{nucleotide+lipid} \cdot n_{nucleotide}} \tag{13}$$

Data availability

The datasets on BSA generated and/or analyzed during the current study are available in the Small Angle Scattering Biological Data Bank (SASBDB), SASDRQ8. The lipoplex SAXS data are accessible under: SASDSH7. No human or other cell lines were used for the present experiments.

Received: 8 July 2023; Accepted: 7 September 2023
Published online: 22 September 2023

References

1. Sahin, U., Karikó, K. & Türeci, Ö. mRNA-based therapeutics–developing a new class of drugs. *Nat. Rev. Drug Discov.* **13**, 759–780. https://doi.org/10.1038/nrd4278 (2014).
2. Chaudhary, N., Weissman, D. & Whitehead, K. A. mRNA vaccines for infectious diseases: Principles, delivery and clinical translation. *Nat. Rev. Drug Discov.* **20**, 817–838. https://doi.org/10.1038/s41573-021-00283-5 (2021).
3. Ragelle, H., Danhier, F., Préat, V., Langer, R. & Anderson, D. G. Nanoparticle-based drug delivery systems: A commercial and regulatory outlook as the field matures. *Expert Opin. Drug Deliv.* **14**, 851–864. https://doi.org/10.1080/17425247.2016.1244187 (2017).
4. Hou, X., Zaks, T., Langer, R. & Dong, Y. Lipid nanoparticles for mRNA delivery. *Nat. Rev. Mater.* **6**, 1078–1094. https://doi.org/10.1038/s41578-021-00358-0 (2021).
5. Schoenmaker, L. *et al.* mRNA-lipid nanoparticle COVID-19 vaccines: Structure and stability. *Int. J. Pharm.* **601**, 120586. https://doi.org/10.1016/j.ijpharm.2021.120586 (2021).
6. Tenchov, R., Bird, R., Curtze, A. E. & Zhou, Q. Lipid nanoparticles—from liposomes to mRNA vaccine delivery, a landscape of research diversity and advancement. *ACS Nano* **15**, 16982–17015. https://doi.org/10.1021/acsnano.1c04996 (2021).
7. Mitchell, M. J. *et al.* Engineering precision nanoparticles for drug delivery. *Nat. Rev. Drug Discov.* **20**, 101–124. https://doi.org/10.1038/s41573-020-0090-8 (2021).
8. Clogston, J. D. *et al.* Sizing up the next generation of nanomedicines. *Pharm. Res.* **37**, 6. https://doi.org/10.1007/s11095-019-2736-y (2019).
9. US Food and Drug Administration. Liposome drug products: Chemistry, manufacturing, and controls; human pharmacokinetics and bioavailability; and labeling documentation. *Guidance for Industry.(CDER)* (2018).
10. Koppel, D. E. Analysis of macromolecular polydispersity in intensity correlation spectroscopy: The method of cumulants. *J. Chem. Phys.* **57**, 4814–4820. https://doi.org/10.1063/1.1678153 (1972).
11. Provencher, S. W. A constrained regularization method for inverting data represented by linear algebraic or integral equations. *Comput. Phys. Commun.* **27**, 213–227. https://doi.org/10.1016/0010-4655(82)90173-4 (1982).
12. Wagner, M., Holzschuh, S., Traeger, A., Fahr, A. & Schubert, U. S. Asymmetric flow field-flow fractionation in the field of nanomedicine. *Anal. Chem.* **86**, 5201–5210. https://doi.org/10.1021/ac501664t (2014).
13. Ventouri, I. K., Loeber, S., Somsen, G. W., Schoenmakers, P. J. & Astefanei, A. Field-flow fractionation for molecular-interaction studies of labile and complex systems: A critical review. *Anal. Chim. Acta* **1193**, 339396. https://doi.org/10.1016/j.aca.2021.339396 (2022).
14. Hupfeld, S., Moen, H. H., Ausbacher, D., Haas, H. & Brandl, M. Liposome fractionation and size analysis by asymmetrical flow field-flow fractionation/multi-angle light scattering: Influence of ionic strength and osmotic pressure of the carrier liquid. *Chem. Phys. Lipid.* **163**, 141–147. https://doi.org/10.1016/j.chemphyslip.2009.10.009 (2010).

15. Parot, J., Caputo, F., Mehn, D., Hackley, V. A. & Calzolai, L. Physical characterization of liposomal drug formulations using multi-detector asymmetrical-flow field flow fractionation. *J. Controll. Release* **320**, 495–510. https://doi.org/10.1016/j.jconrel.2020.01.049 (2020).
16. Haas, H., Bacic, T. & Schumacher, J. *Method for determining at least one parameter of a sample composition comprising nucleic acid, such as RNA, and optionally particles*. US Patent 2022/0381748 (2022) ,
17. Engert, J., Mathaes, R. & Winter, G. Asymmetrical flow field flow fractionation: A useful tool for the separation of protein pharmaceuticals and particulate systems. In *Analytical Techniques in the Pharmaceutical Sciences* (eds Müllertz, Anette *et al.*) 467–488 (Springer, 2016).
18. Orthaber, D., Bergmann, A. & Glatter, O. SAXS experiments on absolute scale with Kratky systems using water as a secondary standard. *J. Appl. Crystallogr.* **33**, 218–225. https://doi.org/10.1107/S0021889899015216 (2000).
19. Manalastas-Cantos, K. *et al.* ATSAS 3.0: Expanded functionality and new tools for small-angle scattering data analysis. *J. Appl. Crystallogr.* **54**, 343–355. https://doi.org/10.1107/S1600576720013412 (2021).
20. Trewhella, J. Recent advances in small-angle scattering and its expanding impact in structural biology. *Structure* **30**, 15–23. https://doi.org/10.1016/j.str.2021.09.008 (2022).
21. Pérez, J., Thureau, A. & Vachette, P. SEC-SAXS: Experimental set-up and software developments build up a powerful tool. *Methods Enzymol.* **677**, 221–249. https://doi.org/10.1016/bs.mie.2022.08.024 (2022).
22. Siewert, C. D. *et al.* Hybrid biopolymer and lipid nanoparticles with improved transfection efficacy for mRNA. *Cells*. https://doi.org/10.3390/cells9092034 (2020).
23. Uebbing, L. *et al.* Investigation of pH-responsiveness inside lipid nanoparticles for parenteral mRNA application using small-angle X-ray scattering. *Langmuir* **36**, 13331–13341. https://doi.org/10.1021/acs.langmuir.0c02446 (2020).
24. Nogueira, S. S. *et al.* Polysarcosine-functionalized lipid nanoparticles for therapeutic mRNA delivery. *ACS Appl. Nano Mater.* **3**, 10634–10645. https://doi.org/10.1021/acsanm.0c01834 (2020).
25. Jeffries, C. M. *et al.* Preparing monodisperse macromolecular samples for successful biological small-angle X-ray and neutron-scattering experiments. *Nat. Protoc.* **11**, 2122–2153. https://doi.org/10.1038/nprot.2016.113 (2016).
26. Mathew, E., Mirza, A. & Menhart, N. Liquid-chromatography-coupled SAXS for accurate sizing of aggregating proteins. *J. Synchrotron Radiat.* **11**, 314–318. https://doi.org/10.1107/S0909049504014086 (2004).
27. Johansen, N. T., Pedersen, M. C., Porcar, L., Martel, A. & Arleth, L. Introducing SEC-SANS for studies of complex self-organized biological systems. *Acta crystallogr. Sect. D Struct. Biol.* **74**, 1178–1191. https://doi.org/10.1107/S2059798318007180 (2018).
28. Quattrini, F., Berrecoso, G., Crecente-Campo, J. & Alonso, M. J. Asymmetric flow field-flow fractionation as a multifunctional technique for the characterization of polymeric nanocarriers. *Drug Deliv. Transl. Res.* **11**, 373–395. https://doi.org/10.1007/s13346-021-00918-5 (2021).
29. Thünemann, A. F., Knappe, P., Bienert, R. & Weidner, S. Online coupling of field-flow fractionation with SAXS and DLS for polymer analysis. *Anal. Methods* **1**, 177–182. https://doi.org/10.1039/B9AY00107G (2009).
30. Kranz, L. M. *et al.* Systemic RNA delivery to dendritic cells exploits antiviral defence for cancer immunotherapy. *Nature* **534**, 396–401. https://doi.org/10.1038/nature18300 (2016).
31. Grabbe, S. *et al.* Translating nanoparticulate-personalized cancer vaccines into clinical applications: Case study with RNA-lipoplexes for the treatment of melanoma. *Nanomedicine (Lond.)* **11**, 2723–2734. https://doi.org/10.2217/nnm-2016-0275 (2016).
32. Rosigkeit, S. *et al.* Monitoring translation activity of mRNA-loaded nanoparticles in mice. *Mol. Pharm.* **15**, 3909–3919. https://doi.org/10.1021/acs.molpharmaceut.8b00370 (2018).
33. Sahin, U. *et al.* An RNA vaccine drives immunity in checkpoint-inhibitor-treated melanoma. *Nature* **585**, 107–112. https://doi.org/10.1038/s41586-020-2537-9 (2020).
34. Rosace, A. *et al.* Automated optimisation of solubility and conformational stability of antibodies and proteins. *Nat. Commun.* **14**, 1937. https://doi.org/10.1038/s41467-023-37668-6 (2023).
35. Manning, M. C., Chou, D. K., Murphy, B. M., Payne, R. W. & Katayama, D. S. Stability of protein pharmaceuticals: An update. *Pharm. Res.* **27**, 544–575. https://doi.org/10.1007/s11095-009-0045-6 (2010).
36. Chiti, F. & Dobson, C. M. Protein misfolding, functional amyloid, and human disease. *Annu. Rev. Biochem.* **75**, 333–366. https://doi.org/10.1146/annurev.biochem.75.101304.123901 (2006).
37. Babcock, J. J. & Brancaleon, L. Bovine serum albumin oligomers in the E- and B-forms at low protein concentration and ionic strength. *Int. J. Biol. Macromol.* **53**, 42–53. https://doi.org/10.1016/j.ijbiomac.2012.10.030 (2013).
38. Ziller, A. *et al.* Incorporation of mRNA in lamellar lipid matrices for parenteral administration. *Mol. Pharm.* **15**, 642–651. https://doi.org/10.1021/acs.molpharmaceut.7b01022 (2018).
39. Pabst, G. *et al.* Structural analysis of weakly ordered membrane stacks. *J. Appl. Crystallogr.* **36**, 1378–1388. https://doi.org/10.1107/S0021889803017527 (2003).
40. Kirby, N. *et al.* Improved radiation dose efficiency in solution SAXS using a sheath flow sample environment. *Acta crystallogr. Sect. D, Struct. Biol.* **72**, 1254–1266. https://doi.org/10.1107/S2059798316017174 (2016).
41. Li, S. *et al.* Payload distribution and capacity of mRNA lipid nanoparticles. *Nat. Commun.* **13**, 5561. https://doi.org/10.1038/s41467-022-33157-4 (2022).
42. Huber, M. J. *et al.* Physicochemical characterization and quantification of nanoplastics: Applicability, limitations and complementarity of batch and fractionation methods. *Anal. Bioanal. Chem.* https://doi.org/10.1007/s00216-023-04689-5 (2023).
43. Blanchet, C. E. *et al.* Versatile sample environments and automation for biological solution X-ray scattering experiments at the P12 beamline (PETRA III, DESY). *J. Appl. Crystallogr.* **48**, 431–443. https://doi.org/10.1107/S160057671500254X (2015).
44. Bragg, W. H. & Bragg, W. L. The reflection of X-rays by crystals. *Proc. R. Soc. Lond. A* **88**, 428–438. https://doi.org/10.1098/rspa.1913.0040 (1913).
45. Goodby, J. W. *et al. Handbook of Liquid Crystals* (Wiley, 2014).
46. Bale, H. D. & Schmidt, P. W. Small-angle X-Ray-scattering Investigation of submicroscopic porosity with fractal properties. *Phys. Rev. Lett.* **53**, 596–599. https://doi.org/10.1103/PhysRevLett.53.596 (1984).
47. Teixeira, J. Small-angle scattering by fractal systems. *J. Appl. Crystallogr.* **21**, 781–785. https://doi.org/10.1107/S0021889888000263 (1988).
48. Franke, D. & Svergun, D. I. DAMMIF, a program for rapid ab-initio shape determination in small-angle scattering. *J. Appl. Crystallogr.* **42**, 342–346. https://doi.org/10.1107/S0021889809000338 (2009).
49. Svergun, D., Barberato, C. & Koch, M. H. J. CRYSOL—a program to evaluate X-ray solution scattering of biological macromolecules from atomic coordinates. *J. Appl. Crystallogr.* **28**, 768–773. https://doi.org/10.1107/S0021889895007047 (1995).
50. Haas, H., Hörner, S., Esparza Borquez, I. H., Hiller, T. M. & Bates, F. *Preparation and storage of liposomal RNA formulations suitable for therapy*. US Patent 11395799 (2022).

Acknowledgements

This research was funded by the "Bundesministerium für Bildung und Forschung BMBF" grant 05K22UM3 and by the "Deutsche Forschungsgemeinschaft DFG" as part of the collaborative research center (CRC) 1066.

Author contributions

Conceptualization: M.G, P.L., and H.H Methodology: M.G., T.B., J.S., F.M. R.D., R.W., P.L., and H.H Investigation: M.G., C.W., T.B. F.M., R.D., R.W., B.K., and K.B. Project administration, supervision: M.G., T.K., D.S., P.L. and H.H Data analysis: M.G., C.W., T.B., J.S., C.B., F.M., R.D., R.W., T.N. D.S. and H.H. Writing—original draft: M.G., C.W., T.B., J.S., F.M., R.D., R.W., P.L. and H.H Writing – review & editing: all.

Competing interests

MAG is consultant to BioSAXS GmbH PL is consultant to BioNTech SE MAG, CW, TB, JS, CB, FM, RD, RW, BK, KB, TN, TK, and HH have no competing interest.

Additional information

Supplementary Information The online version contains supplementary material available at https://doi.org/10.1038/s41598-023-42274-z.

Correspondence and requests for materials should be addressed to M.A.G. or H.H.

Reprints and permissions information is available at www.nature.com/reprints.

Publisher's note Springer Nature remains neutral with regard to jurisdictional claims in published maps and institutional affiliations.

3.1.3 Supporting Information

SUPPLEMENTARY INFORMATION

Quantitative size-resolved characterization of mRNA nanoparticles by in-line coupling of asymmetrical-flow field-flow fractionation with small angle X-ray scattering

Melissa A Graewert[1*], Christoph Wilhelmy[2*], Tijana Bacic[3*], Jens Schumacher[3], Clement Blanchet[1], Florian Meier[4], Roland Drexel[4], Roland Welz[4], Bastian Kolb[2], Kim Bartels[2], Thomas Nawroth[2], Thorsten Klein[4], Dmitri Svergun[1,5], Peter Langguth[2] & Heinrich Haas[2,3,]

[1] European Molecular Biology Laboratory, Hamburg Unit, Hamburg, Germany

[2] Department of Biopharmaceutics and Pharmaceutical Technology, Johannes Gutenberg-University, Mainz, Germany

[3] BioNTech SE, Mainz, Germany

[4] Postnova Analytics GmbH, Landsberg am Lech, Germany

[5] BIOSAXS GmbH, Hamburg, Germany

*These authors contributed equally

melissa.graewert@embl-hamburg.de

haashein@uni-mainz.de

Acknowledgments

This research was funded by the „Bundesministerium für Bildung und Forschung BMBF“ grant 05K22UM3 and by the “Deutsche Forschungsgemeinschaft DFG” as part of the collaborative research center (CRC) 1066.

Declaration of interest

MAG is consultant to BioSAXS GmbH

PL is consultant to BioNTech SE

Supplement Table 1. SAXS sample details, data collection, analysis, and 3D modelling details for BSA in solution.

	Batch	**AF4 monomer peak**
Sample temperature (°C)	20	
In beam sample cell	1-mm quartz capillary	
Sample concentration, mg/mL	5.0	5.0 (40 ul injection volume).
In-line separation	n.a.	semi-preparative frit-inlet AF4 channel PES membrane (10 kDa MW cut-off) and a Mylar spacer of 350µm height
Detector flowrate, mL/min	n.a.	0.5 mL/min
Data acquisition/reduction software	SASFLOW	
Instrument	P12, Petra3@DESY, 6M-Pilatus detector	
Measured q-range (nm^{-1})	0.02 – 5.83	
Exposure time(s), number of exposures.	0.050, 20 frames	1, 2500 frames (23 averaged)
Methods/Software	PRIMUS	CHROMIXS, PRIMUS
Guinier Analysis		
$I(0) \pm \sigma$ ($cm^{-1;}$ a.u)	2639.21 ± 3.84	na
R_g CHROMIXS, PRIMUS σ (nm)	3.43 ± 0.01	2.87 ± 0.01
$min < qR_g < max$ limit (or data point range)	0.16 - 1.21	0.25 – 1.28
PDDF/P(r) analysis		
$I(0) \pm \sigma$ ($cm^{-1;}$ a.u.)	2650 ± 4.22	0.39 ± 0.00
$R_g \pm \sigma$ (nm)	3.53±0.01	2.89 ± 0.01
d_{max} (nm)	13.5	9.1
q-range (nm^{-1})	0.05 – 2.33	0.09 – 2.79
$P(r)$ fit assessment	0.7648	0.9497
Molecular weight (M) estimates (kDa)		
From chemical composition	66.4	66.4
From SAS, concentration-independent method (Bayesian)	94.2 (84.0 – 110.1)	70.6 (68.9 – 105.7)
From SAS-independent measure (MALS)	na	62 kD
Shape modelling method(s)		
Software	DAMMIF	DAMMIF
q-range for fit ($q_{min} – q_{max}$; nm^{-1})	0.05 – 2.33	0.09 – 2.79
Symmetry/anisotropy assumptions	P1	P1
Number of individual model reconstructions	10	10
χ^2, CorMap P-values for fit	1.087, 0.031	1.015, 0.258
Atomistic modelling methods		
Software	CRYSOL	CRYSOL
q-range for fit ($q_{min} – q_{max}$; nm^{-1})	0.03 – 5.00	0.05 – 5.00
χ^2	7.521	1.091
Data and model deposition		
SASBDB IDs	*na.*	SASDRQ8*

Supplement Fig. 1: SAXS data processing

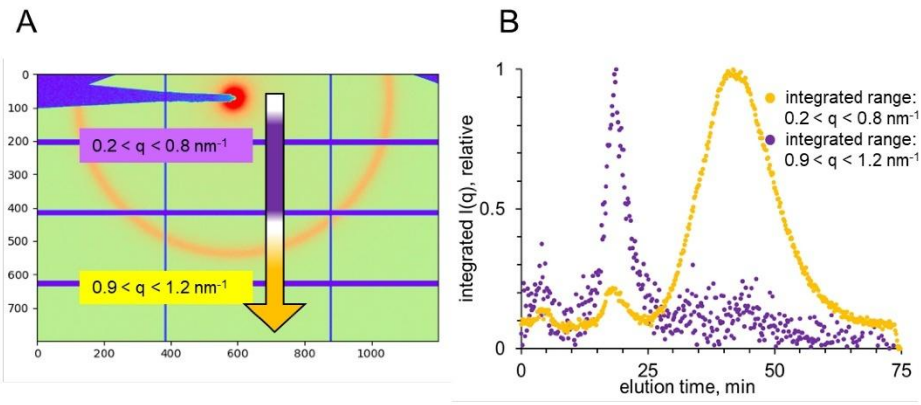

Supplement Fig. 1 Processing of AF4-SAXS data from lipoplex formulation
A. 2D scattering image from LPX formulation indicating the ranges of intensity used for the integration to generate the SAXS fractionation (elution) profiles. For clarity and pronounced visualization of the characteristic Bragg Peak at 1 nm^{-1}, the detector image collected in batch mode at higher concentration is shown.
B. SAXS elution profiles from AF4 separation of LPX formulation. The integration at low q highlights the elution of RNA throughout the run (purple). The integration around the Bragg Peak highlights the elution of the lipoplex particles (orange).

Supplement Fig. 2: LS derived structural information

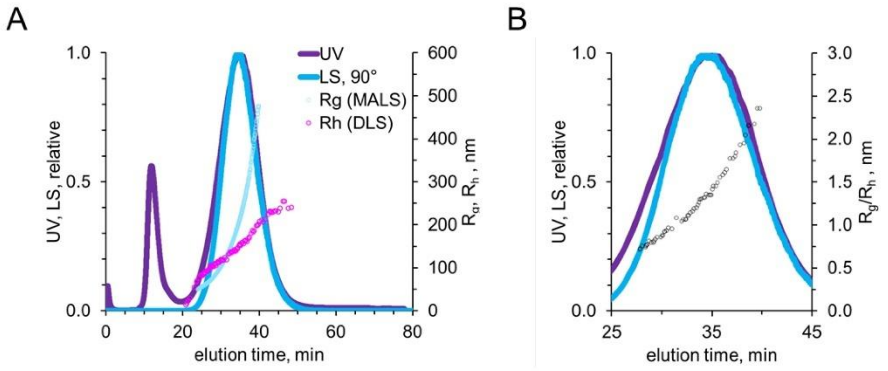

Supplement Fig. 2: Off-line-AF4 measurement
To confirm that the separation of the particles was not compromised with the increased amount of sample that was loaded (to obtain a stronger scattering signal) an off-line measurement was performed. **A.** The elution profiles are in good agreement with the ones presented in Fig. 3B. In addition to the derived R_g values, R_h values could also be determined as the dynamic light scattering was measured in addition. **B.** The ratio R_g/R_h is plotted as open spheres. While for a hard sphere a value of ~0.78 is expected, we observed a continuous increase of R_g/R_h up to >2 with larger particle size indicating an increasing deviation of their morphology towards more elongated particles[46].

Supplement Fig. 3: SAXS analysis of mRNA peak

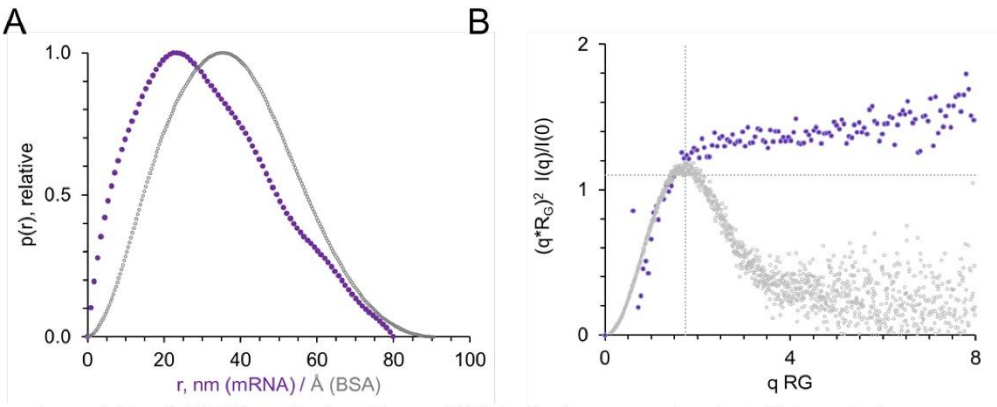

Supplement Fig. 3: SAXS analysis of free mRNA indicates an unstructured/elongated structure

The scattering RNA curve from the fractionation of pure RNA formulation was further characterized and shown here in comparison with BSA as an example of a globular structure.

A. p(r) function, normalized. The skewed peak is typical for unstructured or elongated structures (in contrast to the almost Gaussian distribution displayed by BSA (grey). Note, the BSA data is displayed in Å for better comparison)

B. Dimensionless Kratky plot ($(q^*R_g)^2$ I(q)/I(0) vs q^*R_g). The dotted lines are drawn at $qR_g = \sqrt{3}$ and $(qR_g)^2 I(q)/I(0) = 1.104$. Globular structures (such as BSA (grey)) have a local maximum where the two lines intersect. The lack of a maximum for the RNA scattering is in agreement with an elongated structure. Concentration-independent MW estimates were in the range of the expected monomer (Bayesian, 440-450 kDa) and in accordance with the MW estimated from MALS.

Supplement Figure 4: Limitation of SAXS Guinier analysis for larger LPXs

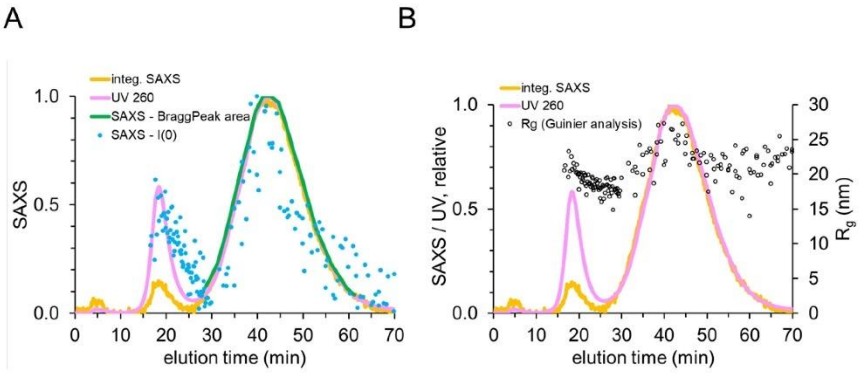

Supplement Figure 4: Limitation of SAXS Guinier analysis for larger LPX
A) I(0) and B) R_G derived from Guinier analysis (determined with AutoRG) of subtracted frames across the complete fractionation process (both peaks) in comparison with UV (pink) and SAXS trace (orange). Note, due to the overall large size of the nanoparticles with and the limited covered q range for these experiments, the Guinier analysis of the second peak does not reflect the scattering of the overall particle, solely that of the lipid complexed RNA molecules. This explains the constant RG across the peak instead of the continuous size distribution detected with MALS (Figure 1C, black trace). However, the overall good fit of the SAXS elution profile derived from fitting of the Bragg peaks at the various elution time points (green curve) to the various other profiles, justifying its use for the subsequent quantitative data analysis.

Supplement Fig. 5: extended peak analysis

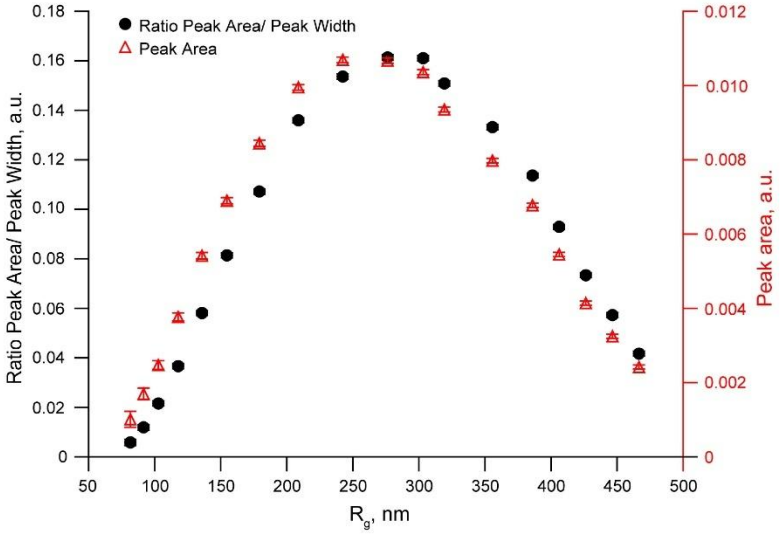

Supplement Figure 5: Peak area and area/with ratio as a function of R_g
Red triangles give the evolution of peak area as a function of R_g, which shows the same qualitative shape as the plot area vs. elution time (Fig. 4B/D) with a maximum around 250 nm, indicative for the highest fraction of ordered material at this size. Black dots give the ratio peak area/peak width, to highlight an eventual preferred type of organization at a certain size (Papst et al., Structural analysis of weakly ordered membrane stacks, Journal of Applied Crystallography 36(6, 2003, DOI: 10.1107/S0021889803017527). With the rather smooth, continuous change of peak width as a function of particle size/elution time (Fig. 4B) only a slight shift of the maximum towards smaller size is obtained.

Supplement Table 2: Peak fitting parameters of lipoplex Bragg peak with Lorentzian function and results of R_g analysis of fractions with different elution times

Elution time (min)	peak position (nm^{-1})	σ (nm^{-1})	peak width (nm^{-1})	σ (nm^{-1})	peak area	σ	d-spacing (nm)	σ (nm)	Correlation length (nm)	σ (nm)	R_g
29.9	1.037	5.26E-03	0.173	2.97E-02	1.01E-03	2.17E-04	6.058	3.07E-02	11,542	1,981	81.6
31.6	1.038	2.30E-03	0.142	1.15E-02	1.70E-03	1.58E-04	6.056	1.34E-02	14,074	1,140	91.6
33.2	1.038	1.13E-03	0.115	5.07E-03	2.47E-03	1.16E-04	6.050	6.57E-03	17,436	0,771	102.8
34.9	1.039	6.64E-04	0.103	2.85E-03	3.77E-03	1.07E-04	6.049	3.87E-03	19,447	0,538	117.8
36.6	1.039	3.91E-04	0.093	1.59E-03	5.41E-03	9.02E-05	6.048	2.27E-03	21,461	0,367	135.8
38.2	1.039	2.80E-04	0.085	1.10E-03	6.90E-03	8.47E-05	6.048	1.63E-03	23,599	0,306	154.7
39.9	1.039	2.17E-04	0.079	8.32E-04	8.44E-03	8.27E-05	6.048	1.26E-03	25,388	0,268	179.2
41.6	1.039	1.60E-04	0.073	5.98E-04	9.95E-03	7.39E-05	6.048	9.30E-04	27,325	0,223	208.8
43.2	1.039	1.49E-04	0.070	5.50E-04	1.07E-02	7.59E-05	6.049	8.71E-04	28,738	0,227	242.4
44.9	1.039	1.43E-04	0.066	5.19E-04	1.07E-02	7.43E-05	6.049	8.33E-04	30,243	0,237	276.3
46.6	1.039	1.32E-04	0.064	4.76E-04	1.04E-02	6.76E-05	6.049	7.70E-04	31,089	0,230	303.2
48.2	1.039	1.41E-04	0.062	5.03E-04	9.35E-03	6.64E-05	6.049	8.21E-04	32,260	0,262	319.3
49.9	1.039	1.48E-04	0.060	5.25E-04	7.98E-03	6.08E-05	6.048	8.63E-04	33,395	0,293	355.67
51.6	1.039	1.67E-04	0.060	5.89E-04	6.78E-03	5.82E-05	6.047	9.69E-04	33,552	0,332	385.97
53.2	1.039	2.03E-04	0.059	7.15E-04	5.45E-03	5.75E-05	6.046	1.18E-03	34,102	0,415	406.17
54.9	1.039	2.52E-04	0.056	8.81E-04	4.14E-03	5.56E-05	6.046	1.47E-03	35,450	0,553	426.35
56.6	1.039	3.13E-04	0.057	1.09E-03	3.25E-03	5.40E-05	6.045	1.82E-03	35,281	0,681	446.51
58.2	1.039	4.42E-04	0.058	1.55E-03	2.42E-03	5.62E-05	6.045	2.57E-03	34,467	0,924	466.59
59.9	1.040	5.21E-04	0.058	1.84E-03	1.83E-03	5.00E-05	6.042	3.03E-03	34,209	1,076	na
61.6	1.040	7.73E-04	0.055	2.69E-03	1.24E-03	5.18E-05	6.041	4.49E-03	36,143	1,758	na
63.2	1.040	1.11E-03	0.059	3.94E-03	9.02E-04	5.25E-05	6.042	6.47E-03	34,038	2,281	na

4

Subproject 2: In-Depth Characterization and Structure-Function-Correlation of mRNA Lipid Nanoparticles using Small Angle X-ray Scattering (SAXS)

4.1 Polysarcosine-Functionalized mRNA Lipid Nanoparticles Tailored for Immunotherapy

4.1.1 Summary and Contributions

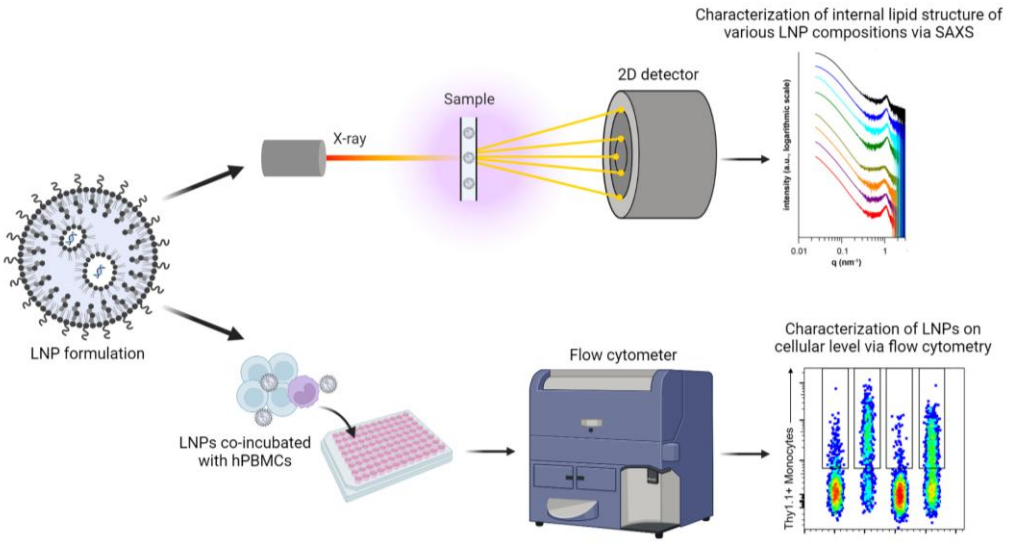

Figure 4.1-1. Graphical abstract of the publication 4.1. LNP formulations of systematically varied lipid composition were tested in SAXS for internal structure investigation as well as for biological performance using hPBMCs to explore structure-function relationships for mRNA LNPs. As published in [89].

This work aimed to derive novel insights into the structure-function relationships of mRNA LNPs by comparing results from physicochemical and structural investigations, utilizing SAXS among other techniques, with *in vitro* cellular uptake and transfection efficacy experiments. As mentioned in Chapter 1.4, the composition of lipid nanoparticles significantly influences their physicochemical properties and, consequently, determines their therapeutic potency. Therefore, it is crucial to gain as much insight as possible into the effects of composition on structural aspects, in order to provide a solid foundation for future developments and further improvements of existing products.

To address this, we systematically varied single lipid excipients of the respective functional lipid components, namely the ionizable lipid (DODMA vs. DLin-MC3-DMA), the helper phospholipid (DOPE vs. DOPC), and the stealth moiety (PEG vs. pSar). The obtained physicochemical results were then compared with the biological assay conducted on hPBMCs with Thy1.1 reporter mRNA for transfection efficacy testing and Cy5-labelled Luc encoding mRNA for cellular uptake studies, respectively.

The SAXS measurements revealed significant structural variation in LNPs based on their lipid composition. The internal structural features of LNPs were influenced by the choice of ionizable lipid and phospholipid but not by the selection of the stealth moiety. In particular, DLin-MC3-DMA, as an ionizable lipid, and DOPE, as a helper lipid, resulted in significantly smaller repeating unit distances in the mRNA-lipid stacks compared to DODMA and DOPC across all tested compositions. The selection of the stealth moiety, on the other hand, had a considerable impact on the surface properties of the mRNA LNPs. While choosing DLin-MC3-DMA as the ionizable component generally increased the surface roughness of the LNPs, substituting PEG with pSar further enhanced the surface roughness properties of LNPs, especially at low pH values, which occur in late endosomes during cellular uptake.

Biological testing revealed that pSar-grafted LNPs demonstrated improved transfection efficacy compared to PEG-grafted LNPs. As shown in cellular binding and uptake studies, pSar also contributes to nearly complete cell binding of LNPs to monocytes, whereas PEG results in much lower values. This could explain the improved transfection efficacy. Furthermore, the choice of DLin-MC3-DMA and DOPE led to enhanced transfection efficacy compared to their tested analogs, with the LNP comprising DLin-MC3-DMA, DOPE, and pSar showing the highest potency. We therefore hypothesize that a high internal packing density of the mRNA-lipid complex, combined with the ability to exhibit high surface roughness at decreasing pH, leads to enhanced biological potency in monocytes, a subfraction of the hPBMCs.

Our results establish a foundation for a deeper understanding of the correlations between structure and potency, as well as how SAXS measurements can aid in the comprehensive characterization and evaluation of mRNA drug products.

This work was published in the following article:

Wilhelmy, C. ‡; Keil, I.S. ‡; Uebbing, L. *et al.* Polysarcosine-Functionalized mRNA Lipid Nanoparticles Tailored for Immunotherapy. *Pharmaceutics* **2023**, *15*, 2068. https://doi.org/10.3390/pharmaceutics15082068

‡ These authors contributed equally to this work.

Own contributions:

Authorship: First author

Methodology, validation, data curation

Formal Analysis and investigation: Preparation of samples, investigation of SAXS experiments, structural analysis

Writing: original draft, visualization, review and editing

Contribution of all authors:

Conceptualization: P.L., H.H., and U.S.

Methodology: C.W., I.S.K., and L.U.

Software: C.W. and I.S.K.

Validation: C.W., I.S.K., H.H., M.B., and P.L.

Formal analysis: C.W. and I.S.K.

Investigation: C.W. and I.S.K.

Resources: P.L., U.S., M.D., and M.B.

Data curation: C.W. and I.S.K.

Writing—original draft preparation: C.W. and I.S.K.

Writing—review and editing: C.W., I.S.K., L.U., M.A.S., D.F., T.N., M.D., H.H., M.B., and P.L.

Visualization: C.W. and I.S.K.

Supervision: P.L., M.D., M.B., U.S., and H.H.

Project administration: P.L., M.D., M.B., and U.S.

Funding acquisition: P.L., M.B., and U.S.

4.1.2 Publication

pharmaceutics

MDPI

Article

Polysarcosine-Functionalized mRNA Lipid Nanoparticles Tailored for Immunotherapy

Christoph Wilhelmy [1,†], Isabell Sofia Keil [2,†], Lukas Uebbing [1], Martin A. Schroer [3,4], Daniel Franke [3,5], Thomas Nawroth [1], Matthias Barz [6,7], Ugur Sahin [8], Heinrich Haas [1,9], Mustafa Diken [2,*] and Peter Langguth [1,*]

1 Department of Biopharmaceutics and Pharmaceutical Technology, Johannes Gutenberg University Mainz, 55128 Mainz, Germany; cwilhelmy@uni-mainz.de (C.W.)
2 TRON—Translational Oncology at the University Medical Center of Johannes Gutenberg University gGmbH, 55131 Mainz, Germany; isabell.keil@tron-mainz.de
3 European Molecular Biology Laboratory (EMBL) Hamburg Outstation, c/o DESY, 22607 Hamburg, Germany
4 Nanoparticle Process Technology (NPPT), Faculty of Engineering, University of Duisburg-Essen, 47057 Duisburg, Germany
5 BIOSAXS GmbH, 22607 Hamburg, Germany
6 LACDR—Leiden Academic Centre for Drug Research, Leiden University, 2333 Leiden, The Netherlands
7 Department of Dermatology, University Medical Center, Johannes Gutenberg University Mainz, 55131 Mainz, Germany
8 Department of Immunology, University Medical Center, Johannes Gutenberg University Mainz, 55131 Mainz, Germany
9 BioNTech SE, 55131 Mainz, Germany
* Correspondence: mustafa.diken@tron-mainz.de (M.D.); langguth@uni-mainz.de (P.L.)
† These authors contributed equally to this work.

Abstract: Lipid nanoparticles (LNPs) have gained great attention as carriers for mRNA-based therapeutics, finding applications in various indications, extending beyond their recent use in vaccines for infectious diseases. However, many aspects of LNP structure and their effects on efficacy are not well characterized. To further exploit the potential of mRNA therapeutics, better control of the relationship between LNP formulation composition with internal structure and transfection efficiency in vitro is necessary. We compared two well-established ionizable lipids, namely DODMA and MC3, in combination with two helper lipids, DOPE and DOPC, and two polymer-grafted lipids, either with polysarcosine (pSar) or polyethylene glycol (PEG). In addition to standard physicochemical characterization (size, zeta potential, RNA accessibility), small-angle X-ray scattering (SAXS) was used to analyze the structure of the LNPs. To assess biological activity, we performed transfection and cell-binding assays in human peripheral blood mononuclear cells (hPBMCs) using Thy1.1 reporter mRNA and Cy5-labeled mRNA, respectively. With the SAXS measurements, we were able to clearly reveal the effects of substituting the ionizable and helper lipid on the internal structure of the LNPs. In contrast, pSar as stealth moieties affected the LNPs in a different manner, by changing the surface morphology towards higher roughness. pSar LNPs were generally more active, where the highest transfection efficiency was achieved with the LNP formulation composition of MC3/DOPE/pSar. Our study highlights the utility of pSar for improved mRNA LNP products and the importance of pSar as a novel stealth moiety enhancing efficiency in future LNP formulation development. SAXS can provide valuable information for the rational development of such novel formulations by elucidating structural features in different LNP compositions.

Keywords: lipid nanoparticles; LNPs; mRNA; small-angle X-ray scattering; polysarcosine; flow cytometry; immunotherapy; cancer; vaccine

check for updates

Citation: Wilhelmy, C.; Keil, I.S.; Uebbing, L.; Schroer, M.A.; Franke, D.; Nawroth, T.; Barz, M.; Sahin, U.; Haas, H.; Diken, M.; et al. Polysarcosine-Functionalized mRNA Lipid Nanoparticles Tailored for Immunotherapy. *Pharmaceutics* **2023**, *15*, 2068. https://doi.org/10.3390/pharmaceutics15082068

Academic Editor: Varaporn Buraphacheep Junyaprasert

Received: 10 July 2023
Revised: 27 July 2023
Accepted: 28 July 2023
Published: 1 August 2023

1. Introduction

Although lipid-based nano-sized drug delivery systems have been available for several decades, advancements in the last decade have significantly improved their potential

to deliver nucleic acids such as DNA, siRNA and most recently mRNA [1–4]. In particular, mRNA lipoplexes (LPXs) and lipid nanoparticles (LNPs) have shown promising results in preclinical and clinical studies, with therapeutic applications such as cancer immunotherapy [5–7]. LNPs were most recently utilized for vaccinations against the SARS-CoV-2 virus, the cause of COVID-19 [8,9]. As a consequence of this success, extensive development activities at all stages, ranging from early research to the clinical stage for LNP-based mRNA products, have emerged. The LNP formulations need to fulfill the following properties for optimal mRNA delivery: encapsulation and protection of nucleic acid from degradation by ubiquitous nucleases, adequate long circulation in the bloodstream to reach their destination and successful delivery of RNA to target cells or organs of interest [4,10].

In general, LNP formulations consist of an ionizable-cationic lipid, cholesterol, a helper lipid or phospholipid and a polyethylene glycol (PEG) lipid as stealth moiety [11]. While most of these LNP drug products share this basic concept, the actual composition can vary considerably between different formulations. However, the structural effects of these variations remain relatively unexplored.

A key component of the LNP is given by the ionizable lipid, which is considered essential for efficient endosomal escape. The increase of positive charge density induced by the drop in pH upon acidification of the late endosome is thought to promote the binding and rupture of the endosomal membrane [12–15]. Jayaraman et al. showed that the ionizable lipid should have a pK_a of ~6.5 for the highest activity of hepatic siRNA delivery [16]. Recently, for the first time, we were able to elucidate the pH-induced changes in the bilayer structure in LPXs comprising ionizable lipids in situ by using small-angle X-ray scattering (SAXS) [17], where we could reveal clear differences as a function of lipid structure and the composition of the systems.

As helper lipids, typically phospholipids comprising either a phosphatidyl ethanolamine (-PE) or phosphatidyl choline (-PC) head group are used, where lipids with saturated or unsaturated hydrocarbon chains may be selected. The helper lipids may have an important influence on the activity and the targeting selectivity of the LNPs. For example, it has been shown that by using dioleyl phosphatidylethanolamine (DOPE) in LPXs as a helper lipid, the mRNA expression in the liver could be reduced to very low levels [18,19]. For many future applications of mRNA, therapeutics such as extrahepatic targeting, or more generally speaking, organ-selective targeting, is still an unmet need, since classical LNPs typically result in the highest expression in the liver. The selection of appropriate helper lipids and lipid compositions may allow the better adjustment of targeting selectivity according to the therapeutic requirements [20].

The use of PEG-functionalized lipids (PEGylated lipids) as an excipient for drug and mRNA delivery has been widely adopted in various nanoparticulate systems, including liposomes, proteins and LNPs. In addition to modulating circulation in the bloodstream, PEGylation is necessary for LNP engineering to avoid aggregation during the mixing of the RNA with the lipid solution. Besides the potential problems in safety and tolerability of the ionizable cationic lipids [21,22], recent studies have also raised concerns about the use of PEG in drug delivery systems, with PEG-lipids being hypothesized to be the cause of several adverse reaction phenomena, such as complement-activation-related pseudoallergy (CARPA) causing hypersensitivities. One further problem is its immunogenicity, which can trigger the production of undesired anti-PEG-antibodies, potentially facilitating the accelerated blood clearance (ABC) phenomenon following repeated administrations [23–25]. Furthermore, it was demonstrated that anti-PEG-antibodies are compromising the bilayer integrity, which can induce premature drug release [26]. The exposure with PEG-containing products, as is often the case for cosmetics and household products, increases the probability of anti-PEG-antibodies in the population [24]. These concerns led to the research for alternative excipients replacing PEG as stealth moiety. In this context, the use of polysarcosine (pSar) has shown promising results as an excipient providing stealth properties [27–30], together with enhanced nanoparticle stability and reduced immunogenicity [31,32]. For mRNA LNPs, we have previously demonstrated that pSar lipids are a versatile tool for LNP

engineering, where equivalent or better activity together with reduced immunogenicity can be obtained [33].

SAXS is a powerful tool to gain information on the structure and lamellarity and internal organization inside lipid nanoparticles, which is also considered a quality parameter in FDA guidance for liposomal drug formulations [34]. Previous studies in our group using SAXS elucidated the importance of structural features for mRNA delivery systems, including polymer and lipid-based formulations [17,35–37].

In this study, we investigated selected fundamental formulation parameters for mRNA LNP manufacturing by characterizing the physicochemical characteristics and activity in vitro. We used an improved, single-step manufacturing process for the LNPs which does not require dialysis or tangential flow filtration to obtain the injectable product. We investigated permutations from combinations between two different well-established ionizable lipids together with phospholipids comprising either a -PE or a -PC headgroup and two different stealth moieties. All systems comprised the same amount of cholesterol. The ionizable lipids were 1,2-dioleyloxy-3-dimethylaminopropane (DODMA), the ionizable variety of one of the longest-known cationic lipids [38], and DLin-MC3-DMA (MC3), which is being used in the marketed product Onpattro [2]. As helper lipids, we compared 1,2-dioleoyl-sn-glycero-3-ethanolamine (DOPE) and 2-Dioleoyl-sn-glycero-3-phosphocholine (DOPC), which share an identical backbone. The stealth moieties were PEG, the gold standard for RNA delivery in the form of C16-PEG-Ceramide lipid, and pSar, a relatively new stealth moiety linked to a C12 bisalkyl amine [39].

Our results show that SAXS enabled the sensitive determination of the influence of the respective lipids on the LNP structure. This accurate insight into the molecular organization of the particles allowed the derivation of refined correlations with their potency, beyond the usually described pK_a value of the ionizable lipid. pSar could be successfully applied for particle manufacturing, resulting in a bit larger LNP sizes, but with low influence on internal structure. pSar formulations showed better in vitro activity compared to those made with PEG. This highlights the potential of pSar as an improved stealth moiety and promising alternative to PEG within mRNA LNP formulations.

2. Materials and Methods

2.1. Materials

1,2-Dioleoyl-sn-glycero-3-phosphocholine (DOPC) and 1,2-dioleoyl-sn-glycero-3-ethanolamine (DOPE) were manufactured by Lipoid GmbH (Ludwigshafen, Germany). 1,2-dioleyloxy-3-dimethylaminopropane (DODMA), N-palmitoyl-sphingosine-1-{succinyl[methoxy(polyethylene glycol)2000]} (C16-PEG2000-Ceramide) and Cholesterol were manufactured by Avanti Polar Lipids (Alabaster, AL, USA). (6Z,9Z,28Z,31Z)-heptatriacont-6,9,28,31-tetraene-19-yl-4-(dimethylamino) butanoate (DLin-MC3-DMA) was purchased from MedChemExpress (Monmouth Junction, NJ, USA). pSar BA12-50 (didodecyl amine initiated polysarcosine with a pSar chain length of 44, as determined by 1H-NMR) was synthesized as previously described [39]. Three types of synthetic mRNA were used, synthetized by BioNTech SE (Mainz, Germany), using internal protocols [40]. Non-coding R159 mRNA consisting of 1900 nucleotides was used for physicochemical characterization. Thy1.1 (CD90.1) encoding reporter mRNA consisting of 1064 nucleotides was used for in vitro transfection assay. Cy5-labeled Luc encoding reporter mRNA consisting of 2135 nucleotides was used for in vitro cell-binding studies. Uridine-Triphosphate (UTP) labeled with Cy5 was purchased from Jena Bioscience (Jena, Germany). 6-(p-toluidino)-2-naphthalenesulfonic acid (TNS), KH_2PO_4 and Na_2HPO_4 were obtained from Sigma-Aldrich (St. Louis, MO, USA), while Ampuwa was purchased from Fresenius Kabi Deutschland GmbH (Bad Homburg vor der Höhe, Germany). Dimethyl sulfoxide (DMSO) was purchased from VWR International GmbH (Darmstadt, Germany). Absolute ethanol (200 proof) and Quant-it™ RiboGreen RNA reagent was purchased from Fisher Scientific (Schwerte, Germany) and glycylglycine was obtained from Carl Roth (Karlsruhe, Germany). For in vitro transfection and cell-binding assay, thawed hPBMCs were resuspended in RPMI medium1640 (1×) + GlutaMAX-I,

Sodium Pyruvate 100 mM (100×), MEM NEAA (100×), 2-Mercaptoethanol (50 mM), Pen Strep, DPBS (1×) 0.5 m EDTA pH 8.0 and Pooled Human Serum (PHS; heat inactivated), purchased from Life technologies (San Diego, CA, USA). Cells were washed during in vitro cell-binding assay in DPBS (1×), 5% FBS (heat inactivated) and 5 mM EDTA (500 mM), purchased from Life technologies (San Diego, CA, USA).

2.2. RNA Constructs and In Vitro Transcription

Plasmid templates for the in vitro transcription of protein-encoding RNA were used as reporters. The Thy1.1 vector encodes the murine Thy1.1 protein, a highly conserved membrane glycoprotein. The Luc vector encodes for luciferase protein. Thy1.1 and Luc RNA were synthesized using 1-methyl-pseudouridine (N1-methylpseudouridine-5′-triphosphate, m1ΨTP, TriLink Biotechnologies, San Diego, CA, USA) [41] and double-stranded mRNA (dsmRNA) contaminants were removed via cellulose purification, as described [42]. The labeling of Luc RNA with fluorescent Cy5-UTP was performed according to the manufacturer's instructions (BioNTech SE, Mainz, Germany). During the in vitro transcription of Luc RNA, 6% of total UTP was replaced with Cy5-labeled UTP.

2.3. LNP Preparation

LNPs were prepared by using the ethanol injection method as used for LPXs [17] in a modified variation. The mRNA was diluted to the predetermined concentration with 10 mM aqueous glycylglycine solution (pH 5.7 ± 0.1) and the ethanolic lipid stock solutions were pre-mixed to obtain the predetermined molar ratios. The aqueous mRNA buffer was pipetted onto the lipid mix and the sample was then immediately vortexed for 10 s. This single-step protocol allows the manufacturing of mRNA LNPs in a directly applicable buffer without further modification. All LNPs were prepared at a molar ratio of ionizable lipid to mRNA (N/P ratio) of 5:1. Molar ratios were calculated as 100 mol% = ∑ mol% (helper lipid, ionizable lipid, cholesterol, stealth moiety). The LNP composition can be seen in Table 1.

Table 1. Composition of investigated formulations.

Formulation	Helper Lipid	Helper Lipid (mol%)	Ionizable Lipid	Ionizable Lipid (mol%)	Cholesterol (mol%)	Stealth Moiety	Stealth Moiety (mol%)	mRNA (mol%)
LNP 1	DOPE	10	DODMA	40	48	PEG	2	8
LNP 2	DOPE	10	DODMA	40	48	pSar	2	8
LNP 3	DOPC	10	DODMA	40	48	PEG	2	8
LNP 4	DOPC	10	DODMA	40	48	pSar	2	8
LNP 5	DOPE	10	MC3	40	48	PEG	2	8
LNP 6	DOPE	10	MC3	40	48	pSar	2	8
LNP 7	DOPC	10	MC3	40	48	PEG	2	8
LNP 8	DOPC	10	MC3	40	48	pSar	2	8

All formulations were manufactured with an N/P ratio of 5. Sample names for lipid nanoparticle (LNP) formulations will be used throughout the manuscript: 1,2-dioleyloxy-3-dimethylaminopropane (DODMA); DLin-MC3-DMA (MC3); 1,2-dioleoyl-sn-glycero-3-ethanolamine (DOPE), 2-Dioleoyl-sn-glycero-3-phosphocholine (DOPC), C16-PEG2000-Ceramide (PEG); polysarcosine BA12-50 (pSar).

2.4. Dynamic Light Scattering and Zeta Potential Measurements

The samples were diluted to an appropriate concentration (1 mg/mL for size, 0.1 mg/mL for zeta potential) in glycylglycine buffer and transferred to a Zetasizer Nano ZS (Malvern Panalytical Ltd., Malvern, UK) for size measurements via dynamic light scattering (DLS) as well as zeta potential determination. The measurements were performed as backscattering measurements (scattering angle: 173°) at 25 °C after a 30 s equilibration time.

2.5. Accessible mRNA

The incorporation of the mRNA cargo into the LNPs was determined via the commercially available Quant-iT™ RiboGreen® assay, as commonly used for this purpose [43]. The fluorescence intensity was measured after the addition of the RiboGreen RNA reagent to

the sample solution (F_0) and compared to that after incubation with 0.02% Triton X-100 used to disrupt the LNPs and release the mRNA load (F_t). The disruption of the LNPs after the addition of Triton X-100 was shown via DLS. The inaccessible mRNA rate was calculated as

$$inaccessible\ mRNA = \left(1 - \frac{F_0}{F_t}\right) \cdot 100\ [\%] \quad (1)$$

2.6. pK_a Fluorescence Assay

A common previously published assay using the fluorescent dye 2-(p-toluidino)-6-naphthalene sulfonic acid (TNS) was performed to determine the apparent formulation pK_a [17,44]. Measurements were performed in triplicates on black TC-coated 96-well plates, with each well containing 10 µL sample (at 0.1 mg/mL total lipid), 90 µL buffer (phosphate buffer as proposed by Sörensen from pH 4.5 to pH 9 [45]) and 2 µL of TNS in DMSO (300 µM). The fluorescence was measured from the top on a TECAN infinite 200Pro plate reader (Tecan Group Ltd., Männedorf, Switzerland) at 325 nm excitation and 435 nm emission wavelength.

2.7. Small-Angle X-ray Scattering

SAXS measurements were performed at the P12 BioSAXS beamline of the European Molecular Biology Laboratory (EMBL) at PETRA III synchrotron, DESY (Hamburg, Germany) [46]. The samples had at a total lipid concentration of 2.5 mg/mL. The samples and the corresponding buffer solutions were measured at a sample-to-detector distance of 3.0 m (corresponding to a q-range of 0.02–7.37 nm^{-1}). The samples and buffers were automatically loaded into an in vacuum flow-through capillary by a robotic sample changer and continuously flowed to reduce radiation damage. The measurements were performed at an X-ray wavelength of 0.124 nm (10 keV energy) and a flux of 5×10^{12} $ph{\cdot}s^{-1}$. A Pilatus 6 M detector (Dectris AG, Baden-Daettwil, Switzerland) was used to collect two-dimensional scattering patterns with an exposure time of 0.095 s. Thirty frames per sample were recorded and only frames without radiation damage were used for averaging. Both the software SASFLOW and the ATSAS software package were used for raw data processing [46–48]. The corresponding buffers for all samples were measured as well and subtracted as background signal from the scattering curves. All SAXS profiles are given as a function of the momentum transfer q,

$$q = \frac{4\pi}{\lambda} \cdot \sin\left(\frac{2\theta}{2}\right) \quad (2)$$

where q is defined as the scattering vector, λ is the X-ray wavelength and 2θ is the scattering angle.

2.8. Data Treatment

Data transformation and analysis were performed using Microsoft Excel (Microsoft, Redmond, DC, USA), QtiPlot 1.0.1 (IONDEV, Bucuresti, Romania) and the ATSAS package (EMBL Hamburg, Hamburg, Germany) [47].

As previously reported, SAXS data for the recorded q-range comprise the LNP form factor as well as Bragg reflections from the (period) mRNA packing within the LNPs [33]. A Lorentzian fit functionality in QtiPlot 1.0.1 was utilized for the peak fitting of the Bragg reflections in the SAXS curves, as given in

$$I(q) = I_0 + \frac{2A}{\pi} \cdot \frac{w}{4 \cdot (q - q_c)^2 + w^2} \quad (3)$$

with I(q) being the scattering intensity, I_0 the baseline intensity, A the peak area, w the peak width (FWHM) and q_c the peak position. Depending on the scattering data, single or double Lorentzian fits were performed. The peak position can be used to calculate the

repeat distance of the scattering moiety (d spacing) for lamellar systems from the Bragg peak using the Bragg equation [49]:

$$d = \frac{2\pi}{q_c} \quad (4)$$

Additional conclusions can be gained from the peak width w, which gives information about the correlation length inside the ordered arrays. Here, the correlation length scales reciprocally with the peak width, meaning that a narrow peak is an indicator for a long correlation length. A generally accepted model for liquid crystalline structures [50] describes the correlation length ξ, which is defined as the distance at which the positional correlation decays to the value 1/e, as:

$$\xi = \frac{2}{w} \quad (5)$$

Additional information can be revealed by analyzing the intensity decay of the whole SAXS profile using the power law as shown in Equation (6), which gives information about fractal dimensionality and the packing compactness of the particles.

$$I(q) = I_0 \cdot q^{-x} \quad (6)$$

For particles with smooth surfaces, a steep exponential decay indicated by the so-called Porod slope x with values between 3 and 4 can be observed, while Porod slopes with lower decay in the range of 2–3 are observed for particles with surface fractals [51].

2.9. In Vitro Thy1.1 Transfection Assay

hPBMCs were isolated via density gradient centrifugation and cryopreserved for further use. For performing in vitro Thy1.1 transfection assay, cryopreserved hPBMCs were thawed at 37 °C in a water bath and resuspended into pre-warmed human DC (hDC) medium (RPMI medium1640 (1×) + GlutaMAX-I containing 5% pooled-human-serum, 1% Sodium Pyruvate 100 mM (100×) and 1% MEM NEAA (100×)). After washing in hDC medium, the total cell number was determined using the automated cell counting device ViCELL XR Cell Analyzer (Beckman Coulter, Brea, CA, USA) and resuspended in the described medium accordingly. Then, 1.0×10^6/mL hPBMCs in hDC medium were seeded in a 96-well ultra-low attachment plate (Corning, Glendale, CA, USA). LNPs were subsequently added at a dose range of 100 ng, 250 ng, 500 ng, 1000 ng and 2000 ng on top of the cell solution in one quick step and resuspended twice. The cells and LNPs were co-incubated at 37 °C and 5% CO_2 for 2 h. The transfected hPBMCs were washed, resuspended in fresh hDC medium and further incubated at 37 °C and 5% CO_2 for 4 h. Extracellular staining was performed after 6 h of total incubation.

2.10. In Vitro Cy5 Cell Binding Assay

hPBMCs were seeded at a cell number of 2.0×10^5/mL in hDC medium per well into a 96-well ultra-low attachment plate (Corning, Glendale, CA, USA). LNPs were added in the appropriate dose and co-incubation was performed at 4 °C for 1 h. hPBMCs were washed three times in Flow Buffer (DPBS (1×), 5% FBS (heat inactivated), 5 mM EDTA (500 mM)). Extracellular staining for flow cytometric measurement was performed.

2.11. Flow Cytometry

Monoclonal antibodies for extracellular staining for Thy1.1 transfection assay included CD3-BV421 (BD Biosciences, San Diego, CA, USA; clone: UCHT1), CD4-PE (BioLegend, San Diego, CA, USA; clone: SK3), CD8-APC (BD Biosciences, San Diego, CA, USA; clone: SK1), CD14-BV510 (BD Biosciences, San Diego, CA, USA; clone: MφP9), CD19-PerCP-Cy5.5 (eBiosience, San Diego, CA, USA; clone: SJ25C1) and CD56-PE-Cy7 (BD Biosciences, San Diego, CA, USA; clone: B-159), Thy1.1-BB515 (BD Biosciences, San Diego, CA, USA; clone: OX7). Viability was determined using fixable viability dye eFluor 780 (eBioscience,

San Diego, CA, USA). hPBMCs were stained for 20 min at 4 °C in the dark. Cells were washed twice in 150 µL Flow Buffer and the cell pellet was resuspended in 1× Stabilizing Fixative (BD Biosciences, San Diego, CA, USA). Flow cytometric measurements were acquired on a BD FACS Canto II (BD Biosciences, San Diego, CA, USA) and analyzed with FlowJo V10.8.1 software (Tree Star Inc., Ashland, OR, USA). For gating relevant cell groups, cell debris was excluded by side scatter-area (SSC-A) versus forward scatter-area (FSC-A). Singlet cells were gated based on FSC-height (FSC-H) against FSC-area (FSC-A). Thy1.1-expressing cells or Cy5-positive cells were then identified based on their viability. Monocytes were gated as CD14+. B cells and NK cells were gated as CD14−/CD19+ and CD14−/CD56+/CD3−, respectively. CD14−/CD19−/CD56−/CD4+ were identified as CD4+ T cells. CD8+ T cells were gated as CD14−/CD19−/CD56−/CD8+ or CD14−/CD19−/CD56−/CD3+/CD4−.

2.12. Statistical Analysis

Data analysis was conducted using GraphPad Prism 9.0 software. The data are presented as mean ± S.D. Comparison of significance between groups was assessed using a two-way analysis of variance (ANOVA II) with Šidák's multiple comparison correction. * p 0.0258, *** $p < 0.001$, **** $p < 0.0001$.

3. Results

3.1. Particle Size, Zeta Potential and mRNA Incorporation

With our manufacturing protocol, described in the methods and materials part, we were able to obtain particle sizes (Z-Average from dynamic light scattering measurements) within a range of 150–250 nm and a polydispersity index (PDI) $\leq$ 0.2 (Table 2). LNP formulations manufactured with MC3 overall showed smaller hydrodynamic diameters compared to their DODMA-containing counterparts. Also, the incorporation of pSar-grafted lipids instead of PEGylated lipids led to slightly higher hydrodynamic diameters. The zeta potentials, as measured via electrophoretic light scattering (ELS), were strongly positive at around 30 mV in the glycylglycine buffer (pH 5.7). When measured in DPBS buffer (pH 7.3), the zeta potential decreased to near neutral values due to the ionizable character of the formulations. The fraction of accessible mRNA, determined with the Quant-it™ RiboGreen assay, was low, indicating high encapsulation efficacies.

Table 2. Physicochemical characterization of mRNA LNPs in application buffer (10 mM glycylglycine, pH 5.7). Data presented as mean ± S.D., $n = 3$.

Formulation	Composition	Diameter (nm)	PDI	Zeta Potential (mV)	Inaccessible mRNA (%)
LNP 1	**DODMA/DOPE/PEG**	201 ± 15	0.202 ± 0.043	27 ± 7	95 ± 3
LNP 2	**DODMA/DOPE/pSar**	239 ± 21	0.173 ± 0.028	34 ± 6	91 ± 4
LNP 3	**DODMA/DOPC/PEG**	221 ± 15	0.205 ± 0.021	28 ± 5	92 ± 4
LNP 4	**DODMA/DOPC/pSar**	242 ± 33	0.193 ± 0.040	35 ± 3	90 ± 4
LNP 5	**MC3/DOPE/PEG**	174 ± 07	0.124 ± 0.021	30 ± 3	96 ± 2
LNP 6	**MC3/DOPE/pSar**	196 ±13	0.170 ± 0.015	33 ± 2	93 ± 2
LNP 7	**MC3/DOPC/PEG**	159 ± 15	0.117 ±.0.024	27 ± 6	97 ± 1
LNP 8	**MC3/DOPC/pSar**	197 ± 17	0.156 ± 0.028	34 ± 1	94 ± 2

3.2. Fluorescence-Based pK_a Determination

The apparent pK_a values of mRNA-LNPs were determined using a fluorescence-based TNS assay. The measured intensities in the different pH buffers (covering pH 4.5–9) were fitted with sigmoidal curves, and the inflection points were defined as the apparent pK_a of the formulations (Table 3 and Figure S1). All formulations show an apparent pK_a of 6.5–6.7, without a notable difference between the varying compositions, in good accordance with former investigations [52].

Table 3. Apparent pK_a of all LNP formulations via fluorescence-based 2-(p-toluidino)-6- naphthalene sulfonic acid (TNS) assay. Data presented as mean ± S.D., $n = 3$.

Formulation (DODMA)	Apparent pK_a	Formulation (MC3)	Apparent pK_a
LNP 1	6.5 ± 0.0	**LNP 5**	6.7 ± 0.0
LNP 2	6.5 ± 0.1	**LNP 6**	6.6 ± 0.0
LNP 3	6.5 ± 0.2	**LNP 7**	6.5 ± 0.1
LNP 4	6.6 ± 0.1	**LNP 8**	6.5 ± 0.1

3.3. Small-Angle X-ray Scattering

SAXS was used to investigate the LNP structure for the different compositions. We systematically varied the helper lipid (DOPE vs. DOPC), the ionizable lipid (DODMA vs. MC3), and the stealth moiety (PEG-grafted lipid vs. pSar-grafted lipid) within all LNP formulations. Scattering curves were recorded in the application buffer (containing 10 mM glycylglycine) and in the phosphate buffer at pH 4.5 to mimic the environment in late endosomal uptake processes. The scattering patterns of each formulation in the two different buffers are displayed in Figure 1A.

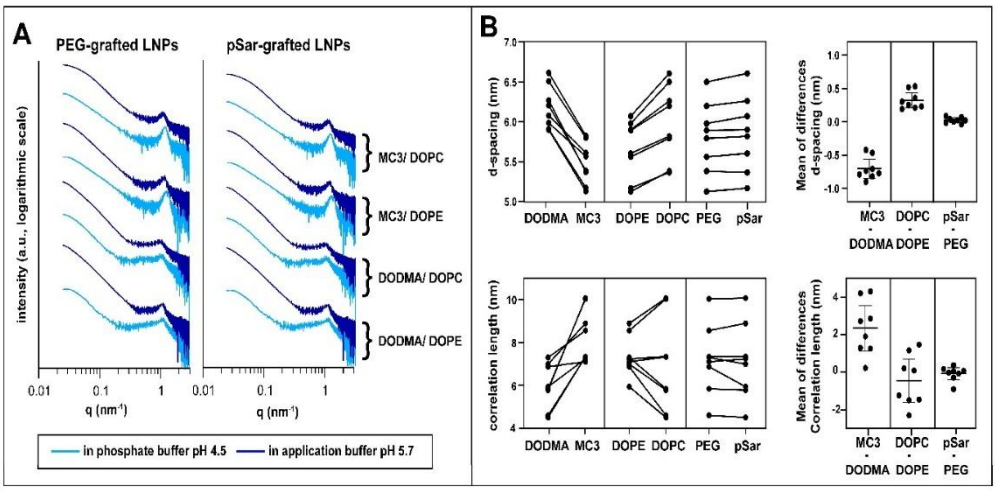

Figure 1. Small-angle X-ray scattering (SAXS) investigation. (**A**) SAXS patterns of different LNP formulations in phosphate buffer (pH 4.5, light blue) and application buffer (pH 5.7, dark blue). Formulations are displayed according to their composition with PEG-grafted LNPs (left) and pSar-grafted LNPs (right) and their ionizable and helper lipid are displayed right to the scattering patterns. Scattering patterns are vertically shifted for better visualization. (**B**) Comparison between LNP formulations in d-spacing (top). Investigated pairs generated with formulations only differing in one lipid component (ionizable lipid, helper lipid, stealth lipid). Mean of the differences in the compared formulations is shown on the right and represents the mean factor in which the formulations differ in d-spacing when comparing the investigated pairs; the same procedure for correlation length is at the bottom. Data displayed as mean ± S.D.

All curves displayed similar features, in accordance with previous measurements [33] for such systems (Table S1), dominated by a single broad maximum at around 1 nm^{-1} with no further pronounced patterns, indicative of rather weak lamellar order, while the overall curve shape represented the particle form factor. Here, as data points at very low q could not be detected, no determination of overall size and shape analysis of the particles was possible;

however, information on the fractal dimension (surface roughness) of the particles could be derived. We interpreted this peak as resulting from lipid and RNA stacks consisting of very few repeating units and almost no long-range order. Systematic differences depending on the LNP composition and environmental buffer could be discerned.

For quantitative analysis, peak position and width were determined by fitting with Lorentzian functions (formalism see Methods section). Using Bragg's law, d-spacings were calculated, whereas the model for liquid crystalline order was taken to calculate the correlation length from the peak width (see Methods section, results displayed in Table 4). With its rather small values in the same order of magnitude as the repeat distance, the correlation length was taken for relative comparison between the different systems only.

Table 4. Results of SAXS data analysis for the LNP formulations as applied and in phosphate buffer pH 4.5, respectively.

Formulation	Application Buffer (pH 5.7)			Phosphate Buffer (pH 4.5)		
	d-Spacing (nm)	Correlation Length (nm)	Porod Exponent	d-Spacing (nm)	Correlation Length (nm)	Porod Exponent
LNP 1	6.0 ± 0.1	6.9 ± 0.3	−3.9 ± 0.1	5.9 ± 0.1	7.3 ± 0.2	−3.4 ± 0.1
LNP 2	6.1 ± 0.1	4.6 ± 0.3	−3.9 ± 0.1	5.9 ± 0.1	7.0 ± 0.2	−3.4 ± 0.1
LNP 3	6.5 ± 0.1	5.9 ± 0.2	−3.9 ± 0.1	6.2 ± 0.1	5.8 ± 0.1	−3.9 ± 0.1
LNP 4	6.6 ± 0.1	4.5 ± 0.2	−3.9 ± 0.1	6.3 ± 0.1	5.8 ± 0.2	−3.9 ± 0.1
LNP 5	5.6 ± 0.1	7.1 ± 0.2	−3.8 ± 0.1	5.1 ± 0.1	8.6 ± 0.2	−3.3 ± 0.1
LNP 6	5.8 ± 0.1	7.3 ± 0.2	−3.5 ± 0.1	5.2 ± 0.1	8.9 ± 0.2	−2.6 ± 0.1
LNP 7	5.6 ± 0.1	7.2 ± 0.3	−3.7 ± 0.1	5.4 ± 0.1	10.0 ± 0.1	−3.5 ± 0.1
LNP 8	5.8 ± 0.1	7.3 ± 0.3	−3.6 ± 0.1	5.4 ± 0.1	10.1 ± 0.2	−2.7 ± 0.1

The fitting results revealed that the internal organization of the various LNPs sensitively depended on the lipid composition (Figure 1B): MC3-based formulations showed a smaller d-spacing than those with DODMA, and the correlation length was higher in comparison to their DODMA-based analogs, as displayed by direct comparison and mean differences of compared pairs in Figure 1B. DOPE-based formulations showed a smaller d-spacing compared to their DOPC counterparts but to a lower extent as for the ionizable lipid. On the other hand, exchanging the stealth moiety had only a minor effect on d-spacing and correlation length, in accordance with the assumption that the grafted moieties are predominantly present at the particle surface and inserted only to a minor extent into the mRNA/lipid complexes [53,54].

For all LNP formulations, we observed a decrease in d-spacing and an increase in correlation lengths when decreasing the pH value of the buffer from 5.7 to 4.5, resulting from increased electrostatic interactions between mRNA and more positively charged ionizable lipids at low pH. These structural changes with decreasing environmental pH were more pronounced for MC3-based LNPs than for DODMA-based analogs.

By using a power law ($I \sim q^{-x}$, with x as the so-called Porod exponent) to represent the intensity decay of the curves in the form factor describing the low q region, one can gain information on the fractal dimension, or, in other words, the surface roughness, of the LNPs from SAXS measurements [55,56]. A Porod exponent of −4 indicates ideally smooth (flat) interfaces (Porod law), and lower numbers indicate increasing surface roughness. All LNPs in the application buffer had a Porod exponent between −4 and −3.5, indicating compact particles with relatively smooth surfaces. Notably, the Porod exponents were lower for MC3-containing formulations than for those with DODMA, and for LNPs with pSar the values were lower than with PEG LNPs. Interestingly, some pSar-containing formulations (LNP6 and LNP8) showed a further decrease of the Porod exponents when transferred to the pH 4.5 buffer, revealing further increased surface roughness. In contrast, their PEG-lipid-containing counterparts (LNP5 and LNP7) did not show such strong effects.

To summarize, the SAXS measurements demonstrate that the structure of the mRNA-lipid complexes sensitively depends on the choice of ionizable lipid and the helper lipid. This was even the case when exchanging only the head group of the phospholipid, which

was present only in a relatively low fraction in the LNPs. In contrast, the choice of the stealth moiety does not impact the internal structure of the LNP. However, it does influence the surface properties, especially with decreasing the pH value.

3.4. In Vitro Transfection Studies

With the information on the internal structure of the LNPs, we investigated mRNA-LNPs on their biological performance by examining transfection and cell binding in primary hPBMCs in vitro. Thy1.1 reporter mRNA was used as cargo to measure transfection efficiency in leukocyte sub populations, such as Monocytes, B-, T- and NK cells. We first evaluated the overall tolerability of all LNP formulations at different doses ranging from 100 ng to 2000 ng. Cell viability for all formulations and dose ranges remained at or above 90%, indicating the good tolerability of the investigated LNPs (Figure 2). Especially Monocytes and to a lesser extent B cells showed Thy1.1 expression and thus a positive transfection. Still, the transfection level in B cells remained under 15% and no transfection signal was detected in T- or NK-cells (Figure S2).

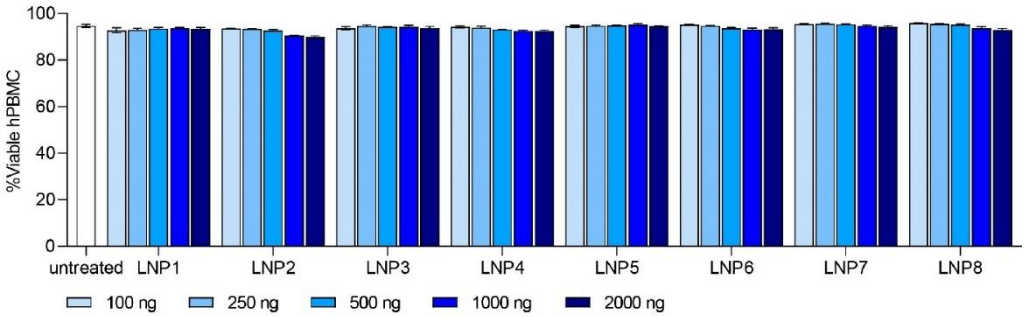

Figure 2. In vitro tolerability of LNP formulation 1–8 in human peripheral blood mononuclear cells (hPBMC). Dose ranged from 100 ng to 2000 ng. Viability of each LNP formulation is shown as %Viable hPBMC. Data are presented as mean ± S.D., $n = 3$ technical replicates per LNP formulation.

Monocytes showed a dose-dependent transfection efficiency for all tested LNP compositions with a transfection level up to 95% at the highest dose of 2000 ng (Figure 3). We selected Monocyte transfection as the main focus for further investigations.

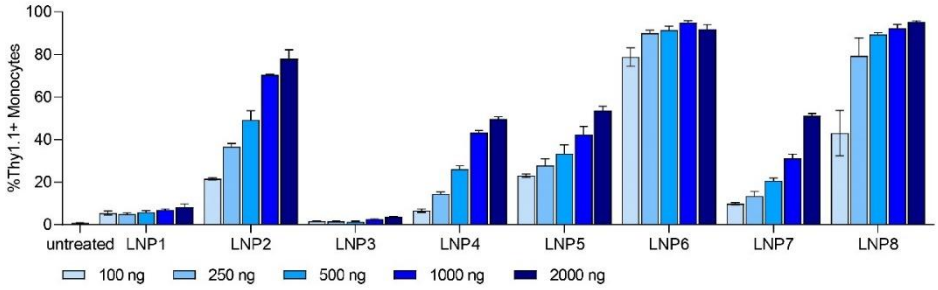

Figure 3. In vitro dose-dependent transfection efficiency of Monocytes for LNP formulations 1–8. Dose ranged from 100 ng to 2000 ng. Transfection efficiency of each LNP formulation is shown as %Thy1.1+ Monocytes. Data are presented as mean ± S.D., $n = 3$ technical replicates per LNP formulation.

At the highest dose of 2000 ng, we observed different expression levels in all tested LNP formulations. With different ionizable lipids in all LNP formulations (DODMA for

LNP1-4; MC3 for LNP5-8), the overall transfection efficiency is higher for MC3-LNPs (Figure S3). For all LNPs, the use of helper lipid DOPE (LNP1-2, LNP5-6) improved the efficiency to a low extent in comparison to DOPC (Figure S4). Interestingly, all pSar-containing LNP formulations (LNP2, LNP4, LNP6, LNP8) showed a significantly higher transfection efficiency than PEG-containing LNP formulations (LNP1, LNP3, LNP5, LNP7), represented in Figure 4. LNP2 reached Thy1.1 expression of greater than 80% in monocytes, while LNP1 only led to 10% Thy1.1 expression. LNP3 showed the lowest transfection rate, with an expression level under 4%, whereas LNP4 reached a Thy1.1 expression above 50%. LNP5 and LNP7 (PEGylated) showed a transfection efficiency of 50%, while LNP6 and LNP8 (pSar-lipid containing) led to a Thy1.1 expression greater than 90% at the same dose (2000 ng). We want to highlight that LNP6 (MC3/DOPE/pSar) achieved the highest Thy1.1 expression in monocytes, starting with more than 75% at the lowest dose (100 ng) and reaching 95%.

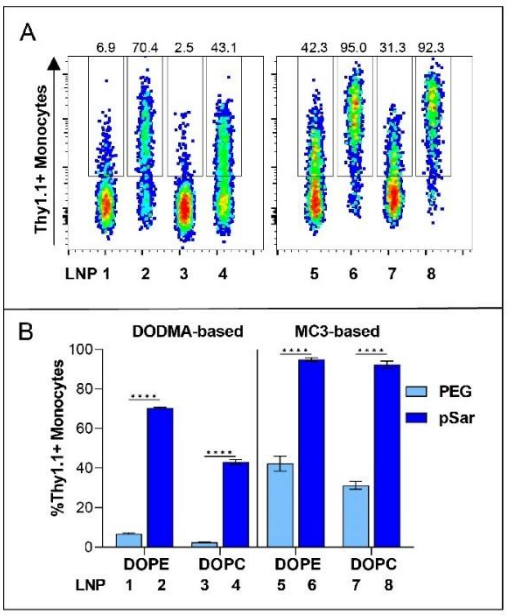

Figure 4. In vitro transfection efficiency of Thy1.1 RNA containing LNPs at a dose of 1000 ng in hPBMC, Monocytes as representative cell group. (**A**) Thy1.1-expressing Monocytes analyzed by flow cytometry. Numbers indicate the percentage of Thy1.1+ Monocytes. (**B**) Transfection efficiency of all PEG-lipid versus pSar-lipid LNPs shown as %Thy1.1+ Monocytes. Data are presented as mean ± S.D., analyzed by a two-way ANOVA with Šidák's multiple comparison test, **** $p < 0.0001$, $n = 3$ technical replicates per LNP formulation.

3.5. In Vitro Cell-Binding Studies

We correlated the internal lipid structure of the LNPs with their transfection efficiency in vitro and identified that DODMA-based LNPs (LNP1-4) showed a significantly lower monocyte transfection compared to MC3-based LNPs (LNP5-8). We therefore investigated the cellular binding affinity to determine if DODMA-LNPs properly reach monocytes or if the lacking transfection can be explained by disturbed uptake in monocytes. For this, DODMA-based LNPs were co-formulated with an mRNA mix of Thy1.1-encoding mRNA and Cy5-labeled Luc mRNA in a weight ratio of 1:1. pSar-shielded DODMA LNPs (LNP2, LNP4) demonstrated almost 100% of Cy5-positive monocytes compared to PEG-shielded

DODMA LNPs (LNP1, LNP3), reaching a cell-binding level between 40–60% (Figure 5A). The choice of helper lipid, again, only minorly improved cell-binding behavior (LNP1 vs. LNP3). Both LNP formulations two and four already reached a cell binding of almost 100%, regardless of the choice of helper lipid. To sum up, pSar as a stealth moiety demonstrated higher cell binding in monocytes compared to PEG-shielded LNPs.

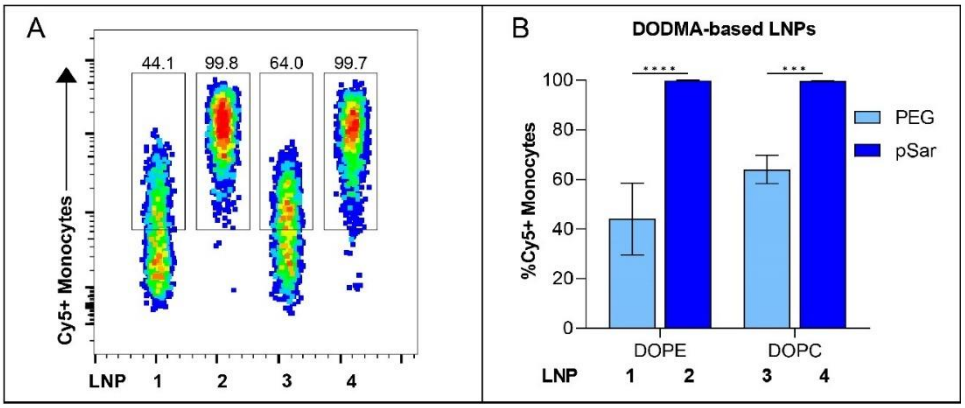

Figure 5. In vitro cell-binding studies of Cy5-labeled RNA containing DODMA-LNP at a dose of 1000 ng in hPBMCs. (**A**) Cy5-labeled RNA-positive Monocytes analyzed by flow cytometry. Numbers indicate the percentage of Cy5+ Monocytes. (**B**) Cell-binding efficiency of each DODMA-LNP formulation is shown as %Cy5+ Monocytes. Data are presented as mean ± S.D., analyzed by a two-way ANOVA with Šidák's multiple comparison test, *** $p < 0.001$, **** $p < 0.0001$, $n = 3$ technical replicates per LNP formulation.

Our in vitro investigations revealed that all tested LNPs exhibited negligible toxicity in all tested dose ranges, while transfection efficiency and cell-binding behavior varied depending on the LNP composition. LNPs containing MC3 as an ionizable lipid, DOPE as a helper lipid, and pSar-grafted lipid showed improved transfection rates among all formulations and exhibited the highest potency in vitro, with high efficacy even at a low tested dose range. Moreover, pSar-containing DODMA-LNP formulations showed outstanding cell-binding affinity to monocytes. These findings substantiate that the choice of specific lipid components, especially regarding the stealth moiety, plays a critical role in enhancing the transfection efficiency of LNPs on primary hPBMCs in vitro.

4. Discussion

Lipid nanoparticles as non-viral RNA delivery vehicles have great potential in various applications, such as vaccines against infectious diseases [4,8,9], protein-replacement therapies [2] or novel cancer immunotherapy approaches [4,18]. Currently approved LNP formulations are characterized by a very specific lipid composition, consisting of four primary components: ionizable-cationic lipid, cholesterol, helper lipid and a PEG stealth moiety [10,57]. The application of mRNA in other therapeutic settings as mentioned above will require the development of delivery systems optimized for the respective application. So far, the development of such tailored therapeutics is challenged by the limited understanding of the intramolecular structure–function features in LNPs, especially regarding the interplay between ionizable lipids, helper lipids and stealth moieties. Therefore, here we have investigated the influence of selected lipids on the structural and functional characteristics of the LNPs. By using SAXS together with other techniques for physicochemical characterization and transfection studies, we were able to directly determine the way the tested molecular groups affected internal LNP structure and also biological functionality.

For the MC3-LNPs, which were more active than the ones with DODMA, the repeat distance was smaller and the long-range order higher, although, with its two linoleyl moieties, MC3 is bulkier and spans a larger distance.

This we interpreted as due to the stronger electrostatic interactions between the charged moieties of the RNA and the lipid head group. Accordingly, the effect increased at low pH, when the charge density at the ionizable lipid head group was higher. Notably, the pK_a values, which are frequently taken as indicators for efficacy, were rather similar for DODMA and MC3. Therefore, the information on structural and electrostatic coherencies obtained here may provide a supplementary indication to explain functional aspects of the ionizable lipids. MC3 facilitates endosomal escape [58] and shows great potential for RNA delivery [16,59]. Our in vitro data can confirm the improved transfection capability of MC3 in the tested cells and provide a potential structural foundation for these findings.

Also, the choice of the helper lipid, even only present at 10 mol% in the lipid mixture, resulted in measurable effects of structure and activity. With DOPE as a helper lipid, the d-spacing was lower than with DOPC, and the activity of the LNPs was higher. For the effect on the structure, it is plausible to assume that the bulkier PC headgroup in comparison to PE contributes to a higher repeating distance. Regarding activity, more complex cooperative effects on the membrane organization may play a role. The fusogenic properties of PE lipids may have facilitated uptake and endosomal release. It has been reported that the helper lipid in LNPs is enriched in the shell of the particles [54]; therefore, even at the low molar fraction as present here, the type of head group can affect membrane interactions on endosomal uptake and release. As well, there may be a specific preference of PE-containing nanoparticles to immune cells as tested here. In fact, for another type of lipid nanoparticles (lipoplexes), DOPE has been identified as the most suitable lipid for targeting antigen-presenting cells in vivo [18,19]. Notably, in these experiments, the presence of PE leads as well to very low expression of the lipoplexes in the liver. Therefore, for future developments, LNPs comprising PE could be of particular interest for extrahepatic targeting of the RNA, which is still an unmet need for many applications. The currently established LNPs (including those used for the COVID-19 vaccines), which comprise PC as the phospholipid moiety [10], are known to target the liver to a large extent.

Concerning the polymer-grafted lipids, we found further evidence for the potency of pSar as a stealth moiety for engineering particles with an improved efficacy profile. There is a need for alternatives to PEG-containing LNPs, which still represent the gold standard for RNA delivery due to their adverse side-effects caused by anti-PEG antibodies [60,61]. pSar demonstrates comparable stealth-like properties and is a bio-based and biodegradable material [39,62]. In previous studies [33], we showed that pSar as a stealth component in mRNA LNPs provides particles with comparable physicochemical properties as LNPs manufactured with PEG moieties together with lower toxicity and improved protein secretion in HepG2 cell line in vitro as well as in Balb/C mice in vivo. It is hypothesized that pSar used in lipid delivery systems can circumvent the ABC phenomena based on multiple injection experiments in rats in comparison to PEG-grafted formulations [63]. The potential of pSar to be readily functionalized brings further possibilities for the targeting of delivery systems. End-group modifications with different amino acids as well as antibodies or fragments of them allows the selection of charge and molecular properties of the particle surface and therefore control of circulation and targeting properties [64]. Careful SAXS data analysis allowed us to correlate distinct structural properties of the pSar LNPs with the improved transfection results. The elevated surface roughness of the pSar-LNPs compared to those with PEG, which even increased at low pH, may foster interaction with the oppositely charged endosomal membrane, resulting in the facilitated rupture of the membrane and the release of the mRNA into the cytosol [65,66]. The at least partial positive charge of the amine head group of pSar may further contribute to this effect. Combining MC3, with its good RNA transfection properties, with DOPE as a helper lipid and pSar as a surface modification, we generated an LNP composition with optimal conditions for transfecting hPBMCs. Thus, we have determined certain compositional and structural 'fingerprints' of

LNPs which led to improved transfection efficacy, here demonstrated for immune cells. Systems with higher activity were obtained when the internal order and packing density were higher and with increased fractal dimension of the particles. Further experiments to investigate targeting and efficacy in vivo in correlation with the structural observations will be necessary to fully elucidate these structure–function correlations. This insight can provide useful guidance for the organization of development experiments toward optimized LNPs for future applications.

5. Conclusions

In this study, the influence of discrete lipid characteristics on the structure and functionality of LNP formulations was determined. SAXS analysis provided valuable insights into the overall morphology and internal structure of the LNPs, while activity was tested on hPBMCs in vitro. Gaining a deeper understanding of these relationships can prove highly valuable for the development of safe and efficient delivery systems and the implementation of quality control measures. pSar-lipids, as an alternative to PEG-lipids, were further validated for the assembly of LNP formulations with controlled size and improved transfection efficiency. The findings may serve as a basis to derive general rules for the development of tailored LNP formulations.

Supplementary Materials: The following supporting information can be downloaded at: https://www.mdpi.com/article/10.3390/pharmaceutics15082068/s1, Figure S1: Fluorescence-based assay for apparent pK_a determination; Figure S2: In vitro Thy1.1 expression in hPBMC sub-populations.; Figure S3: In vitro transfection efficiency of all DODMA-LNPs versus MC3-LNPs at a dose of 1000 ng.; Figure S4: In vitro transfection efficiency of all DOPE-LNPs versus DOPC-LNPs at a dose of 1000 ng.; Table S1: Results of peak fitting using Lorentzian function.

Author Contributions: Conceptualization, P.L., H.H. and U.S.; methodology, C.W., I.S.K. and L.U.; software, C.W. and I.S.K.; validation, C.W., I.S.K., H.H., M.B. and P.L.; formal analysis, C.W. and I.S.K.; investigation, C.W. and I.S.K.; resources, P.L., U.S., M.D. and M.B.; data curation, C.W. and I.S.K.; writing—original draft preparation, C.W. and I.S.K.; writing—review and editing, C.W., I.S.K., L.U., M.A.S., D.F., T.N., M.D., H.H., M.B. and P.L.; visualization, C.W. and I.S.K.; supervision, P.L., M.D., M.B., U.S. and H.H.; project administration, P.L., M.D., M.B. and U.S.; funding acquisition, P.L., M.B. and U.S. All authors have read and agreed to the published version of the manuscript.

Funding: This research is supported by the SFB1066 (funding number: 213555243) funded by the German Research Foundation (DFG).

Institutional Review Board Statement: Not applicable.

Informed Consent Statement: Not applicable.

Data Availability Statement: The data presented in this study are available on request from the corresponding author.

Acknowledgments: Funding by the Deutsche Forschungsgemeinschaft is gratefully acknowl-edged. We would like to thank Avanti Polar Lipid and Lipoid GmbH for gifting some of the lipids, namely DOPC, DOPE, DODMA, C16-PEG2000-Ceramide and Cholesterol. The synchrotron SAXS data were collected at beamline P12 operated by EMBL Hamburg at the PETRA III storage ring (DESY, Hamburg, Germany).

Conflicts of Interest: U.S., P.L. and M.B. received research grants from the German Research Foundation (DFG) for the SFB 1066 B12 project. U.S. is co-founder, shareholder and CEO at BioNTech SE. P.L. is consultant for BioNTech SE. M.D. is an employee at BioNTech SE. M.B. and H.H. are inventors on the patent application: RNA particles comprising polysarcosine. 2018, PCT/EP2018/076633.

References

1. Sahin, U.; Karikó, K.; Türeci, Ö. mRNA-based therapeutics--developing a new class of drugs. *Nat. Rev. Drug Discov.* **2014**, *13*, 759–780. [CrossRef] [PubMed]
2. Akinc, A.; Maier, M.A.; Manoharan, M.; Fitzgerald, K.; Jayaraman, M.; Barros, S.; Ansell, S.; Du, X.; Hope, M.J.; Madden, T.D.; et al. The Onpattro story and the clinical translation of nanomedicines containing nucleic acid-based drugs. *Nat. Nanotechnol.* **2019**, *14*, 1084–1087. [CrossRef]
3. Hou, X.; Zaks, T.; Langer, R.; Dong, Y. Lipid nanoparticles for mRNA delivery. *Nat. Rev. Mater.* **2021**, *6*, 1078–1094. [CrossRef]
4. Tenchov, R.; Bird, R.; Curtze, A.E.; Zhou, Q. Lipid Nanoparticles—From Liposomes to mRNA Vaccine Delivery, a Landscape of Research Diversity and Advancement. *ACS Nano* **2021**, *15*, 16982–17015. [CrossRef] [PubMed]
5. Sahin, U.; Oehm, P.; Derhovanessian, E.; Jabulowsky, R.A.; Vormehr, M.; Gold, M.; Maurus, D.; Schwarck-Kokarakis, D.; Kuhn, A.N.; Omokoko, T.; et al. An RNA vaccine drives immunity in checkpoint-inhibitor-treated melanoma. *Nature* **2020**, *585*, 107–112. [CrossRef]
6. Sahin, U.; Türeci, Ö. Personalized vaccines for cancer immunotherapy. *Science* **2018**, *359*, 1355–1360. [CrossRef]
7. Sahin, U.; Derhovanessian, E.; Miller, M.; Kloke, B.-P.; Simon, P.; Löwer, M.; Bukur, V.; Tadmor, A.D.; Luxemburger, U.; Schrörs, B.; et al. Personalized RNA mutanome vaccines mobilize poly-specific therapeutic immunity against cancer. *Nature* **2017**, *547*, 222–226. [CrossRef]
8. Walsh, E.E.; Frenck, R.W.; Falsey, A.R.; Kitchin, N.; Absalon, J.; Gurtman, A.; Lockhart, S.; Neuzil, K.; Mulligan, M.J.; Bailey, R.; et al. Safety and Immunogenicity of Two RNA-Based COVID-19 Vaccine Candidates. *N. Engl. J. Med.* **2020**, *383*, 2439–2450. [CrossRef]
9. Corbett, K.S.; Edwards, D.K.; Leist, S.R.; Abiona, O.M.; Boyoglu-Barnum, S.; Gillespie, R.A.; Himansu, S.; Schäfer, A.; Ziwawo, C.T.; DiPiazza, A.T.; et al. SARS-CoV-2 mRNA vaccine design enabled by prototype pathogen preparedness. *Nature* **2020**, *586*, 567–571. [CrossRef] [PubMed]
10. Hald Albertsen, C.; Kulkarni, J.A.; Witzigmann, D.; Lind, M.; Petersson, K.; Simonsen, J.B. The role of lipid components in lipid nanoparticles for vaccines and gene therapy. *Adv. Drug Deliv. Rev.* **2022**, *188*, 114416. [CrossRef]
11. Cheng, X.; Lee, R.J. The role of helper lipids in lipid nanoparticles (LNPs) designed for oligonucleotide delivery. *Adv. Drug Deliv. Rev.* **2016**, *99*, 129–137. [CrossRef] [PubMed]
12. Rietwyk, S.; Peer, D. Next-Generation Lipids in RNA Interference Therapeutics. *ACS Nano* **2017**, *11*, 7572–7586. [CrossRef]
13. Torchilin, V.P.; Zhou, F.; Huang, L. pH-Sensitive Liposomes. *J. Liposome Res.* **1993**, *3*, 201–255. [CrossRef]
14. Ramezanpour, M.; Schmidt, M.L.; Bodnariuc, I.; Kulkarni, J.A.; Leung, S.S.W.; Cullis, P.R.; Thewalt, J.L.; Tieleman, D.P. Ionizable amino lipid interactions with POPC: Implications for lipid nanoparticle function. *Nanoscale* **2019**, *11*, 14141–14146. [CrossRef] [PubMed]
15. Semple, S.C.; Akinc, A.; Chen, J.; Sandhu, A.P.; Mui, B.L.; Cho, C.K.; Sah, D.W.Y.; Stebbing, D.; Crosley, E.J.; Yaworski, E.; et al. Rational design of cationic lipids for siRNA delivery. *Nat. Biotechnol.* **2010**, *28*, 172–176. [CrossRef] [PubMed]
16. Jayaraman, M.; Ansell, S.M.; Mui, B.L.; Tam, Y.K.; Chen, J.; Du, X.; Butler, D.; Eltepu, L.; Matsuda, S.; Narayanannair, J.K.; et al. Maximizing the Potency of siRNA Lipid Nanoparticles for Hepatic Gene Silencing In Vivo. *Angew. Chem.* **2012**, *124*, 8657–8661. [CrossRef]
17. Uebbing, L.; Ziller, A.; Siewert, C.; Schroer, M.A.; Blanchet, C.E.; Svergun, D.I.; Ramishetti, S.; Peer, D.; Sahin, U.; Haas, H.; et al. Investigation of pH-Responsiveness inside Lipid Nanoparticles for Parenteral mRNA Application Using Small-Angle X-ray Scattering. *Langmuir* **2020**, *36*, 13331–13341. [CrossRef]
18. Kranz, L.M.; Diken, M.; Haas, H.; Kreiter, S.; Loquai, C.; Reuter, K.C.; Meng, M.; Fritz, D.; Vascotto, F.; Hefesha, H.; et al. Systemic RNA delivery to dendritic cells exploits antiviral defence for cancer immunotherapy. *Nature* **2016**, *534*, 396–401. [CrossRef]
19. Rosigkeit, S.; Meng, M.; Grunwitz, C.; Gomes, P.; Kreft, A.; Hayduk, N.; Heck, R.; Pickert, G.; Ziegler, K.; Abassi, Y.; et al. Monitoring Translation Activity of mRNA-Loaded Nanoparticles in Mice. *Mol. Pharm.* **2018**, *15*, 3909–3919. [CrossRef] [PubMed]
20. Cheng, Q.; Wei, T.; Farbiak, L.; Johnson, L.T.; Dilliard, S.A.; Siegwart, D.J. Selective organ targeting (SORT) nanoparticles for tissue-specific mRNA delivery and CRISPR-Cas gene editing. *Nat. Nanotechnol.* **2020**, *15*, 313–320. [CrossRef]
21. Segalla, G. Chemical-physical criticality and toxicological potential of lipid nanomaterials contained in a COVID-19 mRNA vaccine. *Int. J. Vaccine Theory Pract. Res.* **2023**, *3*, 787–817. [CrossRef]
22. Jörgensen, A.M.; Wibel, R.; Bernkop-Schnürch, A. Biodegradable Cationic and Ionizable Cationic Lipids: A Roadmap for Safer Pharmaceutical Excipients. *Small* **2023**, *19*, e2206968. [CrossRef] [PubMed]
23. Ishida, T.; Masuda, K.; Ichikawa, T.; Ichihara, M.; Irimura, K.; Kiwada, H. Accelerated clearance of a second injection of PEGylated liposomes in mice. *Int. J. Pharm.* **2003**, *255*, 167–174. [CrossRef] [PubMed]
24. Garay, R.P.; Labaune, J.P. Immunogenicity of Polyethylene Glycol (PEG). *Open Conf. Proc. J.* **2011**, *2*, 104–107. [CrossRef]
25. Semple, K.T.; Reid, B.J.; Fermor, T.R. Impact of composting strategies on the treatment of soils contaminated with organic pollutants. *Environ. Pollut.* **2001**, *112*, 269–283. [CrossRef]
26. Estapé Senti, M.; de Jongh, C.A.; Dijkxhoorn, K.; Verhoef, J.J.F.; Szebeni, J.; Storm, G.; Hack, C.E.; Schiffelers, R.M.; Fens, M.H.; Boross, P. Anti-PEG antibodies compromise the integrity of PEGylated lipid-based nanoparticles via complement. *J. Control. Release* **2022**, *341*, 475–486. [CrossRef]
27. Secker, C.; Brosnan, S.M.; Luxenhofer, R.; Schlaad, H. Poly(α-Peptoid)s Revisited: Synthesis, Properties, and Use as Biomaterial. *Macromol. Biosci.* **2015**, *15*, 881–891. [CrossRef] [PubMed]

28. Kidchob, T.; Kimura, S.; Imanishi, Y. Amphiphilic poly(Ala)-b-poly(Sar) microspheres loaded with hydrophobic drug. *J. Control. Release* **1998**, *51*, 241–248. [CrossRef]
29. Birke, A.; Ling, J.; Barz, M. Polysarcosine-containing copolymers: Synthesis, characterization, self-assembly, and applications. *Prog. Polym. Sci.* **2018**, *81*, 163–208. [CrossRef]
30. Bleher, S.; Buck, J.; Muhl, C.; Sieber, S.; Barnert, S.; Witzigmann, D.; Huwyler, J.; Barz, M.; Süss, R. Poly(Sarcosine) Surface Modification Imparts Stealth-Like Properties to Liposomes. *Small* **2019**, *15*, e1904716. [CrossRef]
31. Maurer, P.H.; Subrahmanyam, D.; Katchalski, E.; Blout, E.R. Antigenicity of Polypeptides (Poly Alpha Amino Acids). *J. Immunol.* **1959**, *83*, 193–197. [CrossRef]
32. Fenaroli, F.; Repnik, U.; Xu, Y.; Johann, K.; van Herck, S.; Dey, P.; Skjeldal, F.M.; Frei, D.M.; Bagherifam, S.; Kocere, A.; et al. Enhanced Permeability and Retention-like Extravasation of Nanoparticles from the Vasculature into Tuberculosis Granulomas in Zebrafish and Mouse Models. *ACS Nano* **2018**, *12*, 8646–8661. [CrossRef] [PubMed]
33. Nogueira, S.S.; Schlegel, A.; Maxeiner, K.; Weber, B.; Barz, M.; Schroer, M.A.; Blanchet, C.E.; Svergun, D.I.; Ramishetti, S.; Peer, D.; et al. Polysarcosine-Functionalized Lipid Nanoparticles for Therapeutic mRNA Delivery. *ACS Appl. Nano Mater.* **2020**, *3*, 10634–10645. [CrossRef]
34. US Food and Drug Administration. Liposome Drug Products: Chemistry, Manufacturing, and Controls; Human Pharmacokinetics and Bioavailability; and Labeling Documentation. In *Guidance for Industry.(CDER)*; Food and Drug Administration: Rockville, MD, USA, 2018.
35. Ziller, A.; Nogueira, S.S.; Hühn, E.; Funari, S.S.; Brezesinski, G.; Hartmann, H.; Sahin, U.; Haas, H.; Langguth, P. Incorporation of mRNA in Lamellar Lipid Matrices for Parenteral Administration. *Mol. Pharm.* **2018**, *15*, 642–651. [CrossRef] [PubMed]
36. Siewert, C.; Haas, H.; Nawroth, T.; Ziller, A.; Nogueira, S.S.; Schroer, M.A.; Blanchet, C.E.; Svergun, D.I.; Radulescu, A.; Bates, F.; et al. Investigation of charge ratio variation in mRNA—DEAE-dextran polyplex delivery systems. *Biomaterials* **2019**, *192*, 612–620. [CrossRef]
37. Siewert, C.D.; Haas, H.; Cornet, V.; Nogueira, S.S.; Nawroth, T.; Uebbing, L.; Ziller, A.; Al-Gousous, J.; Radulescu, A.; Schroer, M.A.; et al. Hybrid Biopolymer and Lipid Nanoparticles with Improved Transfection Efficacy for mRNA. *Cells* **2020**, *9*, 2034. [CrossRef] [PubMed]
38. Felgner, P.L.; Gadek, T.R.; Holm, M.; Roman, R.; Chan, H.W.; Wenz, M.; Northrop, J.P.; Ringold, G.M.; Danielsen, M. Lipofection: A highly efficient, lipid-mediated DNA-transfection procedure. *Proc. Natl. Acad. Sci. USA* **1987**, *84*, 7413–7417. [CrossRef]
39. Muhl, C.; Conrad, M.; Unthan, D.; Barz, M. Synthesis and characterization of bisalkylated polysarcosine-based lipopolymers. *Eur. Polym. J.* **2019**, *120*, 109223. [CrossRef]
40. Kuhn, A.N.; Diken, M.; Kreiter, S.; Selmi, A.; Kowalska, J.; Jemielity, J.; Darzynkiewicz, E.; Huber, C.; Türeci, O.; Sahin, U. Phosphorothioate cap analogs increase stability and translational efficiency of RNA vaccines in immature dendritic cells and induce superior immune responses in vivo. *Gene Ther.* **2010**, *17*, 961–971. [CrossRef]
41. Karikó, K.; Muramatsu, H.; Welsh, F.A.; Ludwig, J.; Kato, H.; Akira, S.; Weissman, D. Incorporation of pseudouridine into mRNA yields superior nonimmunogenic vector with increased translational capacity and biological stability. *Mol. Ther.* **2008**, *16*, 1833–1840. [CrossRef]
42. Baiersdörfer, M.; Boros, G.; Muramatsu, H.; Mahiny, A.; Vlatkovic, I.; Sahin, U.; Karikó, K. A Facile Method for the Removal of dsRNA Contaminant from In Vitro-Transcribed mRNA. *Mol. Ther. Nucleic Acids* **2019**, *15*, 26–35. [CrossRef] [PubMed]
43. Leung, A.K.K.; Hafez, I.M.; Baoukina, S.; Belliveau, N.M.; Zhigaltsev, I.V.; Afshinmanesh, E.; Tieleman, D.P.; Hansen, C.L.; Hope, M.J.; Cullis, P.R. Lipid Nanoparticles Containing siRNA Synthesized by Microfluidic Mixing Exhibit an Electron-Dense Nanostructured Core. *J. Phys. Chem. C Nanomater. Interfaces* **2012**, *116*, 18440–18450. [CrossRef] [PubMed]
44. Heyes, J.; Palmer, L.; Bremner, K.; MacLachlan, I. Cationic lipid saturation influences intracellular delivery of encapsulated nucleic acids. *J. Control. Release* **2005**, *107*, 276–287. [CrossRef]
45. Romeis, B. *Taschenbuch der Mikroskopischen Technik*; De Gruyter: Berlin, Germany, 1943; ISBN 9783486764369.
46. Blanchet, C.E.; Spilotros, A.; Schwemmer, F.; Graewert, M.A.; Kikhney, A.; Jeffries, C.M.; Franke, D.; Mark, D.; Zengerle, R.; Cipriani, F.; et al. Versatile sample environments and automation for biological solution X-ray scattering experiments at the P12 beamline (PETRA III, DESY). *J. Appl. Crystallogr.* **2015**, *48*, 431–443. [CrossRef]
47. Manalastas-Cantos, K.; Konarev, P.V.; Hajizadeh, N.R.; Kikhney, A.G.; Petoukhov, M.V.; Molodenskiy, D.S.; Panjkovich, A.; Mertens, H.D.T.; Gruzinov, A.; Borges, C.; et al. ATSAS 3.0: Expanded functionality and new tools for small-angle scattering data analysis. *J. Appl. Crystallogr.* **2021**, *54*, 343–355. [CrossRef]
48. Franke, D.; Kikhney, A.G.; Svergun, D.I. Automated acquisition and analysis of small angle X-ray scattering data. *Nucl. Instrum. Methods Phys. Res. Sect. A Accel. Spectrometers Detect. Assoc. Equip.* **2012**, *689*, 52–59. [CrossRef]
49. Bragg, W.H.; Bragg William, L. The reflection of X-rays by crystals. *Proc. R. Soc. Lond. A* **1913**, *88*, 428–438. [CrossRef]
50. Goodby, J.W.; Tschierske, C.; Raynes, P.; Gleeson, H.; Kato, T.; Collings, P.J. (Eds.) *Handbook of Liquid Crystals*; Wiley-VCH Verlag GmbH & Co. KGaA: Weinheim, Germany, 2014; ISBN 9783527671403.
51. Ciccariello, S.; Goodisman, J.; Brumberger, H. On the Porod law. *J. Appl. Crystallogr.* **1988**, *21*, 117–128. [CrossRef]
52. Carrasco, M.J.; Alishetty, S.; Alameh, M.-G.; Said, H.; Wright, L.; Paige, M.; Soliman, O.; Weissman, D.; Cleveland, T.E.; Grishaev, A.; et al. Ionization and structural properties of mRNA lipid nanoparticles influence expression in intramuscular and intravascular administration. *Commun. Biol.* **2021**, *4*, 956. [CrossRef]

53. Belliveau, N.M.; Huft, J.; Lin, P.J.; Chen, S.; Leung, A.K.; Leaver, T.J.; Wild, A.W.; Lee, J.B.; Taylor, R.J.; Tam, Y.K.; et al. Microfluidic Synthesis of Highly Potent Limit-size Lipid Nanoparticles for In Vivo Delivery of siRNA. *Mol. Ther. Nucleic Acids* **2012**, *1*, e37. [CrossRef]
54. Yanez Arteta, M.; Kjellman, T.; Bartesaghi, S.; Wallin, S.; Wu, X.; Kvist, A.J.; Dabkowska, A.; Székely, N.; Radulescu, A.; Bergenholtz, J.; et al. Successful reprogramming of cellular protein production through mRNA delivered by functionalized lipid nanoparticles. *Proc. Natl. Acad. Sci. USA* **2018**, *115*, E3351–E3360. [CrossRef] [PubMed]
55. Bale, H.D.; Schmidt, P.W. Small-Angle X-Ray-Scattering Investigation of Submicroscopic Porosity with Fractal Properties. *Phys. Rev. Lett.* **1984**, *53*, 596–599. [CrossRef]
56. Teixeira, J. Small-angle scattering by fractal systems. *J. Appl. Crystallogr.* **1988**, *21*, 781–785. [CrossRef]
57. Evers, M.J.W.; Kulkarni, J.A.; van der Meel, R.; Cullis, P.R.; Vader, P.; Schiffelers, R.M. State-of-the-Art Design and Rapid-Mixing Production Techniques of Lipid Nanoparticles for Nucleic Acid Delivery. *Small Methods* **2018**, *2*, 1700375. [CrossRef]
58. Wan, C.; Allen, T.M.; Cullis, P.R. Lipid nanoparticle delivery systems for siRNA-based therapeutics. *Drug Deliv. Transl. Res.* **2014**, *4*, 74–83. [CrossRef]
59. Ramishetti, S.; Kedmi, R.; Goldsmith, M.; Leonard, F.; Sprague, A.G.; Godin, B.; Gozin, M.; Cullis, P.R.; Dykxhoorn, D.M.; Peer, D. Systemic Gene Silencing in Primary T Lymphocytes Using Targeted Lipid Nanoparticles. *ACS Nano* **2015**, *9*, 6706–6716. [CrossRef]
60. Kozma, G.T.; Shimizu, T.; Ishida, T.; Szebeni, J. Anti-PEG antibodies: Properties, formation, testing and role in adverse immune reactions to PEGylated nano-biopharmaceuticals. *Adv. Drug Deliv. Rev.* **2020**, *154–155*, 163–175. [CrossRef]
61. Ju, Y.; Lee, W.S.; Pilkington, E.H.; Kelly, H.G.; Li, S.; Selva, K.J.; Wragg, K.M.; Subbarao, K.; Nguyen, T.H.O.; Rowntree, L.C.; et al. Anti-PEG Antibodies Boosted in Humans by SARS-CoV-2 Lipid Nanoparticle mRNA Vaccine. *ACS Nano* **2022**, *16*, 11769–11780. [CrossRef] [PubMed]
62. Weber, B.; Seidl, C.; Schwiertz, D.; Scherer, M.; Bleher, S.; Süss, R.; Barz, M. Polysarcosine-Based Lipids: From Lipopolypeptoid Micelles to Stealth-Like Lipids in Langmuir Blodgett Monolayers. *Polymers* **2016**, *8*, 427. [CrossRef]
63. Son, K.; Ueda, M.; Taguchi, K.; Maruyama, T.; Takeoka, S.; Ito, Y. Evasion of the accelerated blood clearance phenomenon by polysarcosine coating of liposomes. *J. Control. Release* **2020**, *322*, 209–216. [CrossRef]
64. Barz, M.; Weber, B.; Haas, H.; Heller, P.; Nogueira, S.; Schlegel, A. RNA Particles Comprising Polysarcosine. WO2020069718A1, 1 October 2018.
65. Patel, S.; Ashwanikumar, N.; Robinson, E.; Xia, Y.; Mihai, C.; Griffith, J.P.; Hou, S.; Esposito, A.A.; Ketova, T.; Welsher, K.; et al. Naturally-occurring cholesterol analogues in lipid nanoparticles induce polymorphic shape and enhance intracellular delivery of mRNA. *Nat. Commun.* **2020**, *11*, 983. [CrossRef] [PubMed]
66. Sebastiani, F.; Yanez Arteta, M.; Lerche, M.; Porcar, L.; Lang, C.; Bragg, R.A.; Elmore, C.S.; Krishnamurthy, V.R.; Russell, R.A.; Darwish, T.; et al. Apolipoprotein E Binding Drives Structural and Compositional Rearrangement of mRNA-Containing Lipid Nanoparticles. *ACS Nano* **2021**, *15*, 6709–6722. [CrossRef] [PubMed]

4.1.3 **Supporting Information**

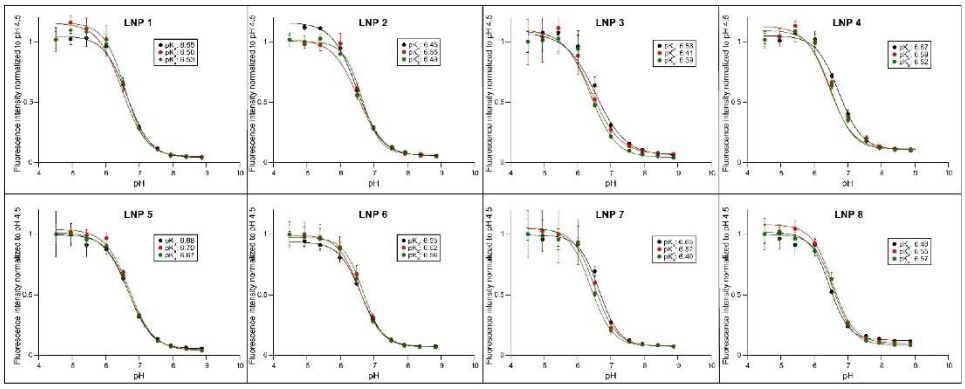

Figure S1: Fluorescence-based assay for apparent pK_a determination. Fluorescence intensity was normalized against the intensity measured at pH 4.5 reflecting a fully protonated state of the ionizable lipid. Boltzmann fitting was utilized to determine the inflection point of each measurement. Data are presented as mean ± S.D.

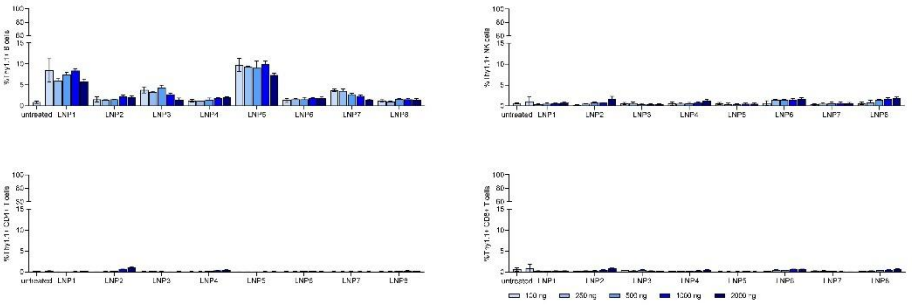

Figure S2. *In vitro* Thy1.1 expression in hPBMC sub-populations. Dose-range from 100 ng to 2000 ng. Transfection efficiency of LNP1-8 is shown in each sub-population. (**A**) %Thy1.1+ B cells, (**B**) %Thy1.1+ NK cells, (**C**) %Thy1.1 CD4+ T cells, (**D**) %Thy1.1+ CD8+ T cells. Data are presented as mean ± S.D., n= 3 technical replicates per LNP formulation.

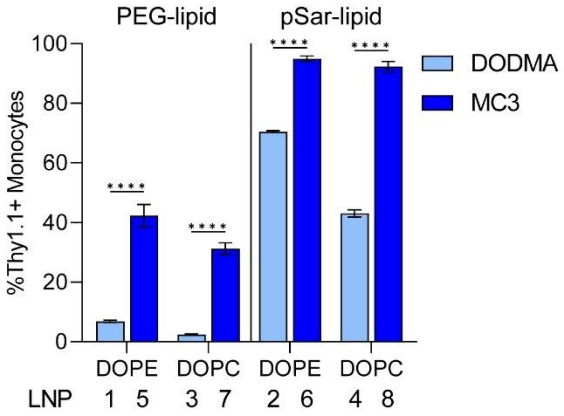

Figure S3. *In vitro* transfection efficiency of all DODMA-LNPs versus MC3-LNPs at a dose of 1000 ng. Transfection efficiency is shown as %Thy1.1+ Monocytes. Data are presented as mean ± S.D., analyzed by a two-way ANOVA with Šidák's multiple comparison test, ****P < 0.0001, n= 3 technical replicates per LNP formulation.

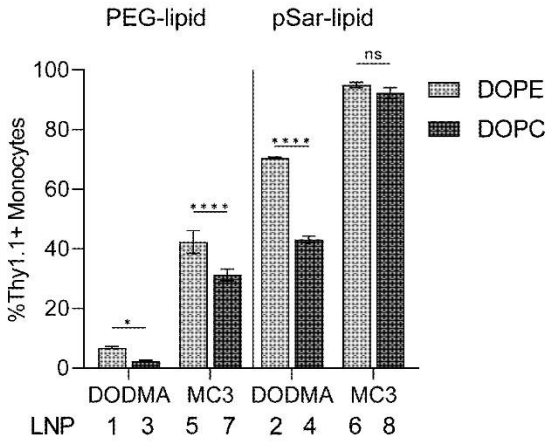

Figure S4. *In vitro* transfection efficiency of all DOPE-LNPs versus DOPC-LNPs at a dose of 1000 ng. Transfection efficiency is shown as %Thy1.1+ Monocytes. Data are presented as mean ± S.D., analyzed by a two-way ANOVA with Šidák's multiple comparison test, *P 0.0258, ****P < 0.0001, n= 3 technical replicates per LNP formulation.

Table S1. Results of peak fitting using Lorentzian function

	Manufacturing buffer						phosphate buffer pH 4.5					
Formulation	area (a.u.)	σ	peak position (nm^{-1})	σ	width (nm^{-1})	σ	area (a.u.)	σ	Peak position (nm^{-1})	σ	width (nm^{-1})	Σ
LNP1	784.6	47.16	1.050	0.001	0.291	0.011	629.5	16.87	1.065	0.001	0.274	0.006
LNP2	756.5	83.51	1.034	0.002	0.435	0.029	571.6	15.02	1.064	0.001	0.286	0.006
LNP3	685.4	46.27	0.965	0.001	0.337	0.014	638.6	17.37	1.012	0.001	0.343	0.008
LNP4	744.2	55.95	0.950	0.003	0.445	0.021	655.6	20.51	1.002	0.002	0.346	0.009
LNP5	591.5	23.83	1.129	0.001	0.282	0.008	480.7	14.27	1.225	0.001	0.234	0.005
LNP6	566.9	17.13	1.083	0.001	0.273	0.006	452.9	11.08	1.215	0.001	0.225	0.005
LNP7	495.5	28.01	1.120	0.002	0.277	0.011	518.2	6.21	1.166	0.001	0.199	0.002
LNP8	452.6	19.94	1.079	0.001	0.272	0.009	498.5	9.41	1.170	0.001	0.198	0.003

4.2 On the Influence of Fabrication Methods and Materials for mRNA-LNP Production: From Size and Morphology to Internal Structure and mRNA Delivery Performance In Vitro and In Vivo

4.2.1 Summary and Contributions

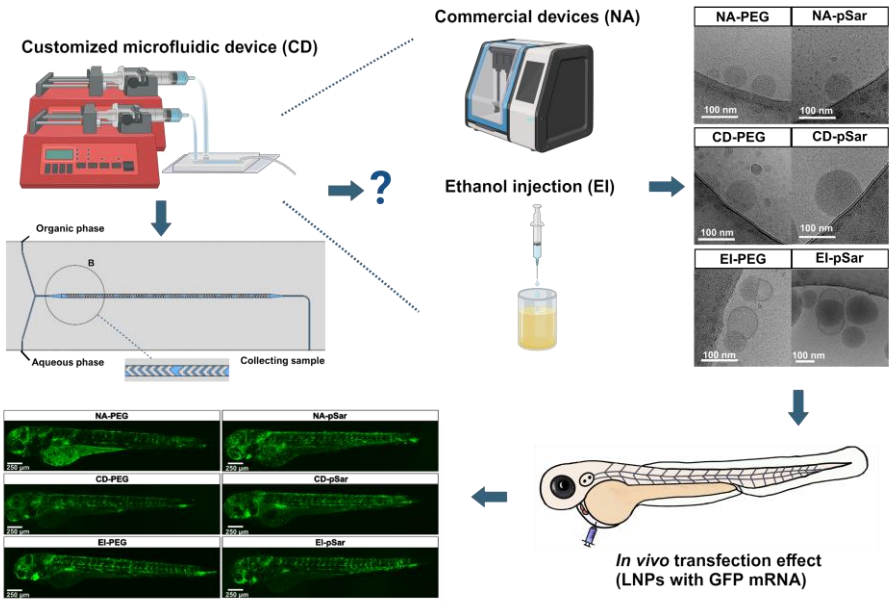

Figure 4.2-1. Graphical abstract of the publication 4.2. A novel microfluidic process (CD) was tested against two established manufacturing methods (NA and EI) by investigating structure and morphology along with biological performance *in vitro* and *in vivo* using a zebrafish embryo model. As published in [88].

Microfluidic approaches to ethanol injection methods are the gold standard for producing mRNA LNPs, ranging from lab scale to batch production for clinical studies and marketed products. Using standardized production methods is crucial to ensure the manufacturing of reproducible batches with consistent quality and efficacy of the drug product. Besides commercially available microfluidic platforms, such as the NanoAssemblr®, various customized chaotic mixing systems are available, all of which lead to nanoparticles with comparable sizes. In this work, we employed physicochemical characterization tools to elucidate the effects of various ethanol injection approaches and stealth moieties on the structure and morphology of LNPs. Ultimately, we conducted various *in vitro* and *in vivo* potency experiments to investigate the impact of structure on transfection performance. Gaining insight into the influence of these properties on structure and function can also help define quality target product profiles, which can be utilized during upscaling processes or product development using Quality-by-Design approaches.

In the first part of the work, a customized microfluidic mixing device was designed based on a staggered herringbone micromixer, and the optimal mixing properties, defined by the total flow rate and the flow rate ratio between the aqueous and ethanolic phases, were explored. LNPs produced with this customized device (CD) were compared with LNPs manufactured using a manual ethanol injection (EI) approach and a commercial microfluidic platform, NanoAssemblr® (NA). Physicochemical investigations were performed, including cryo-EM and SAXS measurements, to elucidate structural aspects of the respective LNPs. While the microfluidic approaches produced LNPs with similar sizes, the manual approach resulted in significantly larger particles. Furthermore, in cryo-EM, the manual produced LNPs exhibited lipidic bleb substructures, which were not visible for the other two manufacturing methods. Despite being similar in size, in-depth analysis revealed discrete differences between the two microfluidically produced LNPs in their internal organization, with CD-derived LNPs exhibiting a higher packing density and greater surface fractality than NA-LNPs. Additionally, using pSar-lipids instead of PEGylated lipids resulted in increased surface roughness, regardless of the production approach employed.

In vitro experiments using adherent HepG2 cells and suspended Jurkat T cells revealed cell-type-dependent differences in transfection efficacy, with larger particles being more effective in HepG2 cells, while smaller particles, particularly when grafted with pSar, were more efficient in Jurkat T cells. *In vivo* biodistribution and transfection studies utilizing a zebrafish embryo model showed higher aggregation levels in circulation for manually produced particles, which can be attributed to their larger size and higher inhomogeneity. Nevertheless, the transfection levels were comparable to those of the other two manufacturing methods.

Our work highlights the influence of the manufacturing procedure for mRNA LNPs and how particles with similar sizes and morphologies, as detected by DLS and cryo-EM, can still differ in their internal organization. Mixing speed and mixing channel geometry highly influence physicochemical properties, but this can still yield comparable transfection potential. Therefore, gaining more insights into how structure ultimately influences the *in vivo* distribution and potency is of crucial interest for improving existing delivery platforms.

This work was published in the following article:

Dongdong Bi‡, Christoph Wilhelmy‡, Dennis Unthan *et al.* On the Influence of Fabrication Methods and Materials for mRNA-LNP Production: From Size and Morphology to Internal Structure and mRNA Delivery Performance In Vitro and In Vivo. *Adv. Healthcare Mater.* 2024, 13, 2401252. doi: 10.1002/adhm.202401252

‡ These authors contributed equally to this work.

Own contributions:

Authorship: First author

Data curation, Formal Analysis, Investigation, methodology

Writing: Original draft, visualization, review and editing

Contributions of all authors:

Conceptualization: P.L., M.B., H.Z.

Data curation: D.B., C.W., H.Z.

Formal analysis: D.B., C.W., H.Z.

Funding acquisition: M.D., P.L., M.B.

Investigation: D.B., C.W., D.U., I.S.K., B.Z, B.K, R.I.K., M.A.G., R.Z, T.H, M.D, H.H

Methodology: H.Z., D.B., C.W., B.W., J.B

Project administration: P.L., M.B., H.Z

Resources: P.L.; M.B.

Supervision: P.L., M.B., H.Z

Visualization: D.B., C.W., H.Z.

Writing – original draft: D.B., C.W., H.Z.

Writing – review & editing H.Z, M.B, P.L.

4.2.2 Publication

RESEARCH ARTICLE

ADVANCED HEALTHCARE MATERIALS
www.advhealthmat.de

On the Influence of Fabrication Methods and Materials for mRNA-LNP Production: From Size and Morphology to Internal Structure and mRNA Delivery Performance In Vitro and In Vivo

Dongdong Bi, Christoph Wilhelmy, Dennis Unthan, Isabell Sofia Keil, Bonan Zhao, Bastian Kolb, Roman I. Koning, Melissa A. Graewert, Bert Wouters, Raphaël Zwier, Jeroen Bussmann, Thomas Hankemeier, Mustafa Diken, Heinrich Haas, Peter Langguth, Matthias Barz,* and Heyang Zhang**

Lipid nanoparticle (LNP) remains the most advanced platform for messenger RNA (mRNA) delivery. To date, mRNA LNPs synthesis is mostly performed by mixing lipids and mRNA with microfluidics. In this study, a cost-effective microfluidic setup for synthesizing mRNA LNPs is developed. It allows to fine-tune the LNPs characteristics without compromising LNP properties. It is compared with a commercial device (NanoAssemblr) and ethanol injection and the influence of manufacturing conditions on the performance of mRNA LNPs is investigated. LNPs prepared by ethanol injection exhibit broader size distributions and more inhomogeneous internal structure (e.g., bleb-like substructures), while other LNPs show uniform structure with dense cores. Small angel X-ray scattering (SAXS) data indicate a tighter interaction between mRNA and lipids within LNPs synthesized by custom device, compared to LNPs produced by NanoAssemblr. Interestingly, the better transfection efficiency of polysarcosine (pSar)-modified LNPs correlates with a higher surface roughness than that of PEGylated ones. The manufacturing approach, however, shows modest influence on mRNA expression in vivo. In summary, the home-developed cost-effective microfluidic device can synthesize LNPs and represents a potent alternative to NanoAssemblr. The preparation methods show notable effect on LNPs' structure but a minor influence on mRNA delivery in vitro and in vivo.

1. Introduction

Messenger ribonucleic acid (mRNA) technologies have emerged as an innovative and efficient approach for the development of new drugs with a wide range of applications, such as regenerative medicine, cancer treatment, gene editing, and vaccine development.[1] As exemplified by FDA approval of delivering small interfering RNA (siRNA, Onpattro) and antigen mRNA (Comirnaty, Spikevax) drugs, lipid nanoparticles (LNPs) are so far among the most clinically advanced platforms. State-of-the-art LNPs are the assembled nanoparticles composed of four lipid components, namely (ionizable) cationic lipid (e.g., Dlin-MC3-DMA, ALC-0315, SM-102), phospholipid (e.g., DSPC, DOPE), cholesterol, polyethylene glycol (PEG)-lipid (e.g., DMG-PEG2k, ALC-0159).[2] An increasing number of studies have shown that the functional delivery of mRNA by an LNP greatly depends on the inclusion of mRNA into the lipid matrix. Libraries of chemically

D. Bi, D. Unthan, B. Zhao, B. Wouters, J. Bussmann, T. Hankemeier, M. Barz, H. Zhang
Leiden Academic Centre for Drug Research (LACDR)
Leiden University
Einsteinweg 55, Leiden 2333 CC, The Netherlands
E-mail: m.barz@lacdr.leidenuniv.nl; h.zhang@lacdr.leidenuniv.nl

The ORCID identification number(s) for the author(s) of this article can be found under https://doi.org/10.1002/adhm.202401252

DOI: 10.1002/adhm.202401252

C. Wilhelmy, B. Kolb, H. Haas, P. Langguth
Department of Biopharmaceutics and Pharmaceutical Technology
Johannes Gutenberg University Mainz
55128 Mainz, Germany
E-mail: langguth@uni-mainz.de

I. S. Keil, M. Diken
TRON-Translational Oncology at the University Medical Center of Johannes Gutenberg University GmbH
55131 Mainz, Germany

R. I. Koning
Electron Microscopy Facility
Department of Cell and Chemical Biology
Leiden University Medical Center
Leiden 2300 RC, The Netherlands

distinct lipids, therefore, have been created to achieve more efficient, specific, and safe mRNA delivery. The advent of novel synthetic, particularly ionizable lipids has accelerated the clinical translation of RNA drugs.[3] In addition, novel shielding lipids, including PEG-lipid alternative, are important for the future success of RNA drugs.[4,5] In this respect, polysarcosine (pSar)-lipids, have been developed.[6] As a polymer, pSar is based on the endogenous amino acid sarcosine (methyl glycine), and can be synthesized by controlled living ring-opening polymerization of the corresponding *N*-carboxyanhydride, possessing comparable main chain flexibility and solubility in buffer.[7] Most importantly, pSar displayed PEG-like properties (e.g., stealth-like properties in vivo) and enables the synthesis of nanoparticles without detectable protein corona.[8–16] We have reported the monoalkyl pSar-lipids and bisalkyl pSar-lipids.[17,18] These pSar-lipids have been applied to lipid formulations, with substantially reduced immunogenicity, cytokine levels, or complement activation of such nanoparticles compared with PEGylated nanoparticles.[6,19–22] Notably, the synthesis of pSar-modified nanoparticles can be performed by the same techniques known for established stealth lipids.[23,24] Therefore, such pSar-lipids are one of the most promising alternatives to established polymer-lipid conjugates.

It is well-established that characteristics of mRNA LNPs, such as lipid composition, size, surface charge, and stability, play a vital role in biodistribution and therapeutic potency, and thus can be optimized to achieve organ or cell-specific delivery and maximal efficacy.[25] Production techniques, ideally featuring low cost, ease of use, small sample size, precise control, high reproducibility, and fast preparation, are therefore required. Microfluidics are a robust, scalable, and reproducible approach to generate LNPs by assembling lipids and mRNA payload into nanoparticles by on-chip technologies. By fine-tuning the process parameters of mixing organic and aqueous phases, LNPs with precisely defined properties can be reproducibly and efficiently synthesized. Of note, microfluidics can produce LNPs on laboratory as well as on industrial scale.[26] With those advantages over traditional lipid-film hydration, microfluidics have emerged as a gold standard for preclinical LNPs production.[27]

Within the microfluidic device, LNPs form at the aqueous-to-ethanol interface by diffusion-based ethanol dilution. When lipid-dissolving ethanol is rapidly diluted with RNA-containing buffer to a critical ethanol concentration, small and homogeneous LNPs form at the liquid–liquid interface.[27] In addition to the flow rate condition, the geometry of the micromixer including the mixing cycles and dimension of the channel greatly influences the size of LNPs and their stability.[28,29] To precisely control the physical properties of LNPs (e.g., size, morphology, structure), various micromixer systems have been constructed and evaluated, such as T-, Y-shaped, chaotic, and baffle mixers. For example, NanoAssemblr has been extensively used to produce RNA LNPs (20–200 nm). The NanoAssemblr Benchtop cartridge employs a chaotic mixer with a staggered herringbone that induces homogeneous mixing in the microchannel by chaotic convection and thus increases the size controllability of LNPs compared to T- or Y-shaped micromixers at ambient flow rates. Such a chaotic mixer structure, however, is preferable for mixing solutions at low flow rates as the mixing performance is reduced under high-flow-rate conditions.[30] Recently, the NanoAssemblr Ignite system with a planar asymmetric split-and-recombine micromixer and a toroidal mixer has been released.[31] By using the Dean vortex, this new microchannel structure is suitable for high-flow-rate conditions, thus reaching scalability without the parallelization of multiple chips. Very interestingly, iLiNP, a microfluidic device with a simple baffle structure and microchannel fluid dynamics relative to the chaotic mixer, has been reported to precisely produce LNPs with a 10 nm size distribution.[32] A layered flow of ethanol and buffer solution is maintained in the microchannel, and ethanol is rapidly diluted by secondary flow at the baffle structures. The iLiNP device shows preferable ethanol dilution performance at high-flow rates.[33,34] The development of novel microfluidic mixing devices may offer enhanced versatility and affordability for small-scale development of nanoparticles with tailored properties. Nevertheless, it is unclear to which extent the microfluidic production method influences the final performance of mRNA LNPs. Since the development of microfluidics for RNA LNPs formulation is in its relative infancy, far less is known about the correlation between the internal structure of mRNA LNPs and their physicochemical properties and biological performance.

In this present study, we developed and optimized a microfluidic device for synthesizing mRNA LNPs with different shielding lipopolymers. The microfluidic chamber is based on the chaotic mixer, which is cost-effective and can be reused more than 40 times. Its performance was evaluated by comparing the mRNA LNPs prepared by the commercially available NanoAssemblr and the traditional ethanol injection, in terms of size, size distribution, surface charge, morphology, internal structure, storage stability, in vitro transgene expression, as well as biodistribution and protein production in zebrafish embryos after intravenous injection.

2. Experimental Section

2.1. Materials

1,2-Dioleoyl-*sn*-glycero-3-phosphorylethanolamine (DOPE) and methoxypolyethylengly-coloxy(2000)-*N*,*N*-ditetradecylacetamide (ALC-0159) were purchased from Avanti Polar Lipids (Alabaster, AL). Ionizable lipid heptratriaconta-6,9,28,31-tetraen-19-yl-4-(dimethylamino)butanoate (DLin-MC3-DMA) was bought from MedChemExpress (Monmouth Junction, NJ). Cholesterol was ordered from Merck (Darmstadt, Germany). BA_{C14}-$pSar_{36}$-Azide (pSar) was synthesized in the Barz Lab as previously described (Leiden, The Netherlands).[24] All lipid stocks were stored at −20 °C in lyophilized form or dissolved in ethanol. Milli-Q water

M. A. Graewert
European Molecular Biology Laboratory (EMBL) Hamburg Outstation
c/o DESY
22607 Hamburg, Germany
R. Zwier
Leiden Institute of Physics Research
Leiden University
Einsteinweg 55, Leiden 2333 CC, The Netherlands
M. Barz
Department of Dermatology
University Medical Center of the Johannes Gutenberg University Mainz
Langenbeckstraße 1, 55131 Mainz, Germany

was prepared using a MILLI-Q Reference A^+ system. Water was used at a resistivity of 18.2 MΩ cm^{-1} and total organic carbon < 5 ppm. CleanCap enhanced green fluorescent protein (EGFP) mRNA was bought from Tebubio (Heerhugowaard, The Netherlands). Cy5-labeled luciferase mRNA was provided by TRON/Biontech SE (Mainz, Germany). The Quant-it RiboGreen RNA Assay Kit was ordered from Thermo Fisher Scientific (Bleiswijk, The Netherlands). Borosilicate glass microneedles with filament was bought from Sutter Instruments (BF100-78-10, USA). HEPES, chloroform, tricaine, agarose, Tris-base, ethylenediaminetetraacetic acid (EDTA), and D-(+)-glucose were purchased from Sigma-Aldrich (Zwijndrecht, The Netherlands). Bovine serum albumin, trypsin/EDTA, and Dulbecco's Modified Eagle's Medium/F12 (DMEM/F12) were purchased from Thermo Fisher Scientific (Bleiswijk, The Netherlands). RPMI1640, L-glutamine, PEN-STREP (10 000 U mL^{-1} penicillin, 10 000 U mL^{-1} streptomycin), and DPBS (without Ca^{2+} or Mg^{2+}) were bought from Lonza Bioscience (Verviers, Belgium). Fetal bovine serum was purchased from SERANA (Brandenburg, Germany). The other reagents and solvents were purchased from Sigma Aldrich (Zwijndrecht, The Netherlands).

2.2. Methods

2.2.1. Preparation of mRNA LNPs

Lipid stock solutions containing DLin-MC3-DMA, DOPE, cholesterol, and stealth lipid (ALC-0159 or pSar) at a molar ratio of 40/10/48/2 were mixed in ethanol at a total lipid concentration of 15 mM. In the preparation of LNPs, the lipid concentration was diluted to 3.75 mM and the final mRNA LNPs formulation was concentrated to 15 mM (5500 g, 10 min). The mRNA stock solution (0.133 mg mL^{-1}) was diluted with citrate buffer (50 mM, pH 5). Lipids and mRNA were mixed using different techniques at N/P ratio 5. To visualize the distribution of mRNA LNPs, Cy5-labeled luciferase mRNA and EGFP encoding mRNA were mixed at a w/w ratio of 1:3 before being loaded into LNPs. LNPs were prepared using the NanoAssembl Ignite platform (NanoAssemblr), Precision Nano-Systems Inc., Vancouver, BC, Canada), customized microfluidic device, and ethanol injection as described below.

mRNA LNPs Prepared by NanoAssemblr: Briefly, the lipids mixture was combined with an acidic buffer of 50 mM sodium citrate (pH 5.0) containing mRNA at a flow rate ratio of 1:3 (3 and 9 mL min^{-1}, respectively) using NanoAssemblr Ignite instrument with NxGen cartridges (Precision Nanosystems, Vancouver, BC, Canada).

mRNA LNPs Prepared by Customized Microfluidic Device: Lipids mixture in ethanol and mRNA in citrate buffer (50 mM, pH 5.0) were loaded into 500 µL and 1 mL Hamilton syringes (Giarmata, Timis County, Romania), respectively, and mixed within a customized microfluidic chamber under defined flow rate conditions.

mRNA LNPs Prepared by Ethanol Injection: LNP formulations were prepared using the previously reported ethanol injection method.[22] In brief, the mRNA/aqueous was pipetted onto the lipid/ethanol, followed by an immediate vortex for 10 s.

All formulations were dialyzed against DPBS (1 x, pH 7.4) overnight in Pur-A-Lyzer 12–14 kDa dialysis cassettes (Sigma-Aldrich, Zwijndrecht, The Netherlands) overnight at 4 °C. Afterward, the formulations were concentrated using Amicon Ultra 100 K Centrifuge Filter (Merck KGaA, Darmstadt, Germany) and centrifuged at 5 500 g for 10 min at 4 °C before use.

2.2.2. Characterization of mRNA LNPs

Dynamic Light Scattering (DLS): The Zetasizer Ultra (Malvern, Worcestershire, UK) was employed to determine the hydrodynamic diameter (intensity distribution) and ζ potential of mRNA LNPs. This analysis was conducted in HEPES buffer (10 mM, pH 7.4) at a final total lipid concentration of 100 µM. The encapsulation efficiency of LNPs was tested by Quant-it RiboGreen RNA Assay Kit following the manufacturing protocol.

Cryogenic Electron Microscopy (cryoEM): Electron microscopy support grids (R2/2, Quantifoil, Germany) were glow discharged in air at 0.2 mbar, 25 mA, and 30 s, using a Pelco Easiglow. Onto the glow discharged grids, 3 µL of sample was placed and subsequently blotted away for 3 s using filter paper (Whatman no.4) at 85%–95% humidity using a Leica EM GP. The grid was directly plunged into liquid-ethane/propane (1:2) kept at −196 °C. Grids were clipped into autogrids, placed into a cassette, and transferred into a Talos Arctica cryo-electron microscope (Thermo Fisher Scientific). Images were recorded using EPU software (Thermo Fisher Scientific) in multigrid mode with a K3 direct electron detector (Gatan) in counting mode and ZLP imaging. Images were recorded in movie mode at a magnification of 15 000 x (corresponding to a pixel size of 0.55 nm at specimen level), a defocus of −5 µm, and an electron dose of ≈4 e/A2/s with 8 s exposure time (corresponding to a total dose of 35 e/A2). Using this magnification/pixel size and electron dose the full 2 µm hole is visible in one image the vesicle bilayer (at 4 nm) can be discerned. Movies were aligned using MotionCorr2 and converted to tiff using EMAN2.[35]

Small Angle X-Ray Scattering: SAXS data were collected at the P12 BioSAXS beamline of the European Molecular Biology Laboratory (EMBL) at the PETRAIII synchrotron, DESY Hamburg (Germany).[36] The measurements were performed at an X-ray energy of 10 keV (wavelength 0.124 nm) and a sample-detector distance of 6 m (q-range 0.01–2.20 nm^{-1}). Utilizing the BioSAXS sample changer, 30 µL of the sample was transferred to a quartz capillary mounted in vacuum.[37] 2D scattering patterns were collected by a Pilatus 6 M detector with an exposure time of 0.095 s. For raw data processing, SASFLOW and ATSAS software (EMBL Hamburg, Hamburg, Germany) were used.[36,38,39] Averaged data were transferred to QTIPlot 1.0.1 software (IONDEV, Bucuresti, Romania) for further data analysis. For buffer subtraction same procedure was executed with DPBS buffer (1 x, pH 7.4, without Ca^{2+} or Mg^{2+}) as a sample. The scattering profile of the buffer was subtracted from the respective sample profiles after proper scaling.

All data are given as scattering internsity $I(q)$ presented as a function of the momentum transfer calculated according to Equation (1)

$$q = \frac{4\pi}{\lambda} \sin(\theta) \quad (1)$$

where λ is the X-ray wavelength and 2 Θ is the scattering angle. The correlation of extrapolated scattering intensity at $q = 0$ I_0, which is a measure for the total scattering intensity, and the particle volume V is described in Equation (2), where n is the number density of particles and $\Delta\rho$ is the contrast of the scattering material[40]

$$I_0 = n \cdot V^2 \cdot (\Delta\rho)^2 \tag{2}$$

SAXS data for the investigated q-range include the form factor of the single nanoparticles, which is determined by overall size, shape and surface of the LNPs, as well as Bragg reflections derived from mRNA-lipid interactions within the LNPs.

For investigation of overall particle size, Guinier plots were used according to Equation (2), to obtain the radius of gyration R_g[41]

$$\ln I(q) = \ln I_0 - \frac{R_g^2}{3} q^2 \tag{3}$$

For spherical particles the average radius can be calculated from the R_g by

$$r = \sqrt{\frac{5}{3}}\, R_g \tag{4}$$

Additional information can be revealed by analyzing the intensity decay of the whole SAXS profile using the power law as shown in the equation below, which gives information about fractal dimensionality and the packing compactness of the particles

$$I(q) = I_0 \cdot q^{-x} \tag{5}$$

For particles with smooth surfaces, a decay indicated by the so-called Porod exponent x with values between 3 and 4 can be observed, while slopes with lower decay in the range of 2–3 is observed for particles with surface fractals.[42]

For investigation of internal structure properties, Lorentzian fit functionality was used for peak fitting of the Bragg refelctions in each SAXS pattern, as given in

$$\mathrm{I}(q) = I_0 + \frac{2A}{\pi} \cdot \frac{\mathrm{w}}{4 \cdot (q - q_c)^2 + w^2} \tag{6}$$

With I_0 being the baseline intensity, A the peak area, w the peak width (FWHM), and q_c the center position of the peak. The peak position can be used to calculate the repeat distance of the scattering moiety (so called d-spacing) for lamellar systems using the Bragg equation[43]

$$d = \frac{2\pi}{q_c} \tag{7}$$

Additional conclusions can be gained from the peak width w, which gives information about the correlation length inside the ordered arrays. Here, the correlation length scales reciprocally with the peak width, meaning that a narrow peak is an indicator for a long correlation length. A generally accepted model for liquid crystalline structures describes the correlation length ξ, which is defined as the distance at which the positional correlation decays to the value 1/e[44]

$$\xi = \frac{2}{\mathrm{w}} \tag{8}$$

Multiangle DLS Analysis: Cylindrical quartz cuvettes (Hellma, Muhlheim, Germany) were meticulously cleaned using dust-free distilled acetone and placed within a dust-free flow box. Solutions were filtered into the cuvettes through Millex-GV filters with a pore size of 0.22 µm. DLS measurements were conducted at 20 °C using a Uniphase He/Ne Laser (22.5 mW output power at λ = 632.8 nm) and an ALV/CGS-8F SLS/DLS 5022F goniometer with eight simultaneously operating ALV 7004 correlators and eight ALV/High QEAPD avalanche photodiode detectors. Multiangle DLS measurements were analyzed by using ALVStat 4.31 software (ALV, Germany) under 26°, 58°, 90°, and 122°.

2.2.3. In Vitro and In Vivo Biological Performance of mRNA LNPs

Cell Culture: HepG2 cells were cultured in DMEM/F12 with 10% Fetal Bovine Serum (FBS), 2 mM L-glutamine, and 100 µg mL^{-1} penicillin/streptomycin at 37 °C, 5.0% CO_2. Cells with 80%–90% confluency were detached from the bottom of the flask with 0.25% trypsin/EDTA. Jurkat T cells were cultured in RPMI1640 medium supplemented with 10% FBS, 100 µg mL^{-1} penicillin/streptomycin and 2 mM L-glutamine, and maintained in a humidified atmosphere of 37 °C, 5.0% CO_2. The culture medium was renewed every 2–4 days. For all in vitro tests, HepG2 cells were seeded in 96-well F-bottom plates (Greiner Bio-one, Alphen aan den Rijn, The Netherlands) at a density of 15 000 cells per well. Jurkat T cells were seeded in 96-well U-bottom plates (Greiner Bio-one, Alphen aan den Rijn, The Netherlands) at a density of 40 000 cells per well. Cells were incubated at 37 °C, 5.0% CO_2 one day before treatment.

2.2.4. In Vitro Transfection

LNPs containing EGFP mRNA were utilized to study the protein expression in HepG2 cells and Jurkat T cells, respectively. In each well, 20 µL mRNA LNPs (containing 0.2 µg EGFP mRNA) was transferred to the cells cultured in fresh culture medium with a final volume of 200 µL. After 24 h incubation at 37 °C, 5.0% CO_2, HepG2 cells were rinsed with DPBS twice, trypsinized and collected by centrifugation at 500 g for 5 min, while Jurkat T cell pellet was harvested after washing with DPBS twice and subsequent centrifugation at 500 g, 5 min. 200 µL flow buffer (1% bovine serum albumin, 0.1% NaN_3, in DPBS) was added to each well to resuspend cell pellets for measurements by flow cytometry (Cytoflex, Beckman Colter, Woerden, The Netherlands), to quantify protein expression.

2.2.5. Zebrafish Husbandry and Strains

Zebrafish (Danio rerio) were used for studies in compliance with the regulations and norms for animal care set forth by the

European Convention for the Protection of Vertebrate Animals (ECPVA) and the local animal welfare council of Leiden University. Fertilized eggs were collected and raised at 28 °C in egg water (60 µg mL^{-1} Instant Ocean sea salts) and embryos were anesthetized and embedded in 0.4% agarose (with 0.01% tricaine) in egg water before microinjection.

2.2.6. Zebrafish Injection and Imaging

A micropipette puller (P-97, Sutter Instruments) was utilized to prepare needles using borosilicate capillaries with filaments. To visualize the biodistribution and protein production of mRNA LNPs, 20 ABTL (wild-type) zebrafish embryos (2.5 dpf) were embedded in 0.4% agarose gel containing tricaine and injected with 2 nL LNPs containing 75 pg EGFP mRNA and 25 pg Cy5 luciferase mRNA using an Eppendorf Femtojet pump. Embryos that had been successfully injected were then taken out of the agarose and cultured at 28 °C. Embryos were re-embedded in confocal dishes and photographed using Leica TCS SP8 confocal microscopy at 3 h postinjection (hpi). A 40 x water immersion objective (HCX APO L) and a 10 x air objective (HCX PL FLUOTAR) were used to take Z-stack images. All stacks and sessions used the same laser intensity, gain, and offset settings. Regarding the quantification, the whole-body images of six ABTL embryos were taken using a 10 x air objective to quantify the transfection effect of mRNA LNPs. The Fiji Image J (1.53 t, Java 1.8.0_322) was used to process the images and the mean fluorescent intensity of EGFP in each embryo was quantified. Mean gray values were recorded under the threshold from 15 to 255.

2.2.7. Statistical Analysis

To evaluate statistical differences between experimental groups in this study multiple *t*-test was performed in DLS data and two-way ANOVA was performed in GraphPad Prism 9 for in vitro test. Values of $p < 0.05$ were considered statistically significant, and asterisks indicate statistical significance: $*p < 0.05$; $**p < 0.01$; $***p < 0.001$, $****p < 0.0001$. Two-way ANOVA followed by Tukey's multiple comparisons test in Graphpad was used for the in vivo study.

3. Results and Discussion

3.1. Fabrication of a Chaotic Mixer for the Preparation of LNPs

As an initial step in this work, we aimed to establish the synthesis of mRNA LNPs using a customized microfluidic device. Here, LNPs comprised of ionizable lipid DLin-MC3-DMA bearing an amine group that is positively charged at pH 5.0, the phospholipid DOPE, cholesterol, and shielding lipid, either PEGylated lipid ALC-0159 or polypeptide-based lipopolymer pSar.[24,45] The hydrophilic PEG or pSar coats the surface of LNPs and thus prevents aggregation of LNPs during production, storage as well as upon injection in vivo.[21,46] For the formulation, when mRNA in aqueous buffer with a low pH is rapidly mixed with lipids in the organic phase, such as ethanol, LNPs form spontaneously due to hydrophobic and electrostatic interactions between the positively charged ionizable lipid and the anionic mRNA. The structure of the generated mRNA LNPs has been thoroughly investigated by a multitude of methods, in particular, cryoEM and SAXS measurements. Despite some differences in the detailed description, all studies point to compact nanoparticles with low internal organization, where the RNA is embedded in an excess of lipidic material.[47–50]

To date, the most widely used microfluidic system to generate mRNA LNPs is the NanoAssemblr, which has the drawback of high cost due to one-time use of microfluidic chip. Since it is reported that chaotic mixer structures enhance the controllability of LNP size, we developed a chaotic mixer to mix mRNA with lipids.[27] The design of the microfluidic chip is depicted in **Figure 1** and can be easy copied. To reach precise control over mixing speed, a long mixing length is required to fully mix two fluids at high flow speeds. The mixer was fabricated from Topas microscopy slides (75 × 25 mm) made of thermoplastic polymer (cyclic olefin copolymer), which is nonpolar, amorphous, and chemical resistant. It also has a very low permeability for water vapor and a low capacity for the absorption of water. The mixer was designed as 46.80 mm in length and 7.73 mm for the length of 1 mixer section. The staggered herringbone micromixers were utilized to enhance mixing by advection rather than diffusion. It consists of a rectangular channel with embossed grooves on the bottom, where these grooves have an asymmetrical V-shape (note that the peak of the V is not in the middle of the geometry's width) and 6 asymmetric grooves followed by a group of 6 reverse asymmetric grooves,[51] as illustrated in Figure 1A,B. The chaotic mixer can be enclosed within a plastic holder with the assistance of a metal bracket to ensure a tight fit (Figure 1C,D). Plastic tubing can be used to connect the syringes on the pump (Fusion 100-X High precision syringe pump) to the chamber and to collect the samples. In addition, this cost-effective chip can be used more than 40 times without notable variation in terms of size, surface charge, and encapsulation efficiency of LNPs.

3.2. Higher Total Flow Rate and Flow Rate Ratio Produced Small-Sized mRNA LNPs

The quality of LNPs is heavily affected by the production procedure.[27] Typically, modulating mixing parameters, like total flow rate (TFR) and flow rate ratio (FRR) of aqueous and ethanol phase, changes the dynamics of the nanoprecipitation reaction and solubility of the lipid components, thus controlling size and dispersity of mRNA LNPs. Here, mRNA LNPs composed of DLin-MC3-DMA, DOPE, cholesterol, and PEG- and pSar-lipids at a molar ratio of 40/10/48/2 were prepared at varying flow conditions, as shown in **Table 1**. Initially, we kept the flow rate ratio (FRR) as 3:1 (mRNA in aqueous: lipids in ethanol) and varied the total flow rate (TFR) at 0.8, 1.2, and 1.6 mL min^{-1}. In general, all the generated mRNA LNPs were negatively charged, around −11 mV. This is inconsistent with previous reports that ionizable lipid MC3 has a pKa of 6.2–6.4 and thus the surface of mRNA LNPs has an almost neutral charge in PBS buffer (pH 7.4).[52] While only slight changes were found in the hydrodynamic diameter of mRNA LNPs, ranging from 120 nm (0.8 mL min^{-1}) to

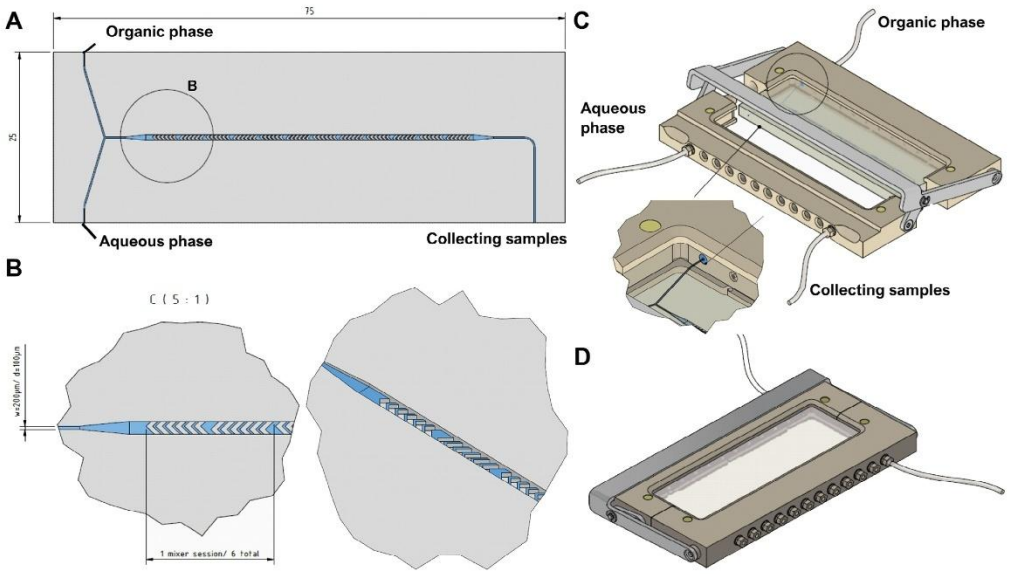

Figure 1. Scheme of chaotic mixer structure within the customized microfluidic device. A) The organic phase and aqueous phase in two channels can be mixed in the chaotic mixer chamber. B) Zoomed view of 1 unit grooves. C) Scheme of microfluidic chip holder with plastic input and output tubes to prepare and collect samples. D) Closed state of microfluidic chip holder.

150 nm (1.2 mL min^{-1}), the polydispersity index (PDI) showed a notable decrease with increasing TFR. Although it was reported that increasing the total volumetric flow rate during formulation increases mixing efficacy and decreases the time scale of particle formation, resulting in smaller particles, we did not see a notable decrease in the particle size of mRNA LNPs by increasing the TFR during mixing.[53] Decreasing the TFR broadens the distribution due to increased particle residence time at lower flow rates, allowing further aggregation to occur and larger particles to form at the outlet, thus an overall increase in PDI is observed. Therefore, higher TFRs are preferable. Moreover, the encapsulation efficiency (EE%), as determined by the RiboGreen assay, increased up to 90% when the TFR increased, indicating the fraction of accessible mRNA is very low for high TFRs. With respect to size, PDI, and EE%, the TFR was kept at 1.6 mL min^{-1} to generate mRNA LNPs in further studies.

Next, we explored the FRR for mRNA LNP production. In general, LNPs became smaller with increased FRR, where aggregates

Table 1. Optimization of CD prepared pSar-LNPs ($n = 6$).

Optimizing total flow rate (TFR)						
mRNA: lipid flow rates [mL min^{-1}]	FRR	TFR [mL min^{-1}]	Size [nm]	PDI	ζ potential [mV]	EE [%]
0.6:0.2	3	0.8	122.5 ± 10.6	0.25 ± 0.04	−10.1 ± 1.4	66.1 ± 2.0
0.9:0.3	3	1.2	149.2 ± 30.4	0.19 ± 0.07	−11.3 ± 0.1	72.4 ± 3.3
1.2:0.4	3	1.6	132.9 ± 6.5	0.10 ± 0.04[a)]	−11.3 ± 0.7	88.8 ± 1.5
Optimizing flow rate ratio (FRR)						
mRNA: lipid flow rates [mL min^{-1}]	FRR	TFR [mL min^{-1}]	Size [nm]	PDI	ζ potential [mV]	EE [%]
0.8:0.8	1	1.6	Aggregation	—	—	—
1.1:0.5	2.2	1.6	153.4 ± 19.8	0.14 ± 0.04	−12.6 ± 1.6	66.7 ± 4.2
1.2:0.4	3	1.6	129.3 ± 3.8	0.17 ± 0.03	−17.5 ± 2.1	91.8 ± 9.4

[a)] Indicated that $p < 0.5$ compared to the mRNA LNPs synthesized at flow rate of 0.6:0.2.

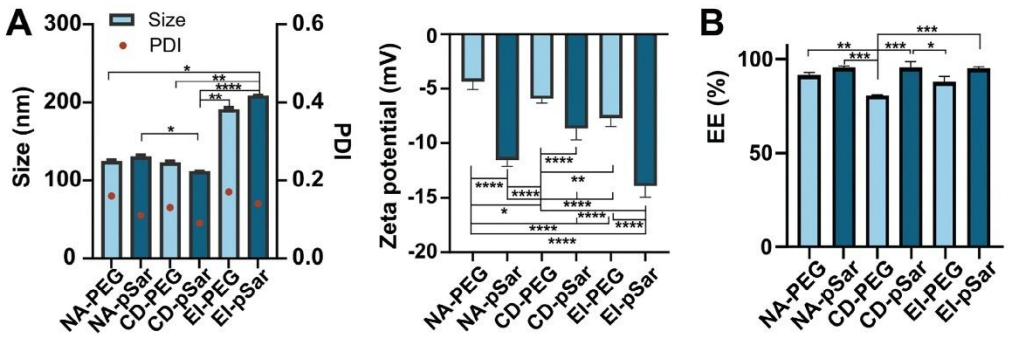

Figure 2. Characterization and stability of PEG/pSar LNPs prepared by NA, CD, and EI methods. A) Size, PDI, and surface charge of all LNPs were measured by DLS ($n = 6$). B) Encapsulation rate of all LNPs. Data are presented as mean ± SD. The formulated mRNA LNPs were named as manufacturing approach-shielding lipopolymers. *$p < 0.05$; **$p < 0.01$; ***$p < 0.001$, ****$p < 0.0001$.

were detected when FRR was 1, while a particle size of 130 nm could be reached with the FRR at 3. These findings align with previously reported literature, indicating that smaller LNPs can be achieved when the ethanol phase is rapidly diluted.[27] Conversely, decreasing the FRR increases ethanol concentration at the mixing interface, thus increasing lipid solubility and lengthening particle formation time, allowing for particle growth. Moreover, when FRR increased from 2.2 to 3, EE% of mRNA LNPs was improved from 67% to 90%. To sum up, both TFR and FRR affect the physicochemical properties of mRNA LNPs substantially. The higher TFR and FRR, the more defined mRNA LNPs can be produced. Considering that i) the higher total flow volumetric rate leads to the higher pressure within the microchannel, and ii) increasing either TFR or FRR generated small-sized LNPs, we synthesized mRNA LNPs at TFR of 1.6 mL min^{-1} and FRR of 3 in the next studies. More importantly, this device showed high reproducibility of size distribution, surface charge, and EE (%) of mRNA LNPs from batch to batch, as shown in the independent runs with the same settings in Table 1.

3.3. Small-Sized, Defined mRNA LNPs were More Stable During Storage

To evaluate the home-developed microfluidic device (CD), mRNA LNPs were synthesized using the commonly used NanoAssemblr (NA) and traditional method of ethanol injection (EI). We aim to understand whether different LNP fabrication methods and materials affect the internal structure and performance of LNPs. Compared with NanoAssemblr, our custom device is more cost-effective and reusable. However the downside is that our pump cannot achieve the high flow rate of the NanoAssemblr, which will be improved in further studies. As an alternative to pSar, PEGylated lipid ALC-0159 was incorporated into mRNA LNPs to investigate its impact on the physicochemical and biological performance of formulated mRNA LNPs (Table S1, Supporting Information).

For the characterization of mRNA LNPs, we examined the size, PDI, and ζ potential of formulated mRNA LNPs (**Figure 2**). By using the microfluidic device, either NA or CD, mRNA LNPs were comparable in terms of size (around 130 nm) and PDI (below 0.2), while the simple mixing of lipids and mRNA (ethanol injection) resulted in larger nanoparticles (up to 200 nm). These findings indicate that the use of higher flow rates and microfluidic channel geometry optimized for those flow conditions can decrease the LNP size. Since the lipid concentration was kept at 3.75 mM for mRNA LNPs synthesis, the difference in size of LNPs produced by microfluidics and EI may attribute to the different mixing conditions. When ethanol was instantaneously diluted within the microchannel, the intermediate planar fragments had little time to grow before closing into vesicles, resulting in smaller particles. When ethanol was diluted slowly by manual mixing, pockets of high ethanol concentration developed, thus favoring stabilization and growth of intermediate fragments that lead to large-sized LNPs.[54] All mRNA LNPs were slightly negatively charged with ζ potential between −5 and −15 mV, and over 80% of mRNA was protected from accessibility to dissolved dyes by the LNPs under all conditions (RiboGreen assay).

Further, we studied the storage stability of mRNA LNPs at 4 °C over 3 months, in terms of size and PDI (Figure S1, Supporting Information). Again, mRNA LNPs produced using microfluidics remained stable, were 100–150 nm in size with PDI below 0.25, and no significant difference was found within 3 months. Using CD, pSar-containing mRNA LNPs were slightly smaller than their PEGylated counterparts but slightly larger than the analogues prepared using NA. Overall, the smallest LNPs with PDIs around 0.1 and EE(%) around 90% can be achieved with the customized microfluidic chip as described above.

In contrast, the size of PEGylated mRNA LNPs gradually increased (180.3 ± 1.2 nm at 1 week vs 199.4 ± 3.3 nm at 3 months), indicating that EI-prepared LNPs may be less stable compared to their counterparts. With the same manufacturing approach of EI, the increase in size of pSar-decorated LNPs from 209.2 ± 0.3 to 213.1 ± 4.4 nm was not as evident as for the PEGylated LNPs, suggesting that pSar can increase the stability of EI-synthesized mRNA LNPs.

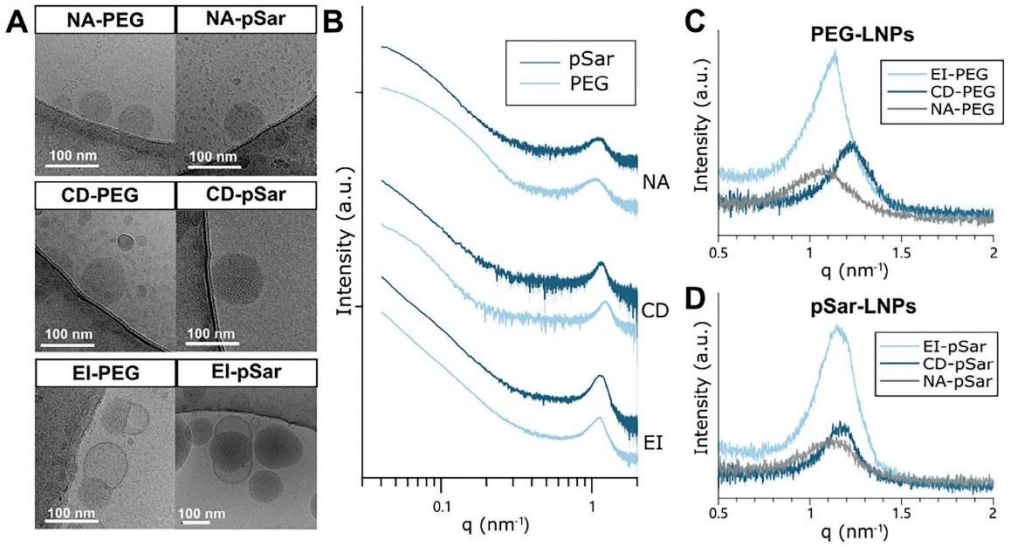

Figure 3. A) Representative CryoEM images of PEG-containing mRNA LNPs (left pane) and pSar-containing mRNA LNPs (right panel) prepared by NA (top panel), CD (middle panel), and EI methods (bottom panel). B) SAXS pattern of PEGylated mRNA LNPs (dark blue) or pSar-containing LNPs (light blue) prepared by NA (top panel), CD (middle panel), and EI (bottom panel). C,D) Bragg peak characteristics of C) PEG-containing mRNA LNPs and D) pSar-containing mRNA LNPs using different manufacturing methods.

3.4. pSar-LNPs have Higher Surface Roughness than PEG-LNPs

To analyze the structure of the mRNA LNPs synthesized by different methods (i.e., NA, CD, and EI), cryoEM imaging was performed, as shown in **Figure 3**A. Microfluidics produced smaller particles while EI generated larger particles (≈200 nm). For small-sized particles prepared by microfluidics, either NA or CD, cryoEM images exhibited a similar feature of ordered electron-dense cores, whereas large-sized particles produced by EI display a different characteristic. The majority of EI-PEG LNPs exhibited an electron-dense core, accompanied by a large aqueous bleb compartment (associated lipid vesicle that was devoid of RNA) situated on one side indicating phase separation of lipid components. Only a minority of them had the typical dense core shape. It is noteworthy that Wang et al. observed similar bleb-shaped structures from siRNA LNPs synthesized by EI.[55] On the other hand, most EI-pSar LNPs shared a similar morphology with NA and CD-prepared LNPs, which had large dense cores. Notably, some of the EI-pSar LNPs exhibited more than one aqueous bleb structure around the dense core. Our observation suggests that also the choice of shielding lipid, i.e., pSar and PEG, can influence the morphological characteristics of LNPs when utilizing the EI method, but this influence is not observed when using higher-speed mixer methods such as NA and CD. Bleb-like substructures are supposed to be derived from lipid components forming a bilayer due to the phase segregation of phospholipids like DSPC, which are not favorably compatible with the inverted hexagonal phase in the electron-dense core.[47] Also the choice of the manufacturing buffer and its ionic strength influences the tendency to formation of blebs on LNP formulations, where these formulations showed an enhanced transfection efficacy compared to nonbleb LNPs.[56] In this experiment, DOPE was used as a phospholipid, which is due to its unsaturated lipid chains being more compatible with this organization and thus does not tend to form subphases.[57] Nevertheless, the formation of bleb-like structures can be observed in cryoEM images, which may be explained by the slower ethanol dilution within manual mixing, leading to more heterogeneous particle formation. Since PEG-lipids reside on the surface of the LNPs, molar fraction also determines particle size as well as the tendency to build blebs.[58] The observation of bleb-like structures as a matter of the manufacturing method highlights that not only the choice of materials but also the formulation process has a tremendous influence on the particle structure. Exchanging PEG with pSar may only slightly affect LNP microstructure and size as visible in Figures 2 and 3A. A multiangle DLS analysis was also performed, and all LNPs exhibited a slight angle dependency (Figure S2, Supporting Information), which may relate to moderate dispersity and the complex structure.

To further investigate differences in the internal structure of LNPs, small angle X-ray scattering (SAXS) measurements were conducted. Figure 3B displays the results of batch SAXS measurements, showcasing the scattering patterns of each sample. These patterns are dominated by a broad peak around 1 nm^{-1}, reflecting the internal organization of particles. The low q range was analyzed using Guinier plots to determine the radius of gyration (R_g). Consistent with DLS and cryoEM findings, NA-produced formulations exhibit the lowest R_g, while

Table 2. SAXS data analysis of PEG- or pSar-containing mRNA LNPs manufactured by NA, CD, and EI.

Name	R_g [nm]	Average calculated radius [nm]	Porod exponent	*d*-spacing [nm]	Correlation length [nm]
NA-PEG	25.8	33.3	3.7 ± 0.1	6.0 ± 0.1	4.7 ± 0.1
NA-pSar	33.3	43.0	3.5 ± 0.1	5.7 ± 0.1	5.5 ± 0.2
CD-PEG	40.1	51.7	3.3 ± 0.1	5.2 ± 0.1	7.1 ± 0.2
CD-pSar	50.6	65.3	3.1 ± 0.1	5.5 ± 0.1	8.0 ± 0.2
EI-PEG	64.9	83.8	3.2 ± 0.1	5.6 ± 0.1	9.1 ± 0.2
EI-pSar	69.9	90.3	3.0 ± 0.1	5.5 ± 0.1	8.3 ± 0.1

LNPs manufactured by EI have a R_g approximately twice as large as those made with microfluidic devices. Assuming spherical particles, the average radius of LNPs can be calculated, yielding comparable results to DLS experiments, with R_g/R_h ratios close to 0.78, which is indicative for uniform spheres (**Table 2**; and Table S2, Supporting Information).

We further analyzed the low q region from 0.08 to 0.25 nm^{-1} by the power law (Equation (5)), to determine the fractal dimension of the LNPs (Figure S3, Supporting Information). Smooth surfaces lead to an exponent, x, of 4 (Porod law), while lower numbers imply increased surface roughness or fractal dimension. As Table 2 displays, pSar-modified LNPs have lower value of Porod exponents than the PEGylated counterparts, regardless of the manufacturing method. In our previous work we found that compared to PEGylated LNPs, the increase of fractal dimension in the presence of pSar is accompanied by higher biological activity.[22]

In addition, surface properties strongly depend on the manufacturing method. NA-LNPs tend to show a Porod exponent of around 3.5 or bigger, indicating smooth surfaces. Conversely, the Porod region decay of CD- and EI-LNPs is closer to 3, suggesting surface fractals. Especially for EI-manufactured LNPs it is well accompanied with findings from cryo-EM, where bleb like structures were observed. It was found that the LNPs' surface was less polar with increasing particle size, and changes in LNPs' size led to changes in the mRNA organization and LNPs' surface properties.[59] High fractal dimensions and irregular surfaces are hypothesized to be beneficial for cell transfection by facilitating membrane rupture within endosomal uptake processes.[60]

The Bragg peak, resulting from internal organization of the LNPs provides insights into packing density of the cargo within the lipid vehicle. Figure 3C,D demonstrates that the peak characteristics differ among LNPs generated by various manufacturing methods. The Bragg reflection area is larger for EI-LNPs compared to the microfluidic produced LNPs, which can be explained by the larger particle size. Accordingly, the extrapolated scattering intensity at $q = 0$, obtained from the Guinier plot, is higher for the EI-LNPs. The particles manufactured by EI exhibit larger diameters and, consequently, higher volumes per particle.[40,61] The peak observed in the EI-LNPs (Figure 3C,D, dark blue), is characterized by two subpeaks, indicating subphases in internal organization, while the microfluidic methods display a single peak. The additional front peak at 0.85 nm^{-1} along with the main peak at 1.1 nm^{-1} contributes to the total scattering pattern of the formulation (Table S3, Supporting Information). This highlights the ability of microfluidic manufacturing processes in producing well-defined nanoparticles without lipidic substructures, such as the observed blebs in cryoEM.

Furthermore, both peak position and width differ among all the LNPs synthesized using various manufacturing methods. NA-produced particles yield broad peaks with peak maxima around 1.05 nm^{-1}. Compared to NA-LNPs, CD-LNPs showed sharper peaks shifted toward higher *q*. This indicates a tighter internal packing of the mRNA, resulting in lower d-spacing. Comparing the correlation length derived from peak width between the two microfluidic mixing procedures, a higher long-range order of mRNA-lipid interactions was observed. However, the level of long-range order remains relatively low in the range of the *d*-spacing, as it is typical for mRNA-LNP systems. Interestingly, despite lower mixing speeds in synthesizing CD-LNPs, which might suggest a looser mRNA packing density, the chaotic mixing chamber in the customized device enables closer lipid-mRNA interaction and thus tighter packing. To check if these internal features can be derived at different flow conditions also using the NA device, LNP formulations manufactured with variable TFRs were investigated with DLS and SAXS (Figure S4, Supporting Information). Independent of TFR, all LNPs showed *d*-spacing values around 6 nm, as for the primary investigated NA samples. Interestingly, the low flow rate at 1 mL min^{-1} resulted in LNPs with an average diameter of around 250 nm, while increasing the TFR decreased LNP size (Table S4, Supporting Information). These results indicate that for NA, the liquid flow rate also influences overall particle size more than the internal organization. Dense packing properties have recently been proposed as beneficial for transfection in specific cell types, such as human peripheral blood mononuclear cells.[22] Moreover, the nonmicrofluidic ethanol injection protocol results in a lower packing density and relatively higher correlation length compared to the NA protocol. Differences in peak behavior were also observed when comparing formulations with different stealth moieties. For NA- and EI-manufactured LNPs, slightly denser RNA-lipid interactions were obtained with pSar-shielded LNPs, while in the customized microfluidic setting the pSar formulation showed slightly higher *d*-spacing compared to its PEG analogs.

Analyzing the scattering profile of the different formulations revealed distinct variations in both the overall particle appearance and internal organization. The microfluidic NA protocol successfully generated smoothly spherical nanoparticles with a discrete diameter below 100 nm, exhibiting a low degree of internal organization. On the other hand, manual EI approaches produced larger LNPs with irregular surfaces and lipidic substructures. In comparison to the well-established and widely used NA

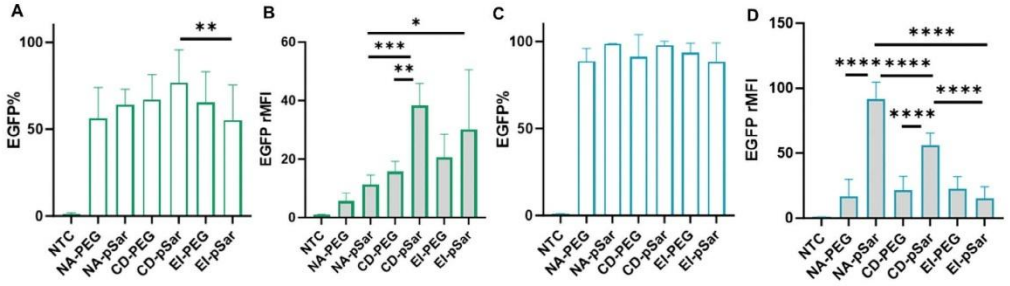

Figure 4. In vitro transfection efficiency of EGFP mRNA LNPs after being exposed to A,B) HepG2 cells and C,D) Jurkat T cells for 24 h, respectively. The transfection efficiency was represented as fraction of A,C) EGFP-positive cells (EGFP%) and B,D) relative mean fluorescence intensity (EGFP rMFI) based on untreated cells (NTC). All the experiments were performed on three independent days ($n = 9$). Data are presented as mean ± SD. *$p < 0.05$; **$p < 0.01$; ***$p < 0.001$, ****$p < 0.0001$.

microfluidic process, the customized microfluidic device presented here can produce LNPs with comparable particle sizes, but with slightly different surface and internal order characteristics. We failed to achieve these characteristics with the NA while changing experimental settings. These differences are hard to distinguish with standard quality control measures, but still can play an important role for therapeutic efficacy. The presence of more irregular surfaces and higher packing density of the mRNA cargo in CD formulations may be potentially advantageous for cellular transfection,[22] as it can play a crucial role for endosomal escape mechanisms. The higher fractal dimension of CD-manufactured LNPs can be explained by the lower TFR and therefore slightly slower ethanol dilution leading to differences in primary particle formation. This is also observable for NA-LNPs with slower TFRs as displayed in Table S4 (Supporting Information). Conversely, the higher packing density cannot be explained by this, since it was not reproducible in NA with lower TFRs. Here the geometry of the microfluidic mixers seems to be one of the driving forces for differences in the mRNA-lipid complex. Further investigation with different lipid compositions and mixer geometries could help to elucidate this phenomenon. Additionally, these LNPs showed lower diameters and reduced polydispersity compared to manually produced EI-LNPs. Thus, the development of the novel microfluidic approach enables the production of robustly monodisperse nanoparticles with uniform structural features without altering the lipid composition.

3.5. 5 pSar-mRNA LNPs Outperformed PEG-mRNA LNPs in Transfection In Vitro

Next, we evaluated the biological performance of mRNA LNPs on two different cell lines, the human liver cancer cell line HepG2 and the human immortalized T lymphocyte cell line derived from an acute T cell leukemia (Jurkat T cells), respectively. After being exposed to the formulated EGFP mRNA LNPs for 24 h, cells were collected and examined by flow cytometry for transfection efficiency. As shown in **Figure 4**A,B, EGFP production was detected in more than 50% of HepG2 cells. Notably, a robust EGFP expression was detected in the cells treated with pSar-modified mRNA LNPs, with a significant difference in the EGFP(%) compared to the counterparts prepared by EI (**, $p = 0.005$). As well, EGFP relative mean fluorescence intensity (rMFI) derived from cells exposed to CD-pSar LNPs was significantly higher than the PEGylated mRNA LNPs generated by CD (**, $p = 0.0021$) and pSar-LNPs generated by NA (***, $p = 0.0001$), respectively. In addition, a dramatic difference in EGFP rMFI was found in the cells exposed to pSar-LNPs synthesized using NA and EI (*, $p = 0.0193$).

In Jurkat T cells, over 90% of cells expressing EGFP were detected, without any significant difference in EGFP-positive cells (%) among all formulations tested in this study (Figure 4C,D). Likely, microfluidic-generated pSar-LNPs resulted in more robust EGFP production than that of PEGylated LNPs using the same manufacturing approach, with a significant difference in EGFP rMFI (****, $p < 0.0001$ for NA; ****, $p < 0.0001$ for CD). Among the different production methods, NA-pSar mRNA LNPs led to the most efficient protein production, which is 1.6-fold and 6.1-fold rMFI compared to pSar-LNPs generated by CD or EI. In contrast to the findings in HepG2 cells, pSar-LNPs produced by EI led to the lowest EGFP rMFI (15.2 ± 9.0), followed by pSar-LNPs produced by CD (56.3 ± 9.3). Surprisingly, EGFP rMFI measured in the cells exposed to PEGylated mRNA LNPs was around 20, independent of the manufacturing method.

Overall, the transfection efficiency of mRNA LNPs is cell line-dependent, where large particles led to more robust protein expression in adherent HepG2 cells, while small-sized particles showed more efficient mRNA delivery in suspended Jurkat T cells. This may be due to the partial aggregation of EI-LNPs in the culture medium and thus the cellular internalization was achieved by difference in endocytosis compared to more stable and small-sized particles. Meanwhile, the shielding lipid is of significance to transfection efficiency, particularly in Jurkat T cells. In accordance with our previous work, pSar as stealth moieties affected the LNPs differently, by changing the surface morphology toward higher roughness. Although stability in serum/culture medium is comparable, the elevated surface roughness of the pSar-LNPs compared to those with PEG, may foster interaction with the oppositely charged endosomal membrane upon cellular uptake and protonation of ionizable lipids, resulting in the facilitated rupture of the membrane and the release of the mRNA into the cytosol.[22,62] Therefore, a higher transfection efficiency was

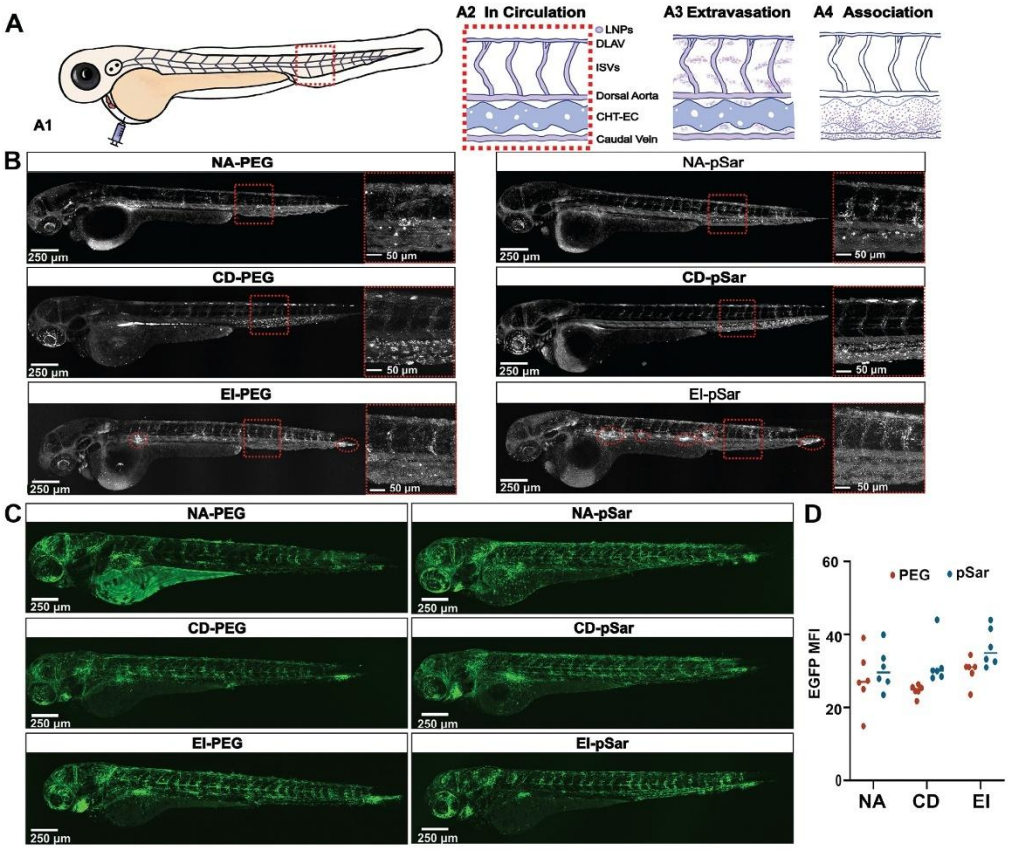

Figure 5. In vivo behavior of NA-PEG/Psar, CD-PEG/pSar, and EI-PEG/Psar LNPs. All LNPs with mixed mRNA (2 nL, EGFP:Cy5 mRNA = 3:1 w/w, 75 pg EGFP mRNA) were injected into zebrafish embryos. A) Scheme for LNPs microinjection into the Duct of Cuvier of 2.5 dpf zebrafish embryos. Zoomed-in tissue-level images depict LNP distributions within the indicated red boxes. Blood vessels are represented by blue lines, while LNPs are shown in purple. CHT-EC: Caudal Hematopoietic Tissue Endothelial Cells, DLAV: Dorsal Longitudinal Anastomotic Vessel, ISV: Intersegmental Vessel. A2) LNPs are located within the lumen of blood vessels, indicating a free circulation pattern. A3) LNPs extravasate from the blood vessels. A4) LNPs are associated with caudal endothelial cells. B) Biodistribution was observed at 3 hpi, red circles show aggregation of LNPs, and red boxes show tissue-level images. C) Transfection effects were observed at 24 hpi. D) Quantification of transfection effect in the whole fish view images ($n = 6$).The scale of the whole fish is 250 µm, and the enlarged tail images in the red square is 50 µm.

observed. In addition, the impact of the manufacturing method or the size of LNPs on the in vitro transfection efficiency is more notable in Jurkat T cells than in HepG2 cells.

3.6. NA, CD, and EI-LNPs Display Robust Transfection Effects In Vivo

To evaluate the different mRNA LNPs in a more complex cellular environment, we loaded Cy5 labeled luciferase mRNA and EGFP mRNA into LNPs, and intravenously injected these LNPs into zebrafish embryos at 2.5 days postfertilization (dpf). The scheme of microinjection in zebrafish embryos and the biodistribution pattern of LNPs are shown in **Figure 5A**. We first examined the biodistribution of mRNA by capturing the Cy5 fluorescence signal (shown in gray) under a confocal microscope at 3 hour postinjection (hpi), as presented in Figure 5B. All LNPs were freely circulating in the blood vessel lumens, owing to the shielding lipid and neutral surface of the LNPs, and began to associate with caudal endothelial cells over time, which have a function similar to that of liver scavenger endothelial cells.[63] Vascular extravasation (leakage of LNPs from blood vessels into the embryonic muscle tissue) was also evident for all LNPs, as it is a common phenomenon for neutral nanoparticles.[63] However, EI-prepared

PEG- and pSar-LNPs display a tendency to form aggregate in circulation, suggesting that EI-LNPs exhibit in general lower stability compared to NA- and CD-LNPs, which is in line with the particle inhomogeneity observed in cryo-EM.

The transfection efficiency was assessed by visualizing the expression of EGFP (represented in green) in Figure 5C. Across all LNPs, the pattern of EGFP mRNA transfection closely mirrored their biodistribution, with notable green fluorescence in blood vessels and muscle tissue. This observation strongly suggests the successful delivery, uptake, and subsequent release of functional mRNA within the cytoplasm in embryos. There was, however, no notable distinction observed among the LNPs based on the representative images. To further assess their in vivo transfection efficacy at the whole zebrafish embryo level, we captured images of six embryos and quantified the mean EGFP fluorescence intensity using ImageJ (Figure 5D). Although the EGFP mean fluorescence intensity (MFI) value for CD-PEG LNPs (24.7 ± 1.6) was relatively lower than that of the other groups (CD-pSar: 34.2 ± 6.0), this variance was still not statistically significant ($p = 0.08$). Interestingly, EI-prepared LNPs and microfluidic-prepared LNPs achieved comparable transfection effects, and the aggregation of EI-LNPs did not considerably influence their transfection effects in muscle and endothelial cells. The bleb structures found in EI-LNPs may play a role in enhancing transfection efficacy in vivo, as previously observed LNPs containing similar blebs.[56]

The transfection after LNP storage of 3 months of at 4 °C was also examined in zebrafish embryos (Figure S5, Supporting Information). The confocal microscope settings used for taking GFP expression images were kept consistent throughout all experiments in this study. NA-PEG, NA-pSar, and EI-pSar exhibited a visible decrease in green fluorescence compared to their freshly prepared analogs. This observation indicates that the transfection efficacy of LNPs decreased after 3 months in solution even though there were only minor changes in the size and PDI of LNPs (Figure 2C). The quantification data exhibited an average of EGFP MFI in the three groups is around 20 (Figure S6, Supporting Information), which is 1.5–2 times lower than that of fresh samples.

4. Conclusion

In this study, we fabricated a customized microfluidic device to synthesize mRNA LNPs. Using this home-developed device, the flow rate of the aqueous-to-ethanol ratio had a notable influence on the size, PDI, and entrapment of mRNA LNPs, while the influence of the total flow rate was modest. Further, the influence of different manufacturing methods (microfluidics and ethanol injection) and different shielding lipids (PEG and pSar) on the morphology, structure, biodistribution, and transfection performance of mRNA LNPs was investigated. With the microfluidic manufacturing approach, the customized microfluidic device was compared to the established commercially available NanoAssemblr. In general, microfluidics generated small-sized, more homogenous, and stable mRNA LNPs compared to the LNPs prepared by ethanol injection. Moreover, the microfluidic-produced mRNA LNPs exhibited the ordered electron-dense cores, whereas ethanol injection-produced LNPs displayed a large aqueous bleb compartment (associated lipid vesicle that was devoid of RNA) around the dense cores. PEGylated and pSar-formulated LNPs were comparable in size, dispersity and internal morphology, while with pSar the surface roughness was systematically higher, which was found to be correlated with higher in vitro transfection effect. Interestingly, SAXS data indicated LNPs generated by custom microfluidics presented more rough surfaces and higher packing density of the mRNA cargo than LNPs produced by commercial device. This highlights the importance of investigations on structural properties, since the differences were not properly detectable with standard quality control measures as DLS, but can have influence on therapeutic potency. Although the transfection efficiency of LNPs prepared by different methods was comparable, ethanol injection-generated LNPs showed aggregation in vivo after systemic injection. In summary, the findings indicate, that by using a customized microfluidic device, LNPs with comparable quality with respect to those obtained from a commercial device can be obtained more cost-effectively, and that microfluidics allows for better control over physicochemical characteristics of mRNA LNPs than ethanol injection. In conclusion, our findings highlight the potential of custom microfluidic devices and materials for mRNA LNPs synthesis to modulate and improve the structure and final performance of mRNA LNPs. The correlation between the internal structure of mRNA LNPs and their physicochemical properties and biological performance can provide valuable insights for mRNA LNPs optimization and production.

Supporting Information

Supporting Information is available from the Wiley Online Library or from the author.

Acknowledgements

D.B. would like to acknowledge the financial support from the China Scholarship Council (No. 201906210053). C.W. and P.L. would like to acknowledge the financial support from CRC 1066 founded by the Deutsche Forschungsgemeinschaft. M.B. acknowledged support by the CRC1066-2/–3 (Project B12) for the development of polysarcosine lipids and formulations thereof.

Conflict of Interest

M.B. and H.H. are co-inventors on PCT/EP2018/076633. M.B. is scientifc advisory board member of Curapath (Paterna, Spain). The other authors do not have any conflicts of interest.

Author Contributions

D.B. and C.W. contributed equally to this work. Conceptualization: P.L., M.B., H.Z.; Data curation: D.B., C.W., H.Z.; Formal analysis: D.B., C.W., H.Z.; Funding acquisition: M.D., P.L., M.B.; Investigation: D.B., C.W., D.U., I.S.K., B.Z, B.K, Rl.K., M.A.G., R.Z, T.H, M.D, H.H; Methodology: H.Z., D.B, C.W, B.W, J.B; Project administration: P.L., M.B., H.Z; Resources: P.L.; M.B.; Supervision: P.L., M.B., H.Z; Validation; Visualization: D.B., C.W., H.Z.; Writing – original draft: D.B., C.W., H.Z.; and Writing – review & editing H.Z, M,B, P.L.

Data Availability Statement

The data that support the findings of this study are available in the supplementary material of this article.

Keywords

LNP internal structure, microfluidics, mRNA delivery, PEGylated lipids, polysarcosine

Received: April 15, 2024
Revised: June 13, 2024
Published online: June 25, 2024

[1] N. Al Fayez, M. S. Nassar, A. A. Alshehri, M. K. Alnefaie, F. A. Almughem, B. Y. Alshehri, A. O. Alawad, E. A. Tawfik, *Pharmaceutics* **2023**, *15*, 1972.
[2] M. Jeong, Y. Lee, J. Park, H. Jung, H. Lee, *Adv. Drug Delivery Rev.* **2023**, 114990.
[3] K. Lam, P. Schreiner, A. Leung, P. Stainton, S. Reid, E. Yaworski, P. Lutwyche, J. Heyes, *Adv. Mater.* **2023**, *35*, 2211420.
[4] H. Seo, L. Jeon, J. Kwon, H. Lee, *Adv. Healthcare Mater.* **2023**, *12*, 2203033.
[5] L. Schoenmaker, D. Witzigmann, J. A. Kulkarni, R. Verbeke, G. F. A. Kersten, W. Jiskoot, D. J. A. Crommelin, *Int. J. Pharm.* **2021**, *601*, 120586.
[6] B. Matthias, B. Weber, H. Haas, P. Heller, S. Nogueira, A. Schlegel, RNA Particles Comprising Polysarcosine US Patent App. 17/281,697, **2022**.
[7] B. Weber, A. Birke, K. Fischer, M. Schmidt, M. Barz, *Macromolecules* **2018**, *51*, 2653.
[8] K. Klinker, O. Schäfer, D. Huesmann, T. Bauer, L. Capelôa, L. Braun, N. Stergiou, M. Schinnerer, A. Dirisala, K. Miyata, *Angew. Chem.* **2017**, *56*, 9608.
[9] Y. Hu, Y. Hou, H. Wang, H. Lu, *Bioconjug. Chem.* **2018**, *29*, 2232.
[10] F. Fenaroli, U. Reprik, Y. Xu, K. Johann, S. Van Herck, P. Dey, F. M. Skjeldal, D. M. Frei, S. Bagherifam, A. Kocere, R. Haag, B. G. De Geest, M. Barz, D. G. Russell, G. Griffiths, *ACS Nano* **2018**, *12*, 8646.
[11] E. J. L. Steen, J. T. Jorgensen, K. Johann, K. Norregaard, B. Sohr, D. Svatunek, A. Birke, V. Shalgunov, P. E. Edem, R. Rossin, C. Seidl, F. Schmid, M. S. Robillard, J. L. Kristensen, H. Mikula, M. Barz, A. Kjaer, M. M. Herth, *ACS Nano* **2020**, *14*, 568.
[12] T. A. Bauer, J. Schramm, F. Fenaroli, S. Siemer, C. I. Seidl, C. Rosenauer, R. Bleul, R. Stauber, K. Koynov, M. Maskos, M. Barz, *Adv. Mater.* **2023**, *35*, 2210704.
[13] N. K. Dal, G. Schäfer, A. M. Thompson, S. Schmitt, N. Redinger, N. Alonso-Rodriguez, K. Johann, J. Ojong, J. Wohlmann, A. Best, K. Koynov, R. Zentel, U. E. Schable, G. Griffiths, M. Barz, F. Fenaroli, J. Controlled Release, (Eds: J. W. Goodby, P. J. Collings, T. Kato, C. Tschierske, H. Gleeson, P. Raynes, V. Vill), **2023**, *354*, 851.
[14] C. Kappel, C. Seidl, C. Medina-Montano, M. Schinnerer, I. Alberg, C. Leps, J. Sohl, A. K. Hartmann, M. Fichter, M. Kuske, J. Schunke, G. Kuhn, I. Tubbe, D. Paßlick, D. Hobernik, R. Bent, K. Haas, E. Montermann, K. Walzer, M. Diken, M. Schmidt, R. Zentel, L. Nuhn, H. Schild, S. Tenzer, V. Mailänder, M. Barz, M. Bros, S. Grabbe, *ACS Nano* **2021**, *15*, 15191.
[15] I. Alberg, S. Kramer, M. Schinnerer, Q. Hu, C. Seidl, C. Leps, N. Drude, D. Möckel, C. Rijcken, T. Lammers, M. Diken, M. Maskos, S. Morsbach, K. Landfester, S. Tenzer, M. Barz, R. Zentel, *Small* **2020**, *16*, 1907574.
[16] I. Negwer, A. Best, M. Schinnerer, O. Schäfer, L. Capeloa, M. Wagner, M. Schmidt, V. Mailänder, M. Helm, M. Barz, H.-J. Butt, K. Koynov, *Nat. Commun.* **2018**, *9*, 5306.
[17] B. Weber, C. Seidl, D. Schwiertz, M. Scherer, S. Bleher, R. Süss, M. Barz, *Polymers* **2016**, *8*, 427.
[18] C. Muhl, M. Conrad, D. Unthan, M. Barz, *Eur. Polym. J.* **2019**, *120*, 109223.
[19] S. Bleher, J. Buck, C. Muhl, S. Sieber, S. Barnert, D. Witzigmann, J. Huwyler, M. Barz, R. Süss, *Small* **2019**, *15*, 1904716.
[20] K. Son, M. Ueda, K. Taguchi, T. Maruyama, S. Takeoka, Y. Ito, *J. Controlled Release* **2020**, *322*, 209.
[21] S. S. Nogueira, A. Schlegel, K. Maxeiner, B. Weber, M. Barz, M. A. Schroer, C. E. Blanchet, D. I. Svergun, S. Ramishetti, D. Peer, P. Langguth, U. Sahin, H. Haas, *ACS Appl. Nano Mater.* **2020**, *3*, 10634.
[22] C. Wilhelmy, I. S. Keil, L. Uebbing, M. A. Schroer, D. Franke, T. Nawroth, M. Barz, U. Sahin, H. Haas, M. Diken, P. Langguth, *Pharmaceutics* **2023**, *15*, 2068.
[23] L. Capelôa, M. Yazdi, H. Zhang, X. Chen, Y. Nie, E. Wagner, U. Lächelt, M. Barz, *Macromol. Rapid Commun.* **2022**, *43*, 2100698.
[24] D. Bi, D. M. Unthan, L. Hu, J. Bussmann, K. Remaut, M. Barz, H. Zhang, *J. Controlled Release* **2023**, *356*, 1.
[25] Q. Cheng, T. Wei, L. Farbiak, L. T. Johnson, S. A. Dilliard, D. J. Siegwart, *Nat. Nanotechnol.* **2020**, *15*, 313.
[26] C. B. Roces, G. Lou, N. Jain, S. Abraham, A. Thomas, G. W. Halbert, Y. Perrie, *Pharmaceutics* **2020**, *12*, 1095.
[27] M. Maeki, S. Uno, A. Niwa, Y. Okada, M. Tokeshi, *J. Controlled Release* **2022**, *344*, 80.
[28] M. Maeki, T. Saito, Y. Sato, T. Yasui, N. Kaji, A. Ishida, H. Tani, Y. Baba, H. Harashima, M. Tokeshi, *RSC Adv.* **2015**, *5*, 46181.
[29] N. Kimura, M. Maeki, A. Ishida, H. Tani, M. Tokeshi, *ACS Appl. Bio. Mater.* **2021**, *4*, 1783.
[30] M. Maeki, Y. Fujishima, Y. Sato, T. Yasui, N. Kaji, A. Ishida, H. Tani, Y. Baba, H. Harashima, M. Tokeshi, *PLoS One* **2017**, *12*, 0187962.
[31] C. Webb, N. Forbes, C. B. Roces, G. Anderluzzi, G. Lou, S. Abraham, L. Ingalls, K. Marshall, T. J. Leaver, J. A. Watts, J. W. Aylott, Y. Perrie, *Int. J. Pharm.* **2020**, *582*, 119266.
[32] N. Kimura, M. Maeki, Y. Sato, Y. Note, A. Ishida, H. Tani, H. Harashima, M. Tokeshi, *ACS Omega* **2018**, *3*, 5044.
[33] N. Kimura, M. Maeki, Y. Sato, A. Ishida, H. Tani, H. Harashima, M. Tokeshi, *ACS Appl. Mater. Interfaces* **2020**, *12*, 34011.
[34] N. Kimura, M. Maeki, K. Sasaki, Y. Sato, A. Ishida, H. Tani, H. Harashima, M. Tokeshi, *RSC Adv.* **2021**, *11*, 1430.
[35] S. Q. Zheng, E. Palovcak, J.-P. Armache, K. A. Verba, Y. Cheng, D. A. Agard, *Nat. Methods* **2017**, *14*, 331.
[36] C. E. Blanchet, A. Spilotros, F. Schwemmer, M. A. Graewert, A. Kikhney, C. M. Jeffries, D. Franke, D. Mark, R. Zengerle, F. Cipriani, S. Fiedler, M. Roesslea, D. I. Svergun, *J. Appl. Crystallogr.* **2015**, *48*, 431.
[37] A. Round, F. Felisaz, L. Fodinger, A. Gobbo, J. Huet, C. Villard, C. E. Blanchet, P. Pernot, S. McSweeney, M. Roessle, D. I. Svergun, F. Cipriani, *Acta Crystallogr., D* **2015**, *71*, 67.
[38] K. Manalastas-Cantos, P. V. Konarev, N. R. Hajizadeh, A. G. Kikhney, M. V. Petoukhov, D. S. Molodenskiy, A. Panjkovich, H. D. T. Mertens, A. Gruzinov, C. Borges, C. M. Jeffries, D. I. Svergun, D. Franke, *J. Appl. Crystallogr.* **2021**, *54*, 343.
[39] D. Franke, A. G. Kikhney, D. I. Svergun, *Nucl. Instrum. Methods Phys. Res. A* **2012**, *689*, 52.
[40] K. A. Rubinson, C. Stanley, S. Krueger, *J. Appl. Crystallogr.* **2008**, *41*, 456.
[41] A. Guinier, *Ann. Phys.* **1939**, *11*, 161.
[42] S. Ciccariello, J. Goodisman, H. Brumberger, *J. Appl. Crystallogr.* **1988**, *21*, 117.
[43] W. H. Bragg, W. L. Bragg, *Proc. R. Soc. London Ser., A* **1913**, *88*, 428.
[44] *Handbook of Liquid Crystals* (Eds: J. W. Goodby, P. J. Collings, T. Kato, C. Tschierske, H. Gleeson, P. Raynes, V. Vill), Wiley-VCH, Weinheim, Germany **2014**.
[45] D. D. Kang, X. Hou, L. Wang, Y. Xue, H. Li, Y. Zhong, S. Wang, B. Deng, D. W. McComb, Y. Dong, *Bioact. Mater.* **2024**, *37*, 86.
[46] C. Hald Albertsen, J. A. Kulkarni, D. Witzigmann, M. Lind, K. Petersson, J. B. Simonsen, *Adv. Drug Delivery Rev.* **2022**, *188*, 114416.

[47] M. Cárdenas, R. A. Campbell, M. Yanez Arteta, M. J. Lawrence, F. Sebastiani, *Curr. Opin. Colloid Interface Sci.* **2023**, *66*, 101705.
[48] Y. Eygeris, S. Patel, A. Jozic, G. Sahay, *Nano Lett.* **2020**, *20*, 4543.
[49] M. A. Graewert, C. Wilhelmy, T. Bacic, J. Schumacher, C. Blanchet, F. Meier, R. Drexel, R. Welz, B. Kolb, K. Bartels, T. Nawroth, T. Klein, D. Svergun, P. Langguth, H. Haas, *Sci. Rep.* **2023**, *13*, 15764.
[50] C. D. Siewert, H. Haas, V. Cornet, S. S. Nogueira, T. Nawroth, L. Uebbing, A. Ziller, J. Al-Gousous, A. Radulescu, M. A. Schroer, C. E. Blanchet, D. I. Svergun, M. P. Radsak, U. Sahin, P. Langguth, *Cells* **2020**, *9*, 2034.
[51] A. G. Hadjigeorgiou, A. G. Boudouvis, G. Kokkoris, *Chem. Eng. J.* **2021**, *414*, 128775.
[52] P. Patel, N. M. Ibrahim, K. Cheng, *Trends Pharmacol. Sci.* **2021**, *42*, 448.
[53] Z. He, Y. Hu, T. Nie, H. Tang, J. Zhu, K. Chen, L. Liu, K. W. Leong, Y. Chen, H.-Q. Mao, *Acta Biomater.* **2018**, *81*, 195.
[54] D. Chen, K. T. Love, Y. Chen, A. A. Eltoukhy, C. Kastrup, G. Sahay, A. Jeon, Y. Dong, K. A. Whitehead, D. G. Anderson, *J. Am. Chem. Soc.* **2012**, *134*, 6948.
[55] S. Wang, X. Wei, X. Sun, C. Chen, J. Zhou, G. Zhang, H. Wu, B. Guo, L. Wei, *Int. J. Nanomed.* **2018**, *13*, 617.
[56] M. H. Y. Cheng, J. Leung, Y. Zhang, C. Strong, G. Basha, A. Momeni, Y. Chen, E. Jan, A. Abdolahzadeh, X. Wang, J. A. Kulkarni, D. Witzigmann, P. R. Cullis, *Adv. Mater.* **2023**, *35*, 2303370.
[57] A. K. K. Leung, Y. Y. C. Tam, S. Chen, I. M. Hafez, P. R. Cullis, *J. Phys. Chem. B* **2015**, *119*, 8698.
[58] M. Y. Arteta, T. Kjellman, S. Bartesaghi, S. Wallin, X. Wu, A. J. Kvist, A. Dabkowska, N. Székely, A. Radulescu, J. Bergenholtz, L. Lindfors, *Proc. Natl. Acad. Sci. USA* **2018**, *115*, E3351.
[59] K. J. Hassett, J. Higgins, A. Woods, B. Levy, Y. Xia, C. J. Hsiao, E. Acosta, Ö. Almarsson, M. J. Moore, L. A. Brito, *J. Controlled Release* **2021**, *335*, 237.
[60] M. Kawaguchi, M. Noda, A. Ono, M. Kamiya, M. Matsumoto, M. Tsurumaru, S. Mizukami, H. Mukai, S. Kawakami, *J. Pharm. Sci.* **2023**, *112*, 1401.
[61] D. Orthaber, A. Bergmann, O. Glatter, *J. Appl. Crystallogr.* **2000**, *33*, 218.
[62] S. Patel, N. Ashwanikumar, E. Robinson, Y. Xia, C. Mihai, J. P. Griffith 3rd, S. Hou, A. A. Esposito, T. Ketova, K. Welsher, K. Welsher, J. L. Joyal, Ö. Almarsson, G. Sahay, *Nat. Commun.* **2020**, *11*, 983.
[63] F. Campbell, F. L. Bos, S. Sieber, G. Arias-Alpizar, B. E. Koch, J. Huwyler, A. Kros, J. Bussmann, *ACS Nano* **2018**, *12*, 2138.

4.2.3 Supporting Information

WILEY-VCH

Title: On the influence of fabrication methods and materials for mRNA-LNP production: From size and morphology to internal structure and mRNA delivery performance *in vitro* and *in vivo*

Author: *Dongdong Bi[1#], Christoph Wilhelmy[2#], Dennis Unthan[1], Isabell Sofia Keil[3], Bonan Zhao[1], Bastian Kolb[2], Roman I. Koning[4], Melissa A. Graewert[5], Bert Wouters[1], Raphaël Zwier[6], Jeroen Bussmann[1], Thomas Hankemeier[1], Mustafa Diken[3], Heinrich Haas[2], Peter Langguth[2]*, Matthias Barz[1,7]*, Heyang Zhang[1]**

Affiliation:

[1]Leiden Academic Centre for Drug Research (LACDR), Leiden University, Einsteinweg 55, 2333 CC, Leiden, The Netherlands

[2]Department of Biopharmaceutics and Pharmaceutical Technology, Johannes Gutenberg University Mainz, 55128, Mainz, Germany

[3]TRON-Translational Oncology at the University Medical Center of Johannes Gutenberg University GmbH, 55131, Mainz, Germany

[4]Electron Microscopy Facility, Department of Cell and Chemical Biology, Leiden University Medical Center, 2300 RC, Leiden, The Netherlands

[5]European Molecular Biology Laboratory (EMBL) Hamburg Outstation c/o DESY, 22607 Hamburg, Germany

[6]Leiden Institute of Physics Research, Leiden University, Einsteinweg 55, 2333 CC, Leiden, The Netherlands

[7]Department of Dermatology, University Medical Center of the Johannes Gutenberg University Mainz, Langenbeckstraße 1, 55131, Mainz, Germany

# These authors contributed equally to this work.

Corresponding author:

h.zhang@lacdr.leidenuniv.nl; m.barz@lacdr.leidenuniv.nl; langguth@uni-mainz.de

Table S1. Different formulations of mRNA LNPs synthesized by NA, CD and EI.

Name	Formulation	molar ratio	Flow rate (mRNA: lipid, mL/min)	Manufacturing approach
NA-PEG	MC3/DOPE/Chol:PEG	40/10/48/2	9:3	NA
NA-pSar	MC3/DOPE/Chol:pSar	40/10/48/2	9:3	NA
CD-PEG	MC3/DOPE/Chol:PEG	40/10/48/2	1.2:0.4	CD
CD-pSar	MC3/DOPE/Chol:pSar	40/10/48/2	1.2:0.4	CD
EI-PEG	MC3/DOPE/Chol:PEG	40/10/48/2	/	EI
EI-pSar	MC3/DOPE/Chol:pSar	40/10/48/2	/	EI

Table S2. Results of dynamic light scattering (DLS) measurement and SAXS. The hydrodynamic radius measured by DLS were averaged from 3 independent measurements (n=3) and shown as mean ± SD. Radius of gyration was determined by SAXS as described in equation 3 of the Methods section. Note that LNPs were derived from another batch as the LNPs presented in Figure 2, which explains differing hydrodynamic diameters.

Name	Average hydrodynamic radius from DLS (R_h, nm)	Radius of gyration (R_g, nm)	R_g/R_h ratio
NA-PEG	32.7 ± 1.1	25.8	0.79
NA-pSar	45.2 ± 2.3	33.3	0.74
CD-PEG	55.1 ± 7.0	40.1	0.73
CD-pSar	70.5 ± 5.8	50.6	0.72
EI-PEG	87.5 ± 10	64.9	0.74
EI-pSar	99.5 ± 7.3	69.9	0.70

Table S3. Peak characteristics derived from Lorentzian fitting of mRNA LNPs manufactured with NA, CD and EI comprising either PEG or pSar as a shielding lipopolymer. Values and errors were calculated by formalism described in equation 6 of Methods section.

Name	Main peak			Front peak		
	Area (a.u.)	Position (nm^{-1})	Width (nm^{-1})	Area (a.u.)	Position (nm^{-1})	Width (nm^{-1})
NA-PEG	52.4 ± 1.0	1.04 ± 0.01	0.42 ± 0.01	-	-	-
NA-pSar	38.9 ± 1.8	1.10 ± 0.01	0.36 ± 0.01	-	-	-
CD-PEG	46.3 ± 1.3	1.21 ± 0.01	0.28 ± 0.01	-	-	-
CD-pSar	33.5 ± 0.9	1.15 ± 0.01	0.25 ± 0.01	-	-	-
EI-PEG	70.0 ± 2.7	1.12 ± 0.01	0.22 ± 0.01	77.7 ± 8.8	0.86 ± 0.01	0.67 ± 0.05
EI-pSar	88.1 ± 2.7	1.14 ± 0.01	0.24 ± 0.01	40.3 ± 7.6	0.83 ± 0.01	0.53 ± 0.08

Table S4. Size, PDI and d-spacing of PEGylated mRNA LNPs produced by NA with varying TFR, measured by DLS (n=3) and SAXS. DLS data was shown as mean ± SD. SAXS derived d-spacing and errors were calculated according to equation 7 in Methods section.

TFR	Average hydrodynamic diameter (nm)	PDI	Porod exponent	d-spacing (nm)
1 mL/min	249.0 ± 12	0.195 ± 0.04	2.88 ± 0.1	6.01 ± 0.01
3 mL/min	142.4 ± 9.7	0.130 ± 0.02	3.29 ± 0.1	5.90 ± 0.01
15 mL/min	110.2 ± 8.8	0.154 ± 0.03	3.74 ± 0.1	6.16 ± 0.01

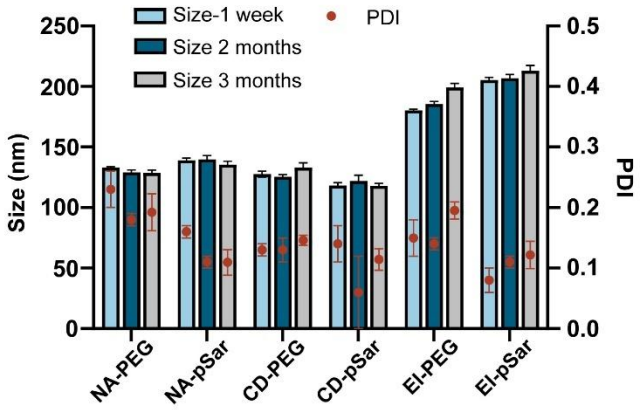

Figure S1. Stability of the LNPs (n=3) after 3 months of storage at 4 °C. Data are presented as mean ± SD. The formulated mRNA LNPs were named as manufacturing approach-shielding lipopolymer.

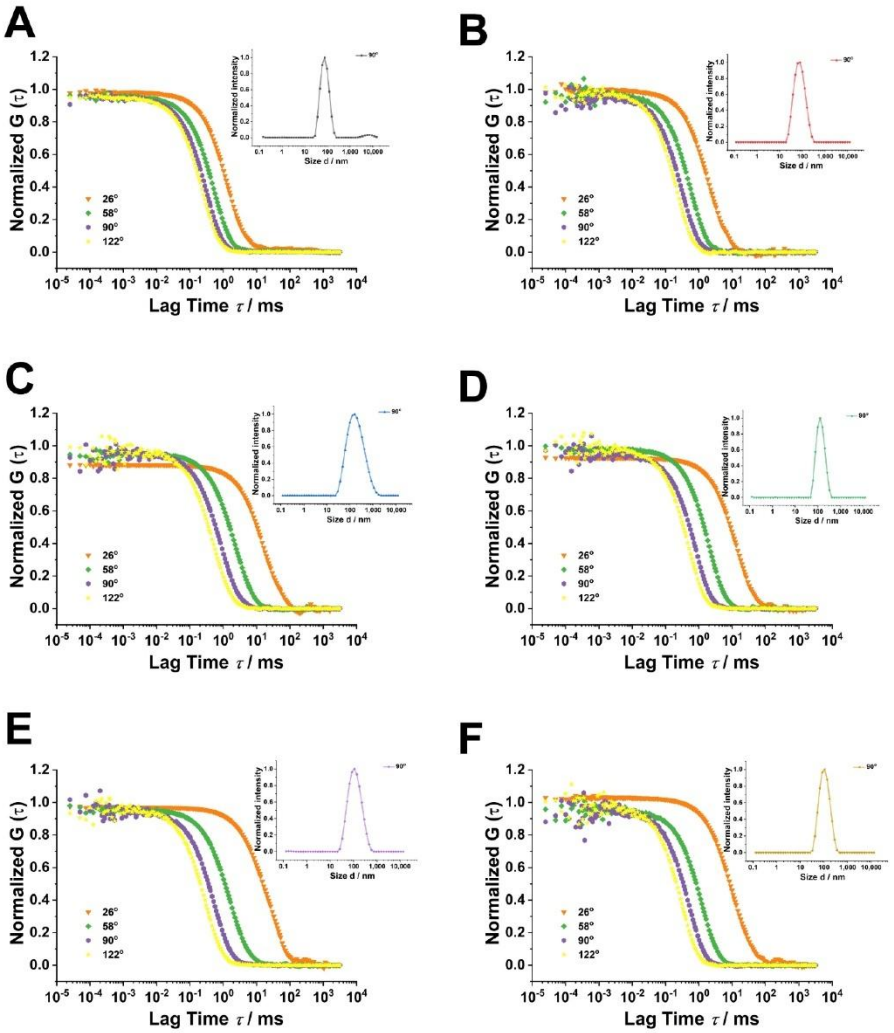

Figure S2. Correlation functions recorded at a scattering angle of 26°, 58°, 90° and 122° of (A, C, E) PEGylated mRNA LNPs synthesized using (A) custom microfluidic device (CD), (C) ethanol injection (EI) and (E) NanoAssemblr (NA), and (B, D, F) pSar-containing mRNA LNPs synthesized using (B) CD, (D) EI and (F) NA.

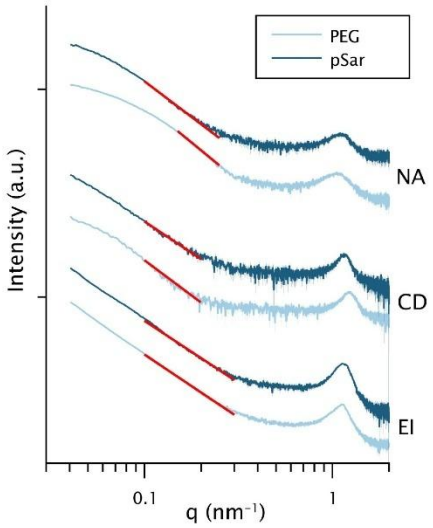

Figure S3. Determination of the Porod exponent for evaluation of surface fractal dimension. SAXS patterns of PEG-containing mRNA LNPs (dark blue) and pSar-containing mRNA LNPs (light blue) produced by NA (top panel), CD (middle panel) and EI (bottom panel) are shown. Scattering patterns are vertically shifted for better visualization. Red lines indicate the fit according to the formalism displayed in equation 5 of Methods section.

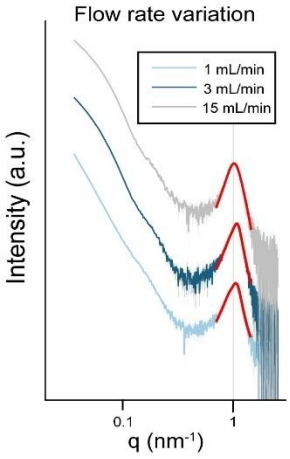

Figure S4. SAXS patterns of PEGylated mRNA LNPs produced using NA at different TFR. Red lines indicate the Lorentzian fit of the Bragg peak at around 1 nm^{-1}, which position is not influenced by the TFR.

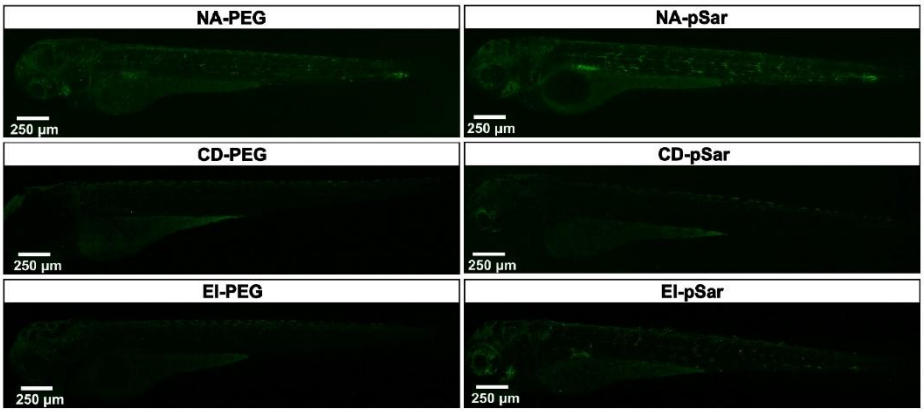

Figure S5. *In vivo* transfection effects of NA-PEG/pSar, CD-PEG/pSar and EI-PEG/pSar LNPs after 3 months of storage (n=6). The scale of the whole fish is 250 μm.

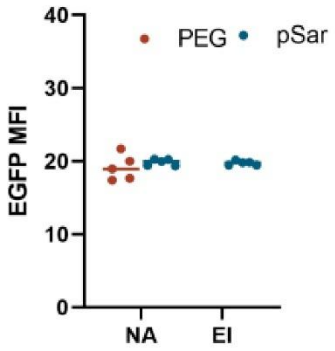

Figure S6. Quantification of transfection effect (as indicated by EGFP MFI) of mRNA LNPs (after 3-months storage at 4 °C) in zebrafish embryos through intravenous injection. EGFP MFI was obtained in the whole fish view images by ImageJ (n=6).

4.3 Direct structural investigation of pH responsiveness in mRNA LNPs: refining paradigms

4.3.1 Summary and Contributions

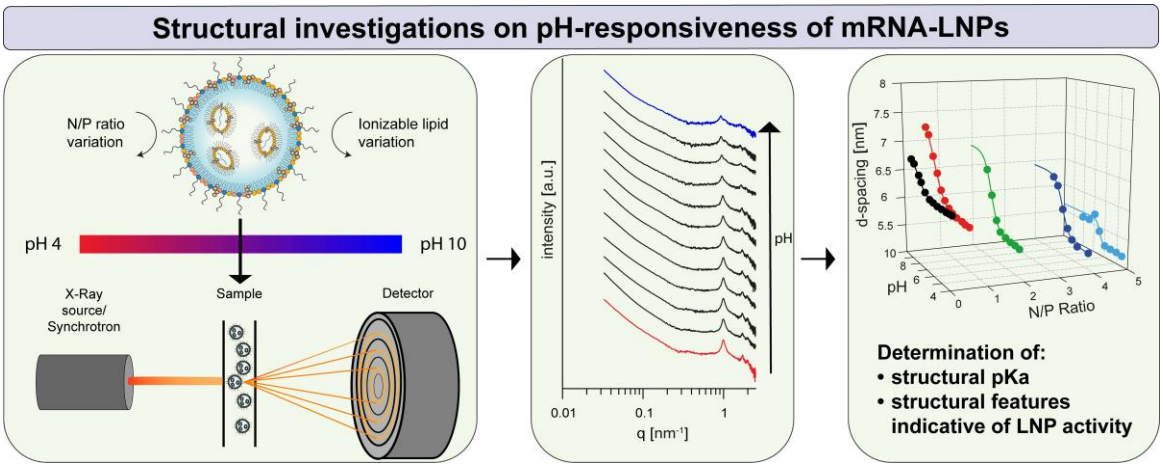

Figure 4.3-1: Graphical abstract of the publication 4.3. Different mRNA LNP formulations with varying compositions (ionizable lipid, N/P ratio) were investigated using SAXS in different environmental pH buffers. Structural investigations revealed organizational features present in highly potent formulations, as well as structural parameters that are altered by pH, allowing for the determination of structural pK_a values. As published in [162].

Despite the extensive research conducted not only since the COVID-19 pandemic, a deep understanding of how the composition of LNPs influences therapeutic performance remains unclear. Specifically, the choice of ionizable lipid has a significant impact on both the physicochemical properties and *in vivo* behavior. During manufacturing, the ionizable lipid component complexes the mRNA due to its cationic charge in acidic media. After administration at near-neutral physiological pH, the formulation possesses no net charge, thereby allowing longer circulation times and reducing charge-related toxicities. During endosomal uptake, the stepwise acidification of the endosomal compartment allows positive charges to reappear, facilitating the release of nucleic acids into the cell's cytosol. Therefore, gaining deeper insights into the structure-function relationships for the ionizable lipid and understanding how environmental pH influences the structural features of the formulation is crucial for improving formulations for future applications.

Within this project, the influence of ionizable lipids, as well as the lipid-to-mRNA ratio (N/P ratio), on structure was investigated as a function of environmental pH. For this, SAXS measurements were performed in different pH buffers, ranging from acidic conditions at pH 4.5 to near-neutral or basic conditions (pH 8 or 10, depending on N/P ratio). In the first part of the work, different ionizable lipids in otherwise similar LNP formulations were investigated, where lipids with known

activity (varying from low to highly potent lipids) were chosen. The distance of the repeating unit changed with pH, allowing for the determination of a structural pK_a value of the formulation. Here, depending on the lipid composition, differences from the standard pK_a determination using fluorescence dyes could be distinguished. Furthermore, distinct structural features that varied along with known transfection potential were revealed, including the repeating unit distance and surface mass fractality. These could serve as predictors of good biological performance if used in screening experiments.

In the second part of the work, the influence of the N/P ratio on SAXS-derived parameters and the pH responsiveness of these were investigated. Here, we tested formulations ranging from mRNA excess (N/P<1) to ionizable lipid excess (N/P>1). While mRNA excess during formulation led to LNPs with uniform structural organization, LNPs with an excess of ionizable lipid exhibit SAXS patterns with overlapping scattering motifs, indicating structural heterogeneity. Furthermore, the repeating unit distance, long-range order, and surface roughness are influenced by the N/P ratio. Notably, the pH-responsive behavior of the LNPs is affected, with an increased molar ratio of RNA leading to a shift in the pK_a value towards higher values. This highlights that not only the choice of ionizable lipids but also the mRNA-to-lipid ratio can be used to fine-tune formulations for different targeted cell types with varying ionizable requirements.

The results of this work can help to elucidate the implications of compositional and environmental changes on the structure and function of formulations. We propose general, applicable standards for analyzing SAXS experiments of mRNA-carrying nanoparticles and identifying parameters that can be used for quality determination or as potency predictors in early formulation development studies.

This work was published in the following article:

Wilhelmy, C.; Uebbing, L.; Kolb, B *et al.* Direct structural investigation of pH responsiveness in mRNA lipid nanoparticles: Refining paradigms. *Journal of Controlled Release* **2025**, 113848, doi:10.1016/j.jconrel.2025.113848.

Own contributions:

Authorship: First author

Formal analysis, Investigation, Methodology

Writing: Original draft, visualization, review and editing

Contributions of all authors:

Conceptualization: H.H., P.L.

Formal analysis: C.W.

Funding acquisition, P.L.

Investigation: C.W., L.U., B.K., M.G.

Methodology: C.W., L.U.,

Project administration: P.L.

Supervision: H.H., P.L.

Visualization: C.W.

Writing- original draft: C.W., H.H.

Writing – review and editing: L.U., B.K., M.G., T.N., H.H., P.L

4.3.2 **Publication**

Journal of Controlled Release 384 (2025) 113848

Contents lists available at ScienceDirect

Journal of Controlled Release

journal homepage: www.elsevier.com/locate/jconrel

Direct structural investigation of pH responsiveness in mRNA lipid nanoparticles: Refining paradigms

Christoph Wilhelmy [a], Lukas Uebbing [a], Bastian Kolb [a], Melissa A. Graewert [b], Thomas Nawroth [a], Heinrich Haas [a,*], Peter Langguth [a,*]

[a] Department of Biopharmaceutics and Pharmaceutical Technology, Johannes Gutenberg-University, Mainz, Germany
[b] European Molecular Biology Laboratory, Hamburg Outstation, Hamburg, Germany

ARTICLE INFO

Keywords:
Messenger RNA
Lipid nanoparticle
LNPs
SAXS
Ionizable lipids
Structure-function correlation

ABSTRACT

Using small angle X-ray scattering measurements, structural coherencies in lipid nanoparticle (LNP) formulations comprising messenger RNA (mRNA) were elucidated in response to pH changes and as a function of RNA to lipid ratio. Formulations were assembled using selected ionizable lipids with well-known activity from previous experiments, with otherwise identical composition. Several structural parameters were determined, including internal organization, fraction of ordered material, the underlying repeating distance, and the fractal dimension of the overall particles. Repeat distances increased with increasing pH, with profiles similar to the shape of pK_a curves, therefore allowing to directly reveal the structural implication of the pH responsiveness inside the particles. The fractal dimension, which so far had not been in the center of attention for quality control, was correlated with biological activity. Such systematic data on structure-function coherencies in LNPs can serve as complementary methods to standard lab-based quality control measures. This can help to facilitate and accelerate the rational formulation development of new RNA therapeutics.

1. Introduction

For the application of messenger RNA (mRNA) in pharmaceutical products, delivery systems tailored for the intended route of application and therapeutic intervention are required [1–5]. Since the authorization of the first RNA-based therapies, with applications in gene silencing therapy [6] and as vaccines for SARS-CoV-2 [7], so-called lipid nanoparticles (LNPs) have become a focal point of interest. These consist, besides the nucleotide cargo, of a specific mixture of four lipids, with an ionizable lipid being a key element for functionality [5,8,9].

Despite the broad interest, many aspects of LNPs related to their activity and quality remain elusive to the developer community. A few generally accepted concepts or paradigms exist, such as regarding the optimum pK_a value of the ionizable lipid [10], or the capacity to undergo lamellar to hexagonal phase transitions [11,12]. However, these are more conceptual than precise directives for selecting suitable systems.

So far, the development of novel delivery systems largely relies on screening lipids, lipid compositions, and the lipid to RNA ratio (known as N/P ratio) [2,13–15]. However, this process can be tedious and time-consuming because of the vast number of potential combinations, along with the risk that not all highly active compositions are recognized. Here, we pursue an approach to identify structural aspects of LNPs that correlate with activity, to provide a knowledge base for better experimental planning towards improved formulations.

One parameter of interest is the pK_a value of the ionizable lipid, which gives information on how the charge of the ionizable lipid changes with pH. It is considered relevant for the efficacy of endosomal escape [16,17]. The pK_a is typically determined by a fluorescence assay using the dye molecule 6-(p-toluidino)-2-naphthalenesulfonic acid (TNS). This process involves the binding of the dye and a change in fluorescence intensity as a function of the lipid's ionization state within the particle [10]. It should be noted that the pK_a value determined by this fluorescence assay is strongly affected by the local environment in the LNP. It differs substantially from that of one of the free ionizable lipid molecules in solution, which is typically much higher [18]. Therefore, it is frequently referred to as the apparent pK_a value.

Although not supported by all experimental data, it is widely accepted that an apparent pK_a value between 6 and 7 is most appropriate for optimal LNP activity. Jayaraman and colleagues stated that a pK_a of

* Corresponding authors.
E-mail addresses: haashein@uni-mainz.de (H. Haas), langguth@uni-mainz.de (P. Langguth).

https://doi.org/10.1016/j.jconrel.2025.113848
Received 14 March 2025; Received in revised form 12 May 2025; Accepted 14 May 2025
Available online 20 May 2025

6.2 to 6.5 is ideal for siRNA delivery to the liver [16]. Hassett et al. published that the optimal pK_a for immunogenicity after intramuscular administration is between 6.6 and 6.8 [19], which led to the development of the SM-102 lipid used in the Spikevax® vaccine. Despite this, the pK_a of the ionizable lipid ALC-0315 used in the Comirnaty® vaccine is reported as 6.09 [20], but it also led to comparable therapeutic results.

This highlights that the apparent pK_a of the LNP determined by the aforementioned method does not always allow for an exact prognosis of potential therapeutic efficiency, without even considering differences among tested cell types and routes of administration [21]. Notwithstanding these unresolved issues, it seems clear that the ability to measure and control the pK_a value is an essential tool for tailoring nanoparticles. For example, it has been shown that by adding a fifth component, the so-called selective organ targeting (SORT) molecule, to the LNP formulation, selectivity towards lung or spleen was achieved, with the apparent pK_a of the formulation being shifted towards higher or lower values [22].

While the TNS assay is a straightforward lab-based method, the obtained apparent pK_a values are highly influenced by experimental conditions such as buffer choice and varying dye sensitivity at extreme pH values [23], which impairs the comparability of results obtained from different laboratories and systems. A general limitation of the fluorescence assay is that it detects only the lipids accessible to the dye from the bulk phase, which does not necessarily reflect the properties of the overall particle. An alternative method to estimate the pK_a of an LNP formulation involves computational techniques that allow for estimation from the lipid structures [24]. Other approaches include molecular dynamics simulations to study pH-driven phase transitions and to determine the actual pK_a inside the LNP formulation [25]. However, although these approaches deliver promising results, they require further verification through comparison with more experimental data.

Here, we applied an approach to directly determine pH-dependent changes in the structural properties of the overall particle using small angle X-ray scattering (SAXS) measurements [26]. In extensive previous SAXS and small angle neutron scattering (SANS) studies [26–30], we revealed several fundamental structural features of mRNA nanoparticles and demonstrated the influences of manufacturing protocols, lipid composition, and polymer grafting on structure and functionality [29,31,32]. By tracking lamellar spacing and other structural parameters as a function of pH in multilamellar model systems, we obtained curves similar in shape to pK_a curves, allowing us to determine the structural analogue of the pK_a value, denominated as structural pK_a.

In the present measurements, we investigated the pH responsiveness of LNPs containing a series of ionizable lipids, namely DODAP, DODMA, Dlin-MC3-DMA (MC3), and ALC-0315, using SAXS measurements. The relative activity of formulations based on the respective ionizable lipids is well-known from several previous studies, which describe potency both in vitro and in vivo [18,33,34]. Based on that, we further classified these model lipids with increasing potency in the order given above. We revealed the structural characteristics of the different systems, including their type of internal organization (lamellar or hexagonal), the repeating distance of the ordered material, and overall particle organization, expressed as the fractal dimension. LNPs from lipids with higher biological activity shared certain structural properties. These insights may lead to refined paradigms for quality evaluation of LNP formulations and criteria for tailoring future mRNA delivery systems.

2. Materials and methods

2.1. Materials

1,2-dioleoyl-sn-glycero-3-ethanolamine (DOPE) was manufactured by Lipoid GmbH (Ludwigshafen, Germany). 1,2-dioleyloxy-3-dimethylaminopropane (DODMA), N-palmitoyl-sphingosine-1-{succinyl [methoxy(polyethylene glycol)2000]} (C16-PEG2000-Ceramide), and Cholesterol were manufactured by Avanti Polar Lipids (Alabaster, AL, USA). DODAP (1,2-dioleoyl-3-dimethylammonium-propane), (6Z,9Z,28Z,31Z)-heptatriacont-6,9,28,31-tetraene-19-yl-4-(dimethylamino) butanoate (DLin-MC3-DMA) and ALC-0315 ([(4-Hydroxybutyl) azandiyl]bis(hexan-6,1-diyl)bis(2-hexyldecanoat)) was purchased from MedChemExpress (Monmouth Junction, NJ, USA). mRNA encoding for eGFP was purchased from etheRNA (Niel, Belgium). 6-(p-toluidino)-2-naphthalenesulfonic acid (TNS), KH_2PO_4, and Na_2HPO_4 were obtained from Sigma-Aldrich (St. Louis, MO, USA), and glycylglycine was obtained from Carl Roth (Karlsruhe, Germany).

2.2. LNP preparation

LNPs were prepared using a dedicated ethanol injection method developed by our group as described earlier [31]. The mRNA was diluted to the intended concentration with a 10 mM aqueous glycylglycine solution (pH 5.7 ± 0.1), and the ethanolic lipid stock solutions were pre-mixed to obtain the targeted molar ratios (Table 1). The aqueous mRNA buffer was pipetted onto the lipid mix, and the sample was then immediately vortexed for 10 s. This single-step protocol allows for the manufacturing of mRNA LNPs in a directly applicable buffer without further modification. The LNPs manufactured with this protocol exhibit larger sizes than those obtained with microfluidic mixing (about 200 nm compared to 100 nm) but were described to be comparable in in vitro and in vivo potency and show similar structural features [32]. Therefore, particularly regarding the structural features observed here, we expect the results to be equally applicable for microfluidically manufactured mRNA LNPs.

All LNPs comparing different ionizable lipids were prepared at a molar ratio of ionizable lipid to mRNA (N/P ratio) of 5:1. For the N/P ratio variation, LNPs between N/P 0.2 and N/P 5 were formulated. Molar ratios were calculated as 100 mol% = $\sum$ mol% (helper lipid, ionizable lipid, cholesterol, stealth moiety). The LNP composition can be seen in Table 1.

2.3. Dynamic light scattering (DLS)

The samples were diluted to an appropriate concentration (1 mg/mL total lipid for size, 0.1 mg/mL for zeta potential) in glycylglycine buffer and then transferred to a Zetasizer Nano ZS (Malvern Panalytical Ltd., UK) for size measurements using dynamic light scattering (DLS) and zeta potential determination. The DLS measurements were conducted as backscattering measurements (scattering angle: 173°) at 25 °C after a 30 s equilibration time. Results are presented in Supplementary Table 1.

2.4. Small-angle X-ray scattering (SAXS)

Data were obtained at the P12 BioSAXS beamline of the European Molecular Biology Laboratory (EMBL) at the PETRAIII synchrotron, located at DESY (Hamburg, Germany) [35]. The experiments were performed with an X-ray energy of 10 keV ($\lambda = 0.124$ nm) at a 3.0 m sample detector distance, resulting in a q range of ~0.03–7 nm^{-1}. Samples had a total lipid concentration of 2.5 mg/mL. Using the BioSAXS automatic sample changer [36], 30 µL of the sample was transferred to a quartz capillary mounted in vacuum, where the sample was exposed 20 times for 0.095 s to the beam. The scattering intensity was collected by a Pilatus 6M detector (Dectris, Baden, Switzerland). The buffer of each sample was measured under the same conditions before and after each sample run for buffer subtraction. For the investigations on LNP pH responsiveness, the samples were mixed with phosphate buffer as proposed by Sörensen [37] from pH 4.5 to 10 for samples with $N/P < 1$ and from pH 4.5 to 8 for samples with $N/P > 1$. Aqueous solutions of KH_2PO_4 and Na_2HPO_4 at 150 mM were mixed in different ratios, and the pH was adjusted with 0.1 M HCl or NaOH. Samples were mixed with phosphate buffers immediately before the SAXS measurements, and the pH was checked. The ATSAS 3.0 software package (EMBL Hamburg, Germany) was used for averaging of repeated measurements

Table 1
Composition of investigated mRNA LNPs.

Formulation	Ionizable Lipid	Ion. Lipid [mol%]	DOPE [mol%]	Cholesterol [mol%]	Stealth lipid [mol%]	mRNA [mol%]
DODAP N/P 5	DODAP	40	10	48	2	8
DODMA N/P 5	DODMA	40	10	48	2	8
MC3 N/P 5	DLin-MC3-DMA	40	10	48	2	8
ALC-0315 N/P 5	ALC-0315	40	10	48	2	8
DODMA N/P 0.2	DODMA	1.6	48.4	48	2	8
DODMA N/P 0.65	DODMA	5.2	44.8	48	2	8
DODMA N/P 2	DODMA	16	34	48	2	8
DODMA N/P 4	DODMA	32	18	48	2	8
MC3 N/P 0.2	DLin-MC3-DMA	1.6	44.8	48	2	8
MC3 N/P 0.65	DLin-MC3-DMA	5.2	44.8	48	2	8
MC3 N/P 2	DLin-MC3-DMA	16	34	48	2	8
MC3 N/P 4	DLin-MC3-DMA	32	18	48	2	8

and buffer subtraction [38]. Subtracted data were further analyzed using QTIPlot 1.0.1 (IONDEV Sr, Bucuresti, Romania), as described in the following section.

All scattering data are given as scattering intensity I as a function of the momentum transfer, q, calculated according to eq. (1), with 2θ being the scattering angle and λ the X-ray wavelength.

$$q = \frac{4\pi}{\lambda}\sin\left(\frac{2\theta}{2}\right) \tag{1}$$

SAXS data for the investigated q-range include the form factor of the single lipid nanoparticles, which is determined by the overall size, shape, and surface properties of the nanoparticles, as well as Bragg reflections derived from mRNA-lipid interactions as part of their internal structure.

Determination of the intensity decay of the SAXS pattern can reveal information about the shape and (surface) fractal dimension of the nanoparticles. Using the power law shown in Eq. (2), the Porod exponent, D, is determined.

$$I(q) = I_0 \cdot q^{-D} \tag{2}$$

Scattering from ideally smooth interfaces is characterized by a Porod exponent of 4 (Porod law [39]), while a value of 2 indicates a diluted Gaussian chain, and a slope of −1 points towards rigid rods. Of interest here are the intermediate values, which reflect the surface roughness. By using eq. (3), the surface fractal dimension, D_s, is obtained [40]. For ideally smooth surfaces, D_s is 2, while with rising value (between 2 and 3), the surface roughness increases [41]. Values above 3 are indicative of conformations of polymers in solution, as stated above.

$$D_s = 6 - D \tag{3}$$

For investigations of internal structure properties, Lorentzian fit functionality was used for peak fitting in the SAXS pattern, as given in eq. (4)

$$\mathrm{I(q)} = \mathrm{I_0} + \frac{2\mathrm{A}}{\pi}\cdot\frac{\mathrm{w}}{4\cdot(\mathrm{q}-\mathrm{q_c})^2 + \mathrm{w}^2} \tag{4}$$

where I_0 is the baseline intensity, A the area under the peak, w the peak width at half maximum (FWHM), and q_c the peak center position (Supplementary Table 2). The peak is derived from the ordered mRNA-lipid complexes [26,30], where from the position of the peak center, the repeat distance (d-spacing) is obtained by the Bragg eq. (5)

$$d = \frac{2\pi}{q_c} \tag{5}$$

The peak width, w, provides information about the extent of the ordered stacks [42], which can be described by the correlation length, ξ. In the model for liquid crystalline structures [43] correlation length, ξ, is calculated by Eq. (6), which is defined as the distance at which the positional correlation decays to the value 1/e:

$$\xi = \frac{2}{\mathrm{w}} \tag{6}$$

For formulations with an N/P ratio > 1, for the Bragg peak, Lorentzian fits with two overlaying peaks were used according to eq. (7)

$$\mathrm{I(q)} = \mathrm{I_0} + \frac{2\mathrm{A_1}}{\pi}\cdot\frac{\mathrm{w_1}}{4\cdot(\mathrm{q}-\mathrm{q_{c_1}})^2 + \mathrm{w_1}^2} + \frac{2\mathrm{A_2}}{\pi}\cdot\frac{\mathrm{w_2}}{4\cdot(\mathrm{q}-\mathrm{q_{c_2}})^2 + \mathrm{w_2}^2} \tag{7}$$

For the determination of the structural pK_a of the LNP formulations, a Boltzmann fit was used to describe the sigmoidal evolution of d-spacing as a function of pH and to determine the inflection point of the function as in eq. (8)

$$d - spacing = d - spacing_{max} - \frac{d - spacing_{max} - d - spacing_{min}}{1 + 10^{\frac{pKa - pH}{pH}}} \tag{8}$$

Where d-$spacing_{max}$ and d-$spacing_{min}$ are the upper and lower limits of the fit, and pK_a is the inflection point of the function, which is taken as structural pK_a.

2.5. pK_a fluorescence assay

A common previously published assay using the fluorescent dye 2-(p-toluidino)-6-naphthalene sulfonic acid (TNS) was performed to determine the apparent formulation pK_a [44]. Measurements were performed in triplicate on black TC-coated 96-well plates, with each well containing 10 μL sample (at 0.1 mg/mL total lipid), 90 μL buffer (phosphate buffer as proposed by Sörensen from pH 4.5 to pH 10 [37]) and 2 μL of TNS in DMSO (300 μM). The fluorescence was measured from the top on a TECAN Infinite 200Pro plate reader (Tecan Group Ltd., Männedorf, Switzerland) at 325 nm excitation and 435 nm emission wavelength. Apparent pK_a of the formulation was determined using a sigmoidal Boltzmann fit,

$$NFI = NFI_{max} - \frac{NFI_{max} - NFI_{min}}{1 + 10^{\frac{pKa - pH}{pH}}} \tag{9}$$

where NFI_{max} and NFI_{min} are the maximal and minimal normalized fluorescence intensity, and pK_a is the inflection point of the fit, which is stated as the apparent pK_a of the formulation.

3. Results

3.1. Comparison of ionizable lipids

We investigated mRNA LNPs bearing four different ionizable lipids (DODAP, DODMA, MC3, and ALC-0315; Table 1, Fig. 1A) under otherwise identical conditions. For manufacturing, we used a proprietary protocol (see Methods and Materials), which does not require complex equipment, and has proven to result in particles with equivalent biological activity. As determined by comparative studies, we assume the

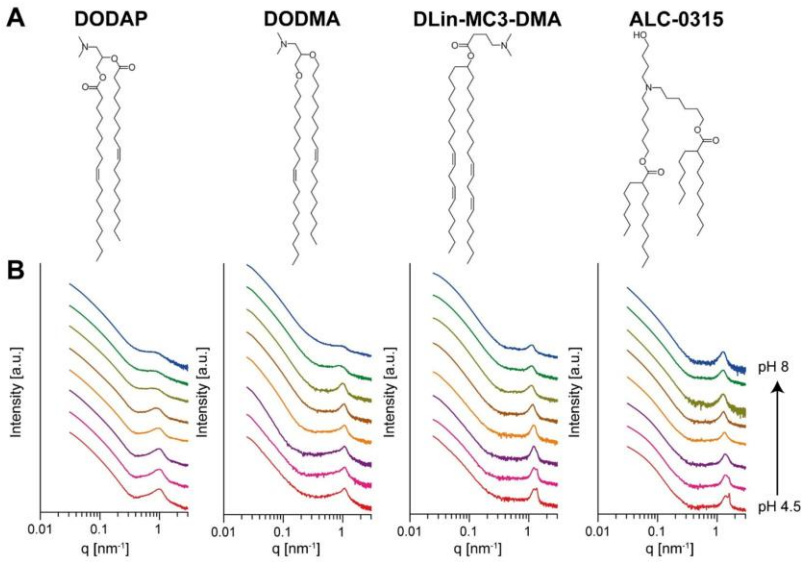

Fig. 1. SAXS measurements for mRNA-LNPs with different ionizable lipids (from left to right: DODAP, DODMA, DLin-MC3-DMA, ALC-0315): A. Structure of the used ionizable lipids in the order mentioned above. B. SAXS curves of mRNA-LNP samples over a pH range from 4.5 (red curves, bottom) to pH 8.0 (dark blue curves, top) in ΔpH = 0.5 steps. In all cases, phosphate buffers were used for pH adjustment. The SAXS curves are shifted on the logarithmic y-axis for better visualization. (For interpretation of the references to colour in this figure legend, the reader is referred to the web version of this article.)

particles to be equivalent in internal structure to LNPs, which are produced with microfluidic approaches [32]. Based on previous studies, the relative potency of these model lipids is well-known, where activity is assumed to increase in the above-mentioned order. The samples' size determination by Dynamic Light Scattering (DLS) revealed average sizes between 170 and 210 nm with a polydispersity index around 0.2, and Zeta-Potentials between 19 and 30 mV for all formulations (see Supplementary Table 1).

To gain insight into structural changes during manufacturing and to mimic the behavior of the LNPs after administration, SAXS measurements were conducted as a function of bulk phase pH. These conditions reflect the transition from near-neutral pH during circulation in the bloodstream to stepwise acidification during endosomal uptake, leading to acidic pH in late endosomal processing [45].

All SAXS patterns shared some common features, including smooth curves with a steep decay in intensity up to a q-value of approximately 0.4 nm^{-1} and a pronounced peak resulting from Bragg reflections of ordered material. For all formulations, the Bragg peak position shifted towards lower q-values (increase of d-spacing) with increased pH. This shift was accompanied by a decrease in the area and a broadening of the peak, where for DODAP and DODMA-LNPs, the peak was barely visible at pH 8 (Fig. 1B). The Bragg peaks originated from repeating lipid and mRNA stacks, consisting of only a very low number of repeating units [26,29,30]. As observed in previous studies, we found indications for the presence of two types of ordered lipid material (e.g., with high and low amounts of mRNA inserted) having slightly different repeat distances. Therefore, we fitted the Bragg reflections using a double Lorentzian function and determined the peak position, peak width, and peak area of each peak. While for the high-q (lower d spacing) peak of the two Bragg peaks, the position decreased with an increasing pH, the second peak, at a lower q-value (higher d spacing), showed only minor changes or even increased for MC3- and ALC-bearing LNPs. Additionally, the area of the peak at higher q-values decreased with increasing pH, while the area of the low-q peak either remained unchanged or increased with increasing pH (Fig. 2). We conclude that the low-q peak derived from lipidic substructures with little or no mRNA content, while the high-q peak originates from mRNA/lipid stacks and is further referred to as the main peak. Additionally, for MC3 and ALC-0315, a third, very sharp peak, corresponding to a repeat distance of about 4 nm, was visible at low pH, which diminished with increasing pH and disappeared above pH 5.5 (Supplementary Fig. 1). Partial phase separation of the lipid mixture, leading to the formation of domains (e.g., rafts) with specific repeat distances, may be the reason for this observation. These results highlight the complexity of the LNPs as pharmaceutical products. Multiple fractions with varying structures and pH-dependence may coexist in the same particles or in the form of different particle populations.

For the main peak, resulting from repeating lipid bilayers with mRNA inserted in the hydrophilic head group regions, the pH dependence of the d-spacing arises from the electrostatic interactions between mRNA and lipids. At acidic pH, the ionizable lipid reaches its highest level of protonation, resulting in the strongest electrostatic attraction with the negatively charged mRNA and, thus, the lowest repeat distance. As the pH increases, the ionizable lipid's protonation level decreases, and the negative charge of mRNA is no longer completely balanced by positive lipid charges. This results in weakening of the attraction forces between mRNA and lipid, and thus, increased repeat distances, and a loss of order. Therefore, the position of the main peak shifted to lower q, the width increased (indicative of a loss of correlation length), and its area decreased as pH increased. For the secondary peak, which corresponds to a higher repeat distance, we expect either a lower amount of mRNA or none to be inserted between the repeating layers. In that case, the reduction of the lipid protonation state with an increase in pH results in a reduction of the repulsive interaction between the adjacent layers, consistent with the observed trend for a decrease in the repeat distance (Fig. 2). The large excess of ionizable lipid in relation to the mRNA (N/P 5) makes segregation into fractions of different composition and

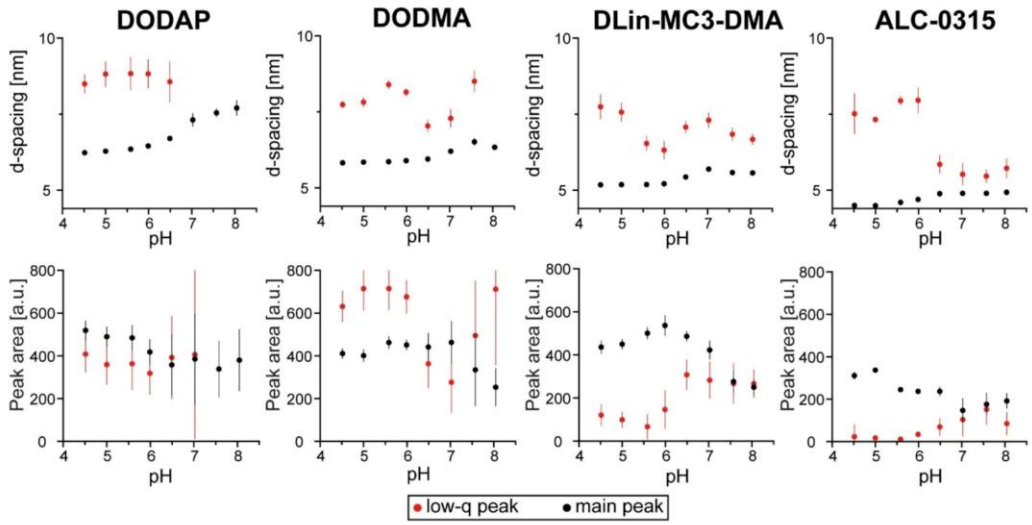

Fig. 2. d-spacing and peak width from both peak fractions. As determined by double-peak Lorentzian fitting, d-spacing (top), and peak area (bottom) of the low-q peak (red) and the main Bragg peak (black) are displayed as a function of pH. Note that for DODAP over pH 7, no low-q peak was detectable due to overlay with intensity decay in the Porod region, and at pH 8, the low-q d-spacing exceeds the scale of the graph.

structure plausible. It is important to note that from the batch SAXS measurements presented here, it is difficult to determine whether the different patterns coexisted in the same particles, or whether different particle populations having the respective structure were present. For a clearer answer, fractionation of the particles based on size, surface charge, or other characteristics before the SAXS measurements would be beneficial. For example, coupling of asymmetrical flow field flow fractionation to SAXS (AF4-SAXS) has successfully been applied to combine a size separating technique with structure analysis for investigation of lipoplexes and LNPs [28,46].

The observations were in accordance with previous findings on multilamellar model systems with and without mRNA [26]. Similar to the above conjectures, multilayers without mRNA displayed decreasing d-spacing with increasing pH, while in the presence of mRNA, the d-spacing increased. Here, we were able to determine such pH-dependent effects for the situation in LNPs, which are of higher practical interest but are more complex and less defined, due to the intrinsically lower degree of order and the coexistence of different characteristic structures.

The pH dependence of the d-spacing for the main peak was analyzed using a Boltzmann formalism (see Methods section). The inflection points of the sigmoidal curves were taken as the structural pK_a and compared to the apparent pK_a, derived from the fluorescence-based assay (Fig. 3A, Table 2). Interestingly, for DODMA and MC3-LNPs, the apparent pK_a determined by the TNS assay (Table 2, Supplementary Fig. 2) showed comparable values to the SAXS-based approach, whereas differences were observed for LNPs composed of DODAP and ALC-0315. While the apparent pK_a of DODAP-LNPs was lower than the structural pK_a, for ALC-0315-LNPs, it was the opposite.

Several structural aspects of the systems derived from different ionizable lipids showed correlation with their activity [18,33,34]. The overall d-spacing of the LNP formulations manufactured from lipids with higher activity showed lower d-spacings than the LNPs made with low activity ionizable lipids (Fig. 3A, Supplementary Table 3). At pH 4.5, the value for DODAP-LNPs was almost 2 nm higher than that for ALC-0315, even though the ALC-0315 lipid possesses a bulkier structure than DODAP. As well, the total shift of d-spacing was lower for the LNPs comprising high activity ionizable lipids (Fig. 3A). While for DODAP-LNPs the increase of the repeat distance was 1.45 nm, for LNPs with MC3- and ALC-0315 it was only about 0.5 nm.

In addition to changes in peak position, we observed differences in peak area and width as a function of pH (Supplementary Fig. 3). The peak area diminished for all tested formulations as the pH increased. The peak width increased for the systems manufactured with the two less active lipids (DODAP and DODMA), resulting in a decrease in correlation length as pH increased. The higher activity MC3- and ALC-0315-LNPs did not show such an effect (Fig. 3B). When investigating the organization of the ordered stack, depicted as the ratio of correlation length to repeating distance, particularly for ALC-0315-containing LNPs, no loss of spatial order within the tested pH range was observed (Supplementary Fig. 4). Therefore, the loss of order with increasing pH is lower for active LNPs than for those with less active lipids.

Another property correlated with activity is the Porod exponent, D. It is derived from a power law analysis of the intensity decay by fitting a function based on eq. (2) to the experimental curve between the Bragg peak and the Guinier region. For scattering from an ideally smooth interface, the intensity decays with the fourth power of q ($I(q) \sim q^{-4}$) [39]. Real interfaces exhibit a certain roughness, which, in this case, results from the distribution of molecular moieties perpendicular to the interface. This leads to decreasing values for D as surface roughness increases. There are several ways to express the surface roughness. In a general mathematical approach, instead of the Porod exponent, the (interfacial) fractal dimension, D_s, is observed (see eq. (3)) [29,47].

D_s has a value of 2 for ideal interfaces, and up to $D_s = 3$, increasing surface roughness is deduced. Values for D_s higher than 3 are better represented by a model of a Gaussian (polymer) chain conformation [40,41]. In earlier studies, a higher biological activity was observed for LNPs with higher surface fractal dimension [31]. Here, further to that previous finding, we observed that LNPs prepared with three higher activity ionizable lipids showed an increase in surface fractal dimension upon pH decrease, while the low activity ionizable lipid DODAP exhibited no change across the entire pH range (see Fig. 3C). Notably, the pH at which the LNPs reorganize towards a higher fractal dimension

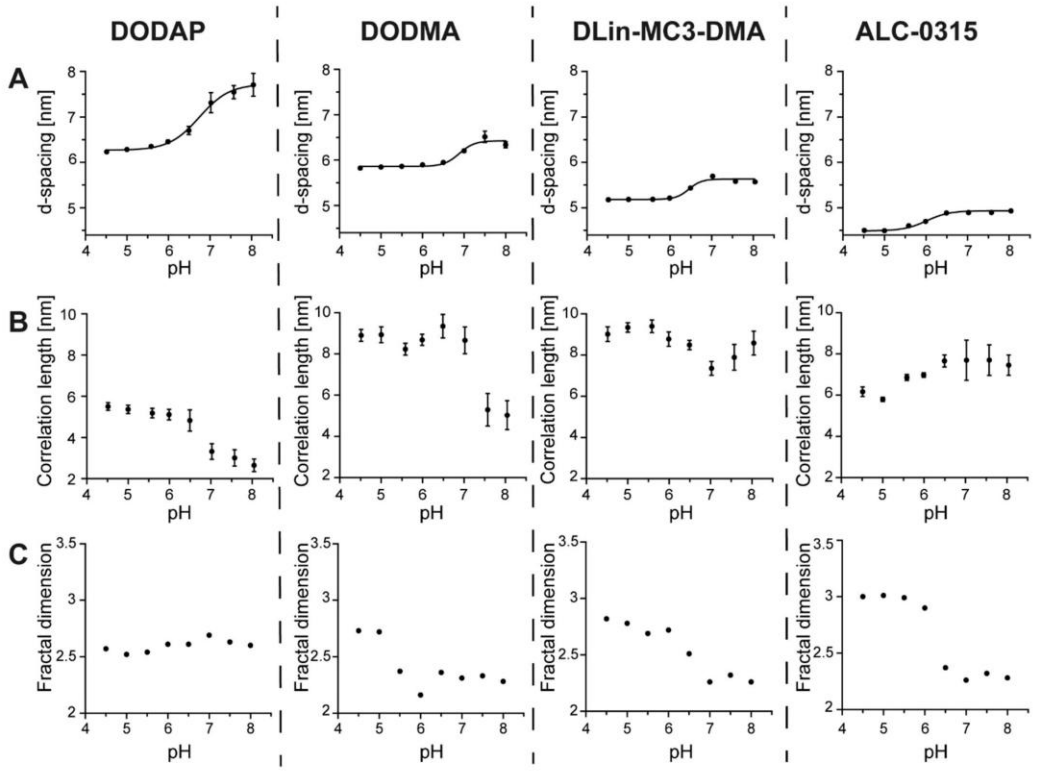

Fig. 3. Analysis of SAXS derived parameters as a function of pH. A. Values for d-spacing calculated by the peak position as described in the methods section (see Eq. (5)) as a function of environmental pH. The black line indicates a sigmoidal fit, whose inflection point can be used as the structural pK_a. B: Correlation length as a function of pH, calculated from the peak width (FWHM). While DODAP and DODMA LNPs show a decrease in correlation length, the more potent lipids maintain their long-range order. C. Fractal dimension from analysis of lower q-range (<0.4 nm^{-1}) using a power law as a function of surrounding pH. Values of 2 indicate smooth surfaces, whereas with growing values, the surface roughness increases.

Table 2
Results of determination of the structural pK_a by SAXS and the apparent pK_a by TNS assay for the investigated mRNA LNP with varying ionizable lipids.

Formulation	SAXS structural pK_a	TNS apparent pK_a
DODAP N/P 5	6.7 ± 0.1	5.8 ± 0.1
DODMA N/P 5	6.9 ± 0.2	6.6 ± 0.1
MC3 N/P 5	6.5 ± 0.1	6.7 ± 0.2
ALC-0315 N/P 5	6.0 ± 0.1	6.7 ± 0.1

differs from the structural pK_a. Differences in changes of internal structure, as indicated by d-spacing, and surface roughness in response to pH changes may be related to a different lipid composition in the LNP surface layer [48]. Interestingly, among the tested ionizable lipids, the ALC-0315 LNPs show the highest fractal dimension and therefore the highest surface roughness at low pH values.

Certain general structural differences between high and low activity LNPs observable over the total pH range were identified. While for the LNPs from the less active lipids, DODAP and DODMA, Bragg peak areas for main and secondary peaks were similar, for MC3 and ALC-0315 the main peak takes ~75 % of the additive total peak area for MC3 and even ~95 % of the total area for ALC-0315 at acidic pH (Fig. 2). This would mean that monophasic formulations tend to have higher activity, while the presence of a second structure, either as an mRNA-poor phase in the particles or an RNA-poor particles population, would point towards lower activity.

As a general observation, we note that slight molecular structure changes can substantially affect overall organization. The two less active lipids, DODAP and DODMA, which only differ by an ether-to-ester substitution (see Fig. 1A), exhibited clearly different d-spacings, with DODMA showing smaller values. It still needs to be clarified if, in this case, it has consequences for biological activity, but it highlights the potential impact of even small molecular changes on LNP properties.

In summary, compared to less potent formulations, LNPs manufactured with highly potent ionizable lipids, such as MC3 and ALC-0315, showed (i) lower overall d-spacing, (ii) a reduced range of d-spacing changes as a function of pH, (iii) no loss of long-range order with increasing pH, and (iv) a pH dependent change in surface roughness, with high fractal dimensions especially at low pH values.

3.2. *Variation of N/P ratio*

To further explore the structural organization properties of LNP formulations, SAXS measurements were conducted on formulations with

varying lipid to mRNA ratios (N/P ratios) for two selected ionizable lipids: the less active DODMA and the more active MC3. The N/P ratio is a critical formulation parameter that determines the quality and activity of LNPs. In standard screening approaches, functional N/P ratios are to be found empirically, as, so far, no direct molecular rationale for determining appropriate N/P ratios is available. In this study, we screened a wide range of N/P ratios, including conditions of mRNA excess (N/P < 1). Such low N/P ratios are of particular interest, since nanoparticle formulations assembled at N/P < 1 have proven high selectivity for spleen targeting upon intravenous injections [2], and products on this basis are currently undergoing different stages of clinical trials for cancer immunotherapy [49]. Formulation parameters are provided in Table 1. The total lipid concentration was kept constant to generate comparable experimental conditions, so that only the ionizable and helper lipid fractions were varied to set the N/P ratio.

Size determination by DLS exhibited a trend towards an increase in LNP size with decreasing N/P ratio. Samples manufactured with an excess of mRNA showed negative Zeta-potentials, while those manufactured with a lipid excess were positively charged in the acidic manufacturing buffer (Supplementary Table 1).

SAXS patterns of LNPs were recorded as a function of bulk phase pH, covering the range from 4.5 to 10 for LNPs with an N/P ratio < 1, and from 4.5 to 8 for LNPs with N/P > 1 (Fig. 4). The overall characteristics of the curves for the samples were similar to those described above. Also, for the additionally tested N/P ratios, a shift of peak position towards lower q-values (as displayed by the d-spacing in Fig. 5A), peak broadening, and a decrease of peak area were observed with increasing pH. Notably, all formulations manufactured at an N/P ratio < 1 exhibited only one peak pattern, with a narrow first-order Bragg peak and additional higher-order peaks (Supplementary Fig. 5), mainly detectable in acidic environmental buffers. Therefore, in contrast to the situation at N/P$> > 1$, only a single type of ordered material with a high degree of organization was present. A clearly higher correlation length (lower peak width) was determined, likely because the order is not disturbed by a second fraction of material (Fig. 5B). The positions of the higher-order peaks correspond to $\sqrt{3}$ and 2 times the q-value of the first-order peak (Supplementary Table 4), indicative of a hexagonal liquid-crystalline organization [50,51]. It was shown before that ionizable lipids can undergo lamellar to hexagonal phase transition upon acidification, which appears to be beneficial for the potency of the respective lipids [12]. Favorable conditions for the hexagonal packing found here can also include the increased content of DOPE within formulations with a decreasing N/P ratio in our experiments (see Materials and Methods). Due to its cone-like shape, with small headgroup and bulky unsaturated hydrocarbon chains, DOPE is known to readily undergo lamellar to hexagonal phase transition [8,51,52].

We assume that for formulations manufactured with an excess of mRNA, the nanoparticles consist of repeating stacks of lipid-complexed mRNA with fixed stoichiometry, where excess mRNA is present as free molecules in the bulk phase. Such patterns were observable up to an N/P ratio of 2. Only at higher N/P ratios did the secondary low-q peak emerge, which is indicative of the mRNA-depleted structural motif. With increasing N/P ratio, the relative area of the secondary peak shows a trend to increase (Supplementary Fig. 6), in accordance with increasing amounts of mRNA-poor ordered material.

The overall d-spacing and the range of d-spacing within the pH spectrum varied for the tested formulations (Fig. 5A, Supplementary Table 5). The d-spacing under acidic conditions, such as in the state of

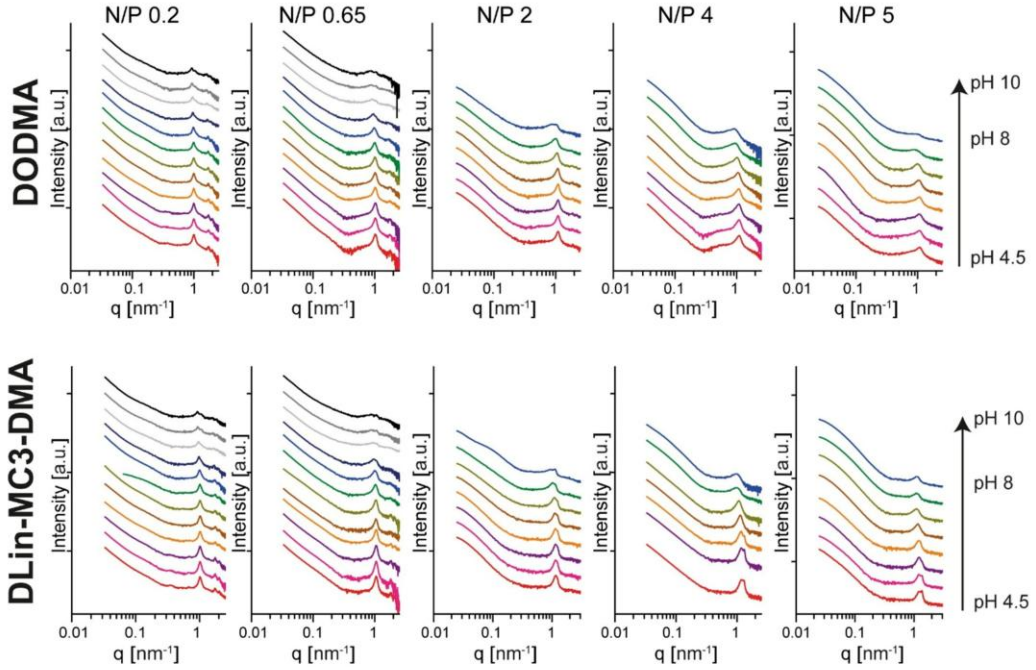

Fig. 4. Results of SAXS measurements of LNPs with N/P ratio variations. SAXS curves of mRNA-LNP samples over a pH range from 4.5 (red curves, bottom) to pH 10 (black curves, top) or to pH 8(blue curves, in case N/P ratio > 1) in ΔpH $= 0.5$ steps. The visualization of pH-dependent structure evolution is similar to that of LNPs described in Fig. 1B. (For interpretation of the references to colour in this figure legend, the reader is referred to the web version of this article.)

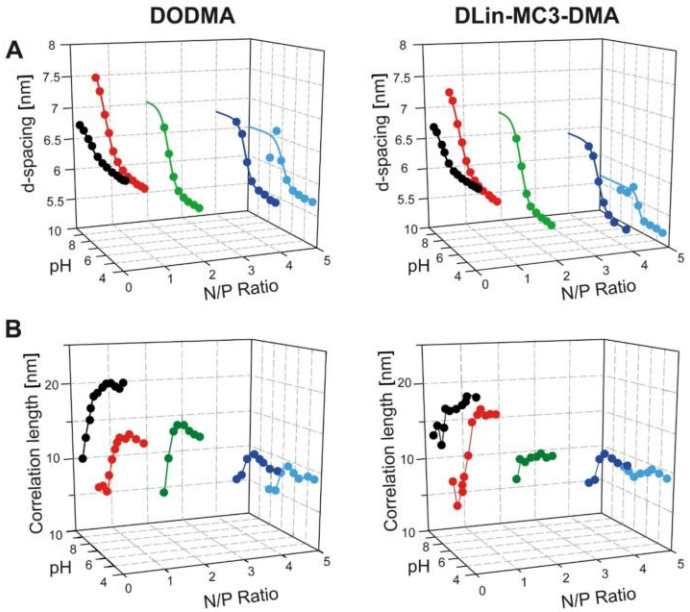

Fig. 5. Results of peak analysis for DODMA (left) and MC3 (right) LNPs of varying N/P ratio (black: N/P 0.2, red: N/P 0.65, green: N/P 2, dark blue: N/P 4, light blue: N/P 5). A: d-spacing of all LNPs as a function of pH value (z-axis) and N/P ratio (x-axis). Sigmoidal fits were added as described before. For LNPs with an N/P ratio > 1, fits were extrapolated to pH 10 for illustration. B: Correlation length of all LNPs as a function of pH and N/P ratio. (For interpretation of the references to colour in this figure legend, the reader is referred to the web version of this article.)

full protonation, decreased with increasing N/P ratio, indicating a higher packing density of the mRNA/lipid stacks. In most LNP formulations, N/P ratios at the higher end of this range are selected, which, according to the results observed here, are characterized by tighter mRNA complexation. Regardless of whether there is a direct correlation between packing density and activity, such structural information can provide a quantitative basis for identifying quality-relevant properties of LNP drug products.

When analyzing the structural pK_a for a given formulation, we observe a clear dependence on the N/P ratio (Table 3). The structural pK_a shifted from about 8.5 to about 6.5 on increasing the N/P from 0.2 to 5. Therefore, this dependence of the pK_a value on the N/P ratio may be applied as a valuable tool for fine-tuning LNP properties with a given ionizable lipid. In fact, also in the fluorescence-based assay, a shift towards higher apparent pK_a was visible for formulations with decreasing N/P ratio but revealing higher discrepancies to the structural pK_a with decreasing N/P ratio (Fig. 6). The controlled variation of the pK_a value has been demonstrated earlier with formulations having optimized organ targeting properties using the SORT technology [22]. By adding a fifth, charged lipid to the LNP, a clear effect on the pK_a value was obtained. At the same time, organ targeting towards the spleen or the lung was improved. This underlines the potential of accurate control of the

Table 3
Results of the determination of structural pK_a by SAXS and apparent pK_a by fluorescence-based TNS assay of the formulations tested for N/P ratio variation.

Formulation	SAXS structural pK_a	TNS apparent pK_a
DODMA N/P 0.2	8.6 ± 0.2	8.3 ± 0.2
DODMA N/P 0.65	8.7 ± 0.1	7.8 ± 0.2
DODMA N/P 2	7.7 ± 0.1	7.5 ± 0.3
DODMA N/P 4	7.2 ± 0.1	6.9 ± 0.1
DODMA N/P 5	7.0 ± 0.2	6.6 ± 0.1
MC3 N/P 0.2	8.6 ± 0.1	7.4 ± 0.2
MC3 N/P 0.65	8.6 ± 0.1	7.6 ± 0.1
MC3 N/P 2	7.7 ± 0.1	7.1 ± 0.1
MC3 N/P 4	7.0 ± 0.1	6.7 ± 0.1
MC3 N/P 5	6.5 ± 0.1	6.7 ± 0.2

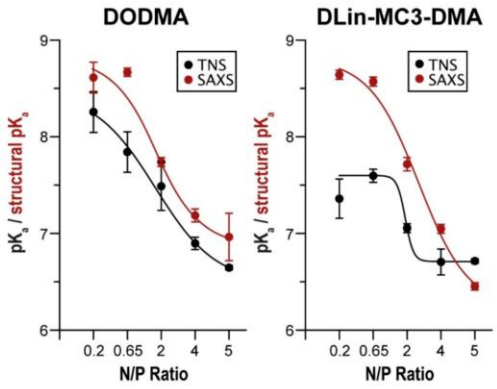

Fig. 6. Apparent pK_a (black, as determined with TNS-assay) and structural pK_a (red, as determined by SAXS analysis) as a function of N/P ratio of the LNP formulations. Lines were added for both parameters for illustration purposes. (For interpretation of the references to colour in this figure legend, the reader is referred to the web version of this article.)

pH responsiveness of the nanoparticles for tailoring their biological activity.

Also, distinct observations were made when looking at the fractal dimension of the particles in the extended range of N/P variation. The fractal dimensions of the LNPs with N/P < 1 were even higher than 3, therefore indicating a conformation more similar to a polymeric chain rather than 'only' elevated surface roughness [41]. We hypothesize that in LNPs assembled at N/P < 1, part of the excess mRNA forms shell-like structures at the surface of the particles, where it also accounts for the negative zeta potential. The conformational organization of the mRNA, essentially being a high molecular weight biopolymer, is responsible for the experimentally measured high fractal dimension. Increasing pH and therefore decreasing electrostatic interactions between the LNP and the RNA layer further foster this phenomenon at mRNA excess (Supplementary Fig. 7). For high N/P formulations (N/P ratio 4 and 5), the absolute fractal dimensions were lower but increased with decreasing pH value for both tested lipids. Considering the low pH in the late endosome, these findings on surface organization may be of relevance also for the efficacy of mechanisms involved in endosomal release.

Taken together, quantitative structure analysis, such as done here by SAXS measurements, provides valuable information on how the N/P ratio influences the internal structural organization, surface properties, as well as the pH-dependent behavior of LNPs. The N/P ratio directly impacts the pH responsiveness, highlighting the potential of N/P ratio variation as a tool for LNP fine-tuning. This complexity should be considered for rational development of mRNA LNP formulations.

4. Discussion

Control strategies are of essential importance for the assessment of the quality of LNP products. They are required during the development of new formulations, as well as for regular quality control and stability evaluation of existing products. Structural information plays a central role in product quality evaluation. SAXS measurements are a powerful tool for determining various structural parameters of LNP formulations at different length scales, ranging from Angstroms to several hundred nanometers. For application in pharmaceutical practice, it is important to quantitatively analyze data, using standardized protocols to allow for better comparability between results from different laboratories and systems. Based on this, generally accepted criteria need to be defined to evaluate product quality.

As a result of the present study, we can suggest a set of defined and quantitative structural parameters to be considered in SAXS data analysis of LNP and similar formulations. For the scattering profiles, Bragg peak analysis should include determination of position, width, and area, with a decision on whether single or double peak fitting is appropriate. Observation of structural features as a function of pH is important for several reasons. Firstly, this reflects the pathway during manufacturing from acidic to neutral conditions. Also, during biological action, the particles undergo an environmental pH change from about neutral in circulation to acidic conditions on endosomal uptake and processing. The observation of pH-dependent structural changes constitutes an important extension to the insight that can be given by the fluorescence-based assay. It provides direct structural information of the overall mRNA/lipid stacks instead of only the accessible interfacial moieties and is not dependent on environmental settings such as buffer choice. These structural parameters are relevant for cellular processing (e.g., endosomal uptake and release) and stability perspectives (e.g., drug substance and lipid integrity). As a further criterion, which has not been extensively considered so far, we propose to analyze the Porod exponent in the low-q region and to determine the (surface) fractal dimension. The interfacial molecular conformation appears to be important for cellular uptake and endosomal release processes and thus affects drug product activity. Following these approaches, we were able to identify certain structural features that varied with the relative activity of the four ionizable model lipids:

i. The more potent lipids exhibited a higher perpendicular packing density of the mRNA-lipid complexes than those with lower potency. The higher packing density was maintained when the pH was increased to neutral levels, as it occurs following intravenous administration in the systemic circulation. This is envisaged to provide better protection against the degradation of the particles within the circulation. Considering that the mRNA-lipid Bragg peak was maintained over the entire pH range tested, it demonstrated the general stability of the complexes in varying pH environments during circulation after administration. However, it should be noted that circulation stability depends on additional variables such as shear forces and protein and membrane interactions.
ii. We found evidence for the coexistence of two different types of ordered material in the same LNP formulation. In fact, in standard LNP formulations, a relatively high excess of ionizable lipid relative to mRNA (N/P ratio > 4) is used. For reasons of charge balance, and supported by previous data [30] mRNA-lipid complexes inside the LNPs are expected to have an N/P ratio close to one. Therefore, we assume that the two patterns in the nanoparticles resulted from complexes with higher and lower (or no) amounts of mRNA inserted between the lipids. As in many LNP systems the excess lipid is important for activity, it appears helpful to gain more insight into the fraction having different structural organization inside the LNPs. It should be noted that several studies have reported the presence of LNPs with varying loads of RNA in a given formulation [53]. In this study, batch measurements averaging the signals from all types of present LNPs were performed, and the data did not allow for clear discrimination between these two options. Separation of different nanoparticle fractions before the SAXS measurement, such as by using AF4, can help to gain better insights into the individual properties of the different fractions in a product [28]. Such separation approaches will be helpful for better evaluation of the quality and activity of LNP formulations.
iii. We found a correlation between activity and the surface fractal dimension of the LNPs, a parameter that has not been widely considered by the community yet. Previously, when we observed higher transfection efficacy of MC3 compared to DODMA in human peripheral blood mononuclear cells (hPBMCs), we already found a higher surface fractal dimension for the more active formulations, particularly at acidic pH [31]. We hypothesize that the increased surface roughness may be favorable for interactions with the endosomal membrane, thereby promoting mechanisms of endosomal escape. Increased fractal dimensions may destabilize endosomal membranes within the phase where positive LNP charges and negative endosomal charges interact. Particles with rough interfaces or molecular moieties which loop away from the surface of the particles may reduce the energy barrier to rupture the (opposite) membrane compared to a particle with smooth interface. This could lead to higher permeability of the endosomal compartment. It will be worthwhile to investigate such membrane effects also in model membrane systems which allow quantitative assessment of the interactions (e.g., Atomic Force Microscopy, Surface Force Apparatus) and to correlate these results with activity.
iv. Some fundamental differences in the structural features of LNPs manufactured at N/P ratio < 1 compared to N/P ratio > 1 were evident. For formulations with an N/P ratio below 1, only a single type of internal organization was present. We conclude that mRNA/lipid complexes of defined stoichiometry had been formed (accounting for charge balance), coexisting with an excess of mRNA, which is not part of the particles and did not contribute to the scattering patterns obtained here. Higher order peaks were visible for the lipid complexed mRNA structure,

indicating inverted hexagonal phase, one of the paradigms in rational lipid synthesis for nucleic acid delivery.

v. The structural pK_a of the formulations determined by SAXS provides extended information compared to the traditional fluorescence-based approach. While the values for DODMA and MC3 were rather similar, ALC-0315 showed a lower SAXS-derived value, and DODAP showed a lower TNS assay-derived value.

vi. We identified a clear dependency of the N/P ratio on the structural pK_a value. The decrease in the pK_a with increasing N/P could be one reason for the high excess of ionizable lipid in current LNP products. This highlights that for developing new LNP formulations, the selection of ionizable lipid, lipid composition, and N/P ratio together contributes to the pH-dependent electrostatic properties of the particles. With a given lipid, the effective pK_a value of the particle can be fine-tuned by adjusting the N/P ratio. Taking this into consideration, this can help to tailor mRNA LNP formulations for a given therapeutic use.

With this, a set of generally applicable tools can be provided that allow us to evaluate and compare product quality and to accelerate the development of tailored LNP formulations for future applications.

5. Conclusion

In this study, model LNP compositions were investigated with SAXS measurements, and structural features were identified that correlated with transfection efficacy. The structural pH responsiveness for LNPs yielded in similar, but refined results, which more accurately display the actual in situ pH-dependent behavior of LNPs compared to the standard fluorescence-based assay for determination of nanoparticle pK_a. We found the structural pK_a value to systematically vary with N/P value, which introduces a further degree of freedom in LNP optimization. The optimal N/P values for active formulations may vary with ionizable lipids having different molecular pK_a values. High perpendicular packing density of the mRNA/lipid stacks and a high increase in surface roughness (fractal dimension) in response to lowering pH were characteristic of the more potent ionizable lipids. Overall, concise structural investigations by SAXS can be helpful in rational LNP design. Structural features characteristic of potent lipid excipients and LNPs can be identified, and general structure-function correlations for mRNA LNPs, a versatile drug delivery system for various therapeutic targets, can be derived.

CRediT authorship contribution statement

Christoph Wilhelmy: Writing – original draft, Visualization, Methodology, Investigation, Formal analysis. **Lukas Uebbing:** Writing – review & editing, Methodology, Investigation. **Bastian Kolb:** Writing – review & editing, Investigation. **Melissa A. Graewert:** Writing – review & editing, Investigation. **Thomas Nawroth:** Writing – review & editing. **Heinrich Haas:** Writing – original draft, Supervision, Conceptualization. **Peter Langguth:** Writing – review & editing, Supervision, Project administration, Funding acquisition, Conceptualization.

Funding sources

This work was funded by the „Deutsche Forschungsgemeinschaft (DFG)“, Sonderforschungsbereich 1066, and the “Bundesministerium für Bildung und Forschung (BMBF)“, grant number 05K22UM3.

Declaration of competing interest

All authors declare no competing interests.

Acknowledgements

We would like to thank Lipoid GmbH for donating some of the lipids, namely DOPE. The synchrotron SAXS data was collected at beamline P12 operated by EMBL Hamburg at the PETRA III storage ring (DESY, Hamburg, Germany).

Appendix A. Supplementary data

Supplementary data to this article can be found online at https://doi.org/10.1016/j.jconrel.2025.113848.

Data availability

Data will be made available on request.

References

[1] U. Sahin, K. Karikó, Ö. Türeci, mRNA-based therapeutics—developing a new class of drugs, Nat. Rev. Drug Discov. 13 (2014) 759–780, https://doi.org/10.1038/nrd4278.

[2] L.M. Kranz, M. Diken, H. Haas, S. Kreiter, C. Loquai, K.C. Reuter, M. Meng, D. Fritz, F. Vascotto, H. Hefesha, et al., Systemic RNA delivery to dendritic cells exploits antiviral defence for cancer immunotherapy, Nature 534 (2016) 396–401, https://doi.org/10.1038/nature18300.

[3] S. Chen, X. Huang, Y. Xue, E. Álvarez-Benedicto, Y. Shi, W. Chen, S. Koo, D. J. Siegwart, Y. Dong, W. Tao, Nanotechnology-based mRNA vaccines, Nat Rev Methods Primers 3 (2023), https://doi.org/10.1038/s43586-023-00246-7.

[4] J.D. Beck, D. Reidenbach, N. Salomon, U. Sahin, Ö. Türeci, M. Vormehr, L. M. Kranz, mRNA therapeutics in cancer immunotherapy, Mol. Cancer 20 (2021) 69, https://doi.org/10.1186/s12943-021-01348-0.

[5] N. Pardi, S. Tuyishime, H. Muramatsu, K. Kariko, B.L. Mui, Y.K. Tam, T.D. Madden, M.J. Hope, D. Weissman, Expression kinetics of nucleoside-modified mRNA delivered in lipid nanoparticles to mice by various routes, J. Control. Release 217 (2015) 345–351, https://doi.org/10.1016/j.jconrel.2015.08.007.

[6] A. Akinc, M.A. Maier, M. Manoharan, K. Fitzgerald, M. Jayaraman, S. Barros, S. Ansell, X. Du, M.J. Hope, T.D. Madden, et al., The Onpattro story and the clinical translation of nanomedicines containing nucleic acid-based drugs, Nat. Nanotechnol. 14 (2019) 1084–1087, https://doi.org/10.1038/s41565-019-0591-y.

[7] E.E. Walsh, R.W. Frenck, A.R. Falsey, N. Kitchin, J. Absalon, A. Gurtman, S. Lockhart, K. Neuzil, M.J. Mulligan, R. Bailey, et al., Safety and immunogenicity of two RNA-based Covid-19 vaccine candidates, N. Engl. J. Med. 383 (2020) 2439–2450, https://doi.org/10.1056/NEJMoa2027906.

[8] C. Hald Albertsen, J.A. Kulkarni, D. Witzigmann, M. Lind, K. Petersson, J. B. Simonsen, The role of lipid components in lipid nanoparticles for vaccines and gene therapy, Adv. Drug Deliv. Rev. 188 (2022) 114416, https://doi.org/10.1016/j.addr.2022.114416.

[9] L. Schoenmaker, D. Witzigmann, J.A. Kulkarni, R. Verbeke, G. Kersten, W. Jiskoot, D.J.A. Crommelin, mRNA-lipid nanoparticle COVID-19 vaccines: structure and stability, Int. J. Pharm. 601 (2021) 120586, https://doi.org/10.1016/j.ijpharm.2021.120586.

[10] P. Patel, N.M. Ibrahim, K. Cheng, The importance of apparent pKa in the development of nanoparticles encapsulating siRNA and mRNA, Trends Pharmacol. Sci. 42 (2021) 448–460, https://doi.org/10.1016/j.tips.2021.03.002.

[11] H. Yu, J. Iscaro, B. Dyett, Y. Zhang, S. Seibt, N. Martinez, J. White, C.J. Drummond, S. Bozinovski, J. Zhai, Inverse cubic and hexagonal Mesophase evolution within Ionizable lipid nanoparticles correlates with mRNA transfection in macrophages, J. Am. Chem. Soc. 145 (2023) 24765–24774, https://doi.org/10.1021/jacs.3c08729.

[12] J. Philipp, A. Dabkowska, A. Reiser, K. Frank, R. Krzysztoń, C. Brummer, B. Nickel, C.E. Blanchet, A. Sudarsan, M. Ibrahim, et al., pH-dependent structural transitions in cationic ionizable lipid mesophases are critical for lipid nanoparticle function, Proc. Natl. Acad. Sci. U. S. A. 120 (2023) e2310491120, https://doi.org/10.1073/pnas.2310491120.

[13] Q. Cheng, T. Wei, L. Farbiak, L.T. Johnson, S.A. Dilliard, D.J. Siegwart, Selective organ targeting (SORT) nanoparticles for tissue-specific mRNA delivery and CRISPR-Cas gene editing, Nat. Nanotechnol. 15 (2020) 313–320, https://doi.org/10.1038/s41565-020-0669-6.

[14] Y. Xu, A. Golubovic, S. Xu, A. Pan, B. Li, Rational design and combinatorial chemistry of ionizable lipids for RNA delivery, J. Mater. Chem. B 11 (2023) 6527–6539, https://doi.org/10.1039/D3TB00649B.

[15] G. Tilstra, J. Couture-Senécal, Y.M.A. Lau, A.M. Manning, D.S.M. Wong, W. W. Janaeska, T.A. Wuraola, J. Pang, O.F. Khan, Iterative Design of Ionizable Lipids for intramuscular mRNA delivery, J. Am. Chem. Soc. 145 (2023) 2294–2304, https://doi.org/10.1021/jacs.2c10670.

[16] M. Jayaraman, S.M. Ansell, B.L. Mui, Y.K. Tam, J. Chen, X. Du, D. Butler, L. Eltepu, S. Matsuda, J.K. Narayanannair, et al., Maximizing the potency of siRNA lipid nanoparticles for hepatic gene silencing in vivo, Angew. Chem. Int. Ed. Engl. 51 (2012) 8529–8533, https://doi.org/10.1002/anie.201203263.

[17] C. Azevedo, M.H. Macedo, B. Sarmento, Strategies for the enhanced intracellular delivery of nanomaterials, Drug Discov. Today 23 (2018) 944–959, https://doi.org/10.1016/j.drudis.2017.08.011.
[18] M.J. Carrasco, S. Alishetty, M.-G. Alameh, H. Said, L. Wright, M. Paige, O. Soliman, D. Weissman, T.E. Cleveland, A. Grishaev, et al., Ionization and structural properties of mRNA lipid nanoparticles influence expression in intramuscular and intravascular administration, Commun. Biol. 4 (2021) 956, https://doi.org/10.1038/s42003-021-02441-2.
[19] K.J. Hassett, K.E. Benenato, E. Jacquinet, A. Lee, A. Woods, O. Yuzhakov, S. Himansu, J. Deterling, B.M. Geilich, T. Ketova, et al., Optimization of lipid nanoparticles for intramuscular administration of mRNA vaccines, Mol. Ther. Nucleic Acids 15 (2019) 1–11, https://doi.org/10.1016/j.omtn.2019.01.013.
[20] M.D. Buschmann, M.J. Carrasco, S. Alishetty, M. Paige, M.G. Alameh, D. Weissman, Nanomaterial delivery systems for mRNA vaccines, Vaccines (Basel) 9 (2021), https://doi.org/10.3390/vaccines9010065.
[21] S.L. Rybak, R.F. Murphy, Primary cell cultures from murine kidney and heart differ in endosomal pH, J. Cell. Physiol. 176 (1998) 216–222, https://doi.org/10.1002/(SICI)1097-4652(199807)176:1<216:AID-JCP23>3.0.CO;2-3.
[22] S.A. Dilliard, Q. Cheng, D.J. Siegwart, On the mechanism of tissue-specific mRNA delivery by selective organ targeting nanoparticles, Proc. Natl. Acad. Sci. U. S. A. 118 (2021), https://doi.org/10.1073/pnas.2109256118.
[23] S.S. Nogueira, E. Samaridou, J. Simon, S. Frank, M. Beck-Broichsitter, A. Mehta, Analytical techniques for the characterization of nanoparticles for mRNA delivery, Eur. J. Pharm. Biopharm. 198 (2024) 114235, https://doi.org/10.1016/j.ejpb.2024.114235.
[24] N.B. Hamilton, S. Arns, M. Shelley, I. Bechis, J.C. Shelley, Calculating apparent pKa values of Ionizable lipids in lipid nanoparticles, Mol. Pharm. (2024), https://doi.org/10.1021/acs.molpharmaceut.4c00426.
[25] M.F.W. Trollmann, R.A. Böckmann, mRNA lipid nanoparticle phase transition, Biophys. J. 121 (2022) 3927–3939, https://doi.org/10.1016/j.bpj.2022.08.037.
[26] L. Uebbing, A. Ziller, C. Siewert, M.A. Schroer, C.E. Blanchet, D.I. Svergun, S. Ramishetti, D. Peer, U. Sahin, H. Haas, et al., Investigation of pH-responsiveness inside lipid nanoparticles for parenteral mRNA application using small-angle X-ray scattering, Langmuir 36 (2020) 13331–13341, https://doi.org/10.1021/acs.langmuir.0c02446.
[27] C.D. Siewert, H. Haas, V. Cornet, S.S. Nogueira, T. Nawroth, L. Uebbing, A. Ziller, J. Al-Gousous, A. Radulescu, M.A. Schroer, et al., Hybrid biopolymer and lipid nanoparticles with improved transfection efficacy for mRNA, Cells 9 (2020), https://doi.org/10.3390/cells9092034.
[28] M.A. Graewert, C. Wilhelmy, T. Bacic, J. Schumacher, C. Blanchet, F. Meier, R. Drexel, R. Welz, B. Kolb, K. Bartels, et al., Quantitative size-resolved characterization of mRNA nanoparticles by in-line coupling of asymmetrical-flow field-flow fractionation with small angle X-ray scattering, Sci. Rep. 13 (2023) 15764, https://doi.org/10.1038/s41598-023-42274-z.
[29] S.S. Nogueira, A. Schlegel, K. Maxeiner, B. Weber, M. Barz, M.A. Schroer, C. E. Blanchet, D.I. Svergun, S. Ramishetti, D. Peer, et al., Polysarcosine-functionalized lipid nanoparticles for therapeutic mRNA delivery, ACS Appl. Nano Mater. 3 (2020) 10634–10645, https://doi.org/10.1021/acsanm.0c01834.
[30] A. Ziller, S.S. Nogueira, E. Hühn, S.S. Funari, G. Brezesinski, H. Hartmann, U. Sahin, H. Haas, P. Langguth, Incorporation of mRNA in lamellar lipid matrices for parenteral administration, Mol. Pharm. 15 (2018) 642–651, https://doi.org/10.1021/acs.molpharmaceut.7b01022.
[31] C. Wilhelmy, I.S. Keil, L. Uebbing, M.A. Schroer, D. Franke, T. Nawroth, M. Barz, U. Sahin, H. Haas, M. Diken, et al., Polysarcosine-functionalized mRNA lipid nanoparticles tailored for immunotherapy, Pharmaceutics 15 (2023), https://doi.org/10.3390/pharmaceutics15082068.
[32] D. Bi, C. Wilhelmy, D. Unthan, I.S. Keil, B. Zhao, B. Kolb, R.I. Koning, M. A. Graewert, B. Wouters, R. Zwier, et al., On the influence of fabrication methods and materials for mrna-lnp production: from size and morphology to internal structure and mrna delivery performance in vitro and in vivo, Adv. Healthc. Mater. (2024), https://doi.org/10.1002/adhm.202401252 e2401252.
[33] B. Binici, Z. Rattray, A. Zinger, Y. Perrie, Exploring the impact of commonly used ionizable and pegylated lipids on mRNA-LNPs: a combined in vitro and preclinical perspective, J. Control. Release 377 (2025) 162–173, https://doi.org/10.1016/j.jconrel.2024.11.010.
[34] O. Escalona-Rayo, Y. Zeng, R.A. Knol, T.J.F. Kock, D. Aschmann, B. Slütter, A. Kros, In vitro and in vivo evaluation of clinically-approved ionizable cationic lipids shows divergent results between mRNA transfection and vaccine efficacy, Biomed. Pharmacother. 165 (2023) 115065, https://doi.org/10.1016/j.biopha.2023.115065.
[35] C.E. Blanchet, A. Spilotros, F. Schwemmer, M.A. Graewert, A. Kikhney, C. M. Jeffries, D. Franke, D. Mark, R. Zengerle, F. Cipriani, et al., Versatile sample environments and automation for biological solution X-ray scattering experiments at the P12 beamline (PETRA III, DESY), J. Appl. Cryst. 48 (2015) 431–443, https://doi.org/10.1107/S160057671500254X.
[36] A. Round, F. Felisaz, L. Fodinger, A. Gobbo, J. Huet, C. Villard, C.E. Blanchet, P. Pernot, S. McSweeney, M. Roessle, et al., BioSAXS sample changer: a robotic sample changer for rapid and reliable high-throughput X-ray solution scattering experiments, Acta Crystallogr. D Biol. Crystallogr. 71 (2015) 67–75, https://doi.org/10.1107/S1399004714026959.
[37] B. Romeis, Taschenbuch der mikroskopischen Technik, De Gruyter, 1943. ISBN 9783486764369.
[38] K. Manalastas-Cantos, P.V. Konarev, N.R. Hajizadeh, A.G. Kikhney, M. V. Petoukhov, D.S. Molodenskiy, A. Panjkovich, H.D.T. Mertens, A. Gruzinov, C. Borges, et al., ATSAS 3.0: expanded functionality and new tools for small-angle scattering data analysis, J. Appl. Cryst. 54 (2021) 343–355, https://doi.org/10.1107/S1600576720013412.
[39] G. Porod, Die Röntgenkleinwinkelstreuung von dichtgepackten kolloiden Systemen, Kolloid-Zeitschrift 124 (1951) 83–114, https://doi.org/10.1007/BF01512792.
[40] H.D. Bale, P.W. Schmidt, Small-angle X-ray-scattering investigation of submicroscopic porosity with fractal properties, Phys. Rev. Lett. 53 (1984) 596–599, https://doi.org/10.1103/PhysRevLett.53.596.
[41] G. Beaucage, Small-angle scattering from polymeric mass fractals of arbitrary mass-fractal dimension, J. Appl. Cryst. 29 (1996) 134–146, https://doi.org/10.1107/S0021889895011605.
[42] W.H. Bragg, William L. Bragg, The reflection of X-rays by crystals, Proc. R. Soc. Lond. A 88 (1913) 428–438, https://doi.org/10.1098/rspa.1913.0040.
[43] Second completely revised and greatly enlarged edition, in: J.W.G. Goodby, P. J. Collings, T. Kato, C. Tschierske, H.F. Gleeson, E.P. Raynes (Eds.), Handbook of Liquid Crystals, Wiley-VCH, Weinheim, 2014. ISBN 9783527671403.
[44] J. Heyes, L. Palmer, K. Bremner, I. MacLachlan, Cationic lipid saturation influences intracellular delivery of encapsulated nucleic acids, J. Control. Release 107 (2005) 276–287, https://doi.org/10.1016/j.jconrel.2005.06.014.
[45] T.F. Martens, K. Remaut, J. Demeester, S.C. Smedt, de; Braeckmans, K., Intracellular delivery of nanomaterials: how to catch endosomal escape in the act, Nano Today 9 (2014) 344–364, https://doi.org/10.1016/j.nantod.2014.04.011.
[46] A.-M. Börjesdotter, H. Bolinsson, T. Dagø, F. Herranz-Trillo, U.C. Palmiero, H. Schagerlöf, L. Nilsson, Lipid nanoparticle properties explored using online asymmetric flow field-flow fractionation coupled with small angle X-ray scattering: beyond average characterisation, Int. J. Pharm. 668 (2025) 124940, https://doi.org/10.1016/j.ijpharm.2024.124940.
[47] S. Ciccariello, J. Goodisman, H. Brumberger, On the Porod law, J. Appl. Cryst. 21 (1988) 117–128, https://doi.org/10.1107/S0021889887010409.
[48] F. Sebastiani, M. Yanez Arteta, M. Lerche, L. Porcar, C. Lang, R.A. Bragg, C. S. Elmore, V.R. Krishnamurthy, R.A. Russell, T. Darwish, et al., Apolipoprotein E binding drives structural and compositional rearrangement of mRNA-containing lipid nanoparticles, ACS Nano 15 (2021) 6709–6722, https://doi.org/10.1021/acsnano.0c10064.
[49] V. Nele, V. Campani, S. Alia Moosavian, G. de Rosa, Lipid nanoparticles for RNA delivery: self-assembling vs driven-assembling strategies, Adv. Drug Deliv. Rev. 208 (2024) 115291, https://doi.org/10.1016/j.addr.2024.115291.
[50] J.M. Seddon, Structure of the inverted hexagonal (HII) phase, and non-lamellar phase transitions of lipids, Biochim. Biophys. Acta 1031 (1990) 1–69, https://doi.org/10.1016/0304-4157(90)90002-T.
[51] I. Koltover, T. Salditt, J.O. Rädler, C.R. Safinya, An inverted hexagonal phase of cationic liposome-DNA complexes related to DNA release and delivery, Science 281 (1998) 78–81, https://doi.org/10.1126/science.281.5373.78.
[52] X. Cheng, R.J. Lee, The role of helper lipids in lipid nanoparticles (LNPs) designed for oligonucleotide delivery, Adv. Drug Deliv. Rev. 99 (2016) 129–137, https://doi.org/10.1016/j.addr.2016.01.022.
[53] J.B. Simonsen, A perspective on bleb and empty LNP structures, J. Control. Release 373 (2024) 952–961, https://doi.org/10.1016/j.jconrel.2024.07.046.

4.3.3 **Supporting Information**

Supplementary Information

For the manuscript:

Direct structural investigation of pH responsiveness in mRNA lipid nanoparticles: Refining paradigms

Christoph Wilhelmy[1], Lukas Uebbing[1], Bastian Kolb[1], Melissa A. Graewert[2], Thomas Nawroth[1], Heinrich Haas[1], Peter Langguth[1]**

[1] Department of Biopharmaceutics and Pharmaceutical Technology, Johannes Gutenberg-University, Mainz, Germany; [2] European Molecular Biology Laboratory, Hamburg Outstation, Hamburg, Germany

Supplementary Table 1: Results of Dynamic Light Scattering (DLS; hydrodynamic diameter and polydispersity index (PDI)) and zeta-potential measurements in manufacturing buffer. Data presented as mean ± S.D., n=3.

Formulation	Diameter [nm]	PDI	Zeta-Potential [mV]
DODAP N/P 5	207.3 ± 13.2	0.23 ± 0.04	20.6 ± 1.6
DODMA N/P 5	184.7 ± 2.9	0.17 ± 0.01	27.3 ± 6.9
MC3 N/P 5	170.3 ± 1.8	0.12 ± 0.01	29.5 ± 2.5
ALC-0315 N/P 5	173.4 ± 14.5	0.19 ± 0.02	19.0 ± 6.0
DODMA N/P 0.2	243.0 ± 13.2	0.21 ± 0.02	-10.9 ± 1.8
DODMA N/P 0.65	233.2 ± 2.8	0.20 ± 0.04	-11.3 ± 6.5
DODMA N/P 2	188.9 ± 25.1	0.16 ± 0.03	23.1 ± 2.3
DODMA N/P 4	219.7 ± 26.3	0.16 ± 0.02	27.0 ±2.9
MC3 N/P 0.2	257.7 ± 11.5	0.23 ± 0.02	-10.7 ± 0.6
MC3 N/P 0.65	250.7 ± 6.6	0.34 ± 0.09	-4.5 ± 5.1
MC3 N/P 2	181.8 ± 5.1	0.15 ± 0.03	20.5 ±1.9
MC3 N/P 4	210.1 ± 14.0	0.20 ± 0.01	24.4 ± 1.6

Supplementary Table 2: Fitting parameters of all tested LNP formulations in the respective environmental pH.

Ionizable Lipids Variation

Formulation	pH	Main peak			Low-q peak		
		Area	Peak center	Peak width	Area	Peak center	Peak width
DODAP N/P 5	4.5	519 ± 46	1.01 ± 0.01	0.36 ± 0.01	408 ± 85	0.74 ± 0.03	0.69 ± 0.07
	5	490 ± 47	1.00 ± 0.01	0.37 ± 0.02	359 ± 94	0.71 ± 0.04	0.73 ± 0.10
	5.5	484 ± 60	0.99 ± 0.00	0.39 ± 0.02	363 ± 123	0.71 ± 0.04	0.75 ± 0.12
	6	418 ± 60	0.97 ± 0.01	0.39 ± 0.02	318 ± 100	0.71 ± 0.05	0.66 ± 0.10
	6.5	358 ± 142	0.94 ± 0.01	0.41 ± 0.03	392 ± 195	0.73 ± 0.04	0.61 ± 0.10
	7	385 ± 213	0.86 ± 0.03	0.60 ± 0.08	406 ± 198	0.51 ± 0.04	0.65 ± 0.40
	7.5	338 ± 133	0.83 ± 0.02	0.67 ± 0.09	-	-	-
	8	380 ± 145	0.82 ± 0.03	0.76 ± 0.09	-	-	-
DODMA N/P 5	4.5	411 ± 24	1.08 ± 0.01	0.22 ± 0.01	631 ± 73	0.81 ± 0.01	0.63 ± 0.05
	5	401 ± 30	1.07 ± 0.01	0.22 ± 0.01	714 ± 101	0.80 ± 0.02	0.70 ±0.06
	5.5	462 ± 29	1.07 ± 0.01	0.24 ± 0.01	714 ± 100	0.75 ± 0.01	0.71 ± 0.07
	6	451 ± 25	1.07 ± 0.01	0.23 ± 0.01	676 ± 78	0.77 ± 0.01	0.66 ± 0.05
	6.5	441 ± 66	1.06 ± 0.01	0.21 ± 0.01	363 ± 114	0.89 ± 0.03	0.40 ± 0.06
	7	463 ± 100	1.01 ± 0.01	0.23 ± 0.02	276 ± 142	0.86 ± 0.04	0.35 ± 0.08
	7.5	334 ±.169	0.96 ± 0.02	0.38 ± 0.06	495 ± 256	0.74 ± 0.03	0.48 ± 0.14
	8	253 ± 89	0.99 ± 0.01	0.40 ± 0.06	711 ± 354	0.58 ± 0.05	0.65 ± 0.23
MC3 N/P 5	4.5	436 ± 31	1.21 ± 0.01	0.22 ± 0.01	121 ± 51	0.81 ± 0.04	0.46 ± 0.17
	5	450 ± 24	1.21 ± 0.01	0.21 ± 0.01	99 ± 38	0.83 ±0.03	0.41 ± 0.14
	5.5	501 ± 28	1.21 ± 0.01	0.22 ± 0.01	67 ± 58	0.96 ±0.04	0.41 ± 0.28
	6	537 ± 46	1.21 ± 0.01	0.23 ± 0.01	147 ± 89	0.99 ± 0.05	0.43 ± 0.17
	6.5	486 ± 24	1.16 ± 0.01	0.24 ± 0.01	308 ± 70	0.89 ± 0.03	0.67 ± 0.09
	7	423 ± 44	1.10 ± 0.01	0.27 ± 0.01	283 ± 86	0.86 ± 0.03	0.55 ± 0.10
	7.5	276 ± 52	1.13 ± 0.01	0.25 ± 0.02	267 ± 94	0.92 ± 0.03	0.47 ± 0.09
	8	250 ± 38	1.13 ± 0.01	0.23 ± 0.02	266 ± 67	0.94 ± 0.03	0.48 ± 0.06
ALC-0315 N/P 5	4.5	311 ± 17	1.40 ± 0.01	0.32 ± 0.01	23 ± 12	0.97 ± 0.33	0.35 ± 0.55
	5	337 ± 7	1.40 ± 0.01	0.35 ± 0.01	17 ± 3	0.86 ± 0.01	0.20 ± 0.04
	5.5	245 ± 10	1.36 ± 0.01	0.29 ± 0.01	11 ± 3	0.79 ± 0.01	0.22 ± 0.06
	6	237 ± 5	1.34 ± 0.01	0.29 ± 0.01	34 ± 14	0.79 ± 0.04	0.70 ± 0.26
	6.5	237 ± 22	1.29 ± 0.01	0.26 ± 0.01	69 ± 41	1.07 ± 0.05	0.48 ± 0.16
	7	147 ± 57	1.28 ± 0.01	0.26 ± 0.03	104 ± 79	1.14 ± 0.07	0.43 ± 0.10
	7.5	176 ± 54	1.28 ± 0.01	0.26 ± 0.03	152 ± 73	1.15 ± 0.05	0.44 ± 0.05
	8	192 ± 36	1.27 ± 0.01	0.27 ± 0.02	85 ± 54	1.10 ± 0.06	0.45 ± 0.12

DODMA N/P Variations

Formulation	pH	Main peak			Front peak		
		Area	Peak center	Peak width	Area	Peak center	Peak width
DODMA N/P 0.2	4.5	237 ± 2	1.00 ± 0.01	0.09 ± 0.01	-	-	-
	5	238 ± 3	1.00 ± 0.01	0.10 ± 0.01	-	-	-
	5.5	222 ± 2	1.00 ± 0.01	0.09 ± 0.00	-	-	-
	6	193 ± 2	1.00 ± 0.01	0.09 ± 0.00	-	-	-
	6.5	176 ± 3	1.00 ± 0.01	0.09 ± 0.00	-	-	-
	7	172 ± 3	1.00 ± 0.01	0.10 ± 0.01	-	-	-
	7.5	164 ± 3	0.99 ± 0.01	0.10 ± 0.01	-	-	-
	8	153 ± 4	0.99 ± 0.01	0.10 ± 0.01	-	-	-
	8.5	124 ± 4	0.97 ± 0.01	0.12 ± 0.01	-	-	-
	9	123 ± 5	0.96 ± 0.01	0.13 ± 0.01	-	-	-
	9.5	109 ± 6	0.95 ± 0.01	0.15 ± 0.01	-	-	-
	10	124 ± 8	0.94 ± 0.01	0.20 ± 0.01	-	-	-
DODMA N/P 0.65	4.5	422 ± 9	1.02 ± 0.01	0.13 ± 0.01	-	-	-
	5	433 ± 9	1.03 ± 0.01	0.13 ± 0.01	-	-	-
	5.5	408 ± 8	1.03 ± 0.01	0.13 ± 0.01	-	-	-
	6	361 ± 8	1.02 ± 0.01	0.13 ± 0.01	-	-	-
	6.5	334 ± 7	1.02 ± 0.01	0.14 ± 0.01	-	-	-
	7	323 ± 6	1.01 ± 0.01	0.14 ± 0.01	-	-	-
	7.5	286 ± 6	1.00 ± 0.01	0.15 ±0.01	-	-	-
	8	281 ± 6	0.98 ± 0.01	0.18 ± 0.01	-	-	-
	8.5	232 ± 10	0.94 ± 0.01	0.22 ± 0.01	-	-	-
	9	239 ± 25	0.90 ± 0.01	0.35 ± 0.02	-	-	-
	9.5	155 ± 14	0.86 ± 0.01	0.31 ± 0.02	-	-	-
	10	146 ± 13	0.84 ± 0.01	0.33 ± 0.02	-	-	-
DODMA N/P 2	4.5	527 ± 10	1.09 ± 0.01	0.13 ± 0.01	500 ± 81	0.78 ± 0.02	0.81 ± 0.09
	5	534 ± 7	1.09 ± 0.01	0.13 ± 0.01	427 ± 49	0.76 ± 0.02	0.80 ± 0.07
	5.5	532 ± 7	1.09 ± 0.01	0.13 ± 0.01	391 ± 41	0.78 ± 0.01	0.73 ± 0.06
	6	544 ± 8	1.09 ± 0.00	0.12 ± 0.01	427 ± 47	0.78 ± 0.01	0.74 ± 0.06
	6.5	537 ± 11	1.08 ± 0.01	0.13 ± 0.01	335 ± 37	0.83 ± 0.01	0.53 ± 0.04
	7	539 ± 17	1.05 ± 0.01	0.13 ± 0.01	391 ± 43	0.82 ± 0.01	0.47 ± 0.04
	7.5	546 ± 29	0.99 ± 0.01	0.18 ± 0.01	440 ± 54	0.77 ± 0.01	0.46 ± 0.04
	8	739 ± 112	0.93 ± 0.01	0.34 ± 0.01	640 ± 219	0.60 ± 0.04	0.63 ± 0.50
DODMA N/P 4	4.5	433 ± 10	1.10 ± 0.01	0.19 ± 0.01	370 ± 53	0.77 ± 0.01	0.79 ± 0.08
	5	449 ± 11	1.09 ± 0.01	0.19 ± 0.01	336 ± 52	0.78 ± 0.02	0.75 ± 0.08
	5.5	438 ± 14	1.08 ± 0.01	0.19 ± 0.01	321 ± 43	0.83 ± 0.02	0.63 ± 0.05
	6	381 ± 11	1.08 ± 0.01	0.18 ± 0.01	337 ± 39	0.82 ± 0.01	0.66 ± 0.05

	6.5	398 ± 12	1.06 ± 0.01	0.18 ± 0.01	421 ± 45	0.83 ± 0.01	0.48 ± 0.04
	7	383 ± 16	1.02 ± 0.01	0.19 ± 0.01	354 ± 43	0.80 ± 0.01	0.41 ± 0.04
	7.5	364 ± 36	0.95 ± 0.01	0.26 ± 0.01	474 ± 82	0.73 ± 0.01	0.51 ± 0.05
	8	305 ± 53	0.93 ± 0.01	0.29 ± 0.02	585 ± 132	0.69 ± 0.02	0.61 ± 0.08

MC3 Formulations

Formulation	pH	Main peak			Front peak		
		Area	Peak center	Peak width	Area	Peak center	Peak width
MC3 N/P 0.2	4.5	302 ± 3	1.02 ± 0.01	0.10 ± 0.01	-	-	-
	5	288 ± 3	1.02 ± 0.01	0.10 ± 0.01	-	-	-
	5.5	273 ± 4	1.02 ± 0.01	0.10 ± 0.01	-	-	-
	6	239 ± 3	1.02 ± 0.01	0.10 ± 0.01	-	-	-
	6.5	240 ± 4	1.02 ± 0.01	0.11 ± 0.01	-	-	-
	7	223 ± 3	1.02 ± 0.01	0.11 ± 0.01	-	-	-
	7.5	232 ± 2	1.02 ± 0.01	0.11 ± 0.01	-	-	-
	8	187 ± 5	1.01 ± 0.01	0.11 ± 0.01	-	-	-
	8.5	143 ± 4	0.99 ± 0.01	0.13 ± 0.01	-	-	-
	9	131 ± 5	0.97 ± 0.01	0.16 ± 0.01	-	-	-
	9.5	78 ± 6	0.95 ± 0.01	0.13 ± 0.01	-	-	-
	10	72 ± 7	0.94 ± 0.01	0.15 ± 0.01		-	-
MC3 N/P 0.65	4.5	406 ± 4	1.06 ± 0.01	0.11 ± 0.01	-	-	-
	5	374 ± 5	1.06 ± 0.01	0.11 ± 0.01	-	-	-
	5.5	392 ± 5	1.06 ± 0.01	0.11 ± 0.01	-	-	-
	6	367 ± 6	1.06 ± 0.01	0.11 ± 0.01	-	-	-
	6.5	171 ± 4	1.05 ± 0.01	0.11 ± 0.01	-	-	-
	7	321 ± 8	1.04 ± 0.01	0.12 ± 0.01	-	-	-
	7.5	374 ± 10	1.03 ± 0.01	0.16 ± 0.01	-	-	-
		375 ± 13	1.00 ± 0.01	0.21 ± 0.01	-	-	-
		279 ± 28	0.96 ± 0.01	0.31 ± 0.02	-	-	-
		226 ± 23	0.93 ± 0.01	0.36 ± 0.03	-	-	-
		227 ± 61	0.88 ± 0.01	0.45 ± 0.08	-	-	-
	8	103 ± 15	0.87 ± 0.01	0.28 ± 0.03	-	-	-
MC3 N/P 2	4.5	569 ± 34	1.14 ± 0.01	0.15 ± 0.01	125 ± 65	0.87 ± 0.03	0.46 ± 0.20
	5	565 ± 35	1.14 ± 0.01	0.16 ± 0.01	109 ± 73	0.84 ± 0.03	0.44 ± 0.25
	5.5	569 ± 26	1.14 ± 0.01	0.16 ± 0.01	104 ± 51	0.88 ± 0.02	0.42 ± 0.17
	6	589 ± 23	1.14 ± 0.01	0.17 ± 0.01	106 ± 49	0.85 ± 0.02	0.40 ± 0.16
	6.5	593 ± 22	1.12 ± 0.01	0.17 ± 0.01	134 ± 43	0.87 ± 0.01	0.37 ± 0.10
	7	605 ± 32	1.09 ± 0.01	0.19 ± 0.01	165 ± 52	0.86 ± 0.01	0.34 ± 0.09
	7.5	431 ± 56	1.02 ± 0.01	0.18 ± 0.01	240 ± 69	0.85 ± 0.01	0.30 ± 0.06
	8	326 ± 103	0.96 ± 0.01	0.27 ± 0.04	278 ± 134	0.76 ± 0.02	0.34 ± 0.11

MC3 N/P 4	4.5	410 ± 9	1.19 ± 0.01	0.18 ± 0.01	54 ± 27	0.81 ± 0.05	0.38 ± 0.16
	5	-	-	-	-	-	-
	5.5	413 ± 5	1.18 ± 0.01	0.18 ± 0.01	45 ± 17	0.81 ± 0.04	0.31 ± 0.10
	6	446 ± 13	1.17 ± 0.01	0.18 ± 0.01	61 ± 39	0.94 ± 0.04	0.49 ± 0.23
	6.5	483 ± 11	1.14 ± 0.01	0.18 ± 0.01	122 ± 53	0.82 ± 0.02	0.56 ± 0.20
	7	414 ± 17	1.08 ± 0.01	0.19 ± 0.01	187 ± 41	0.86 ± 0.02	0.49 ± 0.07
	7.5	316 ± 42	1.01 ± 0.01	0.28 ± 0.01	280 ± 73	0.79 ± 0.02	0.45 ± 0.07
	8	306 ± 29	0.99 ± 0.01	0.31 ± 0.01	261 ± 61	0.68 ± 0.01	0.50 ± 0.09

Supplementary Table 3: Calculated structural parameters derived from Lorentzian fits for the main peaks executed on experimental SAXS data as described in Methods section. Data are presented as fitted mean ± calculated error

pH		d-spacing [nm]	Correlation length [nm]	Fractal dimension		d-spacing [nm]	Correlation length [nm]	Fractal dimension
4.5	DODAP N/P 5	6.23 ± 0.01	5.50 ± 0.19	2.6 ± 0.1	MC3 N/P 5	5.17 ± 0.01	9.01 ± 0.36	2.8 ± 0.1
5		6.28 ± 0.02	5.37 ± 0.20	2.5 ± 0.1		5.18 ± 0.01	9.33 ± 0.23	2.8 ± 0.1
5.5		6.35 ± 0.02	5.18 ± 0.23	2.4 ± 0.1		5.18 ± 0.01	9.39 ± 0.31	2.7 ± 0.1
6		6.45 ± 0.03	5.11 ± 0.25	2.6 ± 0.1		5.20 ± 0.01	8.77 ± 0.35	2.7 ± 0.1
6.5		6.70 ± 0.09	4.82 ± 0.52	2.6 ± 0.1		5.43 ± 0.01	8.48 ± 0.22	2.5 ± 0.1
7		7.31 ± 0.22	3.32 ± 0.37	2.7 ± 0.1		5.69 ± 0.01	7.35 ± 0.34	2.3 ± 0.1
7.5		7.55 ± 0.15	3.01 ± 0.40	2.6 ± 0.1		5.58 ± 0.02	7.88 ± 0.62	2.3 ± 0.1
8		7.71 ± 0.25	2.65 ± 0.31	2.6 ± 0.1		5.57 ± 0.01	8.58 ± 0.58	2.3 ± 0.1
4.5	DODMA N/P 5	5.82 ± 0.01	8.90 ± 0.28	2.7 ± 0.1	ALC-0315 N/P 5	4.50 ± 0.01	6.16 ± 0.23	3.0 ± 0.1
5		5.85 ± 0.01	8.93 ± 0.38	2.7 ± 0.1		4.49 ± 0.01	5.79 ± 0.10	3.0 ± 0.1
5.5		5.86 ± 0.01	8.23 ± 0.29	2.4 ± 0.1		4.60 ± 0.01	6.85 ± 0.14	3.0 ± 0.1
6		5.90 ± 0.01	8.68 ± 0.27	2.2 ± 0.1		4.70 ± 0.01	6.97 ± 0.11	2.9 ± 0.1
6.5		5.95 ± 0.01	9.34 ± 0.57	2.4 ± 0.1		4.89 ± 0.01	7.66 ± 0.29	2.4 ± 0.1
7		6.20 ± 0.03	8.66 ± 0.65	2.3 ± 0.1		4.90 ± 0.03	7.69 ± 0.98	2.3 ± 0.1
7.5		6.51 ± 0.13	5.29 ± 0.79	2.3 ± 0.1		4.90 ± 0.02	7.70 ± 0.75	2.3 ± 0.1
8		6.34 ± 0.07	5.03 ± 0.70	2.3 ± 0.1		4.93 ± 0.02	7.45 ± 0.49	2.3 ± 0.1

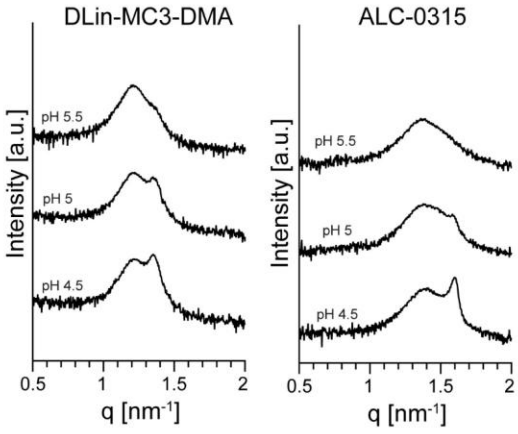

Supplementary Figure 1: Bragg peaks of LNPs at acidic pH values being characterized by three peaks for MC3 (left figure; third high q peak at 1.35 nm^{-1}) and ALC-0315 (right figure; third high-q peak at 1.58 nm^{-1})

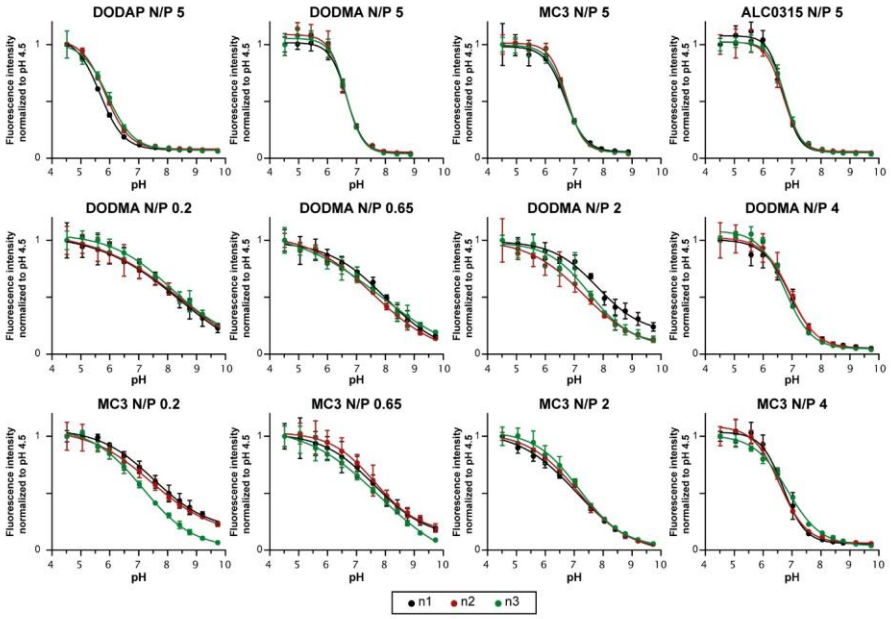

Supplementary Figure 2: TNS assay results of each tested formulation. Fluorescence intensity was normalized against the intensity measured at pH 4.5 reflecting a fully protonated state of the ionizable lipid. Boltzmann fitting was utilized to determine the inflection point of each measurement. Data are presented as mean ± S.D

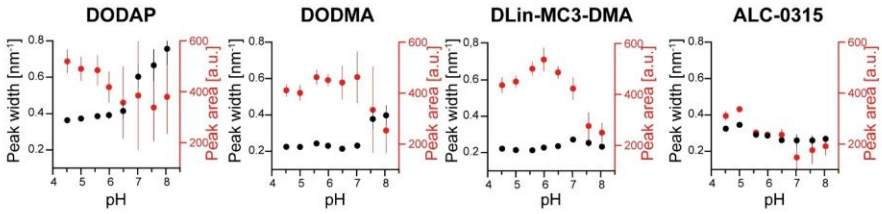

Supplementary Figure 3: Peak width (black) and area (red) for the investigated LNP samples as determined by Lorentzian analysis of the main Bragg peak. While peak width increases enormously for DODAP and DODMA, it does not change as a function of pH for MC3 and ALC-0315 bearing LNPs. For all tested formulations the peak area decreases with increasing pH.

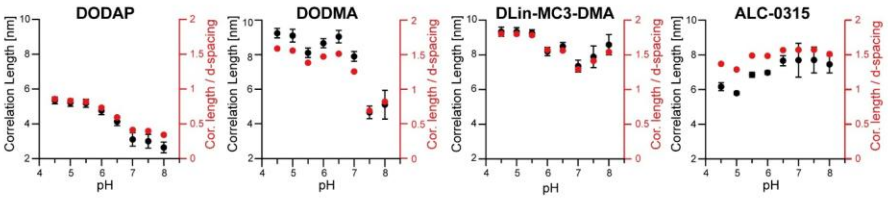

Supplementary Figure 4: Correlation lengths of mRNA-LNPs differing only in the ionizable lipid as a function of environmental buffer pH (left y-axis) and calculated ratios of correlation length and d-spacing (right y-axis, red, values in Fig1C). While especially DODAP- and DODMA-LNPs show a loss in spatial order described by a reduction in the Correlation length/ d-spacing ratio, the ratio for ALC-0315 remains unchanged at a value of approximately 1.5 within the tested pH range.

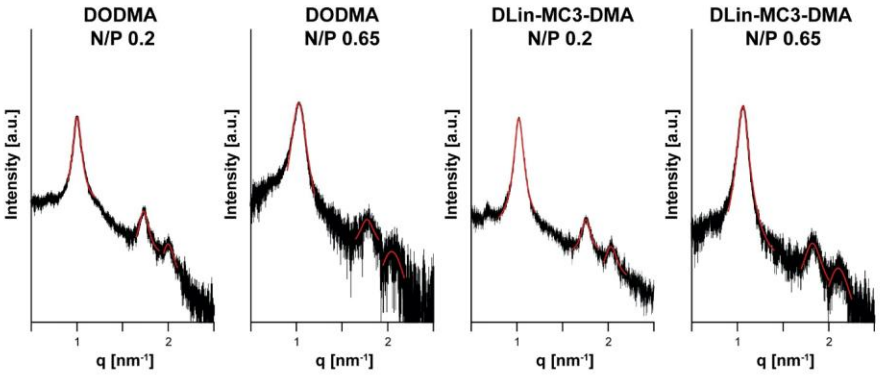

Supplementary Figure 5: Higher order Bragg peaks of Formulations with N/P ratio < 1, respective peak positions are described in Supplementary Table 2

Supplementary Table 4: Peak position of main Bragg peaks and higher order peaks as determined by Lorentzian fitting

	First order peak position [nm^{-1}]	Second order peak position [nm^{-1}]	Third order peak position [nm^{-1}]
DODMA N/P 0.2	1.002 ± 0.001	1.730 ± 0.001	1.998 ± 0.003
DODMA N/P 0.65	1.025 ± 0.001	1.773 ± 0.005	2.043 ± 0.009
MC3 N/P 0.2	1.022 ± 0.001	1.756 ± 0.001	2.030 ± 0.003
MC3 N/P 0.65	1.059 ± 0.001	1.821 ± 0.003	2.103 ± 0.005

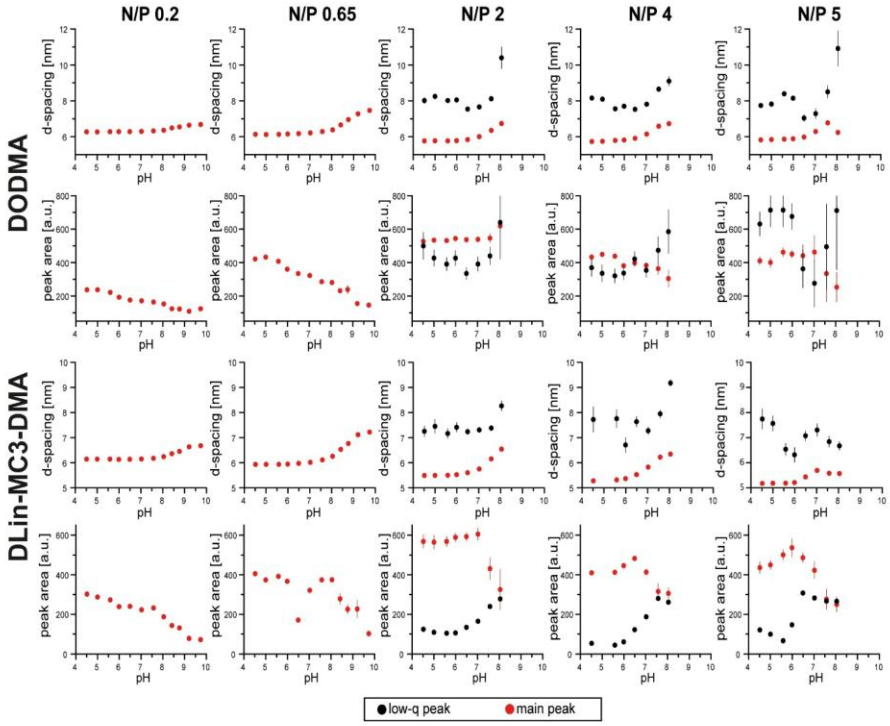

Supplementary Figure 6: Results of d-spacing calculation and peak area determination of main and low-q peak for N/P variation investigation for DODMA (top) and MC3 (bottom).

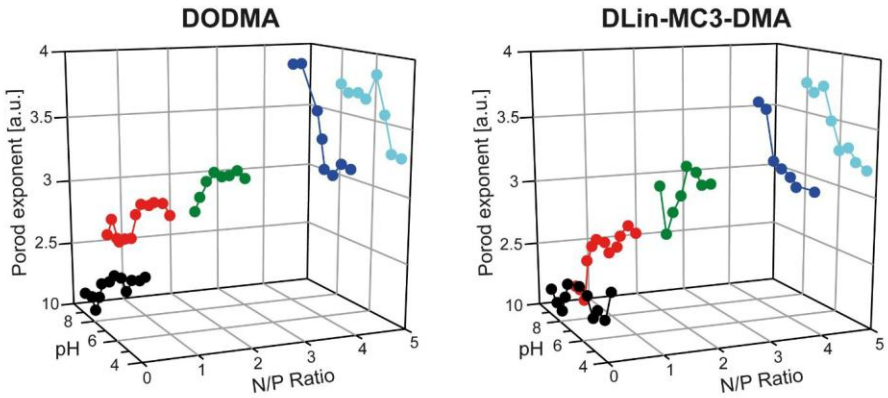

Supplementary Figure 7: Fractal dimension values evolution with varying pH in LNPs (left: DODMA; right: MC3) with different N/P ratio.

Supplementary Table 5: Structural parameters derived from SAXS measurements for LNPs with different N/P ratios, including d-spacing and fractal dimension D_s. Values for d-spacing are presented as calculated repeating distance ± calculated error

	DODMA							
	N/P 0.2		N/P 0.65		N/P 2		N/P 4	
	d-spacing [nm]	Fractal dimen-sion	d-spacing [nm]	Fractal dimen-sion	d-spacing [nm]	Fractal dimen-sion	d-spacing [nm]	Fractal dimen-sion
4.5	6.27 ± 0.01	3.4 ± 0.1	6.13 ± 0.01	3.0 ± 0.1	5.76 ± 0.01	2.8 ± 0.1	5.73 ± 0.01	2.8 ± 0.1
5	6.27 ± 0.01	3.5 ± 0.1	6.12 ± 0.01	3.0 ± 0.1	5.77 ± 0.01	2.8 ± 0.1	5.74 ± 0.01	2.8 ± 0.1
5.5	6.28 ± 0.01	3.5 ± 0.1	6.13 ± 0.01	3.0 ± 0.1	5.77 ± 0.01	2.8 ± 0.1	5.79 ± 0.01	2.8 ± 0.1
6	6.28 ± 0.01	3.6 ± 0.1	6.15 ± 0.01	3.0 ± 0.1	5.78 ± 0.01	2.8 ± 0.1	5.81 ± 0.01	2.4 ± 0.1
6.5	6.28 ± 0.01	3.6 ± 0.1	6.17 ± 0.01	3.0 ± 0.1	5.84 ± 0.01	2.8 ± 0.1	5.91 ± 0.01	2.4 ± 0.1
7	6.29 ± 0.01	3.6 ± 0.1	6.21 ± 0.01	3.1 ± 0.1	6.00 ± 0.01	2.9 ± 0.1	6.15 ± 0.01	2.3 ± 0.1
7.5	6.32 ± 0.01	3.7 ± 0.1	6.29 ± 0.01	3.3 ± 0.1	6.35 ± 0.01	3.1 ± 0.1	6.58 ± 0.01	2.1 ± 0.1
8	6.36 ±.0.01	3.7 ± 0.1	6.38 ± 0.01	3.4 ± 0.1	6.73 ± 0.04	3.2 ± 0.1	6.73 ± 0.02	2.1 ± 0.1
8.5	6.49 ± 0.01	3.8 ± 0.1	6.66 ± 0.01	3.4 ± 0.1				
9	6.54 ± 0.01	3.9 ± 0.1	6.95 ± 0.03	3.4 ± 0.1				
9.5	6.64 ± 0.01	3.9 ± 0.1	7.28 ± 0.03	3.3 ± 0.1				
10	6.68 ± 0.02	3.9 ± 0.1	7.46 ± 0.04	3.4 ± 0.1				
	MC3							
	N/P 0.2		N/P 0.65		N/P 2		N/P 4	
	d-spacing [nm]	Fractal dimen-sion	d-spacing [nm]	Fractal dimen-sion	d-spacing [nm]	Fractal dimen-sion	d-spacing [nm]	Fractal dimen-sion
4.5	6.15 ± 0.01	3.5 ± 0.1	5.93 ± 0.01	3.1 ± 0.1	5.49 ± 0.01	2.8 ± 0.1	5.28 ± 0.01	2.9 ± 0.1
5	6.14 ± 0.01	3.8 ± 0.1	5.93 ± 0.01	3.1 ± 0.1	5.49 ± 0.01	2.9 ± 0.1	-	-
5.5	6.15 ± 0.01	3.8 ± 0.1	5.94 ± 0.01	3.2 ± 0.1	5.50 ± 0.01	2.8 ± 0.1	5.32 ± 0.01	3.0 ± 0.1
6	6.13 ± 0.01	3.9 ± 0.1	5.95 ± 0.01	3.3 ± 0.1	5.52 ± 0.01	2.8 ± 0.1	5.37 ± 0.01	2.9 ± 0.1
6.5	6.14 ± 0.01	3.7 ± 0.1	5.97 ± 0.01	3.4 ± 0.1	5.60 ± 0.01	3.0 ± 0.1	5.53 ± 0.01	2.9 ± 0.1
7	6.15 ± 0.01	3.7 ± 0.1	6.02 ± 0.01	3.4 ± 0.1	5.75 ± 0.01	3.1 ± 0.1	5.83 ± 0.01	2.8 ± 0.1
7.5	6.18 ± 0.01	-	6.11 ± 0.0.1	3.4 ± 0.1	6.15 ± 0.01	3.4 ± 0.1	6.22 ± 0.02	2.4 ± 0.1
8	6.24 ± 0.01	3.7 ± 0.1	6.26 ± 0.01	3.4 ± 0.1	6.54 ± 0.05	3.0 ± 0.1	6.34 ± 0.02	2.4 ± 0.1
8.5	6.36 ± 0.01	3.8 ± 0.1	6.53 ± 0.03	3.6 ± 0.1				
9	6.45 ± 0.1	3.9 ± 0.1	6.77 ± 0.03	3.9 ± 0.1				
9.5	6.64 ± 0.01	3.9 ± 0.1	7.12 ± 0.05	3.8 ± 0.1				
10	6.68 ± 0.02	3.9 ± 0.1	7.22 ± 0.04	3.9 ± 0.1				

5

Discussion and Outlook

Lipid delivery systems for mRNA delivery have emerged from a promising platform to a new class of approved drug products in the last decade. While their success as a vaccine during the COVID-19 pandemic led to the widespread use of mRNA LNPs globally, with the rapid approval of mRNA vaccines by several regulatory agencies, many aspects of this platform remain elusive to the research community. To date, only a few recommendations and guidelines exist for determining the quality of the drug substance and drug product. Especially for determining drug product integrity, numerous established analytical methods, including DLS or MALS, exist and are used in daily quality control routines. However, the results of these methods can be biased by intrinsic polydispersity or structural inhomogeneities and require a deep understanding of the product to be interpreted correctly. This knowledge can be obtained through in-depth characterization during formulation development stages using analytical techniques such as SAXS, which are not applicable as a tool for daily routine but can provide several information that are not obtainable by DLS or other approaches. Likewise, for structure-function relationships that could build a basis for the more rational development of LNP systems, paradigms exist but do not answer every open question and therefore need to be refined to be useful for future development. This results in tedious work for screening lipids and formulations *in vitro* and *in vivo*, which, on the one hand, is very time- and resource-consuming and, additionally, carries the risk of underestimating candidates in early development stages. Elucidating additional organizational features that can be indicative of good biological performance broadens the available methods to estimate the potencies of mRNA LNP drug products and is therefore of high interest to both academia and the pharmaceutical industry.

In this work, a series of structural investigations was conducted to gain an in-depth understanding of the organizational features of mRNA LNPs and their impact on the quality and performance of LNP drug products. One part of the doctoral research comprised the design and implementation of a novel combinational technique, providing a joint analysis of size and size-dependent quality attributes through the hyphenation of AF4 and SAXS. The other project aimed to gain more insights into the influence of manufacturing and composition parameters on the overall and internal structure of LNPs by utilizing SAXS, and further correlating this information with the *in vitro* and *in vivo* performance of the respective formulations. The work presented in this thesis is summarized in four scientific publications, as outlined in Chapters 3 and 4. Together, these studies make a significant

contribution to the field, paving the way for novel applications and improvements to existing mRNA LNP-based nanotherapeutics.

Within the first project, the development of joint AF4-SAXS analysis aimed to fill the gap in missing quantitative determination approaches for the size-dependent properties of pharmaceutical nanoparticles. To tackle this unmet need, an in-line coupling of AF4 separation, accompanied by the typical downstream detection methods (MALS, DLS, UV), with synchrotron solution SAXS was implemented. This enables the orthogonal determination of particle size along with particle-size-related parameters. Here, the ability of SAXS to quantify analytes can be used to generate datasets of distinct sample size fractions, which can be further correlated with the downstream AF4 detectors. This connected setup enabled us to overcome the limitation of batch measurements in SAXS, where samples with intrinsic polydispersity result in the overlay of signals obtained from different particle types. Therefore, it is highly important to provide samples as homogenous in size and morphology as possible for quantitative analysis. A combination of SAXS with SEC has already been established in several synchrotron sources, but it lacks usability with lipidic delivery systems and other pharmaceutically used nanoparticles. High shear forces during SEC separation, for example, can affect the morphology of the particles. Additionally, the fact that larger particles, such as agglomerates, elute lastly after the smaller size fractions with AF4 separation, leads to reduced capillary fouling (reduced performance due to surface depositions within the capillary) in SAXS, as agglomerates are more prone to radiation damage. This often leads to reduced data quality for smaller moieties in SEC-SAXS coupling, where the large moieties elute first. Based on the frequent use of the SEC-SAXS setup, we assumed a high interest also from other groups in using our joint AF4-SAXS setup, since it increases the variety of measurable systems. These include, besides nanoparticular vehicles as lipoplexes and LNPs, also pharmaceutically protein formulations, such as antibodies, nanobodies, or other peptide-based drugs.
For proof of concept of the combinational approach, we investigated the protein sample BSA as well as mRNA-carrying lipoplexes as model systems. These tested lipoplexes, to date, are the subject of several clinical studies, as explained in Chapter 0, and possess several benefits that make them a suitable model system for the initial study. They exhibited (i) relatively large sizes for nanoparticulate drug products (200-800 nm), they (ii) come along with high intrinsic polydispersity (both, in case they are not homogenized downstream of manufacturing), and (iii) they were manufactured with an excess of mRNA, thus, providing a section of free mRNA additionally to the lipoplexes. The latter allowed for the separation of two fractions of material inside the sample, which were significantly different in size and nature of material, and therefore presented an adequate challenge for the setup. Despite proving the application of this setup as described in the respective publication, many questions and tasks remained to be addressed for implementing AF4-SAXS into the beamline facility, located at the EMBL Hamburg outstation at DESY, to make it

accessible to users worldwide. These include the integration of software into the user interface of the beamline, which enables the use of the integrated autosampler and allows for multiple runs within a sequence through the already established software of the P12 beamline. While this work was conducted by the experts at the beamline in Hamburg, we contributed through our hands-on experience from several AF4-SAXS experiments, detecting recurring errors or pitfalls that could be addressed in the subsequent updates. Further improvements, implemented since the pilot experiment, include automatic cleaning in place during longer measurement sequences and a standardized approach to provide the collected data to the user.

The successful experiments from Chapter 3 encouraged us to expand the investigated systems to other already approved drug products in ongoing studies. In the first follow-up studies, currently being prepared for publication, we continued our work with mRNA-carrying LNPs, which are more in focus than lipoplexes for RNA delivery, but exhibit a more complex structure and therefore present additional challenges for the analysis. One often-discussed topic is the payload distribution of mRNA, because it influences pharmacodynamics, pharmacokinetics, and delivery efficacy [163]. Based on the proven ability to provide quantitative data on the size distribution, as well as the mRNA payload distribution within the respective size fractions, we are convinced that our joint analysis can answer remaining questions, such as the presence of empty LNPs in coexistence with loaded LNPs. In addition, we are investigating the *in vitro* potency of different size fractions of LNPs to elucidate how size and loading capacity of LNPs influence their transfection efficacy in different cell types in future works.

Also, other than mRNA-based nanoparticulate drug products, are currently being investigated in this setup. For example, we performed experiments on Amphotericin B loaded generic drug products to assess their comparability to the originating drug product. These medications are used to treat invasive fungal infections, particularly in immunosuppressed patients with a high need in low-income countries [164]. Given the toxicity of the API and the high costs of the treatment, application of generic liposomal Amphotericin B drug products from countries other than Europe or the United States, and the evaluation of their quality, becomes a crucial point for authorizing agencies to overcome supply barriers [164,165]. Due to this, we believe the AF4-SAXS combination could be a valuable tool for determining particle size and payload distribution of generic products, which may serve as the basis for determining pharmaceutical equivalence and eventually bioequivalence for these and comparable drug products.

In the second part of the work, the influences of formulation parameters and external conditions on the structure and function of mRNA LNPs were investigated in different studies (Chapter 4). As explained previously (Chapter 1.3 and 1.4), different manufacturing methods and lipid excipients can be employed to produce mRNA LNPs, resulting in formulations with varying physicochemical properties and therapeutic potencies. While the effect of formulation parameters on *in vitro* and *in*

vivo efficacy is often described, the implications for organizational properties are rarely addressed in recent research approaches. Therefore, we aimed to systematically investigate the LNP structure using SAXS and corresponding physicochemical investigation tools, focusing on changes in composition, manufacturing method, or environmental conditions.

SAXS enables the determination of several structural parameters, both for the overall particle and its internal organization. While the detection of particle size, as explained before, is limited without a respective fractionation technique, the internal features can also be evaluated without upstream separation of particle fractions, since they remain similar in different particle size ranges. Parameters, which are obtainable from these kinds of measurements, are the surface fractal dimension, repeating unit distance, and long-range order of these repeating units. The surface fractal dimension is derived from the intensity decay in the lower q-ranges of the SAXS spectrum. By using a power law, the Porod exponent, which describes the steepness of the intensity decay, can be analyzed. A steeper decay is indicative of smooth surfaces, whereas a decreasing Porod exponent can describe increased surface roughness or even polymer chain-like fractality. Besides this intensity decay in lower q-ranges, SAXS patterns derived from LNPs are characterized by a peak at a distinct q-value, which is attributed to frequently occurring structural motifs. As a matter of the repeating distance of these structural motifs, the peak position is shifted, whereas the extent of ordered stacks influences the width of the derived peak. As shown in several SAXS studies in our group, these detectable repeating distances for lipid mRNA delivery systems are derived from lipid stacks with mRNA inserted in the hydrophilic slab between them [99,166]. While lipoplexes exhibit sharp peaks with frequently occurring higher-order peaks, the reflexes in LNP samples are broader. The sharp peaks, indicating a high long-range order of the mRNA/lipid stacks, are due to the multilayer order of lipoplexes (see **Fehler! Verweisquelle konnte nicht gefunden werden.** in the introduction). Since in LNPs these multilayers are not present and the mRNA is more incorporated into lipid layers with lower long-range order, the peaks appear to be broader. In the following, the long-range order, as derived from peak width, is explained in terms of the correlation length. The peak position is indicative of the length scale of repeating units (e.g., mRNA/lipid stacks) and can be described as the d-spacing, which was originally used to describe crystalline structures but is also applicable to lipid bilayer systems [167].

One scientific goal was to elucidate the effects of substitutions in the stealth moiety of mRNA LNPs, where PEGylated lipids are currently the gold standard, but also pose some risk of rapid in-circulation clearance and adverse effects (see Chapter 1.4.4). The use of PEG alternatives can circumvent, for example, the accelerated blood clearance (ABC) phenomenon as shown in animal models [124]. Polysarcosine as a potential substitute has been shown to exhibit comparable stealth effects and transfection efficacy in several studies within our subproject B12 of the CRC1066 [121–

[123,125]. The biocompatibility and biodegradability can, on one hand, explain the lower immunogenicity as a polypeptoide polymer. The N-methylation of the amine within the sarcosine units, on the other hand, prevents hydrogen bonding, which normally contributes to immune recognition in classical peptides[121]. The N-methylation additionally leads to an impeded enzymatic degradation during circulation, which prevents the. Additionally, due to potential end-group modifications, it enables flexible functionalization with antibodies or antibody fragments. To further broaden the knowledge about pSar as an LNP excipient, the structural implications were investigated in two studies and subsequently correlated with its potency in *in vitro* and *in vivo* models (see Chapters 4.1 and 4.2). While internal structure (e.g., the repeating distance and long-range order of the mRNA-lipid stacks) was not or only to a small extent influenced by the choice of stealth moiety, the surface properties showed a larger effect upon PEG substitution. Particularly, according to the SAXS data, the surface fractal dimension was increased for pSar-grafted LNPs in comparison to PEG-grafted LNPs. These differences became even clearer in acidic media, which is the local environment during endosomal uptake pathways. One explanation may be that the amine headgroup of pSar potentially exhibits a positive charge in acidic media, and therefore shows a higher response to pH changes. The otherwise unaffected structural features are indicative of negligible integration of the stealth moieties within the particle core, where they would contribute to mRNA complexation and, consequently, influence the integrity and stability of the drug substance. In our *in vitro* testing study on hPBMCs, the tolerability of pSar-LNPs was again demonstrated to be good. For transfection efficacy in monocytes, as one subpopulation of the hPBMCs, all pSar-containing LNPs showed significantly higher transfection efficacy than their PEG-containing analogues (see Chapter 4.1). As demonstrated by cell binding assays, the pSar-grafted LNPs also exhibited a higher association with cells, which may be one explanation for the better transfection efficacy. Similarly, in our *in vitro* studies using other cell lines (adherent HepG2 cells and suspended Jurkat T cells), pSar-LNPs outperformed PEG-LNPs, regardless of the manufacturing approach used, with differences varying among the tested cells. In Jurkat T cells, the advantage of pSar in transfection efficacy was highest for microfluidic-produced particles, but was comparable for particles produced using the pipetting ethanol injection approach (which resulted in larger particle sizes). The favorable performance of small particles in suspended cell lines, such as Jurkat T, may explain the lack of pSar benefit in bigger particles, while the benefit was outstanding for small particles. This highlights that variation in transfection efficacy depends not only on the lipid composition, but also on a complex interplay of various factors such as particle size and cell line-specific requirements. Despite the advantages of pSar during *in vitro* experiments, *in vivo* experiments using a zebrafish embryo model did not exhibit significant benefits of pSar, but comparable biodistribution and transfection results compared with PEG. Summarizing our results, we are convinced that pSar is a promising alternative to PEGylation in nanomedicines, having a

minor influence on morphology and biodistribution, while showing cell-type-dependent advantages or at least comparable efficacy in all test systems to PEG.

While a high (surface) fractal dimension could be reached through pSar-grafting, other parameters have also been shown to influence the surface roughness of LNPs. On the one hand, the manufacturing method affects the morphology of the overall particle and, with that, also surface properties. While microfluidic approaches lead to smaller particles with smoother surfaces, especially pipetting-based, unstandardized mixing approaches led to particles twice as big in size, bearing distinct morphologies. As visible in cryo-TEM images, these particles exhibit so-called blebs, lipidic substructures derived from phase segregation of lipid excipients [30,168]. While these are preferably formed from phospholipids not compatible with hexagonal lipid phases, such as DSPC, we were also able to observe these for particles manufactured with DOPE, a phospholipid known for its tendency to undergo hexagonal transitions [104]. We hypothesize that the slow mixing conditions during pipette mixing facilitate the formation of blebs, independent of the lipid composition. This observation of bleb occurrence also contributed to an increased mass surface fractality for these particles, as detected by SAXS. While the comparison of the three manufacturing approaches did not significantly influence *in vivo* transfection efficacy, experiments for biodistribution revealed a higher tendency towards aggregation during circulation for the larger particles with higher surface fractality and bleb formation. Here, it is noteworthy to mention that comparability of the particles was somehow limited because of the significant differences in particle size, so the effects of surface fractality on potency could not properly be assessed.

The choice of ionizable lipids also influences surface fractality. As shown in Chapter 4.1, MC3-based LNPs exhibited significantly higher surface fractality than the LNPs composed of DODMA. Interestingly, this also correlated with transfection efficacy in monocytes. To further investigate this relationship, a comparative study of 4 different ionizable lipids was conducted (see Chapter 4.3), where the potency was varying from weak to high, as it is well known from literature and own experiments [89,96,169,170]. While DODAP-LNPs, comprising an ionizable lipid with known low transfection potency, exhibited the lowest fractal dimension in an acidic environment, with increasing known potency, the surface fractality and thus the surface roughness increased (DODMA<MC3<ALC-0315). Additionally, DODAP-LNPs did not show a pH-responsive change of surface fractality, whereas all LNPs manufactured with other ionizable lipids exhibited an increase upon acidification. Overall, our results from structural studies guide towards a positive influence of high surface fractality, especially at acidic pH, on the transfection potency of the delivery system. We hypothesize that this structural feature of LNPs is favorable during endosomal escape, where positively charged lipids of the LNPs interact with negatively charged endosomal membrane lipids, facilitating membrane rupture and subsequent release of the nucleic acid cargo into the cytosol (see Chapter 1.4.1, Figure 1.4-2). We assume that an increased fractal dimension may reduce the energy barrier for membrane rupture, leading to higher permeability of the

endosomal membrane. To confirm this, experiments on model membrane systems may be applied (e.g., Atomic Force Microscopy) to investigate the interactions between LNPs and oppositely charged lipid membranes in detail.

Another structural feature, which was detectable by SAXS analysis and correlated with LNP activity, is the distance and long-range order of the repeating units, which are derived from the mRNA/lipid interactions (e.g., the d-spacing and correlation length). As described in Chapter 4.1, DOPE and MC3-containing LNPs, which exhibited the highest surface protein expression levels in this experiment, also showed one of the lowest d-spacings and one of the highest correlation lengths. By investigating all formulations only varying in their ionizable lipid, a significant decrease in d-spacing and an increase in correlation length were visible for MC3-LNPs compared to their DODMA analogues. Also, in our comparative study with multiple ionizable lipids, a low d-spacing and relatively high correlation length correlated with the known activity from the lipid excipients. This high perpendicular packing density is a second structural indicator that may be used to estimate the therapeutic potency of mRNA LNP systems. The dense complexation of the mRNA is hypothesized to be beneficial from the perspective of drug substance and drug product stability, both during storage and after administration.

The properties of the mRNA/lipid stacks are additionally influenced by the lipid-to-mRNA ratio (N/P ratio). Increasing molar fractions of mRNA within LNPs lead to an increase in d-spacing and correlation length. Interestingly, most LNP formulations described in the research community are characterized by a high excess of ionizable lipid (N/P ratio>>1). One explanation for the lack of using systems with an excess of mRNA may be the lower perpendicular packing density of mRNA within these formulations, but this needs to be confirmed with further experiments.

In addition to modifications of the mRNA/lipid interactions, N/P ratio variations also led to conversions in the overall organization of the LNP systems. With an excess of mRNA (N/P ratio < 1) the SAXS patterns revealed a single pronounced Bragg peak, indicative of one single type of structural features inside the particle. With increasing molar fraction of ionizable lipids a second Bragg peak has been observed, indicative of a second lipid substructure with larger repeating distances. Because of the pH-responsive behavior of this second peak, indicating no change or, in some cases, a decrease in repeating distance with increasing pH, it may be derived from an mRNA-depleted structural motif. Notably, with the batch measurements, where these results were observed, it is hard to distinguish if these different structural motifs derive from different fractions of LNPs or from LNPs bearing different lipidic motifs in one particle. While batch measurements average the scattering intensities from all measured particles, thus leading to an overlay of different scattering profiles, an upstream fractionation technique, as explained in Chapter 3.1 could clarify the results in this regard, and is the scope of future investigations in our group. Additional measurements using freeze-fracture EM would help to prove the assumptions from the batch measurements. Also, surface properties were influenced by the N/P ratio. With an excess of mRNA,

a fractality was observed, which exceeds the surface fractality observed for LNPs in case of an excess of ionizable lipid. It may be explained by mRNA building shell-like structures at the surface of the particles. Since mRNA is basically a biopolymer, when building a shell on the particle surface, in the SAXS patterns, the surface properties of the "polymeric coat" dominate so that a mass fractality of a polymeric chain is detectable. These results highlight that not only the choice of lipid components and manufacturing methods, but also the mRNA-lipid ratio, highly influence the structural organization of mRNA LNPs and are a valid tool for fine-tuning formulations.

What further underlines this is its influence on the pH-responsive behavior of LNPs as shown in Chapter 4.3. The apparent pK_a of the LNPs, determined by the fluorescence-based TNS assay, is shifted towards higher values with decreasing N/P ratio, with values around 8 at N/P 0.2, whereas at N/P 5 the values are between 6 and 7. The composition is affecting the local environment of the ionizable lipid´s amine groups, therefore influencing their level of protonation with varying pH. The pK_a of the LNP formulation crucially impacts the activity of the mRNA drug product, and thus, determining an optimal pK_a for the intended application is one of the main paradigms for rational formulation design in this field [171]. Thereby, different administration routes and targeted therapeutic intervention require different pK_as of the LNPs (see Chapter 1.4.1), and changes in the formulation's pK_a led to organ/tissue-specific expression *in vivo* [26]. Adjusting the pH-responsive behavior not only with the choice of the ionizable lipids but also with varying N/P ratio, may open another tool to fine-tune the delivery systems according to their intended use.

Because of the observed pH-responsive properties of distinct structural features during SAXS experiments with varying pH environments, a structural analogue to the fluorescence-based value was established within this work. It is derived from the length of the repeating units (e.g., d-spacing) and thus reflects the conditions of the API inside the delivery system. While the TNS assay is a well-established, easy-to-apply method for determining the apparent pK_a, it has distinct limitations. Experimental conditions (e.g., buffer choice) highly influence the results and impede comparability between different labs. Furthermore, it only reflects the pH-dependent behavior of accessible amine groups, most likely describing the situation on the particle surface. In contrast, the SAXS-based structural approach directly displays the situation inside the LNPs where mRNA is complexed and provides a buffer-independent readout for the pK_a. Using this method, it was possible to detect certain variations from the TNS-based results, which underline the potential of our method in detecting information which are not visible for the established assay. For example, there are significant differences in the pK_a of DODAP and ALC-0315-based LNPs between the two approaches. The origin of these differences remains unknown at this point, but needs to be proven and elucidated in upcoming experiments.

Summarizing our results, we paved the way for applying SAXS as a tool for the determination of critical quality attributes for lipid delivery systems carrying mRNA. While SAXS has so far mainly been used descriptively, without in-depth characterization of the respective scattering patterns, we

proposed strategies to use the technique in a standardized approach. By doing so, it is possible to determine the state of the mRNA/lipid complex, which can be used for indications of potency and stability perspectives. Surface fractality as a property, which was not considered for standard SAXS analysis for LNPs so far, was described to be correlated with high therapeutic efficacy. Determination of such structural fingerprints, which could help with potency estimations, may be beneficial in early development stages as complementary measures to biological testing. By investigating the influences of lipid composition, manufacturing approaches, and external conditions on structure and function, we set the basis to describe critical process parameters and critical quality attributes, which can be further used in upscaling from small to large batches and rational development of mRNA LNP drug products using quality by design approaches.

6

Appendix

6.1 List of Figures

Figure 1.1-1: Comparison between structure and function of LNP vehicles tailored for nucleic acid delivery and classic liposomal drug carriers used in many approved drug products. 2

Figure 1.2-1: Schematic overview of the two main lipid delivery systems for mRNA: lipoplexes (LPX) and lipid nanoparticles (LNPs). The main differences are lipid composition, manufacturing process, and subsequently size and internal organization. Further implications are discussed in the following chapters 8

Figure 1.2-2: Evolution of ionizable lipids from permanently cationic transfection agents towards the ionizable lipids used in COVID-19 vaccines. 11

Figure 1.3-1: Manufacturing approaches for liposomes using thin-film hydration (A) or solvent injection (B) procedures. A. During the thin film hydration approach lipids get dissolved in an organic solvent that is subsequently evaporated. The remaining dried thin lipid film is then rehydrated with an aqueous phase, which leads to formation of polydisperse lipid vesicles. These must be homogenized (e.g., using an extruder) to receive relatively monodisperse liposomes. B. During solvent injection procedures, lipids get dissolved in a water miscible solvent (e.g., ethanol) and the aqueous phase is added by, for example, syringe-based injection. Ethanol dilution and homogenization can be supported through vortexing. The remaining liposomes are relatively small and monodisperse without downstream processing. 14

Figure 1.3-2: Microfluidic LNP production technologies based on different micromixer geometries. A. T-junction micromixer. B. Sheath flow or hydrodynamic focusing micromixer. C. Staggered herringbone micromixer. D. Bifurcated or toroidal micromixer. 16

Figure 1.4-1. State of the art composition of mRNA carrying LNPs divided into the four essential lipid components: ionizable lipid (yellow), phospholipids (red), cholesterol (brown), and stealth effect mediating lipopolymers (blue). Together, these lipid components interact to form RNA-carrying LNPs, as illustrated in the center of the figure. For the ionizable and stealth lipids the usage in the respective approved drug products is stated in brackets. 18

Figure 1.4-2. Endosomal escape mechanisms for mRNA LNPs. Following endocytosis, stepwise acidification during endosomal maturation leads to the protonation of ionizable lipids and subsequent interaction with negatively charged lipids within the endosomal membrane, resulting in the destabilization of the endosomal membrane. This facilitates the release of the nucleic acid cargo into the cytosol. Adopted from [102]. 20
Figure 1.5-1: Schematic overview of size determination using Dynamic Light Scattering (DLS). The incoming monochromatic laser beam is scattered by particles and detected, e.g., at an 173° angle in non-invasive back scattering (NIBS) methods. Particles in Brownian motion can be detected at different positions and time points, so the lag time τ of correlating signals from the same particles can be detected. Cumulative events of the whole entity of particles result in a detected count rate of photons. Correlation analysis of the detector signals yields the autocorrelation function, from which the diffusion coefficient can be determined to calculate the hydrodynamic diameter. 29
Figure 1.5-2: Structural features detectable by Lorentzian fitting of the SAXS-derived peak. Repeating structural motifs, as the mRNA/lipid stacks within lipoplexes (as displayed in the right) lead to peaks in the SAXS patterns of these systems (right). Lorentzian fitting (as indicated by the red line in the scattering pattern) of the observed peaks allows detection of peak position and width, which can be converted to length and long-range order of the repeating units, respectively (center). 32
Figure 1.6-1: Schematic illustration of a SAXS experiment (left) and the scattering behavior at single X-Ray scattering events (right). 34
Figure 1.6-2: Relationship between particle structure (left, including internal distances (rij) between internal particles i and j), the pair distance distribution function (p(r) function, middle), and the scattering intensity measured by SAXS (right). The p(r) function can be derived from scattering patterns by indirect Fourier transformations (IFT) and vice versa by Fourier transformations (FT). 35
Figure 4.1-1. Graphical abstract of the publication 4.1. LNP formulations of systematically varied lipid composition were tested in SAXS for internal structure investigation as well as for biological performance using hPBMCs to explore structure-function relationships for mRNA LNPs. As published in [89] 65
Figure 4.2-1. Graphical abstract of the publication 4.2. A novel microfluidic process (CD) was tested against two established manufacturing methods (NA and EI) by investigating structure and morphology along with biological performance *in vitro* and *in vivo* using a zebrafish embryo model. As published in [88]. 89
Figure 4.3-1: Graphical abstract of the publication 4.3. Different mRNA LNP formulations with varying compositions (ionizable lipid, N/P ratio) were investigated using SAXS in different environmental pH buffers. Structural investigations revealed organizational features present

in highly potent formulations, as well as structural parameters that are altered by pH, allowing for the determination of structural pK_a values. As published in [162]. 113

6.2 List of Tables

Table 1.2-1: Selection of parenteral liposomal drug products being approved by the FDA or EMA with their respective details and indications. List adopted from [50,51] 6

Table 1.2-2: Selection of mRNA lipoplex based candidates currently being investigated in clinical trials adopted from [66] 9

Table 1.2-3: Selection of mRNA LNP based drug products and investigational medicinal products currently investigated in clinical trials. Adopted from [6,66] 12

Table 1.5-1 Characterization and Release Testing Criteria for mRNA Drug Substance and their respective analytical procedures proposed by Ph. Eur. (Edition 11.5) and USP (Edition 2025, Issue 3) 25

Table 1.5-2 Characterization and Release Testing Criteria for mRNA Drug Product and their respective analytical procedures proposed by Ph. Eur. (Edition 11.5) and USP (Edition 2025, Issue 3). Alternative methods for quality determination were added according to [131] 27

6.3 List of Abbreviations

(h)DC	(human) dentritic cells
(poly)A tail	polyadenylated tail of an mRNA transcript
(U.S.) FDA	(United States) Food and Drug Administration
µg	Microgram
Å	Angstrom
a.u.	arbitrary unit
ABC	Accelerated blood clearance
AF4	Asymmetrical flow field-flow fractionation
ALC-0159	2-[(polyethylene glycol)-2000]-N,N-ditetradecylacetamide
ALC-0315	[(4-Hydroxybutyl)azandiyl]bis(hexan-6,1-diyl)bis(2-hexyldecanoat)
ANOVA	Analysis of variance
API	active pharmaceutical ingredient
APS	Advanced Photon Source
AUC	Analytical ultracentrifugation
BA12-50 pSar	Didodecyl amine initiated polysarcosine (chain length =44)
BSA	Bovine serum albumin
c	Concentration
C16-PEG2000-Ceramide	N-palmitoyl-sphingosine-1-[succinyl[methoxy(polyethyleneglycol)2000]]
CAD	Charged aerosole detector
CARPA	Complement activation-related pseudoallergy
CD	Customized microfluidic device
COVID-19	coronavirus disease 2019
CPP	Critical process parameter
CQA	Critical quality attribute
Cryo-EM	Cryogenic electron microscopy
Cy5	Cyanine dye 5 (fluorescent dye)
D	Diffusion coefficient
D10/D50/D90	Percentile values of particle size distribution
DESY	Deutsches Elektronen Synchrotron
D_h	Hydrodynamic diameter
DLinDMA	1,2-dilinoleyloxy-N,N-dimethyl-3-aminopropane
Dlin-KC2-DMA	N,N-dimethyl-2,2-di-(9Z,12Z)-9,12-octadecadien-1-yl-1,3-dioxolane-4-ethanamine
Dlin-MC3-DMA	dilinoleylmethyl-4-dimethylaminobutyrate

DLS	Dynamic light scattering
DMEM/F12	Dulbecco´s Modified Eagle´s Medium F12
DMG-PEG2000	1,2-Dimyristoyl-sn-glycero-3-methoxypolyethylene glycol
DNA	deoxyribonucleic acid
DODAP	1,2-dioleyl-3-dimethylammonium propane
DOPC	1,2-dioleyl-sn-glycero-3-phosphocholine
DOPE	1,2-dioleyl-sn-glycero-3-phosphoethanolamine
DOTMA	1,2-di-O-octadecenyl-3-trimethylammonium propane
DPBS	Dulbeccos phosphate buffered saline
dpf	Days post fertilization
DSPC	1,2-distearoyl-sn-glycero-3-phosphocholin
EDQM	European Directorate for the Quality of Medicines & Health Care
EDTA	Ethylenediaminetetraacetic acid
EE	Encapsulation efficacy
eGFP	Enhanced green fluorescent protein
EI	Ethanol injection
ELISA	Enzyme-linked immunosorbent assay
ELS	Electrophoretic light scattering
EMA	European Medicines Agency
EMBL	European Molecular biology Laboratory
EPR effect	enhanced permeability and retention effect
FBS	Fetal bovine serum
FRR	Flow rate ratio
FWHM	Full width at half maximum
GG	Glycylglycine
HEPES	2-[4-(2-Hydroxyethyl)piperazin-1-yl]ethane-1-sulfonic acid
HIV	Human immunodeficiency virus
hPBMC	Human peripheral blood mononuclear cells
hpi	Hours post injection
HPLC	High-performance liquid chromatography
HSPC	Hydrogenated soybean phosphatidylcholine
I	intensity
i.m.	Intramuscular
i.v.	Intravenous
ID	Inner diameter

IgE, G, M	Immunoglobulin E, G, M
k_B	Boltzmann constant
kDa	Kilodalton
keV	Kilo electron volts
LC-MS	Liquid chromatography – mass spectrometry
Lipid H/SM-102	Heptadecan-9-yl-8-{(2-hydroxyethyl)[6-oxo-6-(undecyloxy)hexyl]amino}octanoate
LNP	lipid nanoparticle
LPX	Lipoplex
LS	Light scattering
Luc	Luciferase
MALS	Multi angle light scattering
MEM NEAA	Minimum Essential Medium – nonessential amino acids
mg	Milligram
min	minute
mL	Milliliter
MLV	Multilamellar large vesicle
mm	millimeter
mRNA	messenger ribonucleic acid
mV	Millivolt
MW	Molecular weight
N/P ratio	Cationic lipid to mRNA molar ratio
N_A	Avogadro´s number
NA	NanoAssemblr
ng	Nanogram
NK cells	Natural killer cell
Nm	Nanometer
NMDA	National Medical Product Administration of China
NMR	Nuclear magnetic resonance
NTA	Nanoparticle Tracking analysis
PBS	Phosphate-buffered saline
PC	Phosphatidyl choline
PCR	Polymerase chain reaction
pdb	Protein data bank
PDI	Polydispersity Index

PE	Phosphatidylethanolamine
PEG	Polyethylene glycol
Ph.Eur.	Pharmacopeia Europaea – European Pharamcopeia
pSar	Polysarcosine
PS-NP	Polystyrol nanoparticles
q	Scattering vector
q_c	q-value at peak maximum
R	radius
R^2	Squared correlation coefficient
Rg	Radius of gyration
R_h	Hydrodynamic radius
rMFI	Relative mean fluorescence intensity
RNA	ribonucleic acid
RP-HPLC	Reverse Phase- High-performance liquid chromatography
RSV	Respiratory syncytial virus
S.D.	Standard deviation
SANS	Small angle neutron scattering
SARS-CoV-2	Severe acute respiratory syndrome coronavirus 2
SASBDB	Small angle Scattering biological data bank
SAXS	small angle X-ray scattering
SEC	Size exclusion chromatography
SEM	Scanning electron microscopy
siRNA	Small interfering RNA
SR	Synchrotron radiation
SUV	Small unilamellar vesicle
TEM	Transmission electron microscopy
TFR	Total flow ratio
Thy1.1	Thymocyte differentiation antigen 1.1 (CD90.1 cell surface protein)
TNS	2-(p-toluidino)-6-naphthalene sulfonic acid
USAXS	Ultra small angle X-ray scattering
USP	United States Pharmacopeia
UTP	Uridine triphosphate
UV	Ultraviolet spectroscopy
V	Volume
w/w	Mass fraction

WAXS	Wide angle X-ray scattering
WHO	World Health Organization
ζ	Zeta potential
η	Viscosity
Θ	Half Scattering angle
λ	Wavelength
ξ	Correlation length

7 References

1. Brenner, S., Jacob, F. & Meselson, M. An unstable intermediate carrying information from genes to ribosomes for protein synthesis. *Nature* **190,** 576–581 (1961).
2. Weissman, D. mRNA transcript therapy. *Expert review of vaccines* **14,** 265–281; 10.1586/14760584.2015.973859 (2015).
3. Chabanovska, O., Galow, A.-M., David, R. & Lemcke, H. mRNA - A game changer in regenerative medicine, cell-based therapy and reprogramming strategies. *Advanced Drug Delivery Reviews* **179,** 114002; 10.1016/j.addr.2021.114002 (2021).
4. Wolff, J. A. *et al.* Direct gene transfer into mouse muscle in vivo. *Science (New York, N.Y.)* **247,** 1465–1468; 10.1126/science.1690918 (1990).
5. Sahin, U., Karikó, K. & Türeci, Ö. mRNA-based therapeutics--developing a new class of drugs. *Nature reviews. Drug discovery* **13,** 759–780; 10.1038/nrd4278 (2014).
6. Cullis, P. R. & Felgner, P. L. The 60-year evolution of lipid nanoparticles for nucleic acid delivery. *Nature reviews. Drug discovery* **23,** 709–722; 10.1038/s41573-024-00977-6 (2024).
7. Zhou, D.-W. *et al.* mRNA therapeutics for disease therapy: principles, delivery, and clinical translation. *Journal of materials chemistry. B* **11,** 3484–3510; 10.1039/d2tb02782h (2023).
8. Karikó, K. *et al.* Incorporation of pseudouridine into mRNA yields superior nonimmunogenic vector with increased translational capacity and biological stability. *Molecular therapy : the journal of the American Society of Gene Therapy* **16,** 1833–1840; 10.1038/mt.2008.200 (2008).
9. Andries, O. *et al.* N(1)-methylpseudouridine-incorporated mRNA outperforms pseudouridine-incorporated mRNA by providing enhanced protein expression and reduced immunogenicity in mammalian cell lines and mice. *Journal of controlled release : official journal of the Controlled Release Society* **217,** 337–344; 10.1016/j.jconrel.2015.08.051 (2015).
10. Barbieri, I. & Kouzarides, T. Role of RNA modifications in cancer. *Nature reviews. Cancer* **20,** 303–322; 10.1038/s41568-020-0253-2 (2020).
11. Wang, Z. *et al.* Reducing cell intrinsic immunity to mRNA vaccine alters adaptive immune responses in mice. *Molecular therapy. Nucleic acids* **34,** 102045; 10.1016/j.omtn.2023.102045 (2023).

12. Oude Blenke, E. *et al.* The Storage and In-Use Stability of mRNA Vaccines and Therapeutics: Not A Cold Case. *Journal of pharmaceutical sciences* **112,** 386–403; 10.1016/j.xphs.2022.11.001 (2023).

13. Packer, M., Gyawali, D., Yerabolu, R., Schariter, J. & White, P. A novel mechanism for the loss of mRNA activity in lipid nanoparticle delivery systems. *Nature communications* **12,** 6777; 10.1038/s41467-021-26926-0 (2021).

14. Lewis, L. M., Badkar, A. V., Cirelli, D., Combs, R. & Lerch, T. F. The Race to Develop the Pfizer-BioNTech COVID-19 Vaccine: From the Pharmaceutical Scientists' Perspective. *Journal of pharmaceutical sciences* **112,** 640–647; 10.1016/j.xphs.2022.09.014 (2023).

15. Moderna, Inc. Moderna Science & Technology Day 2022. Available at https://investors.modernatx.com/events-and-presentations/presentations/presentation-details/2022/Science-Day-2022/default.aspx.

16. Hashiba, K. *et al.* Overcoming thermostability challenges in mRNA-lipid nanoparticle systems with piperidine-based ionizable lipids. *Communications biology* **7,** 556; 10.1038/s42003-024-06235-0 (2024).

17. Matthessen, R., van Pottelberge, R., Goffin, B. & Winter, G. de. Impact of mixing and shaking on mRNA-LNP drug product quality characteristics. *Scientific reports* **14,** 19590; 10.1038/s41598-024-70680-4 (2024).

18. Mehta, D. *et al.* Vaccine preparation time, errors, satisfaction, and preference of prefilled syringes versus RSV vaccines requiring reconstitution: randomized, time and motion study. *Journal of medical economics* **27,** 887–896; 10.1080/13696998.2024.2370177 (2024).

19. Saber, N., Senti, M. E. & Schiffelers, R. M. Lipid Nanoparticles for Nucleic Acid Delivery Beyond the Liver. *Human gene therapy* **35,** 617–627; 10.1089/hum.2024.106 (2024).

20. Simonsen, J. B. Lipid nanoparticle-based strategies for extrahepatic delivery of nucleic acid therapies - challenges and opportunities. *Journal of controlled release : official journal of the Controlled Release Society* **370,** 763–772; 10.1016/j.jconrel.2024.04.022 (2024).

21. Akinc, A. *et al.* The Onpattro story and the clinical translation of nanomedicines containing nucleic acid-based drugs. *Nature nanotechnology* **14,** 1084–1087; 10.1038/s41565-019-0591-y (2019).

22. Akinc, A. *et al.* Targeted delivery of RNAi therapeutics with endogenous and exogenous ligand-based mechanisms. *Molecular therapy : the journal of the American Society of Gene Therapy* **18,** 1357–1364; 10.1038/mt.2010.85 (2010).

23. Kimura, S. & Harashima, H. On the mechanism of tissue-selective gene delivery by lipid nanoparticles. *Journal of controlled release : official journal of the Controlled Release Society* **362,** 797–811; 10.1016/j.jconrel.2023.03.052 (2023).

24. Veiga, N., Diesendruck, Y. & Peer, D. Targeted nanomedicine: Lessons learned and future directions. *Journal of controlled release : official journal of the Controlled Release Society* **355,** 446–457; 10.1016/j.jconrel.2023.02.010 (2023).

25. Cheng, Q. *et al.* Selective organ targeting (SORT) nanoparticles for tissue-specific mRNA delivery and CRISPR-Cas gene editing. *Nature nanotechnology* **15,** 313–320; 10.1038/s41565-020-0669-6. (2020).

26. Dilliard, S. A., Cheng, Q. & Siegwart, D. J. On the mechanism of tissue-specific mRNA delivery by selective organ targeting nanoparticles. *Proceedings of the National Academy of Sciences of the United States of America* **118**; 10.1073/pnas.2109256118 (2021).

27. Álvarez-Benedicto, E. *et al.* Spleen SORT LNP Generated in situ CAR T Cells Extend Survival in a Mouse Model of Lymphoreplete B Cell Lymphoma. *Angewandte Chemie (International ed. in English)* **62,** e202310395; 10.1002/anie.202310395. (2023).

28. Chatterjee, S., Kon, E., Sharma, P. & Peer, D. Endosomal escape: A bottleneck for LNP-mediated therapeutics. *Proceedings of the National Academy of Sciences of the United States of America* **121,** e2307800120; 10.1073/pnas.2307800120 (2024).

29. Cheng, M. H. Y. *et al.* Induction of Bleb Structures in Lipid Nanoparticle Formulations of mRNA Leads to Improved Transfection Potency. *Advanced materials (Deerfield Beach, Fla.)* **35,** e2303370; 10.1002/adma.202303370 (2023).

30. Simonsen, J. B. A perspective on bleb and empty LNP structures. *Journal of controlled release : official journal of the Controlled Release Society* **373,** 952–961; 10.1016/j.jconrel.2024.07.046 (2024).

31. Viger-Gravel, J. *et al.* Structure of Lipid Nanoparticles Containing siRNA or mRNA by Dynamic Nuclear Polarization-Enhanced NMR Spectroscopy. *The Journal of Physical Chemistry B* **122,** 2073–2081; 10.1021/acs.jpcb.7b10795 (2018).

32. Parot, J. *et al.* Quality assessment of LNP-RNA therapeutics with orthogonal analytical techniques. *Journal of controlled release : official journal of the Controlled Release Society* **367,** 385–401; 10.1016/j.jconrel.2024.01.037 (2024).

33. A.D. Bangham *et al.* Diffusion of univalent ions across the lamellae of swollen phospholipids. *Journal of molecular biology* **13,** 238–252; 10.1016/S0022-2836(65)80093-6 (1965).

34. Gregoriadis, G. Enzyme Entrapment in Liposomes. *FEBS Letters* **14,** 95–99 (1971).

35. Gregoriadis, G. Liposomes as Carriers of Enzymes and Proteins in Medicine. In *Biomedical Applications of Immobilized Enzymes and Proteins,* edited by T. M. S. Chang (Springer US, Boston, MA, 1977), pp. 191–218.

36. Tyrrell, D. A., Heath, T. D., Colley, C. M. & Ryman, B. E. New aspects of liposomes. *Biochimica et biophysica acta* **457,** 259–302; 10.1016/0304-4157(76)90002-2 (1976).

37. Colley, C. M. & Ryman, B. E. The liposome: From membrane model to therapeutic agent. *Trends in Biochemical Sciences* **1,** 203–205; 10.1016/S0968-0004(76)80030-8 (1976).

38. Kaye, S. B. & Richardson, V. J. Potential of liposomes as drug-carriers in cancer chemotherapy: a review. *Cancer chemotherapy and pharmacology* **3,** 81–85; 10.1007/BF00254977 (1979).

39. Torchilin, V. P. Liposomes as targetable drug carriers. *Critical reviews in therapeutic drug carrier systems* **2,** 65–115 (1985).

40. Gabizon, A. A. Liposome circulation time and tumor targeting: implications for cancer chemotherapy. *Advanced Drug Delivery Reviews* **16,** 285–294; 10.1016/0169-409X(95)00030-B (1995).

41. Abuchowski, A., van Es, T., Palczuk, N. C. & Davis, F. F. Alteration of immunological properties of bovine serum albumin by covalent attachment of polyethylene glycol. *Journal of Biological Chemistry* **252,** 3578–3581; 10.1016/S0021-9258(17)40291-2 (1977).

42. Klibanov, A. L., Maruyama, K., Torchilin, V. P. & Huang, L. Amphipathic polyethyleneglycols effectively prolong the circulation time of liposomes. *FEBS Letters* **268,** 235–237; 10.1016/0014-5793(90)81016-H (1990).

43. Papahadjopoulos, D. *et al.* Sterically stabilized liposomes: improvements in pharmacokinetics and antitumor therapeutic efficacy. *Proceedings of the National Academy of Sciences of the United States of America* **88,** 11460–11464; 10.1073/pnas.88.24.11460 (1991).

44. Working, P. K. *et al.* Pharmacokinetics, Biodistribution and Therapeutic Efficacy of Doxorubicin Encapsulated in Stealth® Liposomes (Doxil®). *Journal of Liposome Research* **4,** 667–687; 10.3109/08982109409037065 (1994).

45. Barenholz, Y. Doxil®--the first FDA-approved nano-drug: lessons learned. *Journal of controlled release : official journal of the Controlled Release Society* **160,** 117–134; 10.1016/j.jconrel.2012.03.020 (2012).

46. Senior, J., Delgado, C., Fisher, D., Tilcock, C. & Gregoriadis, G. Influence of surface hydrophilicity of liposomes on their interaction with plasma protein and clearance from the circulation: studies with poly(ethylene glycol)-coated vesicles. *Biochimica et biophysica acta* **1062,** 77–82; 10.1016/0005-2736(91)90337-8 (1991).

47. Working, P. K. & Dayan, A. D. Pharmacological-toxicological expert report. CAELYX. (Stealth liposomal doxorubicin HCl). *Human & experimental toxicology* **15,** 751–785 (1996).

48. Tenchov, R., Bird, R., Curtze, A. E. & Zhou, Q. Lipid Nanoparticles─From Liposomes to mRNA Vaccine Delivery, a Landscape of Research Diversity and Advancement. *ACS nano* **15,** 16982–17015; 10.1021/acsnano.1c04996 (2021).

49. Bulbake, U., Doppalapudi, S., Kommineni, N. & Khan, W. Liposomal Formulations in Clinical Use: An Updated Review. *Pharmaceutics* **9**; 10.3390/pharmaceutics9020012 (2017).

50. Liu, P., Chen, G. & Zhang, J. A Review of Liposomes as a Drug Delivery System: Current Status of Approved Products, Regulatory Environments, and Future Perspectives. *Molecules (Basel, Switzerland)* **27**; 10.3390/molecules27041372 (2022).

51. Giordani, S., Marassi, V., Zattoni, A., Roda, B. & Reschiglian, P. Liposomes characterization for market approval as pharmaceutical products: Analytical methods, guidelines and standardized protocols. *Journal of pharmaceutical and biomedical analysis* **236,** 115751; 10.1016/j.jpba.2023.115751 (2023).

52. Crick, F. H. On protein synthesis. *Symposia of the Society for Experimental Biology* **12,** 138–163 (1958).

53. Krieg, P. A. & Melton, D. A. Functional messenger RNAs are produced by SP6 in vitro transcription of cloned cDNAs. *Nucleic acids research* **12,** 7057–7070; 10.1093/nar/12.18.7057 (1984).

54. Hald Albertsen, C. *et al.* The role of lipid components in lipid nanoparticles for vaccines and gene therapy. *Advanced Drug Delivery Reviews* **188,** 114416; 10.1016/j.addr.2022.114416 (2022).

55. Dimitriadis, G. J. Entrapment of ribonucleic acids in liposomes. *FEBS Letters* **86,** 289–293; 10.1016/0014-5793(78)80582-1 (1978).

56. Felgner, P. L. *et al.* Lipofection: a highly efficient, lipid-mediated DNA-transfection procedure. *Proceedings of the National Academy of Sciences of the United States of America* **84,** 7413–7417; 10.1073/pnas.84.21.7413 (1987).

57. Farhood, H. *et al.* Cationic liposomes for direct gene transfer in therapy of cancer and other diseases. *Annals of the New York Academy of Sciences* **716,** 23-34; discussion 34-5; 10.1111/j.1749-6632.1994.tb21701.x (1994).

58. Dass, C. R. Lipoplex-mediated delivery of nucleic acids: factors affecting in vivo transfection. *Journal of molecular medicine (Berlin, Germany)* **82,** 579–591; 10.1007/s00109-004-0558-8 (2004).

59. Landesman-Milo, D. & Peer, D. Toxicity profiling of several common RNAi-based nanomedicines: a comparative study. *Drug delivery and translational research* **4,** 96–103; 10.1007/s13346-013-0158-7 (2014).

60. Chonn, A., Cullis, P. R. & Devine, D. V. The role of surface charge in the activation of the classical and alternative pathways of complement by liposomes. *The Journal of Immunology* **146,** 4234–4241; 10.4049/jimmunol.146.12.4234 (1991).

61. Wheeler, J. J. *et al.* Stabilized plasmid-lipid particles: construction and characterization. *Gene therapy* **6,** 271–281; 10.1038/sj.gt.3300821 (1999).

62. Lv, H., Zhang, S., Wang, B., Cui, S. & Yan, J. Toxicity of cationic lipids and cationic polymers in gene delivery. *Journal of controlled release : official journal of the Controlled Release Society* **114,** 100–109; 10.1016/j.jconrel.2006.04.014 (2006).

63. Semple, S. C. *et al.* Efficient encapsulation of antisense oligonucleotides in lipid vesicles using ionizable aminolipids: formation of novel small multilamellar vesicle structures. *Biochimica et biophysica acta* **1510,** 152–166; 10.1016/S0005-2736(00)00343-6 (2001).

64. Walsh, E. E. *et al.* Safety and Immunogenicity of Two RNA-Based Covid-19 Vaccine Candidates. *The New England journal of medicine* **383,** 2439–2450; 10.1056/NEJMoa2027906 (2020).

65. Felgner, P. L. *et al.* Nomenclature for synthetic gene delivery systems. *Human gene therapy* **8,** 511–512; 10.1089/hum.1997.8.5-511 (1997).

66. Nele, V., Campani, V., Alia Moosavian, S. & Rosa, G. de. Lipid nanoparticles for RNA delivery: Self-assembling vs driven-assembling strategies. *Advanced Drug Delivery Reviews* **208,** 115291; 10.1016/j.addr.2024.115291 (2024).

67. Kranz, L. M. *et al.* Systemic RNA delivery to dendritic cells exploits antiviral defence for cancer immunotherapy. *Nature* **534,** 396–401; 10.1038/nature18300 (2016).

68. Lee, J. & Ahn, H. J. PEGylated DC-Chol/DOPE cationic liposomes containing KSP siRNA as a systemic siRNA delivery Carrier for ovarian cancer therapy. *Biochemical and biophysical research communications* **503,** 1716–1722; 10.1016/j.bbrc.2018.07.104 (2018).

69. Sahin, U. *et al.* An RNA vaccine drives immunity in checkpoint-inhibitor-treated melanoma. *Nature* **585,** 107–112; 10.1038/s41586-020-2537-9 (2020).

70. Heyes, J., Palmer, L., Bremner, K. & MacLachlan, I. Cationic lipid saturation influences intracellular delivery of encapsulated nucleic acids. *Journal of controlled release : official journal of the Controlled Release Society* **107,** 276–287; 10.1016/j.jconrel.2005.06.014 (2005).

71. Cheng, X. & Lee, R. J. The role of helper lipids in lipid nanoparticles (LNPs) designed for oligonucleotide delivery. *Advanced Drug Delivery Reviews* **99,** 129–137; 10.1016/j.addr.2016.01.022 (2016).

72. Jeffs, L. B. *et al.* A scalable, extrusion-free method for efficient liposomal encapsulation of plasmid DNA. *Pharmaceutical research* **22,** 362–372; 10.1007/s11095-004-1873-z (2005).

73. Semple, S. C. *et al.* Rational design of cationic lipids for siRNA delivery. *Nature biotechnology* **28,** 172–176; 10.1038/nbt.1602 (2010).

74. Jayaraman, M. *et al.* Maximizing the Potency of siRNA Lipid Nanoparticles for Hepatic Gene Silencing In Vivo**. *Angewandte Chemie* **124,** 8657–8661; 10.1002/ange.201203263 (2012).

75. Pardi, N. *et al.* Expression kinetics of nucleoside-modified mRNA delivered in lipid nanoparticles to mice by various routes. *Journal of controlled release : official journal of the Controlled Release Society* **217,** 345–351; 10.1016/j.jconrel.2015.08.007 (2015).

76. Maier, M. A. *et al.* Biodegradable lipids enabling rapidly eliminated lipid nanoparticles for systemic delivery of RNAi therapeutics. *Molecular therapy : the journal of the American Society of Gene Therapy* **21,** 1570–1578; 10.1038/mt.2013.124 (2013).

77. Gruner, S. M., Cullis, P. R., Hope, M. J. & Tilcock, C. P. Lipid polymorphism: the molecular basis of nonbilayer phases. *Annual review of biophysics and biophysical chemistry* **14,** 211–238; 10.1146/annurev.bb.14.060185.001235 (1985).

78. Hassett, K. J. *et al.* Optimization of Lipid Nanoparticles for Intramuscular Administration of mRNA Vaccines. *Molecular therapy. Nucleic acids* **15,** 1–11; 10.1016/j.omtn.2019.01.013 (2019).

79. Buschmann, M. D. *et al.* Nanomaterial Delivery Systems for mRNA Vaccines. *Vaccines* **9**; 10.3390/vaccines9010065 (2021).

80. Breda, L. *et al.* In vivo hematopoietic stem cell modification by mRNA delivery. *Science (New York, N.Y.)* **381,** 436–443; 10.1126/science.ade6967 (2023).

81. Rurik, J. G. *et al.* CAR T cells produced in vivo to treat cardiac injury. *Science (New York, N.Y.)* **375,** 91–96; 10.1126/science.abm0594 (2022).

82. Rybak, S. L. & Murphy, R. F. Primary cell cultures from murine kidney and heart differ in endosomal pH. *J. Cell. Physiol.* **176,** 216–222; 10.1002/(SICI)1097-4652(199807)176:1<216::AID-JCP23>3.0.CO;2-3 (1998).

83. Mehta, M. *et al.* Lipid-Based Nanoparticles for Drug/Gene Delivery: An Overview of the Production Techniques and Difficulties Encountered in Their Industrial Development. *ACS materials Au* **3,** 600–619; 10.1021/acsmaterialsau.3c00032 (2023).

84. Bangham, A. D., Gier, J. de & Greville, G. D. Osmotic properties and water permeability of phospholipid liquid crystals. *Chemistry and physics of lipids* **1,** 225–246; 10.1016/0009-3084(67)90030-8 (1967).

85. Patil, Y. P. & Jadhav, S. Novel methods for liposome preparation. *Chemistry and physics of lipids* **177,** 8–18; 10.1016/j.chemphyslip.2013.10.011 (2014).

86. Lasch, J., Weissig, V. & Brandl, M. Preparation of liposomes. In *Liposomes. Second Edition - A Practical Approach,* edited by V. P. Torchilin & V. Weissig (2010), pp. 3–29.

87. Maeki, M., Uno, S., Niwa, A., Okada, Y. & Tokeshi, M. Microfluidic technologies and devices for lipid nanoparticle-based RNA delivery. *Journal of controlled release : official journal of the Controlled Release Society* **344,** 80–96; 10.1016/j.jconrel.2022.02.017 (2022).

88. Bi, D. *et al.* On the Influence of Fabrication Methods and Materials for mRNA-LNP Production: From Size and Morphology to Internal Structure and mRNA Delivery Performance In Vitro and In Vivo. *Advanced healthcare materials* **13,** e2401252; 10.1002/adhm.202401252 (2024).

89. Wilhelmy, C. *et al.* Polysarcosine-Functionalized mRNA Lipid Nanoparticles Tailored for Immunotherapy. *Pharmaceutics* **15**; 10.3390/pharmaceutics15082068 (2023).

90. Shepherd, S. J., Issadore, D. & Mitchell, M. J. Microfluidic formulation of nanoparticles for biomedical applications. *Biomaterials* **274,** 120826; 10.1016/j.biomaterials.2021.120826 (2021).

91. Jahn, A., Vreeland, W. N., Gaitan, M. & Locascio, L. E. Controlled vesicle self-assembly in microfluidic channels with hydrodynamic focusing. *Journal of the American Chemical Society* **126,** 2674–2675; 10.1021/ja0318030 (2004).

92. Mehraji, S. & DeVoe, D. L. Microfluidic synthesis of lipid-based nanoparticles for drug delivery: recent advances and opportunities. *Lab on a chip* **24,** 1154–1174; 10.1039/d3lc00821e (2024).

93. Schoenmaker, L. *et al.* mRNA-lipid nanoparticle COVID-19 vaccines: Structure and stability. *International journal of pharmaceutics* **601,** 120586; 10.1016/j.ijpharm.2021.120586 (2021).

94. Hou, X., Zaks, T., Langer, R. & Dong, Y. Lipid nanoparticles for mRNA delivery. *Nature reviews. Materials* **6,** 1078–1094; 10.1038/s41578-021-00358-0 (2021).

95. Samaridou, E., Heyes, J. & Lutwyche, P. Lipid nanoparticles for nucleic acid delivery: Current perspectives. *Advanced Drug Delivery Reviews* **154-155,** 37–63; 10.1016/j.addr.2020.06.002 (2020).

96. Carrasco, M. J. *et al.* Ionization and structural properties of mRNA lipid nanoparticles influence expression in intramuscular and intravascular administration. *Communications biology* **4,** 956; 10.1038/s42003-021-02441-2 (2021).

97. Hamilton, N. B., Arns, S., Shelley, M., Bechis, I. & Shelley, J. C. Calculating Apparent pKa Values of Ionizable Lipids in Lipid Nanoparticles. *Molecular pharmaceutics* **22,** 588–593; 10.1021/acs.molpharmaceut.4c00426 (2025).

98. Trollmann, M. F. W. & Böckmann, R. A. mRNA lipid nanoparticle phase transition. *Biophysical journal* **121,** 3927–3939; 10.1016/j.bpj.2022.08.037 (2022).

99. Uebbing, L. *et al.* Investigation of pH-Responsiveness inside Lipid Nanoparticles for Parenteral mRNA Application Using Small-Angle X-ray Scattering. *Langmuir : the ACS journal of surfaces and colloids* **36,** 13331–13341; 10.1021/acs.langmuir.0c02446 (2020).

100. Yan, X. *et al.* The role of apolipoprotein E in the elimination of liposomes from blood by hepatocytes in the mouse. *Biochemical and biophysical research communications* **328,** 57–62; 10.1016/j.bbrc.2004.12.137 (2005).

101. Paramasivam, P. *et al.* Endosomal escape of delivered mRNA from endosomal recycling tubules visualized at the nanoscale. *The Journal of cell biology* **221**; 10.1083/jcb.202110137 (2022).

102. Hagedorn, L., Jürgens, D. C., Merkel, O. M. & Winkeljann, B. Endosomal escape mechanisms of extracellular vesicle-based drug carriers: lessons for lipid nanoparticle design. *Extracellular vesicles and circulating nucleic acids* **5,** 344–357; 10.20517/evcna.2024.19 (2024).

103. Kauffman, K. J. *et al.* Optimization of Lipid Nanoparticle Formulations for mRNA Delivery in Vivo with Fractional Factorial and Definitive Screening Designs. *Nano letters* **15,** 7300–7306; 10.1021/acs.nanolett.5b02497 (2015).

104. Koltover, I., Salditt, T., Rädler, J. O. & Safinya, C. R. An inverted hexagonal phase of cationic liposome-DNA complexes related to DNA release and delivery. *Science (New York, N.Y.)* **281,** 78–81; 10.1126/science.281.5373.78 (1998).

105. Yan, X., Scherphof, G. L. & Kamps, J. A. A. M. Liposome opsonization. *Journal of Liposome Research* **15,** 109–139; 10.1081/LPR-64971 (2005).

106. Krause, M. R. & Regen, S. L. The structural role of cholesterol in cell membranes: from condensed bilayers to lipid rafts. *Accounts of chemical research* **47,** 3512–3521; 10.1021/ar500260t (2014).

107. Kulkarni, J. A., Witzigmann, D., Leung, J., Tam, Y. Y. C. & Cullis, P. R. On the role of helper lipids in lipid nanoparticle formulations of siRNA. *Nanoscale* **11,** 21733–21739; 10.1039/c9nr09347h (2019).

108. Patel, S. *et al.* Naturally-occurring cholesterol analogues in lipid nanoparticles induce polymorphic shape and enhance intracellular delivery of mRNA. *Nature communications* **11,** 983; 10.1038/s41467-020-14527-2 (2020).

109. Herrera, M., Kim, J., Eygeris, Y., Jozic, A. & Sahay, G. Illuminating endosomal escape of polymorphic lipid nanoparticles that boost mRNA delivery. *Biomaterials science* **9,** 4289–4300; 10.1039/d0bm01947j (2021).

110. Patel, S. K. *et al.* Hydroxycholesterol substitution in ionizable lipid nanoparticles for mRNA delivery to T cells. *Journal of controlled release : official journal of the Controlled Release Society* **347,** 521–532; 10.1016/j.jconrel.2022.05.020 (2022).

111. Patel, S. K. *et al.* Bile acid-containing lipid nanoparticles enhance extrahepatic mRNA delivery. *Theranostics* **14,** 1–16; 10.7150/thno.89913 (2024).

112. Jung, O. *et al.* Modulating Lipid Nanoparticles with Histidinamide-Conjugated Cholesterol for Improved Intracellular Delivery of mRNA. *Advanced healthcare materials* **13,** e2303857; 10.1002/adhm.202303857 (2024).

113. Mui, B. L. *et al.* Influence of Polyethylene Glycol Lipid Desorption Rates on Pharmacokinetics and Pharmacodynamics of siRNA Lipid Nanoparticles. *Molecular therapy. Nucleic acids* **2,** e139; 10.1038/mtna.2013.66 (2013).

114. Lokugamage, M. P. *et al.* Optimization of lipid nanoparticles for the delivery of nebulized therapeutic mRNA to the lungs. *Nature biomedical engineering* **5,** 1059–1068; 10.1038/s41551-021-00786-x (2021).

115. Belliveau, N. M. *et al.* Microfluidic Synthesis of Highly Potent Limit-size Lipid Nanoparticles for In Vivo Delivery of siRNA. *Molecular therapy. Nucleic acids* **1,** e37; 10.1038/mtna.2012.28 (2012).

116. Tenchov, R., Sasso, J. M. & Zhou, Q. A. PEGylated Lipid Nanoparticle Formulations: Immunological Safety and Efficiency Perspective. *Bioconjugate chemistry* **34,** 941–960; 10.1021/acs.bioconjchem.3c00174 (2023).

117. Shi, D. *et al.* To PEGylate or not to PEGylate: Immunological properties of nanomedicine's most popular component, polyethylene glycol and its alternatives. *Advanced Drug Delivery Reviews* **180,** 114079; 10.1016/j.addr.2021.114079 (2022).

118. Verhoef, J. J. F., Carpenter, J. F., Anchordoquy, T. J. & Schellekens, H. Potential induction of anti-PEG antibodies and complement activation toward PEGylated therapeutics. *Drug discovery today* **19,** 1945–1952; 10.1016/j.drudis.2014.08.015 (2014).

119. Deuker, M. F. S., Mailänder, V., Morsbach, S. & Landfester, K. Anti-PEG antibodies enriched in the protein corona of PEGylated nanocarriers impact the cell uptake. *Nanoscale horizons* **8,** 1377–1385; 10.1039/d3nh00198a (2023).

120. Hoang Thi, T. T. *et al.* The Importance of Poly(ethylene glycol) Alternatives for Overcoming PEG Immunogenicity in Drug Delivery and Bioconjugation. *Polymers* **12**; 10.3390/polym12020298 (2020).

121. Birke, A., Ling, J. & Barz, M. Polysarcosine-containing copolymers: Synthesis, characterization, self-assembly, and applications. *Progress in Polymer Science* **81,** 163–208; 10.1016/j.progpolymsci.2018.01.002 (2018).

122. Weber, B., Birke, A., Fischer, K., Schmidt, M. & Barz, M. Solution Properties of Polysarcosine: From Absolute and Relative Molar Mass Determinations to Complement Activation. *Macromolecules* **51,** 2653–2661; 10.1021/acs.macromol.8b00258 (2018).

123. Chen, H. & Zhang, Q. Polypeptides as alternatives to PEGylation of therapeutic agents. *Expert opinion on drug delivery* **21,** 1–12; 10.1080/17425247.2023.2297937 (2024).

124. Son, K. *et al.* Evasion of the accelerated blood clearance phenomenon by polysarcosine coating of liposomes. *Journal of controlled release : official journal of the Controlled Release Society* **322,** 209–216; 10.1016/j.jconrel.2020.03.022 (2020).

125. Nogueira, S. S. *et al.* Polysarcosine-Functionalized Lipid Nanoparticles for Therapeutic mRNA Delivery. *ACS Appl. Nano Mater.* **3,** 10634–10645; 10.1021/acsanm.0c01834 (2020).

126. US Food and Drug Administration. Liposome Drug Products: Chemistry, Manufacturing, and Controls; Human Pharmacokinetics and Bioavailability; and Labeling Documentation. *Guidance for Industry.(CDER)* (2018).

127. World Health Organization. Evaluation of the quality, safety and efficacy of messenger RNA vaccines for the prevention of infectious diseases: regulatory considerations. Available at https://www.who.int/publications/m/item/evaluation-of-the-quality-safety-and-efficacy-of-messenger-rna-vaccines-for-the-prevention-of-infectious-diseases-regulatory-considerations (2021).

128. United States Pharmacopeia. Analytical Procedures for Quality of mRNA Vaccines and Therapeutics. Draft Guidelines: 3rd Edition. Available at https://www.uspnf.com/notices/analytical-procedures-mrna-vaccines-20240802 (2024).

129. EDQM. Text for comment 36.2. Available at https://pharmeuropa.edqm.eu/app/Archives/content/Archives-0/Pharmeuropa3602E.pdf (2024).

130. Hu, C. *et al.* Research progress on the quality control of mRNA vaccines. *Expert review of vaccines* **23,** 570–583; 10.1080/14760584.2024.2354251 (2024).

131. Nogueira, S. S. *et al.* Analytical techniques for the characterization of nanoparticles for mRNA delivery. *European journal of pharmaceutics and biopharmaceutics : official journal of Arbeitsgemeinschaft fur Pharmazeutische Verfahrenstechnik e.V* **198,** 114235; 10.1016/j.ejpb.2024.114235 (2024).

132. Spivak, V. B., Shahrokh, Z. & Issa, W. J. *Analysis of mrna heterogeneity and stability* (Google Patents, 2016).

133. Jones, L. J., Yue, S. T., Cheung, C. Y. & Singer, V. L. RNA quantitation by fluorescence-based solution assay: RiboGreen reagent characterization. *Analytical biochemistry* **265,** 368–374; 10.1006/abio.1998.2914 (1998).

134. Roesch, A. *et al.* Particles in Biopharmaceutical Formulations, Part 2: An Update on Analytical Techniques and Applications for Therapeutic Proteins, Viruses, Vaccines and Cells. *Journal of pharmaceutical sciences* **111,** 933–950; 10.1016/j.xphs.2021.12.011 (2022).

135. Kong, W. *et al.* Role of size, surface charge, and PEGylated lipids of lipid nanoparticles (LNPs) on intramuscular delivery of mRNA. *Journal of nanobiotechnology* **22,** 553; 10.1186/s12951-024-02812-x (2024).

136. Hassett, K. J. *et al.* Impact of lipid nanoparticle size on mRNA vaccine immunogenicity. *Journal of controlled release : official journal of the Controlled Release Society* **335,** 237–246; 10.1016/j.jconrel.2021.05.021 (2021).

137. Stetefeld, J., McKenna, S. A. & Patel, T. R. Dynamic light scattering: a practical guide and applications in biomedical sciences. *Biophysical reviews* **8,** 409–427; 10.1007/s12551-016-0218-6 (2016).

138. Torchilin, V. & Weissig, V. *Liposomes: a practical approach* (Oxford University Press, 2003).

139. Nobbmann, U. *et al.* Dynamic light scattering as a relative tool for assessing the molecular integrity and stability of monoclonal antibodies. *Biotechnology & genetic engineering reviews* **24,** 117–128; 10.1080/02648725.2007.10648095 (2007).

140. Fan, Y., Marioli, M. & Zhang, K. Analytical characterization of liposomes and other lipid nanoparticles for drug delivery. *Journal of pharmaceutical and biomedical analysis* **192,** 113642; 10.1016/j.jpba.2020.113642 (2021).

141. Wyatt, P. J. Multiangle Light Scattering: The Basic Tool for Macromolecular Characterization. *Instrumentation Science & Technology* **25,** 1–18; 10.1080/10739149709351443 (1997).

142. Wyatt, P. J. Light scattering and the absolute characterization of macromolecules. *Analytica Chimica Acta* **272,** 1–40; 10.1016/0003-2670(93)80373-S (1993).

143. Wyatt, P. J. Submicrometer Particle Sizing by Multiangle Light Scattering following Fractionation. *Journal of colloid and interface science* **197,** 9–20; 10.1006/jcis.1997.5215 (1998).

144. Giddings, J. C., Yang, F. J. & Myers, M. N. Flow-field-flow fractionation: a versatile new separation method. *Science (New York, N.Y.)* **193,** 1244–1245; 10.1126/science.959835 (1976).

145. Reschiglian, P., Zattoni, A., Roda, B., Michelini, E. & Roda, A. Field-flow fractionation and biotechnology. *Trends in biotechnology* **23,** 475–483; 10.1016/j.tibtech.2005.07.008 (2005).

146. Graewert, M. A. *et al.* Quantitative size-resolved characterization of mRNA nanoparticles by in-line coupling of asymmetrical-flow field-flow fractionation with small angle X-ray scattering. *Scientific reports* **13,** 15764; 10.1038/s41598-023-42274-z (2023).

147. Da Vela, S. *et al.* AF4-to-SAXS: expanded characterization of nanoparticles and proteins at the P12 BioSAXS beamline. *Journal of synchrotron radiation* **32,** 971–985; 10.1107/S1600577525003959 (2025).

148. Aziz, Z. *et al. Analytical Ultracentrifugation* (The Royal Society of Chemistry, 2005).

149. Vogel, R. *et al.* Measuring particle concentration of multimodal synthetic reference materials and extracellular vesicles with orthogonal techniques: Who is up to the challenge? *Journal of extracellular vesicles* **10,** e12052; 10.1002/jev2.12052 (2021).

150. Simon, C. G. *et al.* Orthogonal and complementary measurements of properties of drug products containing nanomaterials. *Journal of controlled release : official journal of the Controlled Release Society* **354,** 120–127; 10.1016/j.jconrel.2022.12.049 (2023).

151. Fröhlich, M., Brecht, V. & Peschka-Süss, R. Parameters influencing the determination of liposome lamellarity by 31P-NMR. *Chemistry and physics of lipids* **109,** 103–112; 10.1016/S0009-3084(00)00220-6 (2001).

152. Leung, A. K. K. *et al.* Lipid Nanoparticles Containing siRNA Synthesized by Microfluidic Mixing Exhibit an Electron-Dense Nanostructured Core. *The journal of physical chemistry. C, Nanomaterials and interfaces* **116,** 18440–18450; 10.1021/jp303267y (2012).

153. Yanez Arteta, M. *et al.* Successful reprogramming of cellular protein production through mRNA delivered by functionalized lipid nanoparticles. *Proceedings of the National Academy of Sciences of the United States of America* **115,** E3351-E3360; 10.1073/pnas.1720542115 (2018).

154. Sebastiani, F. *et al.* Apolipoprotein E Binding Drives Structural and Compositional Rearrangement of mRNA-Containing Lipid Nanoparticles. *ACS nano* **15,** 6709–6722; 10.1021/acsnano.0c10064 (2021).

155. Svergun, D. I., Koch, M. H. J., Timmins, P. A. & May, R. P. Basics of small angle scattering. In *Small Angle X-Ray and Neutron Scattering from Solutions of Biological Macromolecules,* edited by D. I. Svergun, M. H. J. Koch, P. A. Timmins & R. P. May (Oxford University Press2013), pp. 13–26.

156. Debye, P. Zerstreuung von Röntgenstrahlen. *Annalen der Physik* **351,** 809–823; 10.1002/andp.19153510606 (1915).

157. Glatter, O. Data evaluation in small angle scattering: calculation of the radial electron density distribution by means of indirect Fourier transformation. *Acta Phys. Austriaca;(Austria)* **47** (1977).

158. Svergun, D. I. Restoring Low Resolution Structure of Biological Macromolecules from Solution Scattering Using Simulated Annealing. *Biophysical journal* **76,** 2879–2886; 10.1016/S0006-3495(99)77443-6 (1999).

159. Franke, D. & Svergun, D. I. DAMMIF, a program for rapid ab-initio shape determination in small-angle scattering. *Applied Crystallography* **42,** 342–346 (2009).

160. Mathew, E., Mirza, A. & Menhart, N. Liquid-chromatography-coupled SAXS for accurate sizing of aggregating proteins. *Journal of synchrotron radiation* **11,** 314–318; 10.1107/S0909049504014086 (2004).

161. Jeffries, C. M. *et al.* Preparing monodisperse macromolecular samples for successful biological small-angle X-ray and neutron-scattering experiments. *Nature protocols* **11,** 2122–2153; 10.1038/nprot.2016.113 (2016).

162. Wilhelmy, C. *et al.* Direct structural investigation of pH responsiveness in mRNA lipid nanoparticles: Refining paradigms. *Journal of Controlled Release,* 113848; 10.1016/j.jconrel.2025.113848 (2025).

163. Li, S. *et al.* Payload distribution and capacity of mRNA lipid nanoparticles. *Nature communications* **13,** 5561; 10.1038/s41467-022-33157-4 (2022).

164. Lee, J. S. F. *et al.* Paving the way for affordable and equitable liposomal amphotericin B access worldwide. *The Lancet. Global health* **12,** e1552-e1559; 10.1016/S2214-109X(24)00225-0 (2024).

165. Adler-Moore, J. P., Gangneux, J.-P. & Pappas, P. G. Comparison between liposomal formulations of amphotericin B. *Medical mycology* **54,** 223–231; 10.1093/mmy/myv111 (2016).

166. Ziller, A. *et al.* Incorporation of mRNA in Lamellar Lipid Matrices for Parenteral Administration. *Molecular pharmaceutics* **15,** 642–651; 10.1021/acs.molpharmaceut.7b01022 (2018).

167. Bragg, W. H. & Bragg William L. The reflection of X-rays by crystals. *Proc. R. Soc. Lond. A* **88,** 428–438; 10.1098/rspa.1913.0040 (1913).

168. Cárdenas, M., Campbell, R. A., Yanez Arteta, M., Lawrence, M. J. & Sebastiani, F. Review of structural design guiding the development of lipid nanoparticles for nucleic acid delivery. *Current Opinion in Colloid & Interface Science* **66,** 101705; 10.1016/j.cocis.2023.101705 (2023).

169. Binici, B., Rattray, Z., Zinger, A. & Perrie, Y. Exploring the impact of commonly used ionizable and pegylated lipids on mRNA-LNPs: A combined in vitro and preclinical perspective. *Journal of controlled release : official journal of the Controlled Release Society* **377,** 162–173; 10.1016/j.jconrel.2024.11.010 (2025).

170. Escalona-Rayo, O. *et al.* In vitro and in vivo evaluation of clinically-approved ionizable cationic lipids shows divergent results between mRNA transfection and vaccine efficacy. *Biomedicine & pharmacotherapy = Biomedecine & pharmacotherapie* **165,** 115065; 10.1016/j.biopha.2023.115065 (2023).

171. Simonsen, J. B. & Larsson, P. A perspective on the apparent pKa of ionizable lipids in mRNA-LNPs. *Journal of Controlled Release,* 113879; 10.1016/j.jconrel.2025.113879 (2025).

Curriculum Vitae